Arnfinn Aas Eielsen

Topics in Control of Nanopositioning Devices

Thesis for the degree of philosophiae doctor

Trondheim, November 2012

Norwegian University of Science and Technology
Faculty of Information Technology, Mathematics and Electrical Engineering
Department of Engineering Cybernetics

NTNU
Innovation and Creativity

NTNU
Norwegian University of Science and Technology

Thesis for the degree of philosophiae doctor

Faculty of Information Technology, Mathematics and Electrical Engineering
Department of Engineering Cybernetics

ISBN 978-82-471-3949-3 (printed version)
ISBN 978-82-471-3950-9 (electronic version)
ISSN 1503-8181

ITK Report 2012-6-W

Doctoral theses at NTNU, 2012:315

Printed by NTNU-trykk

To my parents.

Summary

Nanopositioning concerns motion control with resolution down to atomic scale. Positioning devices with such a capability have applications in numerous areas in industry and science. Examples include scanning probe microscopy, adaptive optics, hard disk drive systems, and the production and inspection of high-density semiconductor designs. Scanning probe microscopy is perhaps the most prominent example, as it is a versatile tool, which can be used for imaging, metrology, and physical manipulation. In imaging applications, the achievable resolution, or accuracy, is the most important performance criterion. For metrology and manipulation, trueness is also of importance. Additionally, the maximum achievable throughput, or bandwidth, of nanopositioning systems is an important performance criterion, as it lays the foundation for fast measuring and manipulation of physical properties; capturing processes at the time scale which they occur, reducing time and cost related to metrology, and enabling fabrication of nanoscale features at an industrial scale.

Nanopostitioning devices ubiquitously use piezoelectric actuators, as such actuators enable fast and frictionless motion. Piezoelectric actuators are as such ideal for high resolution positioning tasks. Positioning devices utilizing piezoelectric actuators typically exhibit lightly damped vibration modes, as well as hysteresis and creep non-linearities. Lightly damped vibration modes limits the achievable bandwidth, and hysteresis and creep limits the trueness of such devices. In order to improve bandwidth and trueness, these phenomena can be countered using feed-forward and feedback control.

Part I of this thesis presents an adaptive feed-forward technique to compensate for the hysteresis non-linearity. It is based on the Coleman-Hodgdon model, and provides an open-loop observer for the hysteretic behavior which can be used to linearize the output of an actuator which exhibit hysteresis that can be modeled with said model. The model provides a good description of hysteresis responses that are symmetric, and the compensation method provides the best performance for stationary periodic reference trajectory signals. It is also pointed out that hysteresis can be interpreted as an uncertain gain and an input disturbance, and as such, regular feedback control using high quality position sensors can also effectively reduce the effect of hysteresis if the bandwidth is sufficiently high, and if the control law is robust towards variation in low-frequency gain. The drawback is increased position noise, due to sensor noise being amplified and fed back into to the actuation signal.

Part II concerns so-called damping and tracking control, and presents several low-order control schemes to improve bandwidth by damping lightly damped vibration modes, and by doing so, allowing for higher gain in the feedback control law. A practical tuning procedure is introduced in order to find optimal control law parameters, using an flatness criterion for the complementary sensitivity function. The effect of quantization noise due to implementation on digital signal processing equipment is investigated, and a particular simple damping and tracking control law is introduced, which consists of an integrator and a low-pass filter. The low-pass filter can be implemented using the anti-aliasing and reconstruction filters needed when using digital signal processing equipment, and only the integrator needs to be implemented digitally. The optimal tuning of this control structure turns out to limit the bandwidth of the anti-aliasing and reconstruction filters, and due to the limited bandwidth of the reconstruction filter, quantization noise is effectively attenuated. This control scheme is then coupled with a repetitive control scheme, which provides good tracking of periodic reference signals. A simple time-delay with positive feedback is a model for any periodic signal with a fixed period, and the repetitive control scheme includes this model in the feedback path, and can thus null any exogenous periodic signal with that fixed period to the error signal, due to the internal model principle. A criterion for robust stability of the damping and tracking control law combined with the repetitive control scheme is presented, which ensures stability for a prescribed unstructured uncertainty incorporating variable gain due to, among other factors, hysteresis, and high-frequency non-modeled dynamics.

Part III discusses adaptive control for arbitrary reference trajectory signals. Instrumentation used in nanopositioning systems typically allow for output feedback only, and the application of the standard framework for output feedback for dominantly linear systems, the model reference adaptive control scheme, is investigated. The model reference adaptive control scheme requires the usage of an online adaptive law in order to learn the parameter values of an uncertain model, and two common parameter identification schemes, the recursive least-squares method and the extended Kalman filter, are assessed for their ability to learn the parameters of a mass-spring-damper system using experimental data recorded using a nanopositioning device with two different payload configurations in open-loop. The result is a special pre-filter, which is demonstrated to improve parameter convergence. The model reference adaptive control scheme is then assessed experimentally, and it is demonstrated that a further refinement of the pre-filter is needed in order to obtain reasonable parameter convergence in closed-loop. An integral adaptive law is used in this case, in order to improve the convergence rate of the parameter estimates.

The main contributions of the thesis are methods for feed-forward and feedback control that can achieve similar or better performance than existing methods, but with lower complexity, which improves practical implementability.

Contents

Preface

This thesis is submitted in partial fulfillment of the requirements for the degree of philosophiae doctor (PhD) at the Norwegian University of Science and Technology (NTNU).

The work for this thesis has mainly been carried out at the Department of Engineering Cybernetics, in the period from October 2008 to August 2012. My supervisor has been Prof. Jan Tommy Gravdahl, and my co-supervisors have been Prof. Kristin Ytterstad Pettersen, and Prof. Tomas Tybell.

Funding for the PhD position, as well as laboratory equipment and travel, has been provided by the Norwegian University of Science and Technology, the Department of Engineering Cybernetics, and the Research Council of Norway.

During this period I have had the privilege of two extended visits, to Prof. S. O. Reza Moheimani at the Laboratory for Dynamics and Control of Nano Systems and Dr. Andrew J. Fleming at Centre for Complex Dynamic Systems and Control, both at the University of Newcastle, Australia, as well as to Assoc. Prof. Kam K. Leang and his student Mr. Brian Kenton at the Mechanical Engineering Department at the University of Nevada, Reno, USA. I am very grateful for their hospitality.

I am also grateful for the opportunity for some shorter visits. I visited Prof. Georg Schitter, which at the time was employed at the Delft Center for Systems and Control at the Delft Technical University, the Netherlands, and his former students Dr. Stephan Kuiper and Dr. Jan Roelf van Hulzen, I had a great tour of Leiden University and some of the laboratory facilities there with Dr. Gertjan van Baarle from Leiden Probe Microscopy BV, as well as a visit to Prof. Christoph Ament and his former student Dr. Arvid Amthor at the Faculty of Computer Science and Automation at the Ilmenau University of Technology, Germany.

I also had the pleasure of working with my good colleague for three years, Dr. Mernout Burger, now employed at the Delft University of Technology, as well as as Dr. Tomáš Polóni from the Slovak University of Technology in Bratislava, and Prof. Tor Arne Johansen and Dr. Marialena Vagia at our department.

A special ‘thank you’ goes to the technical staff at our department, especially Terje Haugen, Per Inge Snildal, Stefano Bertelli, John Olav Horrigmo, Torkel Hansen and Rune Mellingseter, who provided invaluable aid in building, operating, and maintaining the lab equipment.

I would also like to thank all my fellow PhD students at the department, present and former. Christian, Christoph, Serge, Øyvind, Anders, Milan, Giancarlo, Esten, Espen, Aleksander, Walter, Mark, Mladen, and all the rest. In total it has been a sizable amount of beer, cake, and bad jokes.

Lastly, I would like to thank my parents, Anne-Kari and Steinar, for all their support and help through four eventful years.

Arnfinn Aas Eielsen
Trondheim, November 2012

Chapter 1

Introduction

1.1 Nanopositioning

Nanopositioning is a neologism used to refer to positioning devices that have the capability to generate mechanical displacements down to atomic scale resolution. Positioning devices with such a capability have applications in numerous areas in science and industry. Perhaps the most prominent example of motion control with this type of resolution requirement is found in the field of scanning probe microscopy [186]. Other application areas of high-resolution motion control can be found in adaptive optics [217], in modern hard disk drive systems [4], and in the production and inspection of high-density semiconductor designs [99].

Scanning probe microscopy is a collective term for a vast array of mechanical surface interrogation and manipulation techniques, which can be done in either a vacuum, air, or a liquid. Common to all the techniques is the need to position a physical probe with extremely high resolution.

In modern scanning probe microscopy instruments, this is typically done by using a lateral positioning mechanism to allow positioning of a point on a sample under a separate, vertically actuated probe. The probe, typically attached to the tip of a small cantilever, can then interact with the surface at that point. Due to the versatility of scanning probe microscopy instruments, it has become an important tool for surface imaging, metrology, and physical manipulation at the nanoscale.

The origin of the field of scanning probe microscopy, appears to be the invention of the Topografiner [228]. The Topografiner measured the field emission current between a probe and the surface of an electrically conducting sample, and used it as a distance measurement. By scanning the surface in a raster pattern it could then be used to build a topographic image of the surface with nanoscale resolution. Since then, notable extensions of the operating principles introduced by the Topografiner, include the scanning tunneling microscope [30], resolving features with atomic resolution [31], the atomic force microscope [32], manipulation of single atoms [72], and so-called video-rate imaging [11].

Imaging applications of scanning probe microscopy aim at collecting qualitative information about the sample surface. Examples of such information can be the topology, various optical, electrical, and magnetic properties, and mechanical

properties, such as friction and roughness. In scanning probe microscopy, these properties are measured using specialized probes and various types of modulation of the probe.

For imaging, the resolution, or precision, is one of the most important performance specifications. This is because it is of importance to detect the smallest possible features. For metrology applications, often the same surface information is sought, but in this context, the trueness of the measured quantities is also of importance. The trueness accounts for the closeness between the measured mean value and the true value of the physical property. Trueness is also important for manipulation applications, in order to repeatedly produce features according to specifications.

For a survey of scanning probe microscopy imaging, metrology, and manipulation applications and techniques, see [28, 41, 52, 59, 189, 205].

For applications of scanning probe microscopy, one of the main challenges is to increase the bandwidth, or throughput, for both measurement and manipulation. Higher throughput is needed to, *e.g.*, reduce the amount of time used to generate a set of measurements, capture the time evolution of physical processes, reduce costs related to metrology in industrial processes, and to enable fabrication of nanoscale features at an industrial scale [44, 58, 97, 191, 209].

1.2 Instrumentation

1.2.1 Positioning Devices

The positioning devices used in scanning probe microscopy systems span from long-range voice-coil actuated devices [8, 19, 149] to shorter range devices using piezoelectric actuators [29, 30, 120, 131, 183, 184, 200].

The mechanical design of nanopositioning stages provides fundamental limitations to the achievable performance for any control scheme. The main performance specifications for nanopositioning stages are the range and the dominant vibration mode, which preferably is the first vibration mode. The resonant frequency of the dominant vibration mode is usually the limiting factor for the attainable bandwidth. One reason is that it can be difficult to control higher-order vibration modes, as they might be practically uncontrollable; having mode shapes and directions that are weakly coupled with the mounted actuator. Another reason is that the control signal amplitude and the amount of power required to drive the system above the dominant resonance can become prohibitive, as driving amplifiers will eventually saturate [83, 137].

As a rule of thumb, there is an inverse relationship between range and bandwidth, thus to achieve high bandwidth, the range is usually limited [44]. The bandwidth can roughly be estimated to be equal to the frequency of the dominant vibration mode of the mechanical structure.

The Topografiner and the scanning tunneling microscope used a tripod configuration of piezoelectric stack actuators [30, 228]. The piezoelectric tube actuator was later introduced as an improvement over this design [29]. Compared to the tripod actuator, the tube actuator increased the achievable range, it had a higher dominant resonant frequency, it experienced less influence from environmental vibration

disturbances, it had smaller physical dimensions, a simpler design which was easier to manufacture and assemble, and it was less susceptible to thermal drift. As such, it is perhaps the most proliferate mechanism in the first generations of scanning probe microscopy systems [5]. A comprehensive analytical model for piezoelectric tube actuators is presented in [74], and a finite-element model is discussed in [147].

Newer device designs use flexure guided mechanisms [120, 131, 200, 223, 225], which provide further improvements; as flexure guided mechanisms allow for longer range, a higher dominant resonant frequency, and experience less cross-coupling and non-linearity in the actuation directions. The main disadvantages are a less compact design, and in some cases a more elaborate manufacturing process, sometimes requiring specialized machining tools, such as a wire electrical discharge machine.

Voice coil actuators typically allow for nanopositioning devices with longer range, compared to devices using piezoelectric actuators [19, 51, 149]. These devices can then accommodate for large samples and large surface features. Depending on the design, these devices generally have a much lower bandwidth than devices using piezoelectric actuators. The designs in [19, 51] uses flexures to guide the motion, but for longer range motion, guides in the form of bearings is used [149], which adds the additional problem of friction [8].

1.2.2 Positioning Devices using Piezoelectric Actuators

As piezoelectric actuators can produce large forces, provide frictionless motion, and the resolution is only limited by instrumentation noise, they are ideal for high-bandwidth, high-resolution positioning. As such, they are ubiquitous in nanopositioning devices. An introduction to standard piezoelectric transducer modeling is found in Appendix A.

Mechanical vibrations

A positioning device utilizing piezoelectric actuators typically exhibits lightly damped vibration modes. This is a disadvantage, as it limits the usable bandwidth because reference signals with high frequency components will excite the vibration modes, prohibiting accurate positioning. It also makes the device susceptible to environmental vibration disturbances, such as sound and floor vibrations. An introduction to standard mechanical vibration modeling is found in Appendix B.

Hysteresis and creep

The hysteresis and creep non-linearities in piezoelectric actuators is an additional challenge. These are loss phenomena that prevent the system from having a linear response, introducing bounded input disturbances dependent on the driving voltage signal.

Creep is mainly a problem when applying feed-forward control for low-frequency and static positioning, as the phenomenon can be observed as a slow creeping motion after applying, *e.g.*, a voltage step to the piezoelectric actuator. An example of this kind of response is shown in Fig. 1.1.

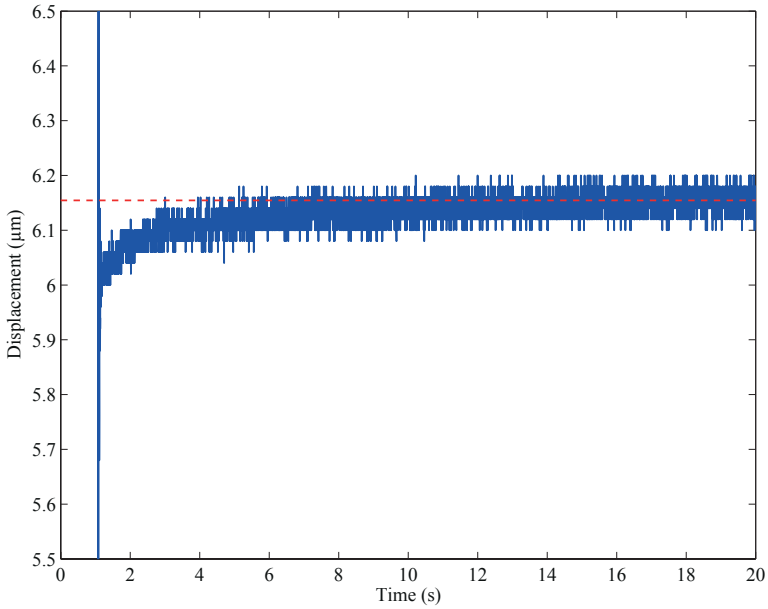

Figure 1.1: Piezoelectric actuator creep response to a voltage step.

Hysteresis is a problem for any time-varying reference signal tracking, because it introduces a rate-independent lag when applying a voltage signal to the actuator, and consequently to the resulting displacement of the piezoelectric transducer. This lag can be interpreted as a bounded input disturbance to the system. Examples of hysteretic responses to sinusoidal voltage signals are shown in Fig. 1.2a.

An introduction to common hysteresis and creep models is found in Appendix C.

Parameter and model uncertainty

The mechanical vibration dynamics of a point on a positioning device structure can be modeled with very high accuracy using linear ordinary differential equations for specific operating points. However, there are several sources of parameter and model uncertainty.

Hysteresis, in addition to introducing an input disturbance, change the effective gain of the actuator depending on the amplitude and frequency of the driving voltage signal [107, 171]. This is illustrated in Fig. 1.2b. The piezoelectric actuator gain is also dependent on temperature, and reduces over time due to depolarization [25].

In addition, users typically need to position payloads of various masses, thus resonant frequencies and the effective gain of the mechanical structure change as a result [140].

The observed dynamic response is also affected by how well the sensors can be co-located with the actuators [172]. Also, the dominant vibration mode of the positioning device dynamics is usually designed to have a shape that provides motion in a desired direction, and higher-order vibration modes are likely to have

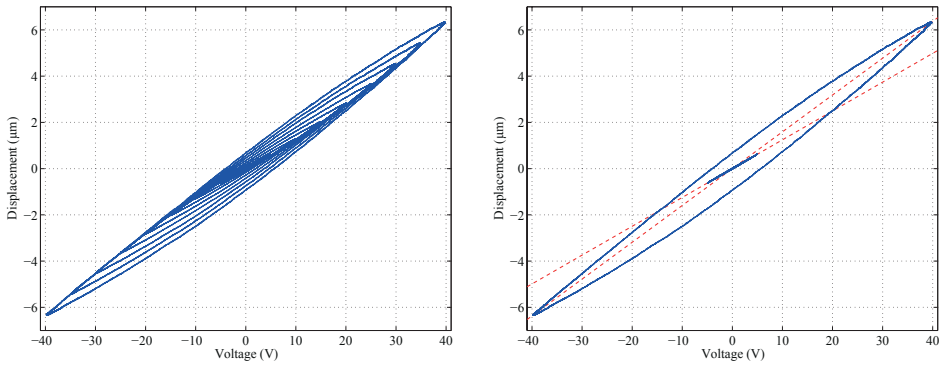

(a) Ensemble of measured hysteresis responses for different voltage signal amplitudes.

(b) Change in average linear gain for low amplitude voltage signals and high amplitude voltage signals.

Figure 1.2: Piezoelectric actuator hysteretic responses to sinusoidal voltage signals.

shapes and directions that will make them difficult to control using the mounted actuator. Thus, the model structure might be uncertain and it will have practically uncontrollable modes.

1.2.3 High-Resolution Sensors

To enable high-resolution motion control, high-resolution sensors are necessary. They are needed for system identification when utilizing feed-forward control, and the performance of the sensor determines the precision and trueness achievable when using feedback control.

The noise specifications for a sensor is in general much stricter when applied in feedback control, as the noise will be fed back to the input and will increase the overall noise level in the system. For system identification, noise is of less importance, and can then often be reduced substantially by averaging.

The most common types of sensors found in nanopositioning devices are inductive probes [49], capacitive probes [78, 85], piezoelectric transducers [78, 81, 84, 158], strain gauges [81, 192, 195], linear variable differential transformers [188], optical linear encoders [20, 131], and the Michelson interferometer [149]. Vertical control of the probe in modern scanning probe microscopy instruments is almost exclusively done using an optical lever and a charge-coupled device [5].

System identification for the dynamic models is often done using displacement sensors and dynamic signal analyzer instruments, applying swept-sine or broadband noise excitation signals. The first generations of scanning probe microscopy instruments did not have displacement sensors for the lateral motion, but it is possible in some circumstances to perform system identification for the lateral dynamics using vertical measurements from the probe [39, 43].

1.2.4 The Signal Chain

The instrumentation dynamics of the components in the signal chain of the control system should also be considered. The positioning device response will be influenced by the dynamics, saturation limits, and time-delays of amplifiers, sensors, anti-aliasing and reconstruction filters, as well as digital-to-analog and analog-to-digital converters. Some of these components exhibit significant non-linear responses which can introduce systematic errors and noise. Typical examples include bad calibration of measurement instruments, which measurement principles exhibit a non-linear characteristic, and noise due to sampling, quantization, and limited numeric representation precision. These are general instrumentation and measurement limitations, and an introduction can be found in [163].

The implementation of the control laws can typically be done using digital signal processing equipment, or analog circuit elements. Digital control is the norm for most modern control systems [9], although the control systems for early scanning probe microscopy instruments was realized using traditional analog operational amplifier circuits [130].

Microprocessors or microcontrollers for high-bandwidth digital control is limited by the attainable closed-loop sampling frequency. As a rule of thumb, the maximum practical closed-loop sampling frequency for digital signal processing using microprocessors or microcontrollers is around 100 kHz. This excludes feedback control for very high bandwidth mechanical systems [191].

In order to increase the sampling frequency, field-programmable gate arrays (FPGA) can be used [120, 128, 184]. Field-programmable analog arrays (FPAA) is an analog alternative to FPGAs, and allows for fairly high-order control laws to be implemented using analog circuit elements, and thus avoids sampling and allows for high-bandwidth control [129, 190, 199]. Regular operational amplifier circuits can also be used for high-bandwidth control [78, 85].

The noise performance of a digital control system is limited by the noise floor determined by both sampling frequency and quantization unit [145, 175, 220]. This does not seem to be discussed much in literature pertaining to scanning probe microscopy.

1.2.5 The Environment

Imaging with atomic resolution puts very high requirements on the environmental conditions in which an instrument operates, even though enabling instrumentation with sufficient performance is readily available. This includes suppressing mechanical vibration noise from the environment, such as floor vibrations or sound, as well as controlling ambient conditions, such at the temperature and humidity. Sometimes vacuum or special atmospheric conditions are necessary, as sample surfaces can oxidize, or meniscus layers can form [41, 130, 229].

1.3 Control Schemes Survey

Motion control for nanopositioning devices appears to be a well-researched field. The literature regarding scanning probe microscopy appear to be coarsely divided

into research related to vertical and lateral positioning. For scanning probe microscopy, both vertical and lateral positioning is necessary.

Vertical positioning is often coupled with a specific surface measurement or manipulation technique [124]. For imaging applications, two common surface measurement techniques are the so-called contact mode and intermittent contact mode [5, 186]. In both these cases, when applying feedback control, the control objective is to enforce a constant distance from the surface, treating the surface topology as a disturbance signal. In contact mode, the probe is dragged with constant interaction force over the sample, where the force exerted on the surface through the probe is due to the deflection of the cantilever. In intermittent contact mode the cantilever oscillates with a constant amplitude, and the interaction force determines the amplitude. One of the main challenges for the control system design is therefore to provide high-bandwidth control to suppress arbitrary disturbance signals, in order to maintain a constant force or a constant oscillation amplitude.

For lateral positioning, the control objective is to provide accurate reference trajectory tracking. The trajectory is often periodic, such as a triangle-wave signal, in order to produce the raster pattern needed in imaging applications. Many control schemes for lateral positioning are therefore geared towards providing accurate tracking of such signals.

1.3.1 Feed-Forward Control

Inversion techniques

Feed-forward motion control can provide very good tracking results, if accurate and invertible models can be found for the system to be controlled. For stable, minimum phase linear systems it is especially straight forward, as it is in principle possible to obtain perfect tracking by inverting the model of the system and by applying a sufficiently smooth reference trajectory. In the first generations of scanning probe microscopy instruments, feed-forward control was used for lateral positioning. The control signal was then generated simply by using a proportional reference signal based on the DC-gains of the system, which did not provide any compensation of creep, hysteresis, and mechanical vibrations [44]. This is sufficient for low-bandwidth reference trajectories and imaging, where artifacts due to creep and hysteresis can be removed in image post-processing [20]. However, very good tracking performance can be achieved for positioning devices using piezoelectric actuators when utilizing feed-forward control, when combining inverse models of the hysteresis, creep, and the mechanical vibration dynamics [50, 137, 177].

There are several examples of applying the inverse model of the mechanical vibration dynamics to reduce motion-induced vibrations [48, 49, 123, 140, 193, 197, 213, 230]. Some of these methods incorporate various optimization methods in order to deal with parameter and model uncertainty, non-minimum phase zeros, to limit the control effort, and to handle only partially known reference signals.

Feed-forward inversion and linearization of hysteresis is most often done using the Preisach model [50, 212], or the Prandtl-Ishlinskii model [116, 159]. Another class of hysteresis models, called Duhem models, have found some use, such as in [154], where a static map derived from the Coleman-Hodgdon equations is used.

Feed-forward inversion of creep has also been investigated, using either static maps or linear ordinary differential equations [50, 116, 117, 159].

Trajectory generation

Another approach to reduce motion induced vibrations, is input shaping, where instead of using the plant inverse, the reference signal is chosen or modified in a manner which avoids excitation of lightly damped vibration modes. In this case, information about the mechanical vibration dynamics can be used either to reduce the frequency content of the reference signal, or to shape it to use the dynamic response of the positioner to good effect. Some examples are found in [83, 200]. Work has also been done in order to reduce dynamic excitation by using sinusoidal scanning [22, 108, 216], and to use variable resolution in order to reduce the amount of time needed to cover a sample [10, 40].

1.3.2 Feedback Control

Feedback control can provide better tracking performance when combined with feed-forward control, since feedback control reduces the sensitivity to unknown disturbances and plant uncertainties for the controlled system. The main disadvantage is the increased noise level due to sensor noise feedback.

Model-based control

Modern model-based control for *output feedback* on linear systems is commonly done within the $\mathcal{H}_\infty$-synthesis framework. It is perhaps the most practical framework for synthesizing robust control laws for arbitrary linear systems, as it guarantees a solution to the control design problem by convex optimization [206]. As such, one would expect that control laws based on $\mathcal{H}_\infty$-synthesis to be extensively explored for nanopositioning systems, and several results can be found in the literature [138, 187, 188, 192, 192, 194, 196, 198, 201, 211, 226]. Polynomial based, or pole-placement, control [94, 111] has also found some use [14]. Other model-based control schemes, such as the linear-quadratic-gaussian regulator [94], or model reference control [94, 111], does not seem to have been applied to nanopositioning systems. However, such control schemes can be seen as a subset of control schemes derived using $\mathcal{H}_\infty$ or $\mathcal{H}_2$-synthesis.

Fixed-order, fixed-structure control

Traditional feedback control is often considered to be concerned with the application and tuning of the proportional–integral–derivative (PID) control law [17]. For scanning probe microscopy systems, it is the standard choice for vertical control [5, 194]. For lateral control in later generations scanning probe microscopy systems, proportional–double-integral–derivative (PIID) control laws and variants thereof seem to be common, where double integral action is sometimes used to obtain asymptotic tracking of the flanks of a triangle signal, due to the internal model principle [20]. In order to increase the bandwidth and asymptotic tracking performance for these systems, the control laws have sometimes been augmented

with notch filters, feed-forward control, and by using limited derivative and integral action, also known as lead-lag control [6, 20, 75, 148, 187, 188, 194, 211, 231].

Since lightly damped vibration modes is the main problem for high-bandwidth tracking control, the sensitivity due to these modes can be reduced by using the actuator to increase the damping in the structure.

There exist several control schemes for introducing damping in active structures. These include fixed-structure, low-order control laws such as positive position feedback [76], integral force feedback [174], passive shunt-damping [96], resonant control [170] and integral resonant control [13]. For co-located sensors and actuators, many of the control laws have some good robustness and stability properties due to positive-realness or negative-imaginariness for certain input-output pairs [166]. A few damping control schemes using displacement feedback combined with feed-forward control have been investigated in [15, 26, 179, 202].

Piezoelectric actuators, or transducers, have a so-called self-sensing property, since any piezoelectric transducer can be used both for actuation and for sensing. The production of charge when a stress is applied is called the direct piezoelectric effect, and the production of strain when an electric field is applied is called the converse piezoelectric effect. By using the charge produced when operating the actuator, damping can be introduced without additional sensors [12, 82, 127]. The main advantage of this technique is that there is very little, or no, increase in noise due to sensor noise feedback.

By using so-called damping and tracking control schemes, reference tracking performance can be further improved. This is done by coupling a damping control scheme with an integral control law [14, 78, 85]. The main reason for the increased performance is that a reduction of the dominant resonant peak of the system leads to an increased gain margin, enabling much higher gain to be used for the disturbance-rejecting integral control law [78]. Due to the increased disturbance rejection, the adverse effects of creep and hysteresis can be reduced significantly. Environmental and other disturbances should also be reduced.

1.3.3 Other Approaches

Learning-type control

In many applications of nanopositioning devices, reference trajectories and disturbances are periodic, or repetitive. This includes, *e.g.*, tracking of raster patterns, producing a series of identical features in a manufacturing process, or measuring surfaces with regularities in the topography.

Iterative learning control is a method that attempts to use the error signal produced by successive periods of a reference signal to produce a feed-forward control signal that will invert the dynamic response of a systems, and cancel any deterministic disturbances [35, 160]. There are several examples of the method being applied to nanopositioning systems [36, 43, 101, 103, 122, 135, 141, 214, 221]. In many of these cases, the method can provide practically perfect reference tracking.

Repetitive control is another control scheme that is tailored to provide small errors when using periodic reference signals, or in the presence of periodic distur-

bances. It is based on the internal model principle, and thus operates by embedding a model of periodic signals in the control loop [98]. Due to the internal model principle, any exogenous signal that corresponds to the embedded model will be therefore be nulled in the error signal. Examples of applications to nanopositioning systems are found in [16, 155, 156].

Adaptive least mean squares filtering is also a technique that has also been investigated for use on a nanopositioning device when applying periodic reference trajectories [77].

Dual-stage actuation

In order to combine long range with high bandwidth, the principle of dual-stage actuation can be used. When using this technique, the mechanical system is modified to use a high-bandwidth short-range actuator attached to a low-bandwidth long-range actuator. The control schemes applied to these systems are often extensions to the ones already mentioned, such as damping and tracking control laws, and schemes derived using $\mathcal{H}_\infty$-synthesis. Some examples of dual-stage actuation can be found in [79, 105, 121, 128, 199].

Charge drive

With regards to the hysteresis in piezoelectric actuators, it is known that it appears between applied voltage and induced charge [161]. By using a transconductance amplifier, or charge drive, rather than a voltage amplifier, the hysteresis can effectively be eliminated [80, 118, 125].

Non-linear control

The vast majority of feedback control schemes in the literature are linear, likely due to the fact that the dynamics of nanopositioning devices is dominantly linear and open-loop stable. Non-linear feed-forward schemes are found in the form of the hysteresis and creep compensation schemes already discussed. There are some examples of classic non-linear feedback schemes applied to nanopositioning devices, in the form of sliding mode control [21, 61, 142].

1.4 Topics of This Thesis

The thesis is divided in three parts. Each part is concerned with a particular topic in control theory, and its application to nanopositioning devices. In this Section, the objectives and rationale for the work behind this thesis will first be presented, followed by a short discussion of the three parts.

1.4.1 Objectives and Rationale

The overall objective for the thesis work was to investigate and develop control schemes for accurate trajectory tracking for nanopositioning devices, focussing

on practical and implementable methods, as well as verification of the methods through physical experiments.

It was therefore necessary to assemble laboratory facilities to experimentally assess the performance of motion control schemes applied to nanopositioning devices. The main guideline for acquiring laboratory equipment was that it should preferably be generic and readily available from commercial manufacturers. It was a goal that the laboratory set-up should resemble, as much as possible, a standard instrumentation set-up for motion control. It was not a goal to aim for nanometer accuracy or extremely high bandwidth, but rather have equipment that exhibited the main characteristics for devices used in nanopositioning applications. As such, it should be sufficient to verify the general operating principles for any developed methods for motion control.

By the survey of the current literature on the subject of nanopositioning, it is apparent that it is well researched, and many approaches for control have been proposed, experimentally verified, and found to be performing well. In the context of nanopositioning devices, applied control theory can broadly be categorized into feed-forward control, standard feedback control using linear filters, and adaptive, or learning, control. Here, feed-forward control chiefly deals with linear model inversion and inverse hysteresis operators, feedback control is most often done using $\mathcal{H}_\infty$-synthesis or a combination of damping and tracking control laws, and adaptive control is done for periodic signals using iterative learning control, or similar techniques.

A common characteristic for inverse hysteresis operators, iterative learning control, and control laws found using $\mathcal{H}_\infty$-synthesis, is that the schemes yield good results, but can be of high order and computationally demanding. Iterative learning control is also limited to tracking of periodic reference signals. This may limit the applicability as implementation may require specialized numerical tools, fast digital signal processing equipment, and an analog implementation can be practically difficult or impossible. It is noticeable from the current literature that there is little discussion on quantization noise, although control laws implemented using modern analog circuit elements will provide superior noise performance compared to a digital implementation. Control schemes that are suitable for analog implementation are the low-order damping and tracking schemes, but many of these schemes lack tools for systematic tuning.

The above assessment of the state of the art in the field of nanopositioning has therefore motivated the investigation of control methods that are simpler with regards to implementation, but will produce similar performance to what has already been done. The resulting work concerns hysteresis compensation (inversion), low-order damping and tracking control laws, robust low-order repetitive control, and robust adaptive control for arbitrary reference signals.

1.4.2 Part I – Feed-Forward Control of Hysteresis

This part contains Chapter 2, which presents a simple adaptive hysteresis compensation scheme. It is based on the material presented in [66, 69], but includes more extensive analysis and discussion on the method, trajectory generation, the

hysteresis phenomenon, and how to couple the method with an integral control law.

1.4.3 Part II – Damping & Tracking Control

Several low-order damping and tracking control schemes are presented and discussed, as well as a repetitive control scheme for periodic reference trajectory tracking. It is based material found in [63] concerning passive shunt damping, material found in [67] concerning optimal tuning of a modified proportional-integral (PI) control laws and anti-windup when using a proportional-double-integral (PI^2) control law, material found in [65, 71] concerning the implementation and tuning of all the presented control schemes, as well as material found in [70] concerning robust repetitive control.

Chapter 3 presents three damping and tracking control schemes already found in the literature, as well as three control schemes based on passive shunt damping, a modified integral control law, and model reference control (MRC). A tuning procedure for all the control schemes except the MRC scheme is presented. Extensive analysis of the different control schemes is also presented.

Chapter 4 presents a robust low-order approach to repetitive control for nanopositioning, based partially on the modified integral control law from Chapter 3.

1.4.4 Part III – Adaptive Control

This part concerns adaptive control for arbitrary reference trajectories, using standard adaptive control theory in the form of model reference adaptive control (MRAC). Chapter 5 is based on the material found in [68, 168, 169] concerning experimental parameter identification for a nanopositioning device, and Chapter 6 is based on material in [64] concerning implementation issues for a standard MRAC applied to a nanopositioning device. The work is mainly focussed on techniques for obtaining parameter convergence, and it is demonstrated experimentally that a pre-filter is needed to order to achieve this, both in open-loop and closed-loop.

1.4.5 Appendices

The appendices included are a collation of the standard theory on piezoelectricity, mechanical vibrations, and hysteresis modeling. It is included for reference, as it forms the theoretical foundation for the system modeling of nanopositioning devices.

1.5 Publications

A. A. Eielsen and A. J. Fleming. Passive Shunt Damping of a Piezoelectric Stack Nanopositioner. In *American Control Conference, Proceedings of the*, pages 4963–4968, 2010.

A. A. Eielsen, J. T. Gravdahl, K. Y. Pettersen, and L. Vogl. Tracking Control for a Piezoelectric Nanopositioner Using Estimated States and Feedforward Compen-

sation of Hysteresis. In *5th IFAC Symposium on Mechatronic Systems, Proceedings of the*, pages 96–104, 2010.

A. A. Eielsen, M. Burger, J. T. Gravdahl, and K. Y. Pettersen. PI^2-Controller Applied to a Piezoelectric Nanopositioner Using Conditional Integrators and Optimal Tuning. In *18th IFAC World Congress, Proceedings of the*, pages 887–892, 2011.

A. A. Eielsen, T. Polóni, T. Johansen, and J. T. Gravdahl. Experimental Comparison of Online Parameter Identification Schemes for a Nanopositioning Stage With Variable Mass. In *Advanced Intelligent Mechatronics, 2011 IEEE/ASME International Conference on*, pages 510–517, 2011.

A. A. Eielsen, J. T. Gravdahl, and K. Y. Pettersen. Adaptive feed-forward hysteresis compensation for piezoelectric actuators. *Review of Scientific Instruments*, 83(8):085001, 2012.

A. A. Eielsen, K. K. Leang, and J. T. Gravdahl. Robust Damping PI Repetitive Control for Nanopositioning. In *American Control Conference, Proceedings of the*, pages 3803–3810, 2012.

T. Polóni, A. A. Eielsen, B. Rohal'-Ilkiv, and T. A. Johansen. Moving Horizon Observer for Vibration Dynamics with Plant Uncertainties in Nanopositioning System Estimation. In *American Control Conference, Proceedings of the*, pages 3817–3824, 2012.

A. A. Eielsen and J. T. Gravdahl. Adaptive Control of a Nanopositioning Device. In *51st IEEE Conference on Decision and Control, Proceedings of the*, 2012. (Accepted).

A. A. Eielsen, M. Vagia, J. T. Gravdahl, and K. Y. Pettersen. Damping and Tracking Control Schemes for Nanopositioning. *Mechatronics, IEEE/ASME Transactions on*. (Second version in review).

T. Polóni, A. A. Eielsen, B. Rohal'-Ilkiv, and T. A. Johansen, Adaptive Model Estimation of Vibration Motion for a Nanopositioner with Moving Horizon Optimized Extended Kalman Filter. *Journal of Dynamic Systems Measurement and Control, Transactions of the ASME*. (Second version in review).

A. A. Eielsen, M. Vagia, J. T. Gravdahl, and K. Y. Pettersen. Fixed-Structure, Low-Order Damping and Tracking Control Schemes for Nanopositioning. *6th IFAC Symposium on Mechatronic Systems, Proceedings of the*, 2013. (Submitted).

Part I

Feed-Forward Control of Hysteresis

Chapter 2

Hysteresis Compensation

2.1 Introduction

When applying piezoelectric actuators for low-bandwidth reference trajectory tracking, the largest error contribution comes from the hysteresis and creep non-linearities [44, 58, 137].

Due to hysteresis, the average gain of a piezoelectric actuator depends on the amplitude of the driving voltage [107, 171]. The observed piezoelectric response also change over time, as the gain is dependent on temperature variations and depolarization, as well as other factors [25].

Feedback control effectively reduces the sensitivity to such uncertainty, as well as the disturbance introduced by hysteresis, if integral action is used [20, 138]. The reduction in error when using feedback control is dependent on the obtainable closed-loop bandwidth, but it is well known from control engineering literature that high bandwidth control also increases the overall noise in the system due to sensor noise [34, 60].

By using a feed-forward scheme in addition to feedback control, better tracking performance can be obtained. For reduction of the error introduced by hysteresis there are several methods based on inversion of the Preisach model or the Prandtl-Ishlinskii model [50, 116, 137, 159, 212]. In general, performance when using feed-forward control depends directly on the accuracy of the model [57]. In the presence of uncertainties and changing responses, online adaptation can be used to improve the accuracy [114]. Such models tend to be large if an accurate description is required, and can therefore be computationally demanding, and this has led to specialized field programmable gate array implementations in order to enable inversion at high bandwidths [212]. An example of a standard implementation of the discrete Preisach model can be found Appendix C.

Another class of hysteresis models, called Duhem models, have found some use [154]. Here, the hysteresis compensation comes in the form of a static map derived from a modified version of the Coleman-Hodgdon model. The main drawback of using a static map to compensate for a dynamic effect is the difficulty in handling arbitrary and unknown reference signals, as a dynamic response is both dependent on initial values and the specific time evolution of an excitation signal.

Driving a piezoelectric actuator using charge rather than voltage is known to provide excellent suppression of hysteresis [80, 161]. Even though the hysteresis disturbance can be suppressed, driving the piezoelectric actuator using charge will not remove the uncertainty in actuator gain. Also, charge drives are often not part of existing instrumentation configurations, as voltage amplifiers have been the standard choice for positioning tasks when using piezoelectric actuators.

2.1.1 Contributions

An online adaptive non-linear feed-forward hysteresis compensation scheme is presented, based on the dynamic Coleman-Hodgdon model. It is suitable for symmetric hysteretic responses and certain periodic reference trajectories. Being adaptive, the method retains good accuracy in the presence of uncertainties in the response, both with regards to the gain and the shape of the hysteretic response. The method has low complexity and is amenable to real-time implementation.

Furthermore, experimental results are presented to verify and illustrate the theoretical result. The presented method is then applied to a standard instrumentation configuration, utilizing a capacitive displacement sensor and a voltage drive. In the experiments it is seen that the error due to hysteresis can be reduced by more than 90% compared to when assuming a linear response.

2.1.2 Outline

The Chapter is organized as follows. In Section 2.2 models for the ideal linear response and for the hysteretic response are presented. In Section 2.3 two feed-forward schemes are described, one assuming an ideal linear response, and a scheme to compensate for the hysteretic behavior, based on the hysteresis model from Section 2.2.1. The experimental results when applying the two feed-forward schemes are presented in Section 2.4. Sections 2.6 and 2.7 describe the details of the derivation of the hysteresis compensation scheme. Some remarks on the passivity properties of the Coleman-Hodgdon model, interpreting hysteresis as an uncertain gain and an input disturbance, and how to augment the presented scheme with an integral control law are found in Sections 2.8, 2.9, and 2.10, respectively.

2.2 System Description & Modeling

In this section, models for the system are presented. The system at hand is a flexure based nanopositioning stage with a piezoelectric stack actuator. Using an input signal with a low fundamental frequency, the system response can be described using a hysteresis model and a simple mechanical model.

2.2.1 Hysteresis Model

The hysteretic behavior of piezoelectric actuators is due to ferroelectric loss phenomena. The hysteresis exhibited in such actuators will appear between applied voltage and induced charge [161]. The force developed by the actuator will therefore exhibit hysteresis when driving such actuators using voltage.

A phenomenological model that can be used to describe the hysteresis in piezoelectric actuators is the Coleman-Hodgdon model [18], which is given as

$$\dot{\eta} = \beta\dot{u} - \alpha\eta|\dot{u}| + \gamma|\dot{u}|u \ , \ \eta(0) = \eta_0 \ , \tag{2.1}$$

where u is the input, and η is the output. The parameters must satisfy the conditions $\alpha > 0$, $\beta > 0$, $\frac{\gamma}{\alpha} > \beta$, and $\frac{\gamma}{\alpha} \leq 2\beta$, in order for the model to yield a response that is in accordance with the laws of thermodynamics [45]. This means that the slope $\dot{\eta}$ will have the same sign as the slope $\dot{u}$, that is $\frac{\mathrm{d}\eta}{\mathrm{d}u} > 0$. This is the same as saying that the output will never move in the opposite direction of the input.

The input-output map generated by the model (2.1) has a symmetric stationary response to periodic inputs which are monotonically increasing and decreasing between two extrema. The model is therefore best suited to describe hysteretic responses that are dominantly symmetric, and for such periodic input signals. The solution of the model is defined, however, for a larger class of input signals. The input signal u must be bounded, piecewise continuous, and connected. This also implies that the time derivative $\dot{u}$ exists and is bounded, *i.e.*, $u \in C^0$. This includes signals such as triangle-waves or low-pass filtered steps and square-waves, but not unfiltered steps and square-waves.

The hysteresis model (2.1) can also be expressed in a different form, with an identical input-output response. That is, the output η can be found from

$$\eta = cu + \eta_h \tag{2.2}$$

where η_h is the solution to

$$\dot{\eta}_h = -b\dot{u} - a\eta_h|\dot{u}| \ , \ \eta_h(0) = \eta_{h0} \ . \tag{2.3}$$

The parameters in this formulation can be found using the parameters in (2.1), and the relations are

$$a = \alpha \, , \ b = \frac{\gamma - \alpha\beta}{\alpha} \, , \text{ and } c = \frac{\gamma}{\alpha} \ . \tag{2.4}$$

The derivation of the expressions in (2.2), (2.3), and (2.4) can be found in Section 2.6.

The alternative model formulation in (2.2) and (2.3) will be used to develop a hysteresis compensation scheme in Section 2.3.2.

2.2.2 Mechanical Model

A well designed nanopositioning stage has one dominant vibration mode, which is due to a piston movement in the desired direction. Any additional vibration modes will in general have other shapes, and produce motions which are counterproductive to the desired behavior. A two degree of freedom positioning stage can therefore be accurately described using the simplified free-body diagram shown in Fig. 2.1, and the dynamic model will therefore be on the form described in Appendix B. Thus, the dynamic response for the displacement w (m) of a point on the mechanical structure in, *e.g.*, the x-direction, is

$$m\ddot{w} + d\dot{w} + kw = f_a \ , \tag{2.5}$$

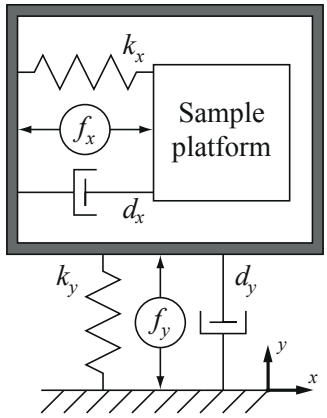

Figure 2.1: Serial kinematic configuation.

where m (kg) is the mass of the moving sample platform, d (N s m^{-1}) is the damping coefficient, k (N m^{-1}) is the spring constant, and f_a (N) is the force developed by the actuator.

Here it is assumed that reference trajectories, r, will have a fundamental frequency below approximately 1% of the natural undamped frequency $\omega_0 = \sqrt{k/m}$, and that the contribution of the damping and inertial forces therefore can be neglected, *i.e.*, $d\dot{w} \approx 0$ and $m\ddot{w} \approx 0$. The forces depending on the velocity and acceleration of the moving platform will be relatively small when the movements are slow, that is, the higher frequency components of the reference signal will be small close to the resonant frequency of the mechanical structure. The displacement w is therefore taken to be given by Hooke's law

$$w = \frac{1}{k} f_a \ . \tag{2.6}$$

Ideally, the actuator has a linear response. This is the standard assumption [2], and practical modeling of ideal piezoelectric transducers is explained in Section A.5. In this case, the force developed by the actuator should be

$$f_a = e_a u \ ,$$

where e_a (N V^{-1}) is the voltage-to-force gain coefficient. Here it is assumed that the additional stiffness introduced by the presence of the actuator in the mechanical structure is accounted for in the spring constant k. The relation between the applied voltage u and the displacement w, will then be according to (2.6),

$$w = \frac{e_a}{k} u = Ku \ , \tag{2.7}$$

where the lumped parameter K (m V^{-1}), a voltage-to-displacement gain coefficient, is introduced for convenience.

Since the actuator response is actually hysteretic, using the hysteresis model (2.1), or equivalently (2.2), provides a more accurate description of the observed

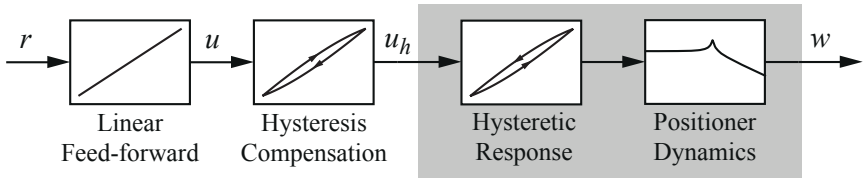

Figure 2.2: Feed-forward tracking control scheme.

displacement. The displacement will therefore be taken to be the output of the hysteresis model, *i.e.*,

$$w = \eta \, . \tag{2.8}$$

2.3 Feed-Forward Tracking Control

The objective for a tracking control scheme applied to a nanopositioning stage, is to force the displacement w to follow a specified reference trajectory r. In order to achieve this, feed-forward and feedback control can be used. Feed-forward techniques can be very effective if an invertible and accurate system model can be found. Applying feedback will typically reduce sensitivity to model errors and unknown disturbances, but at the expense of a higher overall noise level.

For positioning devices utilizing piezoelectric actuators, when using reference trajectories with low fundamental frequencies, the disturbance due to hysteresis is the main source of error. In this Section, two feed-forward schemes will be described. The first is simply assuming that the system has a linear response. The second scheme provides a method for inverting the response of the hysteresis model (2.1). The overall scheme is illustrated in Fig. 2.2.

2.3.1 Linear Feed-Forward

Assuming that the response of the system is linear, such as in (2.7),

$$w = Ku \, ,$$

the applied voltage signal u should be

$$u = \frac{1}{K} r \tag{2.9}$$

in order to achieve tracking.

Due to creep and hysteresis, the gain K will depend on the amplitude of the input signal u. Other effects also affect the observed gain, such as actuator temperature and depolarization. An estimate of the gain, $\hat{K}$, can be found from input-output data using, *e.g.*, the least-squares method. Depending on the positioning device, the gain can change significantly. For the positioning device used in the experiments in Section 2.4, a relative change of more than 150% was observed from the minimal observable displacement to the maximal displacement.

As the gain changes depend on the input signal, using a static gain estimate $\hat{K}$ for feed-forward control can result in very large errors. In order to minimize the error for all reference signals, an online estimate of K should be used. This can be achieved by using the recursive least-squares method with the model (2.7) on the form

$$z = \theta\varphi$$

where $z = w$, $\theta = K$, and $\varphi = u$. The parameter identification scheme is described in detail in Appendix D.

2.3.2 Hysteresis Compensation

In this section, a feed-forward scheme that takes into account the hysteresis is presented. The scheme is based on inverting the response of the hysteresis model (2.1). Using the relations in (2.2) and (2.8), but defining a new input signal u_h, that is,

$$w = cu_h + \eta_h \ , \tag{2.10}$$

the above relation can be linearized by choosing the input signal

$$u_h = \frac{K}{c}u - \frac{1}{c}\hat{\eta}_h \ , \tag{2.11}$$

where $\hat{\eta}_h$ is an estimate of the term η_h. By substituting (2.11) into (2.10), the linear relationship between voltage u and the expression for the displacement as given in (2.7) is recovered,

$$w = cu_h + \eta_h = c\left(\frac{K}{c}u - \frac{1}{c}\hat{\eta}_h\right) + \eta_h = Ku \ ,$$

if $\hat{\eta}_h = \eta_h$. Thus, generating an input signal using (2.9) and applying (2.11), the error introduced by the hysteresis is removed. In order for this to work, an estimate of η_h is required.

Assuming the parameters of the hysteresis model (2.1) are known, and the new set of parameters is found from the relations in (2.4), an estimate of η_h when using the new input signal u_h can be found by substituting (2.11) into (2.3), that is,

$$\dot{\hat{\eta}}_h = -b\dot{u}_h - a\hat{\eta}_h\left|\dot{u}_h\right| = -b\left(\frac{K}{c}\dot{u} - \frac{1}{c}\dot{\hat{\eta}}_h\right) - a\hat{\eta}_h\left|\frac{K}{c}\dot{u} - \frac{1}{c}\dot{\hat{\eta}}_h\right| \ . \tag{2.12}$$

In Section 2.7 it is shown that solving (2.12) is equivalent to solving

$$\dot{\hat{\eta}}_h = \begin{cases} K\frac{-a\hat{\eta}_h - b}{-a\hat{\eta}_h - b + c}\dot{u} \ , & \dot{u} \geq 0 \\ K\frac{a\hat{\eta}_h - b}{a\hat{\eta}_h - b + c}\dot{u} \ , & \dot{u} < 0 \end{cases} \ , \quad \hat{\eta}_h(0) = \hat{\eta}_{h0} \ . \tag{2.13}$$

The initial value $\hat{\eta}_{h0}$ can in principle be chosen arbitrarily. For the case of periodic inputs which are monotonically varying between two extrema, the solution will converge to a stationary input-output map after some cycles of the input signal. Assuming the system is at rest in an equilibrium where $u(0) = 0$ and $\eta(0) = 0$ when starting the integration, the initial value will be $\hat{\eta}_{h0} = 0$.

Inspecting (2.1), it can be seen that the parameters appear affinely with signals comprising of u and η and their time derivatives, *i.e.*, the model can be put on the form

$$z = \theta^{\mathrm{T}} \varphi \tag{2.14}$$

where

$$\theta = [\alpha,\ \beta,\ \gamma]^{\mathrm{T}} \ , \tag{2.15}$$

$$\varphi = [-\eta|\dot{u}|,\ \dot{u},\ |\dot{u}|u]^{\mathrm{T}} \ , \tag{2.16}$$

and

$$z = \dot{\eta} \ . \tag{2.17}$$

Here, θ is the called the parameter vector and φ the regressor. Having the model on the form (2.14) enables the usage of the recursive least-squares method to find the parameters in θ, as the displacement $w = \eta$ can be measured, and the applied voltage u and the time derivative $\dot{u}$ are known and defined. The relations in (2.4) can then be used to find the parameters to be used in this hysteresis compensation scheme. The parameters in the model given by (2.2) and (2.3) can not be identified, as it is not possible to measure the signal η_h. The parameter identification scheme is described in detail in Appendix D.

2.4 Experimental Results & Discussion

2.4.1 Experimental Set-Up

The experimental set-up consisted of a dSPACE DS1103 hardware-in-the-loop system, an ADE 6810 capacitive gauge and an ADE 6501 capacitive probe from ADE Technologies, a Piezodrive PDL200 voltage amplifier, the custom-made long-range serial-kinematic nanopositioner from EasyLab (see Fig. 2.3), two SIM 965 programmable filters and a SIM983 scaling amplifier from Stanford Research Systems. Details on the design of nanopositioner can be found in [120].

The capacitive measurement has a sensitivity of 1/5 V/μm and the voltage amplifier has a gain of 20 V/V. The programmable filters were used as reconstruction and anti-aliasing filters. The scaling amplifier was used to amplify the signal from the capacitive gauge in order to maximize the resolution of the quantized signal. With the DS1103 system, a sampling frequency of 50 kHz was used in all the experiments. For numerical integration, a third-order Runge-Kutta scheme (Bogacki-Shampine) [62] was used.

The first part of the experiments were done using a triangle-wave reference signal, where 10% of the signal was replaced by a smooth polynomial around the extremal points to reduce vibrations. A second set of experiments was done using a filtered pseudo random binary signal (PRBS). This signal had a length of 38750 samples, a bandwidth of 40 Hz, a ± 5 μm range, and was filtered by a second-order low-pass Butterworth filter with a 10 Hz cut-off frequency. All the experiments were performed using feed-forward compensation only.

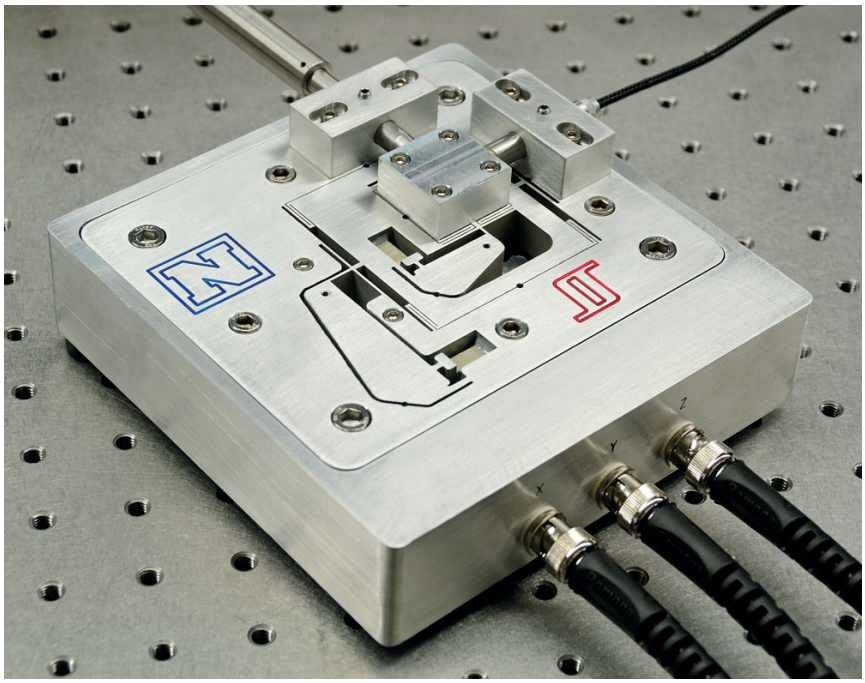

Figure 2.3: Nanopositioning stage.

2.4.2 Results & Discussion

The efficacy of the hysteresis model (2.1) and the parameter identification scheme presented in Section 2.3.2 can be seen from Fig. 2.4. Here a triangle-wave signal has been applied, but the response is very similar for any periodic input which is monotonically increasing and decreasing between two extrema. Note that the observed hysteresis is highly symmetric, and the hysteresis model is therefore well suited to describe the response. Identified parameters for the hysteresis model can be found in Tab. 2.1. As can be seen, the parameters depend on the input signal. The identified parameters appear to provide a good fit to the observed response, but there is some model discrepancy, especially at the extremal values where the input signal switches direction.

Fig. 2.5a displays time-series for the reference, measured displacement, and the error when using the linear feed-forward scheme and a triangle-wave reference signal. Adapting the gain coefficient K makes it possible to match the extremal values of the measured response and the reference with very high accuracy, and the residual error is almost exclusively due to the hysteresis non-linearity. The corresponding reference-to-displacement map is shown in Fig. 2.5b. Note that despite the high accuracy in adapting the gain coefficient K, the hysteretic character of the response is clearly visible.

Applying the hysteresis compensation scheme proposed in Section 2.3.2, it can be seen from both the time-series plots in Fig. 2.5c and the reference-to-

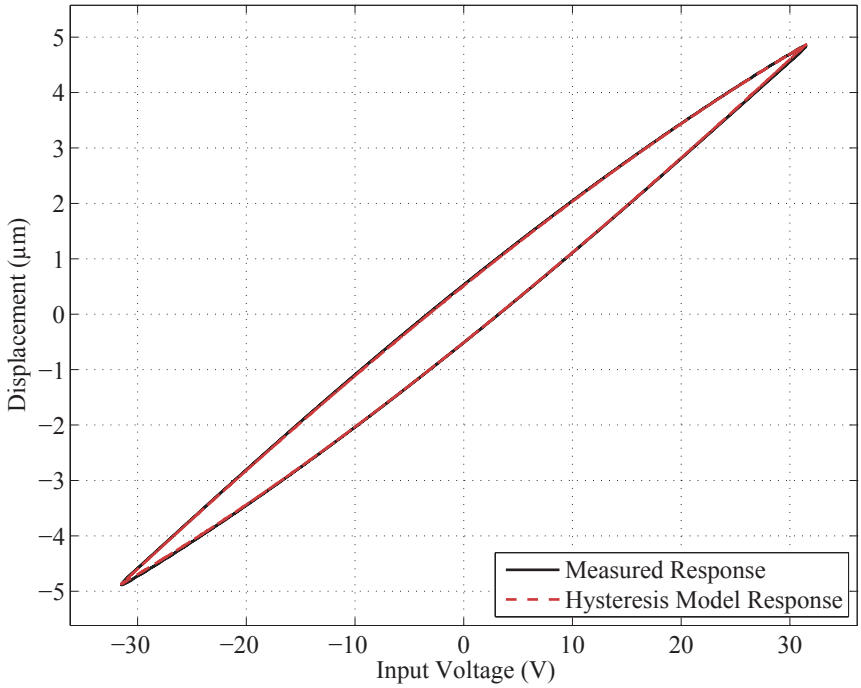

Figure 2.4: The input-output map when using a 5 Hz triangle-wave reference signal with 5 μm amplitude.

displacement map in Fig. 2.5d, that there is a significant reduction in the error. The reduction in maximum error is approximately 90% from when applying a linear feed-forward scheme, to when applying the hysteresis compensation scheme. Most of the residual error when applying the hysteresis compensation scheme is due to the model discrepancy near the extremal values of the reference signal.

Assessing the performance under non-ideal conditions was done using the filtered PRBS reference. The continuous repetition of a PRBS sequence is a periodic signal, but for the duration of the sequence it behaves as a non-periodic signal, and the filtered signal is therefore not monotonically varying between only two extrema. The results for the linear feed-forward scheme are shown in Fig. 2.6a, and the results when using the hysteresis compensation scheme are found in Fig. 2.6b. The error obtained when using the hysteresis compensation scheme is still significantly lower than when using the linear feed-forward scheme, producing a reduction in maximum error of approximately 59%. It is apparent, however, that the effectiveness is reduced compared to when applying the triangle-wave signal.

The maximum errors observed for some different configurations of the reference signal are presented in Tab. 2.2. The reduction in error is found as $100 \times (1 - e_h/e_l)$ where e_h and e_l are the maximal errors, $\max(|r - w|)$, when using the hysteresis compensation scheme, and linear feed-forward, respectively.

If the parameters of the hysteresis model are fixed, applying the compensation

Table 2.1: Identified parameters for the stationary response of the hysteresis model (2.1) and the linear approximation (2.7).

Reference Signal	α	β	γ	K
2.5 μm @ 5.0 Hz	3.26×10^{-2}	1.36×10^{-1}	5.96×10^{-3}	0.141
5.0 μm @ 2.5 Hz	1.91×10^{-2}	1.49×10^{-1}	4.05×10^{-3}	0.156
5.0 μm @ 5.0 Hz	2.10×10^{-2}	1.47×10^{-1}	4.29×10^{-3}	0.155
7.5 μm @ 5.0 Hz	1.59×10^{-2}	1.55×10^{-1}	3.55×10^{-3}	0.165
Filtered PRBS	3.32×10^{-2}	1.36×10^{-1}	6.15×10^{-3}	0.154

scheme for a different signal than what the parameter were found for, the compensation scheme can produce very poor results. Error figures illustrating this is summarized in Tab. 2.3. This suggests that the parameter identification scheme should be running while using the compensation scheme, or that hysteresis model parameters should be found for a family of reference signals, and that some form of gain scheduling should be used if a displacement measurement is not always available while using the equipment.

Due to the low order of the hysteresis model, the parameter identification scheme requires little computational effort, and can be run online using high sampling rates (in excess of 50 kHz for the experimental set-up when compiled using the Simulink Coder from an inefficient Simulink implementation). The computational effort can be somewhat reduced using, *e.g.*, the recursive gradient method [111] rather than the recursive least-squares method. An efficient implementation of the parameter identification scheme using a complied programming language such as C or C++, as was done for the implementation used in the experiments in Chapter 6, can greatly increase the real-time performance.

2.5 Parameter Identification

The parameter identification scheme used is the recursive least-squares method, and it is described in Section D.1. For the system at hand, the input signal u and the time derivative $\dot{u}$ are known, as u is generated by the expression (2.9), and by using a reference signal that is differentiable, *i.e.*, r and $\dot{r}$ being known and bounded. The displacement w is measured by the capacitive probe, and the time derivative of this signal is needed to identify the parameters for the hysteresis model. To avoid pure numerical differentiation, the output $z = \dot{\eta} = \dot{w}$ and regressor vector φ was in this case filtered using proper filters, that is, $\bar{z}(s) = sW_p(s)w(s)$, and $\bar{\varphi}(s) = W_p(s)\varphi(s)$, where $W_p(s)$ is a first-order low-pass filter with a 2.5 kHz

Table 2.2: Maximum stationary error when using linear feed-forward and the hysteresis compensation scheme.

Reference Signal	Linear Feed-Forward		Hysteresis Compensation		Error Reduction
	Absolute Error	Relative Error	Absolute Error	Relative Error	
2.5 μm @ 5.0 Hz	0.20 μm	8.3%	0.016 μm	0.67%	92%
5.0 μm @ 2.5 Hz	0.54 μm	11%	0.055 μm	1.1%	90%
5.0 μm @ 5.0 Hz	0.54 μm	11%	0.045 μm	0.92%	92%
7.5 μm @ 5.0 Hz	0.93 μm	13%	0.053 μm	0.72%	94%
Filtered PRBS	0.71 μm	13%	0.30 μm	5.4%	59%

Table 2.3: Maximum stationary error when using the hysteresis compensation scheme with parameter values found for a reference signal other than the one applied.

Reference Signal	Absolute Error	Relative Error	
2.5 μm @ 5.0 Hz	0.28 μm	12%	using parameters found for 7.5 μm amplitude reference
7.5 μm @ 5.0 Hz	0.67 μm	9.2%	using parameters found for 2.5 μm amplitude reference

cut-off frequency. Pure numerical differentiation is not desired as it will amplify measurement noise, degrading the performance of the identification scheme. If the measured signal w contains a bias component, filtering $\bar{z}$ and $\bar{\varphi}$ by identical high-pass filters with a cut-off frequency lower than the lowest frequency component in the input signal u can be used to improve estimates.

2.6 Derivation of the Equivalent Coleman-Hodgdon Model

Eq. (2.1) can be solved explicitly, by observing that is can be written as

$$\dot{\eta} = (\beta - \alpha\eta + \gamma u)\,(\dot{u})^+ + (\beta + \alpha\eta - \gamma u)\,(\dot{u})^-$$

where $(\dot{u})^+ = \dot{u}$ and $(\dot{u})^- = 0$ when $\dot{u} \geq 0$, and $(\dot{u})^+ = 0$ and $(\dot{u})^- = \dot{u}$ when $\dot{u} < 0$. The dependence on time can then be cancelled. What is left are two linear

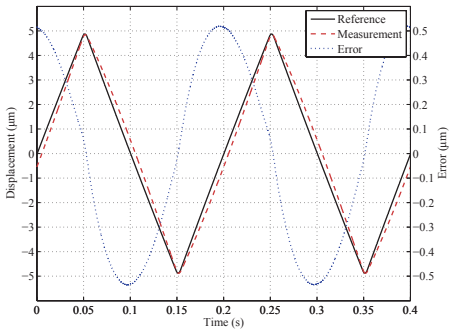

(a) Time-series for the reference signal, and the stationary measured displacement and error when using linear feed-forward.

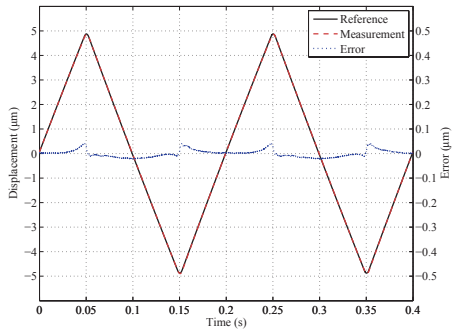

(b) Time-series for the reference signal, and the stationary measured displacement and error when using hysteresis compensation.

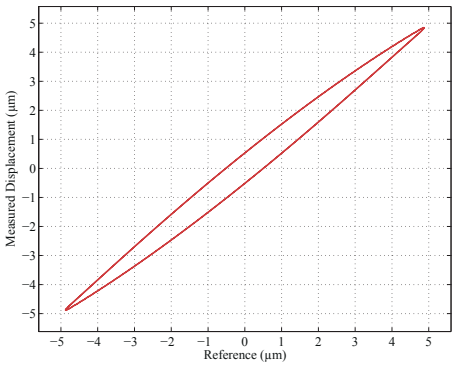

(c) Reference-to-displacement map when using linear feed-forward.

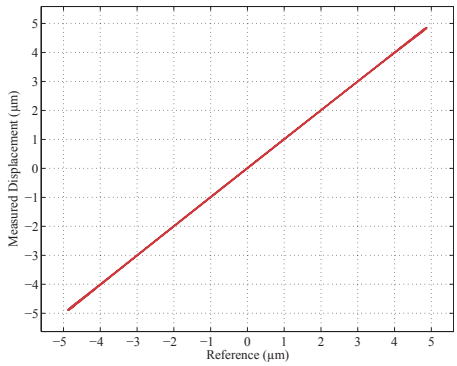

(d) Reference-to-displacement map when using hysteresis compensation.

Figure 2.5: Triangle-wave reference at 5 Hz with 5.0 μm amplitude (4.5 μm linear range), *cf.* Tabs. 2.1 and 2.2.

differential equations for the two cases. For the case $\dot{u} \geq 0$ the solution of

$$\mathrm{d}\eta = (\beta - \alpha\eta + \gamma u)\ \mathrm{d}u \ \Rightarrow\ \frac{\mathrm{d}\eta}{\mathrm{d}u} + \alpha\eta = \beta + \gamma u$$

can be found as

$$\eta = \mathrm{e}^{-h} \int \mathrm{e}^{h}\ (\beta + \gamma u)\ \mathrm{d}u = \mathrm{e}^{-\alpha u} \left[\frac{(\alpha\beta - \gamma + \alpha\gamma u)\mathrm{e}^{\alpha u}}{\alpha^2} + C_1 \right] ,$$

where e^{h}, $h = \int\ \alpha\,\mathrm{d}u = \alpha u$ has been used as the integrating factor. This yields

$$\eta^{+} = \frac{\gamma}{\alpha} u + \frac{\alpha\beta - \gamma}{\alpha^2} + C_1 \mathrm{e}^{-\alpha u} , \tag{2.18}$$

where

$$\eta_0 = \frac{\gamma}{\alpha} u_0 + \frac{\alpha\beta - \gamma}{\alpha^2} + C_1 \mathrm{e}^{-\alpha u_0} \Rightarrow\ C_1 = \mathrm{e}^{\alpha u_0} \left(\eta_0 - \frac{\alpha\beta - \gamma}{\alpha^2} - \frac{\gamma}{\alpha} u_0 \right) .$$

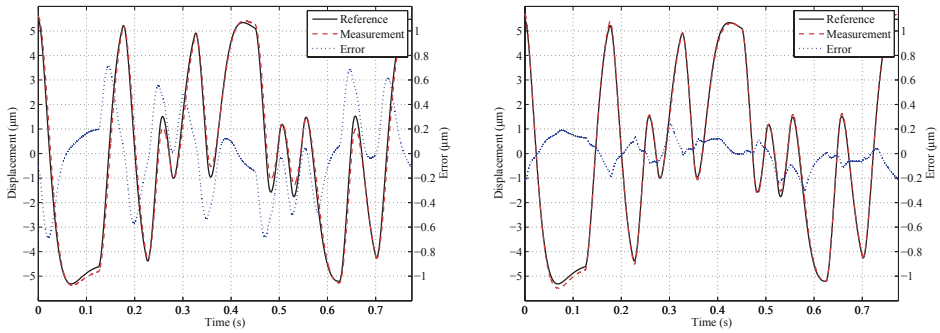

(a) Time-series for the reference signal, and the stationary measured displacement and error when using linear feed-forward.

(b) Time-series for the reference signal, and the stationary measured displacement and error when using hysteresis compensation.

Figure 2.6: Filtered PRBS reference, *cf.* Tabs. 2.1 and 2.2.

Similarly, for the case $\dot{u} < 0$ the solution is

$$\eta^- = \frac{\gamma}{\alpha}u + \frac{\gamma - \alpha\beta}{\alpha^2} + C_2 \mathrm{e}^{\alpha u} \,, \tag{2.19}$$

where

$$C_2 = \mathrm{e}^{-\alpha u_0}\left(\eta_0 - \frac{\gamma - \alpha\beta}{\alpha^2} - \frac{\gamma}{\alpha}u_0\right) \,.$$

The solutions (2.18) and (2.19), can be put on the form

$$\eta = \frac{\gamma}{\alpha}u + \eta_h, \tag{2.20}$$

which is the form in (2.2), where η_h accounts for the hysteretic behavior. As it happens, η_h can be taken to be the solution of the differential equation in (2.3), which is

$$\dot{\eta}_h = -b\dot{u} - a\eta_h|\dot{u}| \,. \tag{2.21}$$

The parameters of this formulation are related to the parameters in (2.1) by

$$a = \alpha > 0 \,,\; b = \frac{\gamma - \alpha\beta}{\alpha} > 0 \,,\; \text{and } c = \frac{\gamma}{\alpha} > 0 \,. \tag{2.22}$$

Eq. (2.3) is similar to a case of the well known Dahl solid friction model [53], except for the sign of the parameter b. This equation can also be solved for the cases $\dot{u} \geq 0$ and $\dot{u} < 0$ in a similar fashion as above, using, *e.g.*, separation of variables. The solution for $\dot{u} \geq 0$ is

$$\eta_h^+ = \frac{1}{a}\left(-b - C_3\mathrm{e}^{-au}\right) = \frac{\alpha\beta - \gamma}{\alpha^2} - \frac{1}{\alpha}C_3\mathrm{e}^{-\alpha u} \,, \tag{2.23}$$

where

$$C_3 = \mathrm{e}^{au_0}\left(-b - a\eta_{h0}\right) = -\alpha\mathrm{e}^{\alpha u_0}\left(\eta_0 - \frac{\alpha\beta - \gamma}{\alpha^2} - \frac{\gamma}{\alpha}u_0\right) = -\alpha C_1 \,,$$

and for $\dot{u} < 0$ it is

$$\eta_h^- = \frac{1}{a}\left(b - C_4 \mathrm{e}^{au}\right), \tag{2.24}$$

where

$$C_4 = \mathrm{e}^{-au_0}\left(b - a\eta_{h0}\right) = -\alpha C_2 .$$

By substitution of (2.23) and (2.24) into (2.20) and using the relations in (2.22), it can be seen that the two formulations are equivalent, by comparison to (2.18) and (2.19).

It can be noted that the solution of (2.21), η_h, is bounded. As

$$\lim_{u\to+\infty} \eta_h^+(u) = -\frac{b}{a} \tag{2.25}$$

and

$$\lim_{u\to-\infty} \eta_h^-(u) = \frac{b}{a} \tag{2.26}$$

it is apparent that $\|\eta_h\|_\infty = \frac{b}{a}$.

2.7 Derivation of the Hysteresis Compensation Scheme

As was shown in Section 2.3.2, by applying the input (2.11), *i.e.*,

$$u_h = \frac{K}{c}u - \frac{1}{c}\hat{\eta}_h , \tag{2.27}$$

using an estimate of η_h, the effect of the hysteresis can be cancelled.

An open-loop observer to estimate η_h can be obtained from (2.3), substituting u_h for the input u, which results in (2.12), that is,

$$\dot{\hat{\eta}}_h = -b\dot{u}_h - a\hat{\eta}_h\left|\dot{u}_h\right| = -b\left(\frac{K}{c}\dot{u} - \frac{1}{c}\dot{\hat{\eta}}_h\right) - a\hat{\eta}_h\left|\frac{K}{c}\dot{u} - \frac{1}{c}\dot{\hat{\eta}}_h\right| .$$

This expression can be rewritten as

$$\dot{\hat{\eta}}_h = \begin{cases} K\frac{-a\hat{\eta}_h - b}{-a\hat{\eta}_h - b + c}\dot{u} , & \dot{u}_h \geq 0 \\ K\frac{a\hat{\eta}_h - b}{a\hat{\eta}_h - b + c}\dot{u} , & \dot{u}_h < 0 \end{cases} , \tag{2.28}$$

but the switching criterion can not be determined causally, as it is dependent on $\dot{u}_h$ and not $\dot{u}$.

The expression (2.28) can again be solved explicitly by separation of variables by canceling the dependence on time. For the case $\dot{u}_h \geq 0$,

$$\frac{\mathrm{d}\hat{\eta}_h^+}{\mathrm{d}u} = K\frac{-a\hat{\eta}_h^+ - b}{-a\hat{\eta}_h^+ - b + c} ,$$

which solution is found as

$$\hat{\eta}_h^+ - \frac{c}{a}\ln\left(a\hat{\eta}_h^+ + b\right) = Ku + C_5 ,$$

where

$$C_5 = \hat{\eta}_{h0} - \frac{c}{a}\ln\left(a\hat{\eta}_{h0} + b\right) - Ku_0 \ .$$

This implicit equation can be solved explicitly for η_h as a function of u by using the Lambert W function [47], denoted $L_W(\cdot)$:

$$\hat{\eta}_h^+ = -\frac{c}{a}L_W\left(-\frac{1}{c}\exp\left(-\frac{aKu + aC_5 + b}{c}\right)\right) - \frac{b}{a} \tag{2.29}$$

Similarly, for the case $\dot{u}_h < 0$,

$$\hat{\eta}_h^- + \frac{c}{a}\ln\left(-a\hat{\eta}_h^- + b\right) = Ku + C_6 \ ,$$

where

$$C_6 = \hat{\eta}_{h0} + \frac{c}{a}\ln\left(-a\hat{\eta}_{h0} + b\right) - Ku_0 \ ,$$

and the explicit solution is found as

$$\hat{\eta}_h^- = \frac{c}{a}L_W\left(-\frac{1}{c}\exp\left(\frac{aKu + aC_6 - b}{c}\right)\right) + \frac{b}{a} \ . \tag{2.30}$$

Now, differentiating (2.29) or (2.30) by u yields

$$\frac{\mathrm{d}\hat{\eta}_h}{\mathrm{d}u} < 0$$

in either case. Thus, since

$$\frac{\mathrm{d}\hat{\eta}_h}{\mathrm{d}u} = \frac{\dot{\hat{\eta}}_h}{\dot{u}} \ , \tag{2.31}$$

$\dot{u} \geq 0 \Rightarrow \dot{\hat{\eta}}_h \leq 0$, and $\dot{u} \leq 0 \Rightarrow \dot{\hat{\eta}}_h \geq 0$. Therefore $\dot{u}_h \geq 0 \Rightarrow \dot{u} \geq 0$ and $\dot{u}_h < 0 \Rightarrow \dot{u} < 0$. This shows that (2.28) is equivalent to (2.13).

The solution of (2.13), $\hat{\eta}_h$, is also bounded, by similar argument as in Section 2.6, and since $L_W(0) = 0$. Thus $\|\hat{\eta}_h\|_\infty = \frac{b}{a}$.

2.8 Passivity of the Hysteresis Model

If a storage function is chosen as

$$V = \frac{1}{2}\left(cu^2 + \frac{1}{b}{\eta_h}^2\right) + u\eta_h,$$

the total derivative of V along the trajectories of (2.2) and (2.3) is

$$\dot{V} = cu\dot{u} + \frac{1}{b}\eta_h\left(-b\dot{u} - a\eta_h|\dot{u}|\right) + u\dot{\eta}_h + \dot{u}\eta_h = \\ \left(c\dot{u} + \dot{\eta}_h\right)u - \frac{a}{b}{\eta_h}^2|\dot{u}| = \dot{\eta}u - \frac{a}{b}{\eta_h}^2|\dot{u}| \leq \dot{\eta}u \ ,$$

thus, the model (2.2) and (2.3) is passive from u to $\dot{\eta}$.

The energy expended in a single traversal of the hysteresis loop (see Fig. 2.4), if the applied voltage u cycle between a some minimum $u(\tau_0) = u(\tau_2) = u_m$ and some maximum $u(\tau_1) = u_M$ during a period $\tau_2 - \tau_0$, can be found from the work done, which is

$$\begin{aligned} W &= -\int_{\tau_0}^{\tau_2} \eta \dot{u} \, \mathrm{d}t = -\int_{\tau_0}^{\tau_1} \eta \dot{u} \, \mathrm{d}t - \int_{\tau_1}^{\tau_2} \eta \dot{u} \, \mathrm{d}t \\ &= -\int_{u_m}^{u_M} \eta^+ \, \mathrm{d}u - \int_{u_M}^{u_m} \eta^- \, \mathrm{d}u \\ &= -\underbrace{\int_{u_m}^{u_m} cu \, \mathrm{d}u}_{=0} - \int_{u_m}^{u_M} \eta_h^+ \, \mathrm{d}u - \int_{u_M}^{u_m} \eta_h^- \, \mathrm{d}u. \end{aligned}$$

Since $\eta_h^+(u_M) = \eta_h^-(u_M)$ and $\eta_h^+(u_m) = \eta_h^-(u_m)$, C_3 and C_4 can be expressed in terms of u_m and u_M as

$$\begin{aligned} \eta_h^+(u_M) &= \frac{1}{a}\left(-b - C_3 \mathrm{e}^{-a u_M}\right) = \frac{1}{a}\left(b - C_4 \mathrm{e}^{a u_M}\right) = \eta_h^-(u_M) \\ \eta_h^+(u_m) &= \frac{1}{a}\left(-b - C_3 \mathrm{e}^{-a u_m}\right) = \frac{1}{a}\left(b - C_4 \mathrm{e}^{a u_m}\right) = \eta_h^-(u_m) \end{aligned}$$

which yields

$$\begin{aligned} C_3 &= b(\mathrm{e}^{a u_m} - \mathrm{e}^{a u_M}) \operatorname{csch} a(u_M - u_m) < 0 \\ C_4 &= b(\mathrm{e}^{-a u_m} - \mathrm{e}^{-a u_M}) \operatorname{csch} a(u_M - u_m) > 0 \, . \end{aligned}$$

The work done can now be found to be

$$W = 2\frac{b}{a^2}\left(a\left(u_M - u_m\right) - 2\tanh\frac{a}{2}\left(u_M - u_m\right)\right). \tag{2.32}$$

It can be noted that the work is due to the term given in (2.21), and that the new formulation of the hysteresis model (2.2) and (2.3), yields the same work as found for the original formulation of the Coleman-Hodgdon model (2.1) [45].

2.9 Hysteresis as an Uncertain Gain & an Input Disturbance

For the applied voltage signal defined in Section 2.8, the linearized sensitivity K of (2.7) can be found from, *e.g.*,

$$K = \frac{\left(cu_M + \eta_h^+(u_M)\right) - \left(cu_m + \eta_h^+(u_m)\right)}{u_M - u_m} \, , \tag{2.33}$$

using the expressions in Section 2.8. Thus, according to (2.33), the gain coefficient $K = e_a/k$ depends on the voltage signal u. Assuming that the stiffness k of the structure is constant, the gain coefficient e_a can therefore be interpreted as uncertain and input signal dependent. This interpretation is in accordance to the

results in Section 2.4 and Tab. 2.1, as well as to the measured responses found in Fig. 1.2b. This relationship is also experimentally investigated in [107, 171]. The gain coefficient e_a is close to constant for a specific stationary voltage signal, and can then be denominated as the *effective gain* of the actuator.

It can also be noted that the parameter β in (2.1) is the slope of η at $u = 0$ when $\eta_0 = u_0 = 0$, thus β and K should be close in numerical value, which provides a quick verification of the validity of estimates for β, as K is usually known from linear system identification.

Considering the output to be generated by a linear combination of the input u and a disturbance term d_u,

$$w = \frac{1}{k} f_a = \eta = cu + \eta_h = K(u + d_u) = \frac{e_a}{k}(u + d_u) \,, \tag{2.34}$$

it is apparent that the actuator force can be expressed as

$$f_a = e_a(u + d_u) \,, \tag{2.35}$$

and the disturbance term is given as

$$d_u = \left(\frac{k}{e_a}c - 1\right) u + \frac{k}{e_a}\eta_h \,, \tag{2.36}$$

which according to the Coleman-Hodgdon model must be bounded, if u is bounded.

This is verified by the inspection of Fig. 2.5a, where the error is almost exclusively due to hysteresis, and is obviously bounded and dependent on the input signal, having the same fundamental frequency. Boundedness is also implied by the passivity of the hysteresis model. In the cases where the hysteresis model is not an exact description of the behavior of the hysteresis phenomenon, it can be understood from the fact that hysteresis in ferroelectric material is a loss phenomenon, thus dissipating energy and heating up the material. For sustained excitation by high-bandwidth signals, the temperature of a piezoelectric actuator can therefore increase substantially. This can be verified in a straight-forward manner by touching a piezoelectric actuator before and after applying a sinusoidal signal with a large amplitude and high frequency, but **be sure to disconnect the amplifier in order to avoid electric shock!**

The nonlinear behavior can also be interpreted in terms of the frequency spectrum of the response of the hysteresis model (2.1) to a sinusoidal input. By definition, a linear system will always produce the same frequencies in the states as was present in the excitation signal. Hysteresis, on the other hand, will produce several frequencies in response to excitation by a signal with a single frequency. An example of this is shown in Fig. 2.7, where a power spectral density estimate has been found for the hysteresis model (2.1) and the linear model (2.7) excited by a sinusoidal signal. The hysteresis response has frequency components at odd harmonics of the fundamental frequency.

When a hysteretic actuator is coupled to a lightly damped mechanical structure, the vibration modes of the structure can be exited by the harmonics generated by the hysteresis, if the harmonics coincide with the resonant frequencies. An example is shown in Fig. 2.8, where a piezoelectric actuator is driven by two different

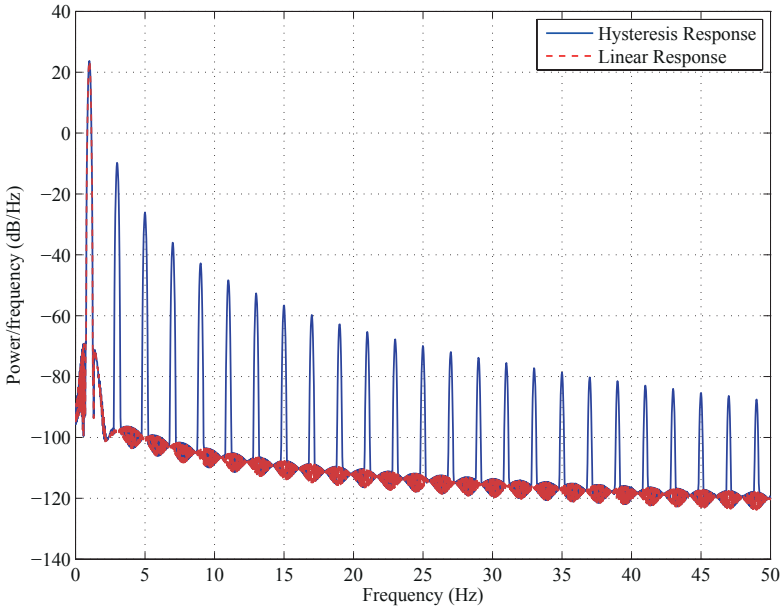

Figure 2.7: Power spectral density estimate for the hysteresis model and the linear model, when excited using a 1 Hz sinusoid.

sinusoidal voltage signals and the coupled mechanical structure has a dominant vibration mode with a resonant frequency at 535 Hz. If the input signal has a frequency of 150.0 Hz, there does not seem to be any significant excitation of any vibration modes, but if the frequency is increased to 178.3 Hz, which has a first odd harmonic of 534.9 Hz, the dominant vibration mode is excited.

2.10 Adding Integral Control

The hysteresis compensation scheme requires both signal u and the time derivative $\dot{u}$. As such, the scheme lends itself conveniently to an augmentation by an integral control law.

The integral control law is on the form

$$u_c = k_i \int_{t_0}^{t} e \, \mathrm{d}\tau \tag{2.37}$$

where

$$e = r - w \ . \tag{2.38}$$

By augmenting the signal u by the output of the control law u_c,

$$u' = u + u_c \ , \tag{2.39}$$

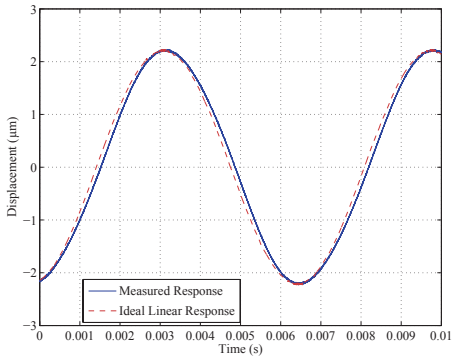

(a) Measured response using a 30 V amplitude sinusoid at 150.0 Hz.

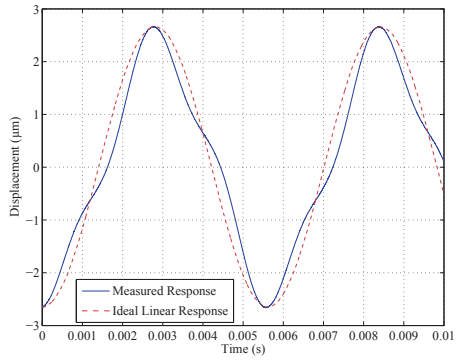

(b) Measured response using a 30 V amplitude sinusoid at 178.3 Hz.

Figure 2.8: Excitation of vibration dynamics with a resonant frequency of 535 Hz by actuator hysteresis.

it is straight forward to see that the time derivative of u' required to use the hysteresis compensation scheme is

$$\dot{u}' = \dot{u} + \dot{u}_c \tag{2.40}$$

where

$$\dot{u}_c = k_i e \ . \tag{2.41}$$

Thus, integral action, using, *e.g.*, the modified integral control law presented in Chapter 3, can be added with minimal increase in complexity, and can be used to reduce the error due to model discrepancy.

2.11 Trajectory Generation

For scanning applications, the desired reference signal is a triangle wave. A triangle wave can only be differentiated once and still be defined at the maxima and minima of the signal. For the purposes of output tracking for a second-order system, this means that perfect tracking is not possible, since the input required to obtain tracking is not defined (*i.e.*, of infinite magnitude) at the maxima and minima of the triangle wave signal. One solution is to remove some part of the triangle wave and replace it with a sufficiently smooth signal, such as a polynomial of sufficient degree. This is illustrated in Fig. 2.9.

Of the initial amplitude α of the triangle wave signal, a fraction $h = \lambda/\alpha$ of the signal can be chosen that will still be linear, where λ is the amplitude of the remaining linear segments. An interpolating polynomial must then be found for the interval $\delta \in [t_1, t_2] = \tau_p/4 \cdot [1-h, 1+h]$ between the linear parts of the signal. If a twice differentiable reference is desired, the interpolating polynomial will be second-order, *i.e.*,

$$P(t) = p_2 t^2 + p_1 t + p_0.$$

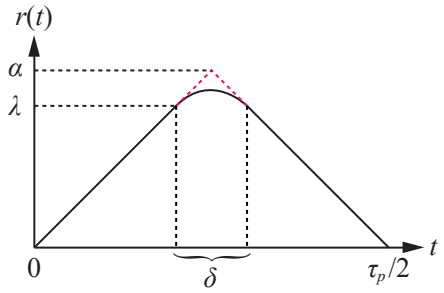

Figure 2.9: Modified triangle wave.

The coefficients p_i can be found solving the linear equations

$$\begin{bmatrix} t_1^2 & t_1 & 1 \\ 2t_1 & 1 & 0 \\ 2t_2 & 1 & 0 \end{bmatrix} \begin{bmatrix} p_2 \\ p_1 \\ p_0 \end{bmatrix} = \begin{bmatrix} \lambda \\ 4\alpha/\tau_p \\ -4\alpha/\tau_p \end{bmatrix}$$

where $t_1 = \tau_p/4 \cdot (1-h)$ and $t_2 = \tau_p/4 \cdot (1+h)$. Similarly, if a higher number of derivatives is desired, higher order polynomials should be used. With this method, to ensure that only the highest order derivative necessary will be discontinuous, the polynomial must be of order $n_p = 2n_d - 2$, where n_d is the number of desired derivatives.

The first half of the reference signal can now be computed as

$$r(t) = \begin{cases} \frac{4\alpha}{\tau_p} t \ , & t \in [0, t_1) \\ p_2 t^2 + p_1 t + p_0 \ , & t \in [t_1, t_2] \\ -\frac{4\alpha}{\tau_p} t \ , & t \in (t_2, \tau_p/2) \end{cases} ,$$

$$\dot{r}(t) = \begin{cases} \frac{4\alpha}{\tau_p} \ , & t \in [0, t_1) \\ 2p_2 t + p_1 \ , & t \in [t_1, t_2] \\ -\frac{4\alpha}{\tau_p} \ , & t \in (t_2, \tau_p/2) \end{cases} ,$$

and

$$\ddot{r}(t) = \begin{cases} 0 \ , & t \in [0, t_1) \\ 2p_2 \ , & t \in [t_1, t_2] \\ 0 \ , & t \in (t_2, \tau_p/2) \end{cases} .$$

The last half can be generated by inverting the first half and shifting it by $\tau_p/2$.

2.12 Conclusions

In this Chapter a feed-forward hysteresis compensation scheme was proposed for piezoelectric actuators. The scheme is based on a reformulation of the Coleman-Hodgdon model, where the reformulation produces a mathematically equivalent input-output map. The original Coleman-Hodgdon model can be used for parameter identification, while the reformulation can be used to generate an estimate the hysteretic response and to linearize the input-output map.

Since the parameters used in the scheme are identified online, the method will provide consistent performance, even when the hysteretic response changes due to different reference signals and other factors such as depolarization of the material and actuator temperature.

The proposed method is well suited for the case of symmetric hysteretic responses and certain periodic reference trajectories. The method has low complexity and is thus readily applicable for real-time implementation.

Experimental results are presented to illustrate the hysteresis compensation scheme. The experiments showed that the method reduced the hysteretic behavior of a piezoelectric actuator significantly, providing a reduction of more than 90% compared to when when assuming a linear response.

In addition, the reformulation of the Coleman-Hodgdon model has a form that makes it straight forward to show passivity of the model. The reformulation, since it is equivalent, has the same energy dissipation for a primitive hysteresis loop as the original formulation. The response of the model can also be interpreted as an uncertain gain and an input disturbance, and the hysteresis compensation scheme can be augmented with a integral control law in a straight forward manner, which can improve tracking performance.

Part II

Damping & Tracking Control

Chapter 3

Damping & Tracking Control Schemes for Nanopositioning

3.1 Introduction

Tracking control for nanopositioning devices can be achieved using feed-forward and feedback control techniques. Although feed-forward techniques can provide very good results [44], feedback control may be necessary in order to reduce sensitivity to uncertainty and disturbances. In order to control lightly damped vibrational modes in active structures, several control schemes that introduce damping have been developed. These include fixed-structure, low-order control laws, such as positive position feedback [76], integral force feedback [174], passive shunt-damping [96], resonant control [170], and integral resonant control [13]. By coupling such schemes with an integral control law, significantly better reference tracking performance can be achieved. With the exception of passive shunt-damping, this has been experimentally demonstrated in [14, 78, 85]. The main reason for the increased performance, is that a reduction of the dominant resonant peak in the frequency response of the system leads to an increased gain margin, enabling much higher gain to be used for the reference tracking integral control law [78].

General model-based control laws can also be used, such as $\mathcal{H}_\infty$-synthesis [206], the linear-quadratic-gaussian regulator [94], or output feedback control laws found using pole-placement and model reference control [94, 111]. There are several examples of control laws derived using $\mathcal{H}_\infty$-synthesis applied to nanopositioning systems [138, 187, 188, 192, 192, 194, 196, 198, 201, 211].

The advantage of using fixed-structure, low-order control laws is mostly practical, as such control laws are simple to implement and have low computational complexity [9]. The simplicity also makes them feasible for implementation using analog circuit elements. This can be beneficial, as avoiding sampling and quantization reduces the noise floor [175, 220]. The disadvantage of using fixed-structure, low-order control laws, is a lack of methods for optimal tuning, and this is a long standing and challenging control engineering problem. Although there exist some results for fixed-order control problems solved using linear matrix inequalities [56, 73, 95, 104, 109, 113, 210], these methods do not allow for the use of

unstructured uncertainty, do not guarantee global, or in some cases not even local convergence, and might not accommodate for control laws where the structure is fixed in addition to the order.

3.1.1 Contributions

Six different damping and tracking control schemes are presented and applied to a nanopositioning system for experimental comparison. All the schemes combine integral action with a control law that introduces damping of the dominant vibration mode of the system. The damping control schemes considered, are positive position feedback (PPF), integral resonant control (IRC), integral force feedback (IFF), and passive shunt-damping (PSD).

A simple damping and tracking control scheme using only a low-pass filter and an integrator is presented, *i.e.*, a modified integral control law, which will be labeled as damping integral control (DI). A tuning methodology is also presented, and is applied to the presented control schemes based on PPF, IRC, IFF, and PSD, as well as the DI scheme. Furthermore, a pole-placement control scheme in the form of model reference control (MRC) is also presented.

The presented control schemes based on IRC, IFF, and PPF, closely follows schemes already presented in the literature. IRC combined with an integral control law has been applied in [85], and a dual-sensor damping and tracking control scheme based on IFF has been applied in [78]. PPF combined with an integral control law, as well as a pole-placement control scheme is applied in [14]. Compared to the pole-placement control scheme in [14], the MRC scheme presented in this Chapter also incorporates integral action and low-pass filtering, in order to reduce sensitivity to disturbances and uncertainty, and to reduce quantization noise. The combination of PSD and an integral control law has not been investigated before.

3.1.2 Outline

The Chapter is organized as follows. Section 3.2 describes the experimental set-up as well as the dynamic models needed to develop the control schemes; a model for the mechanical vibrations of the nanopositioning device, a model for the generated charge in a piezoelectric actuator due to mechanical displacements, and a model for the measured response from piezoelectric force transducer. The parameters in the models are subsequently identified from frequency response data. The control design and tuning methodology used for all the control schemes is described in Section 3.3. In Section 3.4 the various control schemes are described and analyzed in detail. The experimental results are presented and discussed in Section 3.5. In addition, a simple integral anti-windup scheme is discussed in Section 3.6.

3.2 System Description & Modeling

3.2.1 Description of the Experimental System

The experimental set-up consists of a dSPACE DS1103 hardware-in-the-loop (HIL) system, an ADE 6810 capacitive gauge, an ADE 6501 capacitive probe from ADE

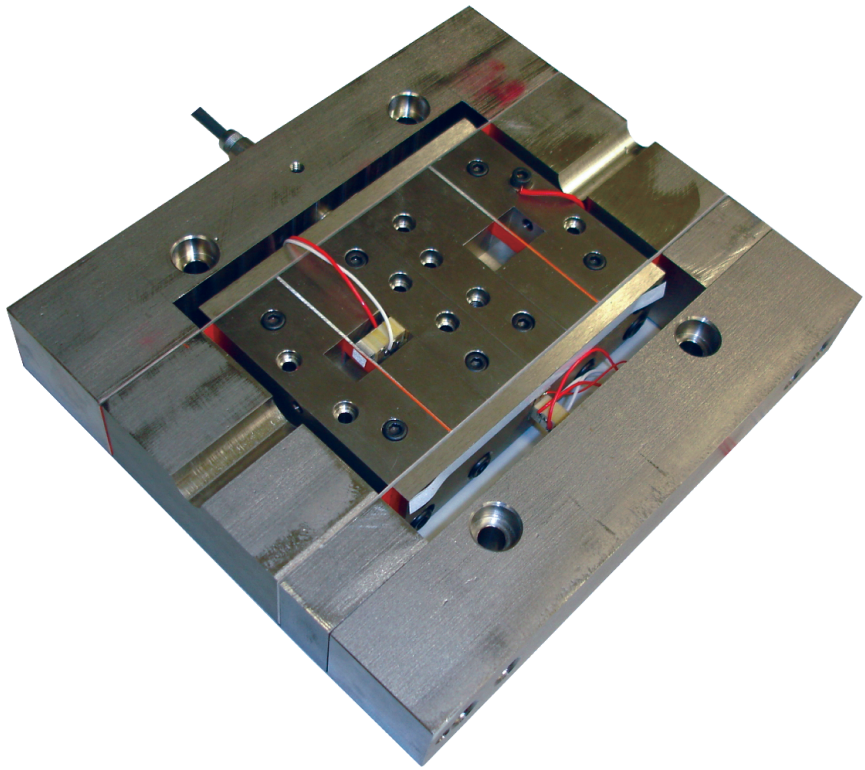

Figure 3.1: Custom flexure-guided nanopositioning stage.

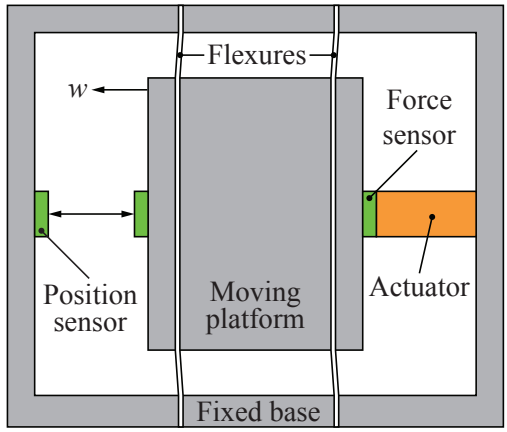

Figure 3.2: Simplified schematic of the single degree-of-freedom flexure guided positioning stage.

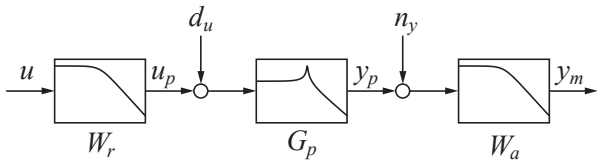

Figure 3.3: System diagram.

Technologies, a Piezodrive PDX200 voltage amplifier, two SIM 965 programmable filters from Stanford Research Systems, and the custom-made long-range serial-kinematic nanopositioner shown in Fig. 3.1. The nanopositioner is fitted with a Noliac SCMAP07-H10 actuator, where one of the stack elements is used as a force transducer. The transducer current is measured using a Burr-Brown OPA2111 configured with a 10 kΩ resistor, thus having a sensitivity of -10 V/mA. The capacitive probe has a bandwidth of 100 kHz, and the voltage amplifier with the capacitive load of the actuator, has a bandwidth in excess of 100 kHz. The voltage amplifier is also fitted with a current monitor with a sensitivity of 1 V/A, which enables the current in the actuator circuit to be measured. The capacitive measurement has a sensitivity of 1/5 V/μm and the voltage amplifier has a gain of 20 V/V. With the DS1103 board, a sampling frequency of $f_s = 100$ kHz is used for all the experiments. For numerical integration, a third-order Runge-Kutta scheme [62] is used.

A diagram of the system used is shown in Fig. 3.3. The positioner dynamics is represented by $G_p(s)$, the amplifier and reconstruction filter dynamics by $W_r(s)$, and the sensor and anti-aliasing filter dynamics by $W_a(s)$. The signal u is the input generated by the digital-to-analog converter, y_m is the output from the anti-aliasing filter, n_y is the sensor noise, and d_u is the input disturbance, mostly caused by hysteresis, creep, and environmental vibration noise.

3.2.2 Mechanical Model

The nanopositioning stage used is shown in Fig. 3.1, and a simplified schematic is shown in Fig. 3.2. The serial-kinematic motion mechanism is designed to make the dominant vibration mode to occur in the actuation direction, generating a piston motion. More details on the design of this stage can be found in [136].

The displacement is generated using a piezoelectric actuator. Such actuators generate a force proportional to an applied voltage, as a result of the converse piezoelectric effect, as described in Section A.5. The applied external force from the piezoelectric actuator f_a (N) can be expressed as

$$f_a = e_a(u_a + d_u) \,, \tag{3.1}$$

where e_a (N V^{-1}) is the effective gain of the piezoelectric actuator from voltage to force, and u_a (V) is the applied voltage. Here it is assumed that the additional stiffness introduced by the presence of the actuator in the mechanical structure is accounted for in the mechanical vibration model presented below. Piezoelectric actuators introduce hysteresis and creep when driven by an external voltage signal.

These effects occur in the electrical domain [161], and it is a reasonable assumption to consider this behavior as a bounded disturbance added to the input, represented by the term d_u (V), as discussed in Section 2.9.

As demonstrated in Appendix B, the dynamics due to the applied force f_a of a point w (m) on the flexible structure, as observed by a co-located sensor in a non-gyroscopic reference frame, is adequately described by the following lumped parameter, truncated linear model

$$G_w(s) = e_a \frac{w}{f_a}(s) \approx \sum_{i=1}^{n_w} \frac{\beta_i}{s^2 + 2\zeta_i \omega_i s + {\omega_i}^2} + D_r \ , \tag{3.2}$$

where n_w is the number of vibration modes included. Here, $\{\beta_i\}$ (m s^{-2} V^{-1}) are the control gains, $\{\zeta_i\}$ are the damping coefficients for each mode, and $\{\omega_i\}$ (rad s^{-1}) are the natural frequencies for the modes. The term D_r (m V^{-1}) is the residual mode, which is an approximation of the non-modeled higher frequency modes, and can be included to improve prediction of zero-locations. It produces a model that is not strictly proper, but as the instrumentation, such as the amplifier and sensors, have limited bandwidth, D_r can be considered equal to zero for this system. Eq. (3.2) has a pole-zero interleaving property [172], which is the origin of positive-realness (passivity) and negative-imaginariness for certain input-output pairs [166]. The inclusion of instrumentation dynamics, and sensor-actuator pairs that are not perfectly co-located, will in general invalidate the pole-zero interleaving property [172].

3.2.3 Charge

When applying passive shunt-damping, the generated charge due to the direct piezoelectric effect in the actuator circuit is utilized. This is sometimes referred to as self-sensing. As is shown in Section A.4, or equivalently from the constitutive equations in stress-charge from Section A.5, the induced charge in the actuator is

$$q = e_a w + C_p u_a = C_p(u_a + \alpha w) \ ,$$

where C_p (F) is the capacitance of the piezoelectric stack actuator, and $\alpha = e_a/C_p$ (V m^{-1}) is a constant determining the amount of charge generated by the direct piezoelectric effect due to the displacement w of the mechanical structure. The transfer-function from applied voltage u_a to induced charge q is therefore

$$G_q(s) = \frac{q}{u_a}(s) = C_p(1 + \alpha G_w(s)) \ . \tag{3.3}$$

3.2.4 Force Transducer

The integral force feedback scheme utilizes a co-located sensor in the form of a piezoelectric force transducer. The force sensor generates a charge, depending on the applied force, due to the direct piezoelectric effect.

From Section A.5 it is known that the constitutive equations in strain-charge form provides an expression for the charge in a piezoelectric transducer as

$$q = d_a f_a + C_p(1 + k^2)u_a \ .$$

For sensing, there is no applied voltage, thus $u_a = 0$, and the charge on the electrodes of the sensor can be found to be

$$q = d_a f_a \ .$$

Since the force working on the sensor is the same as the force working on the actuator, the force must be according to the constitutive equations in stress-charge form,

$$f_a = k_a w - e_a u_a \ ,$$

and the induced charge in the sensor can be found to be

$$q = d_a(k_a w - e_a u_a) \ .$$

The current or charge produced by the force transducer is typically converted to a voltage signal using a simple op-amp circuit with a high input impedance and gain g_s (V/C). The output voltage from such a sensor when measuring the charge, can be found to be [78, 172]

$$v_f = k_s(w - k_f u_a) \ ,$$

where w is the displacement of the mechanical structure, u_a is the applied voltage to the actuator, $k_f = e_a/k_a$ (m V^{-1}) is the gain of the feed-through term, and $k_s = g_s d_a k_a$ (V m^{-1}) is the sensor gain. The transfer-function from applied voltage u_a to measured sensor voltage v_f can therefore be found as

$$G_f(s) = \frac{v_f}{u_a}(s) = k_s(G_w(s) - k_f) \ . \tag{3.4}$$

3.2.5 Identification & Uncertainty

In order to identify the parameters in (3.2), (3.3), and (3.4), the frequency responses for the displacement, charge, and force are recorded using a SR780 Dynamic Signal Analyzer from Stanford Research Systems, applying a 150 mV RMS bandwidth-limited white noise excitation signal. The models are fitted into the procured data using the MATLAB System Identification and Optimization Toolboxes. As the noise from the force transducer is orders of magnitude lower than the noise from the displacement sensor [78], the frequency response for the displacement is inferred from (3.4). The frequency response obtained using the displacement sensor is used to find the parameters in (3.3) and (3.4). The responses for $G_w(s)$, $G_q(s)$, and $G_f(s)$ are displayed in Figs. 3.4a, 3.5a, and 3.6a, respectively. The identified parameter values are presented in Tab. 3.1. For the displacement model (3.2), three vibration modes, $n_d = 3$, are included. By inspection of Fig. 3.4a, it can be seen that the second mode at 1660 Hz is the dominant piston mode.

The uncertainty of the models can be quantified as unstructured multiplicative perturbations. Since the control schemes considered are either single-input-single-output (SISO), or single-input-multiple-output (SIMO), the uncertainty description of the models from the scalar input u_p to the output vector y_p has the form [100]

$$y_{p_i} = G_i(s)(1 + \delta_i(s)\Delta_i(s))u_p \ ; \ \|\Delta_i(s)\|_\infty \leq 1 \ , \tag{3.5}$$

Table 3.1: Identified model parameters.

Parameter	Value	Unit
Displacement model (3.2)		
β_1	$1.80{\cdot}10^4$	μm s^{-2} V^{-1}
ζ_1	0.0726	
ω_1	$2\pi{\cdot}490$	rad s^{-1}
β_2	$2.54{\cdot}10^6$	μm s^{-2} V^{-1}
ζ_2	0.0196	
ω_2	$2\pi{\cdot}1660$	rad s^{-1}
β_3	$4.83{\cdot}10^6$	μm s^{-2} V^{-1}
ζ_3	0.0312	
ω_3	$2\pi{\cdot}3400$	rad s^{-1}
Charge model (3.3)		
C_p	195	nF
α	3.95	V μm^{-1}
Force model (3.4)		
k_s	$2.52{\cdot}10^{-7}$	V μm^{-1}
k_f	0.0451	μm V^{-1}

where i denotes the index into the output vector y_p, such that $G_i(s)$ corresponds to the transfer-function from the input u_p to the output y_{p_i}, and $\delta_i(s)$ is the corresponding frequency dependent uncertainty weight. The uncertainty weights $\{\delta_i(s)\}$ are determined experimentally, for each of the outputs, and are presented in Figs. 3.4b, 3.5b, and 3.6b. Over-bounding weights were also found to introduce more conservativeness. The gain uncertainty discussed in Section 2.9 is here downplayed somewhat as the maximum range of the nanopositioning device will not be used in the experiments and to simplify the choice of uncertainty weights, as they are actually coupled.

3.3 Control Design

The control schemes presented will be analyzed with regards to the general control structure shown in Fig. 3.7.

3.3.1 Performance Measures

The control schemes considered are either single-input-single-output (SISO), or single-input-multiple-output (SIMO). Considering the general SIMO case, it can

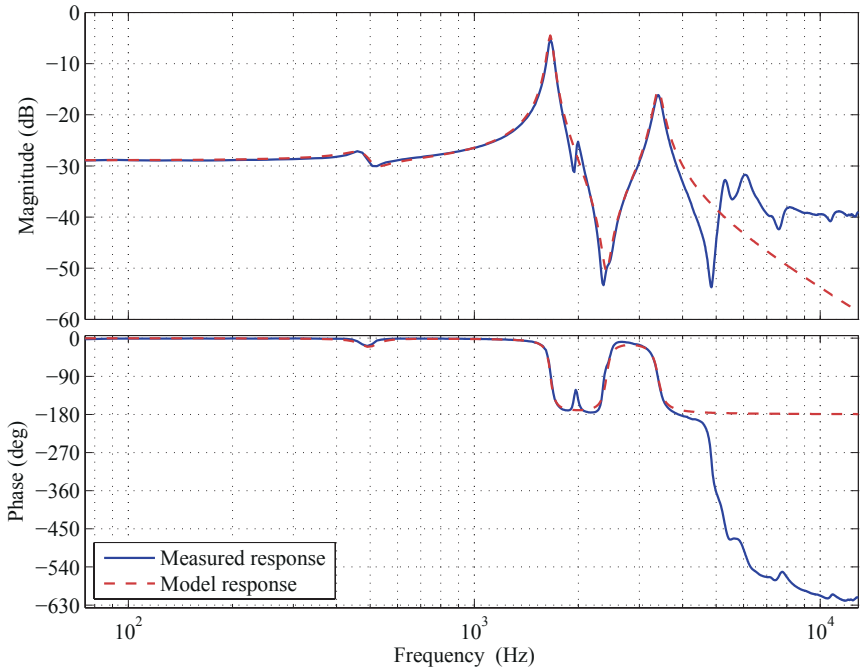

(a) Frequency response for the displacement model $G_w(s)$.

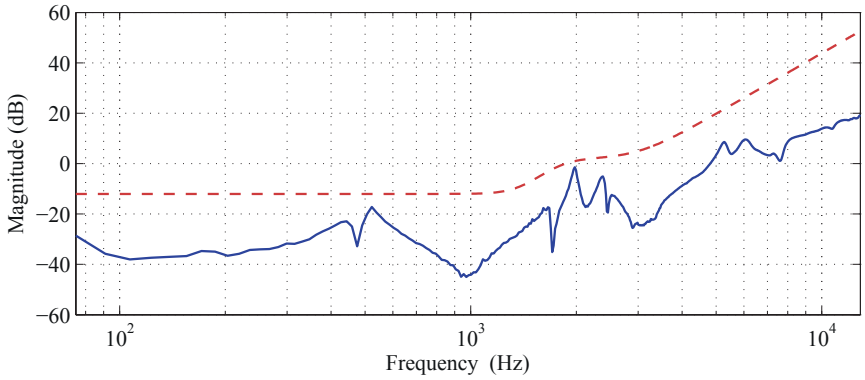

(b) Multiplicative uncertainty weight $\delta_w(s)$.

Figure 3.4: Response and uncertainty for the displacement.

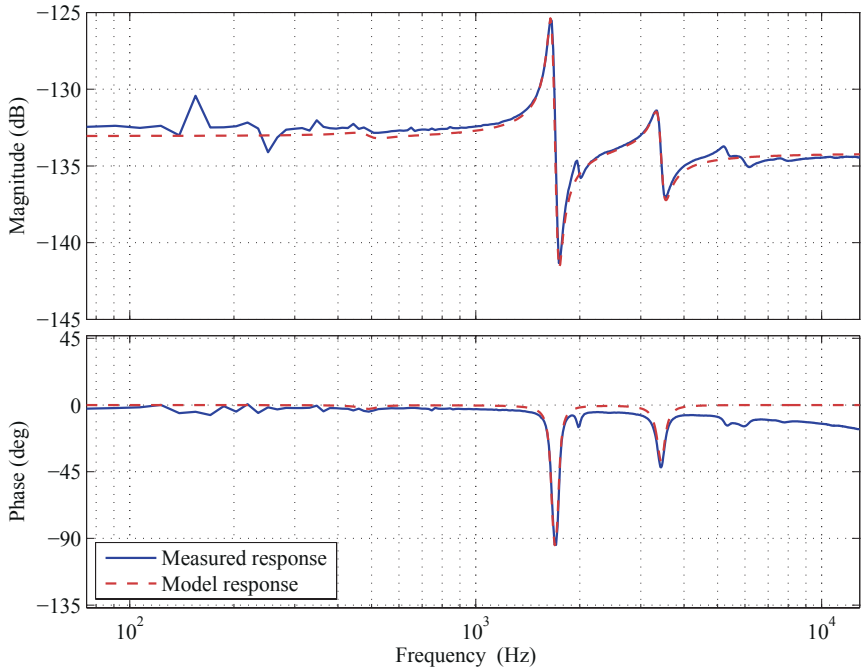

(a) Frequency response for the charge model $G_q(s)$.

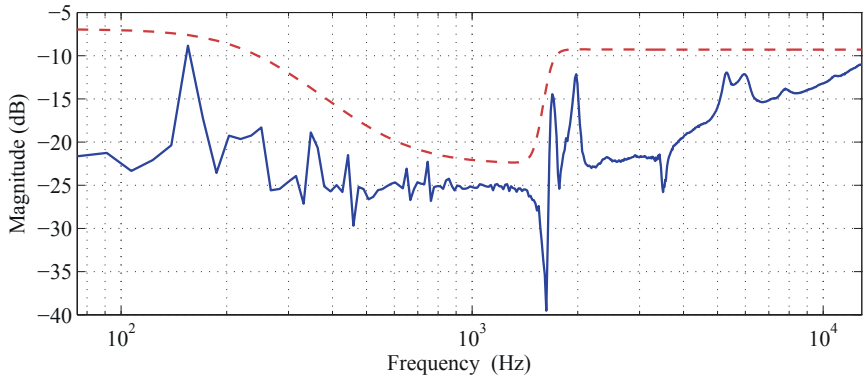

(b) Multiplicative uncertainty weight $\delta_q(s)$.

Figure 3.5: Response and uncertainty for the charge.

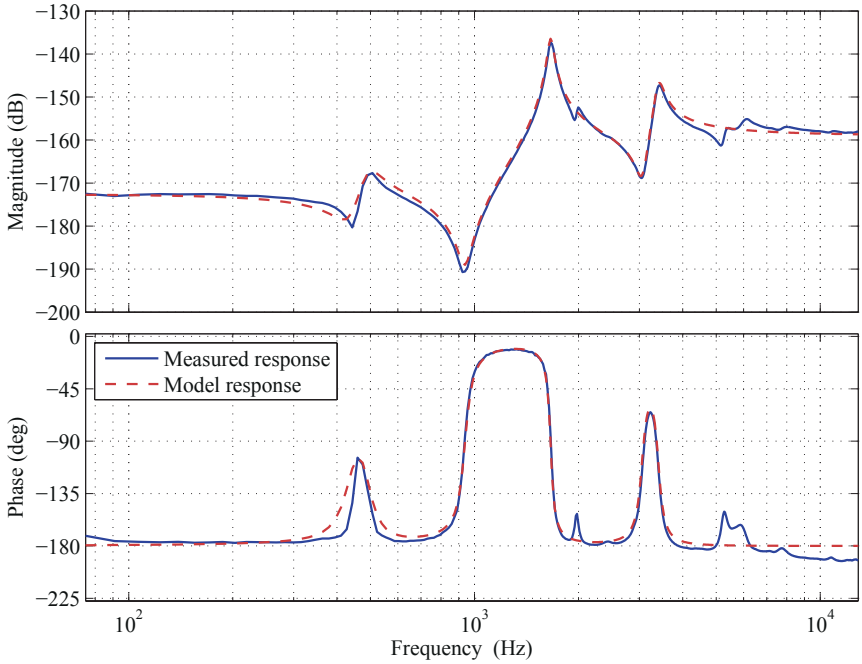

(a) Frequency response for the force model $G_f(s)$.

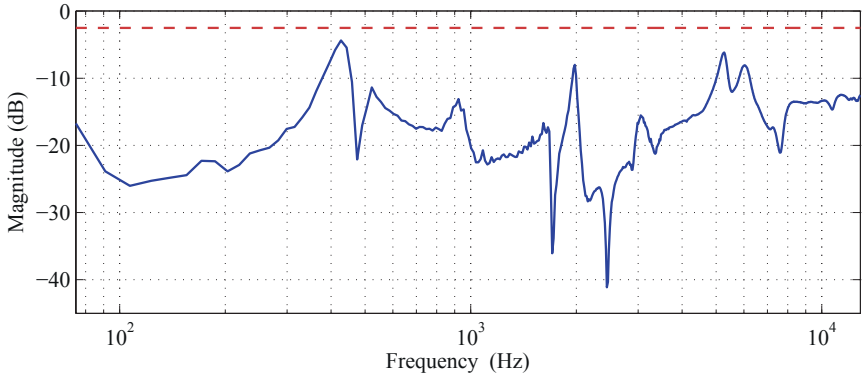

(b) Multiplicative uncertainty weight $\delta_f(s)$.

Figure 3.6: Response and uncertainty for the force.

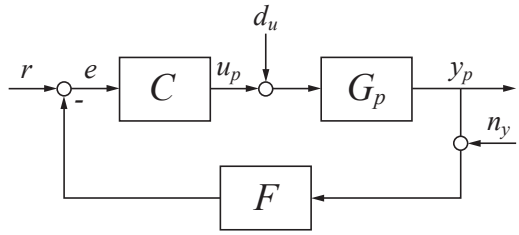

Figure 3.7: General control law structure.

be seen that for the control structure in Fig. 3.7, the control input is given as

$$u_p = C(s)(r - F(s)y_p) \ , \tag{3.6}$$

where $C(s)$ is a one-row feed-forward transfer-matrix, and $F(s)$ is a diagonal feedback transfer-matrix.

Breaking the loop at the error e of the one-column plant transfer-matrix $G_p(s)$, the loop transfer-matrix is

$$L(s) = F(s)G_p(s)C(s) \ ,$$

which defines the output sensitivity transfer-matrix $S_O(s)$ as

$$e = S_O(s)r = (I + L(s))^{-1}r \ , \tag{3.7}$$

where $e = r - F(s)y_p$. The complementary sensitivity transfer-matrix $T(s)$ becomes

$$y_p = T(s)r = G_p(s)C(s)S_O(s)r \ . \tag{3.8}$$

In addition, the transfer-matrix $N(s)$ from the additive sensor noise n_y to the output y_p is

$$y_p = N(s)n_y = -T(s)F(s)n_y \ , \tag{3.9}$$

and the transfer-matrix $E(s)$, measuring the deviation of the plant output y_p from the reference trajectory r, $\epsilon = r - y_p$, is

$$\epsilon = E(s)r = (I - T(s))r \ . \tag{3.10}$$

Note that $\epsilon \neq e$, if $F(s) \neq I$.

Breaking the loop at the input u_p of the plant, the loop transfer-matrix is

$$L_I(s) = C(s)F(s)G_p(s) \ ,$$

and the input sensitivity transfer-matrix $S_I(s)$ from the disturbance d_u to the input u_p is therefore

$$u_p = S_I(s)d_u = (I + L_I(s))^{-1}d_u \ , \tag{3.11}$$

which provides the transfer-matrix $D(s)$ from the disturbance d_u to the output y_p as

$$y_p = D(s)d_u = G_p(s)S_I(s)d_u \ . \tag{3.12}$$

The performance will be evaluated with regards to the flatness of the response of $T(s)$, the bandwidth of $E(s)$, the attenuation of the input disturbance d_u to the displacement w, and the amplification of sensor noise n_y to the displacement w. The bandwidth of $E(s)$ is defined as the frequency where $|E(j\omega)|$ first crosses the line of -3 dB from below in the frequency response diagram. At this frequency the tracking error ϵ is 50% of the reference r, thus there is effectively no tracking of frequency components above the bandwidth. The attenuation of the input disturbance is measured by the $\mathcal{H}_\infty$-norm, $\|D(s)\|_\infty$, which corresponds to the peak magnitude of $D(s)$. The added displacement noise is measured by the $\mathcal{H}_2$-norm, $\|N(s)\|_2$, which provides the root-mean-square displacement noise response if n_y is taken to be equal to unity variance Gaussian white noise. Thus, the displacement variance due to sensor noise can be found as ${\sigma_d}^2 = \|N(s)\|_2^2 {\sigma_n}^2$.

3.3.2 Robust Stability Measure

The SIMO robust stability criterion described in [100], for multiplicative uncertainty on the form (3.5), can be adapted to the control structure in Fig. 3.7. Robust stability can be ensured if

$$\sup_\omega \sum_{i=1}^{n_y} |S_I(j\omega)G_i(j\omega)C_i(j\omega)F_i(j\omega)\delta_i(j\omega)| = \gamma_s \leq 1 \,, \tag{3.13}$$

where the matrix elements $C_i(s)$ and $F_i(s)$ correspond to the output y_{p_i}, and n_y is the number of outputs. The inverse value of the norm, $1/\gamma_s$, provides a measure of the minimum amount of additional multiplicative uncertainty that the system can tolerate before it becomes unstable, for the given frequency weights, δ_i.

3.3.3 Tuning

Control design for fixed-structure, low-order control laws using output feedback is a long-standing and challenging problem in control engineering. A common approach to output feedback problems, is to use $\mathcal{H}_\infty$-synthesis. If the control law is allowed to have any order and every matrix of the control law is freely tunable, $\mathcal{H}_\infty$-synthesis guarantees a solution to the control design problem by convex optimization.

For a control law with a fixed structure and with a lower order than the plant, this approach can not be applied. In general, since model-based control synthesis is based on model matching, the control law must be of sufficient order with respect to the plant and the control law structure is determined by the plant. The simplest example of model-based control is perhaps control law synthesis using pole-placement. In general, for arbitrary pole-placement, producing a proper control law for a strictly proper plant, the control law must be of order $n_p - 1$, where n_p is the order of the plant. This produces a closed-loop characteristic polynomial of order $2n_p - 1$ [94].

Example 3.1:
For the second-order system, $n_p = 2$,

$$\frac{w}{u}(s) = G(s) = k_p \frac{Z_p}{R_p} = \frac{\beta_0}{s^2 + 2\zeta_0\omega_0 s + {\omega_0}^2} \,,$$

a first-order proper control law of

$$C(s) = \frac{B(s)}{A(s)} = \frac{b_1 s + b_0}{s + a_0} \ ,$$

can be found for arbitrary pole-placement conforming to the third-order polynomial

$$P(s) = s^3 + p_2 s^2 + p_1 s^1 + p_0 \ ,$$

by solving the Bézout identity

$$R_p(s)A(s) + k_p Z_p(s)B(s) = P(s) \ .$$

The solution for the control law parameters $\theta_c = [a_0, b_1, b_0]^{\mathrm{T}}$ *is*

$$S\theta_c = p = \begin{bmatrix} 1 & 0 & 0 \\ 2\zeta_0\omega_0 & \beta_0 & 0 \\ {\omega_0}^2 & 0 & \beta_0 \end{bmatrix} \begin{bmatrix} a_0 \\ b_1 \\ b_0 \end{bmatrix} = \begin{bmatrix} p_2 - 2\zeta_0\omega_0 \\ p_1 - {\omega_0}^2 \\ p_0 \end{bmatrix} \ \Rightarrow \ \theta_c = S^{-1}p \ .$$

Here, three freely tunable control law parameters are needed in order to specify the poles. If the plant model is of higher order, the control law order grows, and in general, for a control law of minimal order, no constraints on the control law structure can be made. Second-order pole-placement is also possible for the second-order system using a proportional-derivative (PD) control law, but in this case the control law is not proper, and might cause implementation problems in terms of noise amplification and insufficient roll-off for the loop transfer-function $G(s)C(s)$ *at higher frequencies, due to the derivative action.*

For standard mixed $\mathcal{H}_\infty$-synthesis, the minimum control law order is also determined by the plant order, but the performance and robust stability weights will typically add to the complexity of the control law. Moreover, the exact choice of weighs directly impacts the closed-loop performance. If the resulting control law is of very high order, practical problems related to numerical stability, discretization, and computational complexity can arise. Due to the limited computational power available when using high sampling frequencies, or if an implementation using analog circuit elements is desired, the model order should be as low a possible. Applying model or control law order reduction techniques can provide some remedy, but can in some cases lead to unexpected results, and will in any case add a complicating step in the control design.

There exist some results for direct synthesis of low-order robust control problems, solved with the use of linear matrix inequalities. However, these methods do not allow for the use of unstructured uncertainty, do not guarantee global, and in many cases not even local, convergence, and might not accommodate for control laws where the structure is fixed in addition to the order [56, 73, 95, 104, 109, 113, 210].

In other words, there does not exist any general control design method for output feedback using fixed-structure, low-order control laws. A practical optimization procedure is therefore proposed in order to obtain good tracking performance.

Tuning Methodology

Control design is often a trade-off between conflicting goals. For nanopositioning systems, it is desirable to have a high bandwidth for $E(s)$ in order to have good reference tracking. Also, the system is required to well damped in order to avoid excessive vibrations. This translates to an absence of peaks in $T(s)$. To counter hysteresis and creep, as well as environmental disturbances, $D(s)$ must provide a high degree of attenuation. In addition, the amplification of sensor noise should be as small as possible, meaning that $N(s)$ should have the smallest bandwidth possible. Due to the restriction imposed by the Bode sensitivity integral [94], it is impossible to meet these criteria simultaneously. As the purpose of damping control is to reduce peaks in the closed-loop response due to lightly damped vibration modes, and since ideal tracking performance is achieved when $T(s) = 1$, it appears that a good overall performance criterion is the flatness of $T(s)$, *i.e.*, the minimization of

$$J(\theta_c) = \| 1 - |T(j\omega, \theta_c)| \|_2 \ , \tag{3.14}$$

by some optimal control law parameter vector $\theta_c{}^\star$.

For the control schemes presented in the following sections, with the exception of model reference control, a practical and straight forward method to find control law parameters θ_c that provide good tracking performance for a particular scheme is to solve

$$\arg\min_{\theta_c} J(\theta_c) \ \text{ s.t. } \ \mathrm{Re}\{\lambda_i\} \in \mathbb{R}^- \ \wedge \ \gamma_s < 1 \ , \tag{3.15}$$

where $\{\lambda_i\}$ is the set of eigenvalues for the closed-loop system.

The optimization problem can be solved either by using an exhaustive grid search over a domain of reasonable control law parameter values, as is demonstrated for the DI scheme in Chapter 4, or by using an unstructured optimization algorithm, such as the Nelder-Mead method [133]. In this Chapter, all the control schemes were tuned using the Nelder-Mead method.

3.4 Damping & Tracking Control Schemes

3.4.1 Integral Control Law

An integral control law applied to a mass-spring-damper system has a fairly limited gain margin. When applied to a lightly damped structure, the integral gain is primarily limited by the resonant frequency and relative damping of the dominant vibration mode.

Considering an integral control law

$$C_i(s) = \frac{k_i}{s}$$

where $k_i > 0$, applied to a mass-spring-damper system

$$\frac{w}{u}(s) = \frac{\beta_0}{s^2 + 2\zeta_0\omega_0 s + {\omega_0}^2} \ ,$$

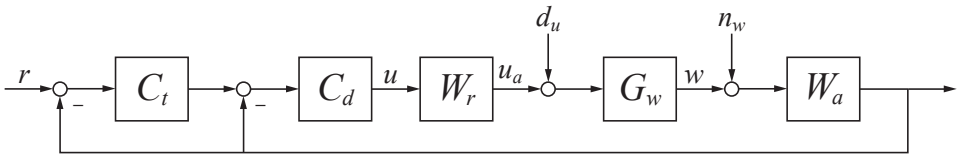

Figure 3.8: Control structure when using positive position feedback and integral resonant control.

where $\beta_0 > 0$, an analytical expression for the maximum gain k_i^* that renders a stable closed-loop system can be found by application of the Routh-Hurwitz criterion, as

$$k_i < \frac{2\zeta_0 {\omega_0}^3}{\beta_0} = k_i^* \ . \tag{3.16}$$

Given a lightly damped system, $0 < \zeta_0 \ll 1/\sqrt{2}$, knowing the resonant frequency ω_p and the amplitude response at resonance $|G(j\omega_p)|$, *cf.* Section B.3,

$$\omega_p = \omega_0\sqrt{1-2{\zeta_0}^2} \quad \text{and} \quad |G(j\omega_p)| = \frac{\beta_0}{2\zeta_0{\omega_0}^2\sqrt{1-{\zeta_0}^2}} \ ,$$

the maximum gain (3.16) can be expressed as

$$k_i < \frac{\omega_p}{|G(j\omega_p)|} < \kappa_1 \cdot \frac{\omega_p}{|G(j\omega_p)|} = k_i^* \tag{3.17}$$

where ${\kappa_1}^{-1} = \sqrt{1-{\zeta_0}^2} \cdot \sqrt{1-2{\zeta_0}^2} < 1$. This corresponds well with the result found in [78], where (3.17) is derived by graphical arguments. The example above is for a single degree of freedom system, but the analysis corresponds well to multiple degree of freedom systems where there is one dominant vibration mode and no rigid body modes.

It is clear that the integral gain is limited by both the natural frequency of the dominant vibration mode, and the amount of damping in the structure. It can be therefore be conjectured that attenuating the resonant peak or increasing the resonant frequency improves the gain margin, and thus the bandwidth of the closed-loop system.

3.4.2 Positive Position Feedback (PPF)

Damping and tracking control using positive position feedback (PPF) [76, 172] combined with an integral control law can be implemented using the control structure in Fig. 3.8. This is equivalent to the control scheme in [14]. The damping control law consists of a low-pass filter with negative gain

$$C_d(s) = \frac{-k_d}{s^2 + 2\zeta_d\omega_d s + {\omega_d}^2} \ , \tag{3.18}$$

were $k_d > 0$ is the control law gain, ζ_d the damping coefficient and ω_d is the cut-off frequency. The tracking control law, is an integral control law with a negative gain,

which will be inverted by the negative gain of the filter (3.18),

$$C_t(s) = \frac{-k_t}{s} \ . \tag{3.19}$$

Here, $k_t > 0$ is the gain of the integral term.

To analyze the nominal performance of the control scheme, the control structure in Fig. 3.8 can be put on the equivalent formulation adhering to the control structure in Fig. 3.7. The feed-forward filter is found as

$$C(s) = W_r(s)C_d(s)C_t(s) \ , \tag{3.20}$$

and the feedback filter is found as

$$F(s) = W_a(s)(1 + C_t^{-1}(s)) \ . \tag{3.21}$$

Using the above expressions, and assuming

$$G_p(s) = G_w(s) \ ,$$

it is straight forward to find the transfer-functions for the sensitivity (3.7), the complementary sensitivity (3.8), the noise attenuation (3.9), the error attenuation (3.10), and the disturbance rejection (3.12). Here, $W_r(s) = W_a(s)$, and are second-order Butterworth filters with cut-off frequency at 20 kHz.

The robust stability with regards to the multiplicative model uncertainty can be evaluated using the stability criterion (3.13), using (3.8), (3.20) and (3.21).

There are four tunable control law parameters

$$\theta_c = [k_d, \ \zeta_d, \ \omega_d, \ k_t]^{\mathrm{T}} \ ,$$

the feedback filter gain k_d, the damping ratio ζ_d, the cut-off frequency ω_d, and the tracking integral control law gain k_t. The optimal control law parameters for (3.18) and (3.19) found when solving (3.15) are presented in Tab. 3.2. The resulting nominal frequency responses for $T(S)$, $E(s)$, and $D(s)$ are shown in Fig. 3.16a.

Table 3.2: Optimal parameters for (3.18) and (3.19).

Parameter	Value
k_d	$2.32{\cdot}10^8$
ζ_d	0.564
ω_d	$2\pi{\cdot}1470$
k_t	$2.31{\cdot}10^4$

Additional Analysis

Stability of the PPF scheme is straight forward to analyze considering the negative-imaginary property of the low-pass filter (3.18) and the mechanical vibration model (3.2) [166].

Inverting the gain of the low-pass filter (3.18), *i.e.*,

$$\bar{C}(s) = \frac{k_d}{s^2 + 2\zeta_d\omega_d s + {\omega_d}^2} , \tag{3.22}$$

it is known that this is a strictly negative-imaginary (SNI) transfer-function [166]. The mechanical vibration model (3.2) is also SNI, as it is a linear combination of SNI transfer-functions, where each transfer-function has the same form as (3.22), and since the real constant term D_r does not influence the negative imaginary properties. Negative imaginariness can also be established by the pole-zero interleaving property described in Appendix B, as $\angle G_w(j\omega) \in [-180°, 0°]$.

Since both transfer-functions are SNI, the *positive* feedback connection of $\bar{C}(s)$ and $G_w(s)$ is therefore internally stable if $\bar{C}(0)G_w(0) < 1$.

However, the closed-loop transfer-function

$$T_{ppf}(s) = \frac{-\bar{C}(s)G_w(s)}{1 - \bar{C}(s)G_w(s)} = \frac{C_d(s)G_w(s)}{1 + C_d(s)G_w(s)} ,$$

is not negative-imaginary (NI), and further analysis using negative-imaginary properties can not be done. Also, including instrumentation dynamics and not having perfect co-location of the sensor and actuator precludes the usage of NI analysis. It should be noted, however, that with reasonably good co-location for the dominant vibration modes, and instrumentation with significantly higher bandwidth than the dominant vibration modes, modeling the control law and plant dynamics using (3.18) and (3.2) provides a good approximation and good results in practice.

3.4.3 Integral Resonant Control (IRC)

Damping and tracking control applying integral resonant control (IRC) [13] to introduce damping can also be implemented using the control structure in Fig. 3.8. In this control scheme [85] the damping control law is

$$C_d(s) = \frac{-k_d}{s + k_d D_f} . \tag{3.23}$$

Eq. (3.23) is the result of rearranging the IRC scheme to a form suitable for tracking control [85], consistent with the control structure in Fig. 3.8. Here, $k_d > 0$ is the called the integral damping gain, while $D_f > 0$ is a feedthrough term. The tracking control law is

$$C_t(s) = \frac{-k_t}{s} , \tag{3.24}$$

where $k_t > 0$ is the gain of the integral term.

As this scheme uses the same control structure as the one using PPF in Section 3.4.2, the scheme can be analyzed using the same equivalent formulation with regards to the general control structure in Fig. 3.7, *i.e.*, with

$$C(s) = W_r(s)C_d(s)C_t(s) \tag{3.25}$$

and

$$F(s) = W_a(s)(1 + C_t^{-1}(s)) . \tag{3.26}$$

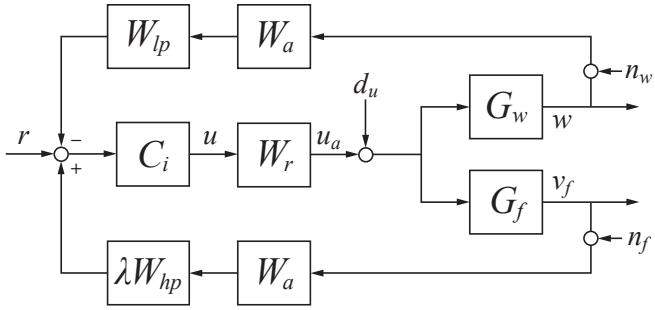

Figure 3.9: Control structure when using integral force feedback.

Here, $W_r(s) = W_a(s)$, and are second-order Butterworth filters with cut-off frequency at 20 kHz.

There are three tunable control parameters

$$\theta_c = [D_f,\ k_d,\ k_t]^{\mathrm{T}} ,$$

the feedthrough term D_f, the integral damping gain k_d, and the tracking integral control law gain k_t. The optimal control law parameters for (3.23) and (3.24) found when solving (3.15) are presented in Tab. 3.3. The resulting nominal frequency responses for $T(S)$, $E(s)$, and $D(s)$ are shown in Fig. 3.16b.

Table 3.3: Optimal parameters for (3.23) and (3.24).

Parameter	Value
D_f	0.116
k_d	$8.75{\cdot}10^4$
k_t	$7.12{\cdot}10^3$

Remark 3.1. Inverting the gain of the transfer-function (3.23), *i.e.*,

$$\bar{C}(s) = \frac{k_d}{s + k_d D_f} ,$$

it is known that it is a strictly negative-imaginary transfer-function [27, 166]. The exact same arguments can then be made for internal stability as in the PPF case, assuming perfect co-location and no instrumentation dynamics.

3.4.4 Integral Force Feedback (IFF)

The dual-sensor damping and tracking control scheme proposed in [78], is based on integral force feedback (IFF) [172, 174], and can be implemented using the control structure shown in Fig. 3.9, where $G_f(s)$ is described in (3.4).

The advantage of using this scheme, is that the piezoelectric force transducer has a noise density orders of magnitude lower than a capacitive probe, thus allowing

high bandwidth, but with substantially lower displacement noise due to feedback. The drawback is reduced range, as the force sensor replaces parts of the actuator, and additional instrumentation to amplify the charge generated by the transducer. The force sensor also requires good calibration, and the response is slightly non-linear, but this is an insignificant source of error at higher frequencies.

The control scheme requires an integral control law,

$$C_i(s) = \frac{k_i}{s} \ , \tag{3.27}$$

to be implemented, where $k_i > 0$ is the gain. In addition, two splitting filters, a low-pass and a high-pass filter, must be implemented. The low-pass filter is given as

$$W_{lp}(s) = \frac{\omega_f}{s + \omega_f} \ , \tag{3.28}$$

while the high-pass filter is given as

$$\lambda W_{hp}(s) = \lambda \frac{s}{s + \omega_f} \ , \tag{3.29}$$

where the gain λ is found as

$$\lambda = \left| \frac{G_w(0)}{G_f(0)} \right| \ . \tag{3.30}$$

The cut-off frequency ω_f determines split between the frequency range for where to use displacement feedback, and where to use force feedback. For the implementation, this was chosen to be $\omega_f = 2\pi \cdot 50$. Better noise properties can be achieved by reducing ω_f, but this is limited to some extent by the need to high-pass filter the force measurement. The high-pass filter is used both to allow the use of the capacitive probe measurement at low frequencies, and to remove bias components in the charge measurement. As the force transducer response is slightly non-linear, sufficient bandwidth for the capacitive probe measurement is required to improve linearity.

This is a single-input-multiple-output (SIMO) system, and the measurement vector is given as

$$y_p = [w, \ v_f]^{\mathrm{T}} \ , \tag{3.31}$$

while the input is the applied voltage u_a. With regards to Fig. 3.7, the plant transfer-matrix is

$$G_p(s) = [G_w(s), \ G_f(s)]^{\mathrm{T}} \ , \tag{3.32}$$

the feed-forward transfer-matrix is given as

$$C(s) = [W_r(s)C_i(s), \ -W_r(s)C_i(s)] \ , \tag{3.33}$$

and the feedback transfer-matrix is given as

$$F(s) = \begin{bmatrix} W_{lp}W_a(s) & 0 \\ 0 & \lambda W_{hp}W_a \end{bmatrix} \ . \tag{3.34}$$

Here, $W_r(s) = W_a(s)$, and are second-order Butterworth filters with cut-off frequency at 20 kHz.

There is one tunable control parameter

$$\theta_c = k_i \ ,$$

the integral gain k_i. The optimal control law parameter for (3.27) found when solving (3.15) is presented in Tab. 3.4. It can also be found using a root-locus plot, or an approximate analytical expression [78, 172]. The resulting nominal frequency responses for $T(s)$, $E(s)$, and $D(s)$ are shown in Fig. 3.16c.

Table 3.4: Optimal parameter for (3.27).

Parameter	Value
k_i	$1.37{\cdot}10^5$

Additional Analysis

Neglecting the instrumentation dynamics and assuming perfect co-location, stability of the IFF scheme can be analyzed using the negative-imaginary property of (3.4) and the product of (3.27) and (3.29), *i.e.*,

$$\bar{C}(s) = \lambda W_{hp}(s) C_i(s) = \frac{\lambda k_i}{s + \omega_f} \ . \tag{3.35}$$

By the definition of a strictly negative-imaginary (SNI) transfer-function [166], the transfer-function (3.4) is SNI since all the poles of $G_f(s)$ are in the open left half of the complex plane, and since

$$j\left[G_f(j\omega) - G_f(-j\omega)\right] = k_s \sum_{i=1}^{n_w} \frac{4\beta_i \zeta_i \omega_i \omega}{({\omega_i}^2 - \omega^2)^2 + (2\zeta_i \omega_i \omega)^2} > 0 \ \forall \ \omega > 0 \ .$$

Similarly, for (3.35), the pole of $\bar{C}(s)$ is in the open left half of the complex plane, and

$$j\left[\bar{C}(j\omega) - \bar{C}(-j\omega)\right] = \frac{2\lambda k_i \omega}{{\omega_f}^2 + \omega^2} > 0 \ \forall \ \omega > 0 \ ,$$

thus (3.35) is also SNI. The *positive* feedback connection of $G_f(s)$ and $\bar{C}(s)$ is therefore internally stable, if $\bar{C}(0)G_f(0) < 1$.

Closing the loop for the force feedback path in Fig. 3.9 yields

$$\bar{G}_w(s) = \frac{w}{u_a}(s) \ = \frac{G_w}{1 - \lambda W_{hp}(s) C_i(s) G_f(s)}$$

for the response from applied voltage u_a to the displacement w, which is stable by the above arguments. This is not a negative-imaginary (NI) transfer-function, and further analysis using NI properties can not be done.

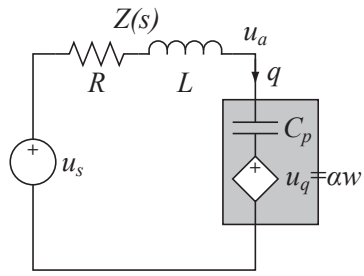

Figure 3.10: Actuator circuit with shunt.

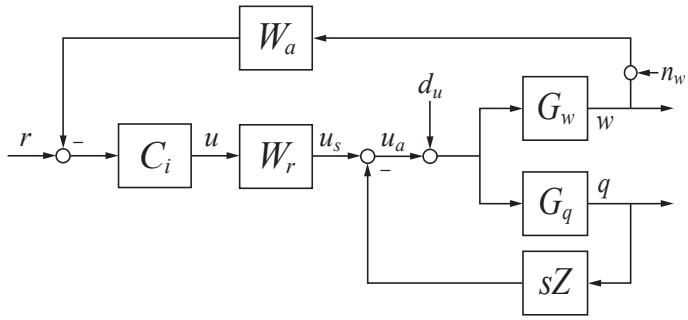

Figure 3.11: Control structure when using passive shunt-damping.

Now, closing the loop for the displacement feedback path in Fig. 3.9 yields

$$T_{11}(s) = \frac{w}{r}(s) = \frac{C_i(s)\bar{G}_w(s)}{1 + W_{lp}(s)C_i(s)\bar{G}_w(s)} = \frac{C_i(s)G_w(s)}{1 + C_i(s)(W_{lp}(s)G_w(s) - \lambda W_{hp}(s)G_f(s))},$$

and for a model $G_w(s)$ with more than one vibration mode, or if instrumentation dynamics is included, no algebraic roots can be found. However, using a sufficiently low cut-off frequency ω_f, the complementary sensitivity function from r to w can, since $W_{lp}(s) + W_{hp}(s) = 1$, be approximated as

$$T_{11}(s) = \frac{C_i(s)G_w(s)}{1 - \lambda C_i(s)G_f(s) + W_{lp}(s)C_i(s)\left(G_w(s) + \lambda G_f(s)\right)} \approx \frac{C_i(s)G_w(s)}{1 - \lambda C_i(s)G_f(s)},$$

which is an unconditionally stable transfer-function [81]. It corresponds to the case when *only* applying IFF without the high-pass filter [172], and feed-forward filtering the reference through the integral control law. The approximation is also valid for instrumentation dynamics with sufficiently high bandwidth.

3.4.5 Passive Shunt-Damping (PSD)

Passive shunt-damping [96] can introduce damping by adding an inductor and a resistor in series with the piezoelectric actuator, which acts as a capacitor, due

to the large dielectric constant of the piezoelectric material. Tuning the resulting LCR-circuit for maximal damping creates a resonant LCR-circuit that works analogously to a tuned mechanical absorber. This is physically realized as shown in Fig. 3.10. Adding an integral control law for tracking, results in the control structure shown in Fig. 3.11, where $G_q(s)$ is as given in (3.3). As discussed below, this configuration does not result in the same tuning of the LCR-circuit when optimizing for a flat frequency magnitude response for the complementary sensitivity function, compared to the case when optimizing for maximum damping (in the absence of the integral control law).

The transfer-function for the added shunt in Fig. 3.10 is

$$Z(s) = sL + R \,, \tag{3.36}$$

where L (H) is the inductance, and R (Ω) is the resistance. The integral control law is

$$C_i(s) = \frac{k_i}{s} \,, \tag{3.37}$$

where $k_i > 0$ is the gain.

This can be interpreted as a single-input-multiple-output (SIMO) system, where the measurement vector is given as

$$y = [d,\ v_f]^{\mathrm{T}} \ , \tag{3.38}$$

and the input is the applied voltage u_a. With regards to Fig. 3.7, the plant transfer-matrix is

$$G_p(s) = [G_w(s),\ G_q(s)]^{\mathrm{T}} \ , \tag{3.39}$$

the feed-forward transfer-matrix is

$$C(s) = [W_r(s)C_i(s),\ sZ(s)] \ , \tag{3.40}$$

and the feedback transfer-matrix is given by

$$F(s) = \begin{bmatrix} W_a(s) & 0 \\ 0 & 1 \end{bmatrix} \ . \tag{3.41}$$

Here, $W_r(s) = W_a(s)$, and are second-order Butterworth filters with cut-off frequency at 20 kHz.

There are three tunable control parameters

$$\theta_c = [L,\ R,\ k_i]^{\mathrm{T}} \ ,$$

the shunt inductance L, the shunt resistance R, as well as the tracking integral control law gain k_i. The optimal control law parameters for (3.36) and (3.37) found when solving (3.15) are presented in Tab. 3.5. The resulting nominal frequency responses for $T(S)$, $E(s)$, and $D(s)$ are shown in Fig. 3.16d.

The shunt was implemented using an inductor constructed using a closed ferrite core and approximately 45 turns of copper wire. A potentiometer was used to implement the required resistance. The inductor and resistor were tuned to their required values using an Agilent U1733C LCR meter.

Table 3.5: Optimal parameters for (3.36) and (3.37).

Parameter	Value
L	49.5 mH
R	613 Ω
k_i	$7.50{\cdot}10^4$

Additional Analysis

By Kirchhoff's law, the voltages in the mesh loop in Fig. 3.10 sum up to

$$u_s = sqZ(s) + u_a = (1 + sG_q(s)Z(s))u_a \ ,$$

where $Z(s)$ is the shunt impedance (3.36), u_s is the source voltage, and u_a is the applied voltage to the actuator. The source voltage u_s from the amplifier is therefore filtered by the filter

$$W_s(s) = \frac{u_a}{u_s}(s) = \frac{1}{1 + sG_q(s)Z(s)} \ ,$$

before being applied to the actuator.

The time derivative of (3.3), $sG_q(s)$, is a positive-real (PR) transfer-function [166], *i.e.*, $\angle j\omega G_q(j\omega) \in [-90°, 90°]$, since all the poles of $G_q(s)$ are in the closed left half of the complex plane, and since

$$\angle jG_q(j\omega) + \angle jG_q(-j\omega) = \alpha C_p \sum_{i=1}^{n_w} \frac{4\beta_i\zeta_i\omega_i\omega^2}{({\omega_i}^2 - \omega^2)^2 + (2\zeta_i\omega_i\omega)^2} \geq 0 \ \forall \ \omega \in \mathbb{R} \ .$$

The transfer-function $Z(s)$ is a strictly positive-real (SPR) transfer-function [166], *i.e.*, $\angle Z(j\omega) \in (-90°, 90°)$, since $Z(s)$ have no poles, and since

$$Z(j\omega) + Z(-j\omega) = 2R > 0 \ \forall \ \omega \in \mathbb{R} \ .$$

The *negative* feedback interconnection of $sG_q(s)$ and $Z(s)$ is therefore internally stable.

This can also be interpreted as a feedback connection from $\dot{w}$, as it is known that $sG_w(s)$ is a positive-real transfer-function [166], and since it can be shown that

$$W_s(s) = \frac{W_f(s)}{1 + sG_w(s)F_s(s)} \ , \ W_f(s) = \frac{1}{1 + sZ(s)C_p} \ , \ F_s(s) = \alpha C_p Z(s) W_f(s) \ ,$$

using (3.3). It is straight forward to show that $F_s(s)$ is a SPR transfer-function, thus the *negative* feedback interconnection of $sG_d(s)$ and $F_s(s)$ is internally stable.

It should be noted that the values for L and R found using (3.15) are not the same as when optimizing for maximum damping. Maximum damping is measured

with regards to the increase in disturbance rejection when adding the shunt to the piezoelectric actuator, *i.e.*,

$$\bar{D}(s) = \frac{w}{d_u}(s) = \frac{G_w(s)}{1 + sG_w(s)F_s(s)} \ .$$

For applications when reduced sensitivity to environmental disturbances is desired, and there is no need for reference tracking or if reference tracking is preformed by feed-forward control, this can be achieved solving, *e.g.*,

$$\arg\min_{R,L} \left\| \bar{D}(j\omega, R, L) \right\|_2 \ . \tag{3.42}$$

For the system at hand, this results in $L = 46.6$ mH and $R = 165\ \Omega$, which produces a *resonant* LCR-circuit response, due to the much smaller resistance value. An approximate value for the inductance can also be found assuming the shunt-circuit forms an harmonic oscillator with an undamped natural frequency equal to the undamped natural frequency of the vibration mode that should be damped. Then the inductance will be

$$L \approx \frac{1}{C_p {\omega_2}^2} = 47.1\text{mH} \ . \tag{3.43}$$

The resonant response can be seen in Fig. 3.12a, which displays the response of $W_f(s)$, which accounts for the LCR-circuit alone.

An example of the decreased input disturbance sensitivity due to the presence of a shunt tuned for maximum damping is shown in Fig. 3.13. Here, experimental time responses to the signal $u_s = W_f(s)^{-1} r$, r being a triangle-wave signal, are shown. It is immediately apparent that the excitation of a vibration mode is significantly reduced due to the shunt.

The response obtained for $W_f(s)$ when using the values of L and R from Tab. 3.5 is almost identical to that of a second-order low-pass Butterworth filter with cut-off frequency $\omega_c = \sqrt{1/LC_p}$.

From Fig. 3.12b, which displays the response of $W_s(s)$, where also the generated charge is taken into account, it can be seen that for the values from Tab. 3.5, the response is still very similar to the Butterworth filter, although there is some additional damping introduced due to the $u_q = \alpha G_w(s)$ term in (3.3).

Since

$$\bar{G}_w(s) = \frac{w}{u_s}(s) = \frac{G_w(s)}{1 + sZ(s)G_q(s)} = W_s(s)G_w(s) = \frac{W_f(s)G_w(s)}{1 + sG_w(s)F_s(s)} = W_f(s)\bar{D}(s)$$

when the shunt is present, the source voltage u_s is filtered by $W_s(s)$ before it is applied to the actuator, or equivalently, the source voltage u_s can be seen as a input disturbance filtered by $W_f(s)$, where $F_s(s)$ can be interpreted to be a feedback filter. Responses for $\bar{D}(s)$ and $\bar{G}_w(s)$ are shown in Figs. 3.12c and 3.12d, respectively, for different parameter values for L and R. Although the parameter values obtained

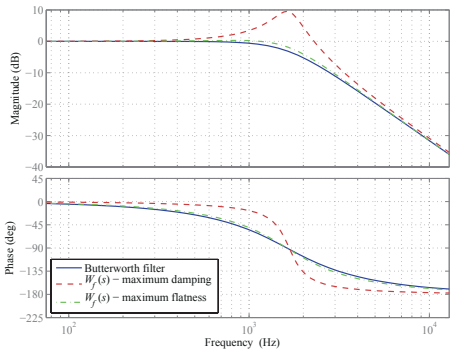

(a) LCR filter, $W_f(s)$, compared to a Butterworth filter.

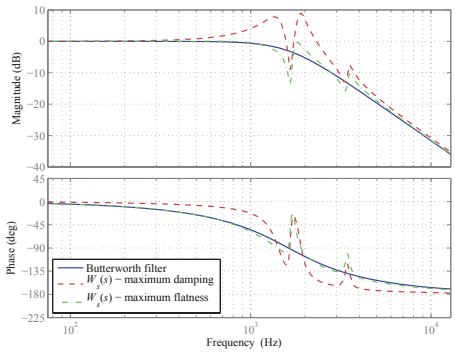

(b) Source voltage filter, $W_s(s)$, compared to a Butterworth filter.

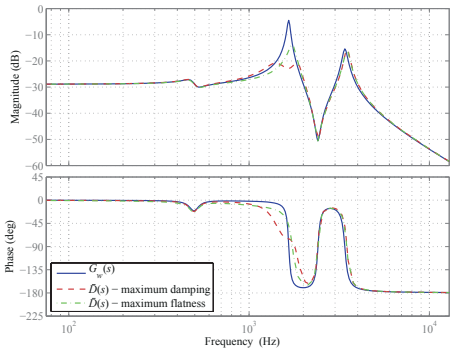

(c) Disturbance attenuation, $\bar{D}(s)$, compared to the system without the shunt, $G_w(s)$.

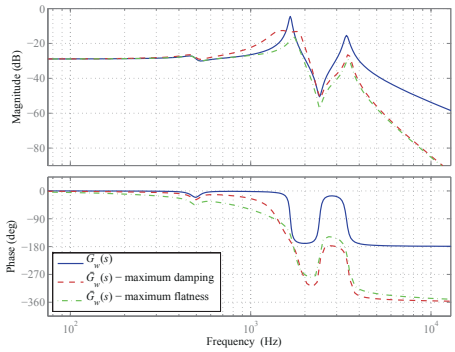

(d) Response from source voltage to displacement, $\bar{G}_w(s)$, compared to the system without the shunt, $G_w(s)$.

Figure 3.12: Results when considering passive shunt-damping alone, using different optimality criteria.

when solving (3.42) provides greater damping of the dominant vibration mode, the parameter values obtained when solving (3.15) produces the flattest response for $T_{11}(s)$ when also including feedback using the integral control law (3.37).

For tracking control, using the optimality criterion (3.14), this means that the shunt can be approximated by a low-pass Butterworth filter, which is done in Section 3.4.6, where the anti-aliasing and reconstruction filters are used to introduce damping.

It might also be noted that when using passive shunt-damping, the low-pass filter $W_s(s)$ makes the use of the anti-aliasing filter $W_a(s)$ unnecessary. However, a potential practical problem when implementing the shunt using passive components, is to find a high-quality inductor with a sufficiently high inductance value, especially when the dominant resonant frequency is fairly low, due to (3.43).

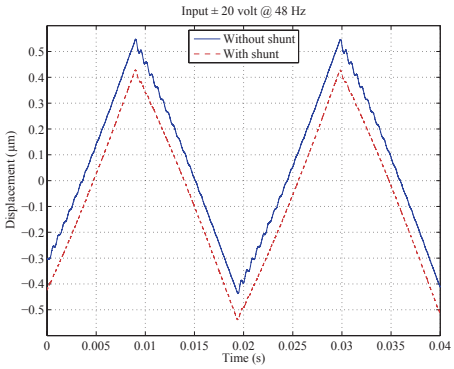

(a) Response to filtered triangle wave with fundamental frequency at 48 Hz.

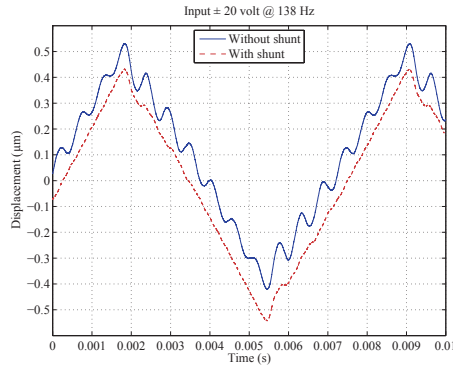

(b) Response to filtered triangle wave with fundamental frequency at 138 Hz.

Figure 3.13: Time-series of the response when applying feed-forward control when shunt circuit is present, using $u_s = W_f(s)^{-1}r$.

3.4.6 Damping Integral Control (DI)

As noted in Section 3.4.5, the optimal values for the resistance and inductance for the shunt, when solving (3.15), result in a low-pass filter when connected to the capacitance of the actuator, with approximately the same response as a second-order low-pass Butterworth filter. Implementing a control scheme on a microcontroller or a computer, there must be anti-aliasing and reconstruction filters present in order to avoid aliasing and to reduce quantization noise. Instead of applying a shunt circuit, the reconstruction and anti-aliasing filters that are already present as part of the instrumentation can be used, as long as the cut-off frequency is below the Nyquist frequency. The resulting control structure is shown in Fig. 3.14.

Similarly to the case when using passive shunt-damping, only an integral control law needs to be implemented, *i.e.*,

$$C_i(s) = \frac{k_i}{s} \,, \tag{3.44}$$

where $k_i > 0$ is the gain. The cut-off frequency, ω_c, for the filters $W_r(s)$ and $W_a(s)$ must be tuned as well. Here it is assumed that $W_r(s) = W_a(s)$ for simplicity. The filters used in the experimental set-up are second order Butterworth filters, *i.e.*,

$$W_r(s) = W_a(s) = \frac{{\omega_c}^2}{s^2 + \sqrt{2}\omega_c s + {\omega_c}^2} \,. \tag{3.45}$$

The combined filter $W_r(s)W_a(s)$ is of fourth order, but the closed-loop response of the system is almost identical to the case when using a passive shunt. The added benefit is that the shunt is no longer needed, and that off-the-shelf programmable filters that are easy to tune can be used.

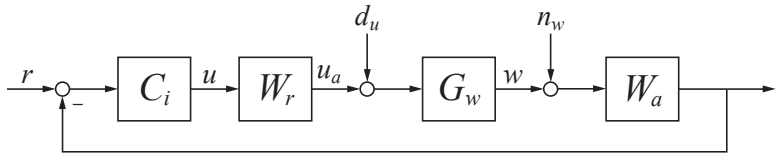

Figure 3.14: Control structure when introducing damping by applying a low-pass filter in the signal chain, in this case by utilizing the filter $W_r(s)W_a(s)$.

Table 3.6: Optimal parameters for (3.44) and (3.45).

Parameter	Value
ω_c	$2\pi{\cdot}2150$
k_i	$6.68{\cdot}10^4$

Formulating the control scheme in terms of the general control structure in Fig. 3.7, the feed-forward filter is

$$C(s) = W_r(s)C_i(s) \tag{3.46}$$

and the feedback filter is

$$F(s) = W_a(s)\ . \tag{3.47}$$

There are two tunable control parameters

$$\theta_c = [\omega_c,\ k_i]^{\mathrm{T}}\ ,$$

the filter cut-off frequency ω_c, and the tracking integral control law gain k_i. The optimal control law parameters for (3.44) and (3.45) found when solving (3.15) are presented in Tab. 3.6. The resulting nominal frequency responses for $T(S)$, $E(s)$, and $D(s)$ are shown in Fig. 3.16e.

Additional Analysis

The combined control law, consisting of (3.44) and (3.45), has an extra degree of freedom, in the choice of the cut-off frequency ω_c of the filters (3.45). In the simplest form, the control law consist of an integrator and a second-order low-pass filter, and is applied to a second-order mass-spring-damper system. The closed-loop system is therefore, at minimum, of fifth order, and has no algebraic roots. The control law has two free parameters, k_i and ω_c. The control law will therefore not lend itself to polynomial coefficient matching. The practical solution is to investigate the effects of the low-pass filters in the signal chain using numerical analysis.

This is done in Fig. 3.15, where the eigenvalue loci for the closed-loop system is plotted as a function of the cut-off frequency ω_c. Here, $G_d(s)$ together with $C(s)$ and $F(s)$, as defined in (3.46) and (3.47), is used.

The integral control law gain k_i is in this example set using (3.17). It is apparent that tuning the integral control law to the stability margin $k_i^* = 1.75 \cdot 10^4$,

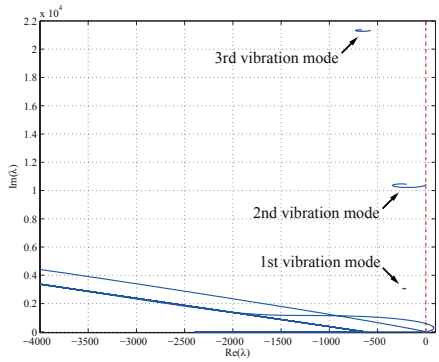

(a) The positive imaginary part of the complex conjugate eigenvalue loci for the vibration modes in addition to the modes due to the filters (3.45), and the real valued mode due to the integral control law (3.44).

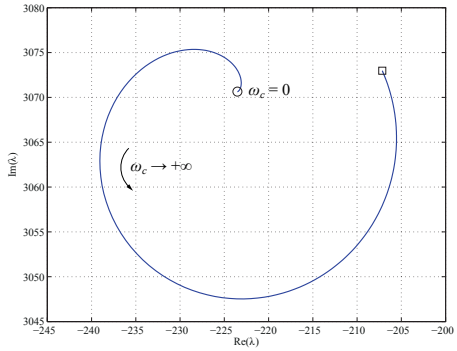

(b) The first vibration mode, cf. Tab. 3.1.

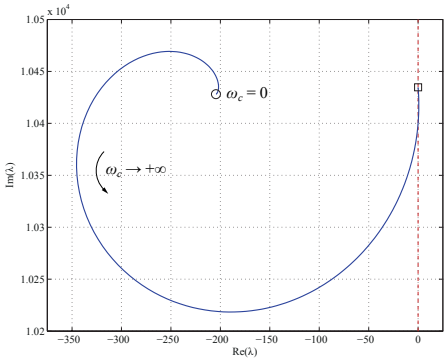

(c) The second vibration mode, cf. Tab. 3.1.

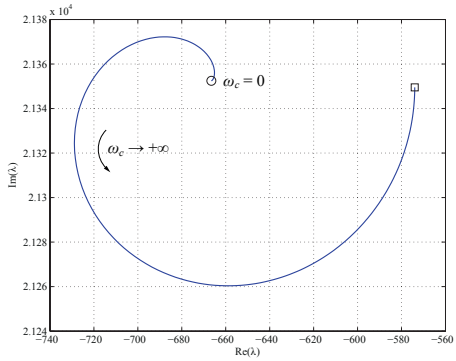

(d) The third vibration mode, cf. Tab. 3.1.

Figure 3.15: Eigenvalue loci for the closed-loop system as a function of the filter cut-off frequency ω_c. The loci are symmetric about the real axis.

the system is either unstable or close to being unstable when using high cut-off frequencies for the anti-aliasing and reconstruction filters. However, as the root loci in Fig. 3.15 indicate, reducing the cut-off frequencies for the filters, all eigenvalues can be moved further into the left-half plane, and there appears to be an optimal value for the cut-off frequency. By moving the poles further into the right half-plane, the gain margin for the closed-loop system will be larger. This should allow for a higher closed-loop bandwidth.

It should be noted the reducing the cut-off frequency ω_c all the way towards zero, one of the modes close to the origin will move into the right half-plane. There is therefore a domain of values of ω_c for which the system is stable.

Inspecting Fig. 3.15, one might expect that minimizing the maximum value of the real part of the eigenvalues for the closed-loop system as a function of the cut-off frequency ω_c will provide the fastest system. For the model $G_d(s)$, this results

in

$$\arg\min_{\omega_c\in\mathbb{R}^+/\{0\}}\left[\arg\max_{\mathrm{Re}(\lambda)\in\mathbb{R}^-}[\det(A(\omega_c)-\lambda I)=0]\right]=2\pi\cdot 1110\ \text{rad/s}\ , \tag{3.48}$$

where $A(\omega_c)$ is a state matrix realization for the closed-loop system for a given ω_c. Solving (3.48) will move *all* the eigenvalues as far into the left-half plane as possible, but will not necessarily result in the flattest response when increasing the integral control gain k_i to take advantage of the increased gain margin. The closed-loop pole locations are also dependent on the value of k_i, thus solving (3.15) seem to be a better approach, as it provides optimal values for both k_i and ω_c.

According to the results in Section 3.4.5, one might expect the optimal cut-off frequency ω_c to be close to $\sqrt{1/LC_p}=2\pi\cdot 1620$ rad/s, and the integral gain k_i close to be close to the value in Tab. 3.5. Using these values in the filters $C(s)$ and $F(s)$ as defined in (3.46) and (3.47), provides a fairly flat response for the complementary sensitivity function, but as would be expected, better results are obtained using the values in Tab. 3.6.

An advantageous side-effect of tuning the anti-aliasing and reconstruction filters to a cut-off frequency close to the bandwidth of the resulting complementary sensitivity function, is an effective attenuation of quantization noise and higher-frequency sensor noise. This provides an improvement in the actual displacement noise floor of the system. A similar effect is obtained using passive shunt-damping, but in that case only quantization noise is attenuated. For good noise attenuation, it is ideal that the bandwidths of the anti-aliasing and reconstruction filters are as low as possible, and this idea is also applied in the control design of the model reference control in Section 3.4.7.

For the experimental set-up, the anti-aliasing and reconstruction filters have a user-programmable cut-off frequency ω_c. However, most filter topologies are fairly straight forward to tune, especially the state-variable topology. One-component filters with the state-variable topology are readily available from major producers of integrated circuits.

3.4.7 Model Reference Control (MRC)

The model reference control (MRC) [111] objective is to make the plant output y_p track the output of a reference model y_m. Similar to polynomial-based control, or pole-placement [94, 111], MRC provides a control law for arbitrary closed-loop pole placement, but also allows for arbitrary minimum phase zero placement. A second-order pole-placement control law, similar to the control law in Example 3.1, was applied to a nanopositioning stage in [15]. The synthesis equations for the MRC scheme are summarized in Appendix E.

For the MRC design, the displacement model of the system $G_w(s)$ is truncated to only include the dominant piston mode at 1660 Hz, the second mode of the positioning stage,

$$\tilde{G}_w(s)=\frac{G_d(0)}{\beta_2/{\omega_2}^2}\frac{\beta_2}{s^2+2\zeta_2\omega_2 s+{\omega_2}^2}\ . \tag{3.49}$$

This is done in order to keep the control law order as low as possible, and to avoid excitation of the vibration modes above the dominant mode. The above model is

augmented with an integrator, in order to reduce the sensitivity to plant uncertainty at lower frequencies. In addition, the anti-aliasing and reconstruction filters $W_r(s)$ and $W_a(s)$ are incorporated into the control design. The filters provide an additional degree of freedom when tuning the control law, and can be used to attenuate non-modeled high-frequency dynamics, as well as to attenuate quantization and sensor noise. The complete plant model, with regards to the synthesis equations in Appendix E, is thus taken to be

$$\tilde{G}_p(s) = \frac{1}{s}\tilde{G}_w(s)W_r(s)W_a(s) \ , \tag{3.50}$$

and is of seventh-order. In addition to the plant model $\tilde{G}_p(s)$, there are two additional design choices with regards to the control law; the reference model $W_m(s)$ and the output filter $1/\Gamma(s)$. The main limiting factor in determining these filters, is the uncertainty of the plant model, which for the system at hand is mostly due to non-modeled high-frequency dynamics.

For simplicity, the reference model $W_m(s)$ is chosen to be a seventh-order Butterworth filter with cut-off frequency ω_m. Since the plant model $\tilde{G}_p(s)$ does not have any zeros, $\Lambda(s)$ should be a polynomial of sixth order. The zeros of $\Lambda(s)$ were chosen to have a Butterworth pattern with radius ω_l. The anti-aliasing and reconstruction filters have a user-programmable cut-off frequency ω_c, which can be tuned, given that ω_c is below the Nyquist frequency.

The design problem is as such reduced to three tunable control parameters

$$\theta_c = \left[\omega_c, \ \omega_m, \ \omega_l\right]^{\mathrm{T}} \ ,$$

the cut-off frequencies ω_c, ω_m, ω_l. The reference model is a Butterworth filter, which is maximally flat by definition. The optimality criterion described in Equation (3.14) is therefore satisfied for all ω_m, ω_l, and ω_c that render a stable closed-loop system. The cut-off frequencies were therefore tuned manually, attempting to obtain the highest bandwidth for $E(s)$ while still having a robustly stable closed-loop system. The control law parameters used are presented in Tab. 3.7.

The implementation of the scheme is done by moving the integrator in (3.50) to the feed-forward filter, *i.e.*, compared to the scheme as presented in Appendix E, the feed-forward filter (E.7) is augmented as

$$\tilde{C}(s) = \frac{1}{s}\bar{C}(s) \ , \tag{3.51}$$

but the feedback filter (E.8) is left as it is, *i.e.*,

$$\tilde{F}(s) = \bar{F}(s) \ . \tag{3.52}$$

The parameters for the feed-forward filter $\bar{C}(s)$ and feedback filter $\bar{F}(s)$ are found using (E.5) and (E.6).

With regards to the general control structure in Fig. 3.7, the analysis in terms of the sensitivity (3.7), complementary sensitivity (3.8), noise attenuation (3.9), error attenuation (3.10), and disturbance rejection (3.12) is done using

$$G_p(s) = G_w(s) \ , \tag{3.53}$$

$$C(s) = \tilde{C}(s)W_r(s) \ , \tag{3.54}$$

and

$$F(s) = \tilde{F}(s)W_a(s) \ . \tag{3.55}$$

The resulting nominal frequency responses for $T(S)$, $E(s)$, and $D(s)$ are shown in Fig. 3.16f.

Table 3.7: Control law parameters for MRC.

Parameter	Value
ω_c	$2\pi{\cdot}3000$
ω_m	$2\pi{\cdot}2000$
ω_l	$2\pi{\cdot}2250$

3.5 Experimental Results & Discussion

The six different control schemes were implemented on the hardware-in-the-loop system, and the tracking performance when using a triangle-wave reference signal with a fundamental frequency of 80 Hz and an amplitude of 1 μm was recorded for each scheme. The fundamental frequency of the reference signal was chosen in order for the 21st harmonic of the signal to be close to the dominant vibration mode. The displacement for all the schemes was measured on a separate channel using an anti-aliasing filter with a 35 kHz cut-off frequency. The generated current from the force transducer was measured, and integrated numerically. The cut-off frequency for the anti-aliasing filter for this measurement was always set to 20 kHz, for all the experiments.

3.5.1 Results

Nominal frequency responses for the various schemes are presented in Figs. 3.16a, 3.16b, 3.16c, 3.16d, 3.16e, and 3.16f. The measures from Section 3.3 are summarized in Tab. 3.8. Note that the values for $1/\gamma_s$ are not directly comparable between SISO and SIMO systems.

The results when tracking a triangle-wave reference signal are presented in Figs. 3.17 and 3.18. The maximum error (ME) ranges from 15% to 24%, and the root-mean-square error (RMSE) ranges from 0.11 μm to 0.20 μm. The error values are also summarized in Tab. 3.8. Note that tracking performance can be increased by adding feed-forward, but this is not done in order for the error signals to be significantly larger than the noise in the measured displacement signal, to avoid obfuscating the actual results achieved due to feedback.

3.5.2 Discussion

The best performing control schemes in terms of the error are the scheme using integral force feedback (IFF) and the model reference control (MRC) scheme. The

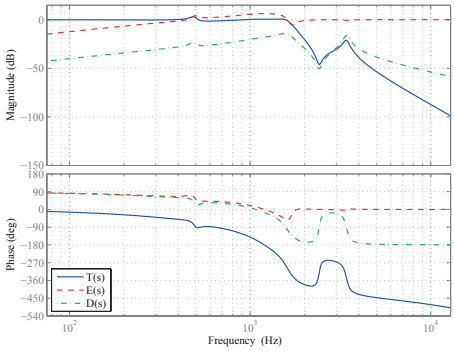

(a) Positive position feedback (PPF).

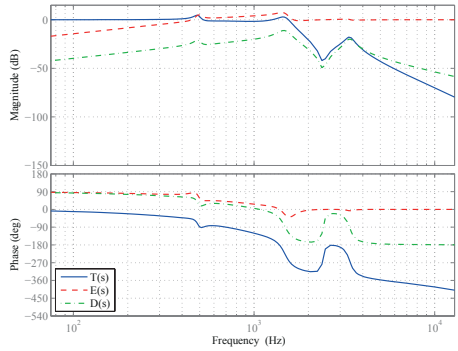

(b) Integral resonant control (IRC).

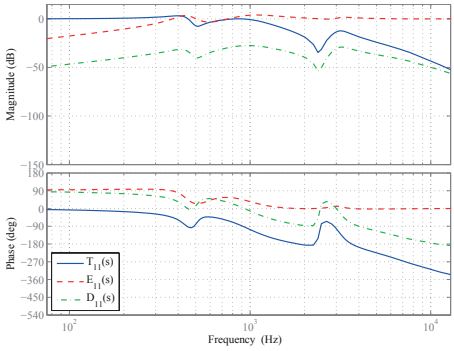

(c) Integral force feedback (IFF).

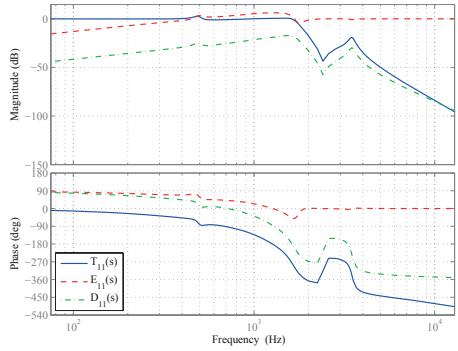

(d) Passive shunt-damping (PSD).

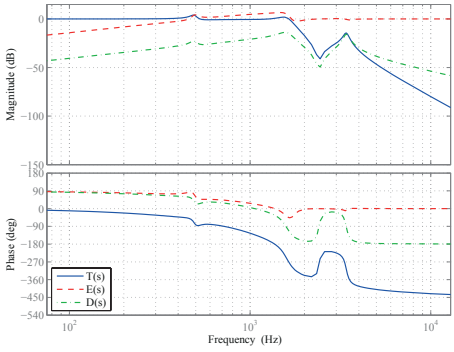

(e) Damping integral control (DI).

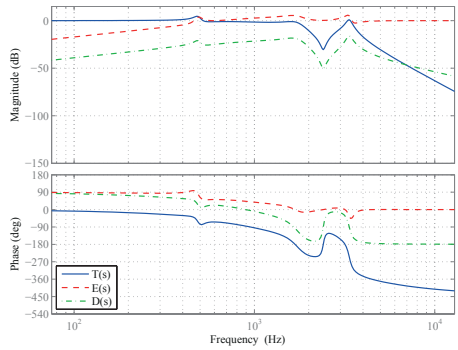

(f) Model reference control (MRC).

Figure 3.16: Nominal frequency responses.

Table 3.8: Bandwidth of $E(s)$, $||N(s)||_2$ from n_w to w, $||D(s)||_\infty$ from d_u to w, $1/\gamma_s$, root-mean-square error (RMSE), and maximum error (ME) obtained for the control schemes.

Scheme	BW	$\|\|N(s)\|\|_2$	$\|\|D(s)\|\|_\infty$	$1/\gamma_s$	RMSE	ME
PPF	318 Hz	61.1	191×10^{-3}	1.66	0.194 μm	0.231 μm
IRC	369 Hz	78.4	281×10^{-3}	1.01	0.173 μm	0.213 μm
IFF	329 Hz	12.6	424×10^{-4}	1.14	0.123 μm	0.146 μm
PSD	338 Hz	60.0	139×10^{-3}	1.14	0.178 μm	0.218 μm
DI	372 Hz	58.6	204×10^{-3}	1.66	0.197 μm	0.235 μm
MRC	434 Hz	55.2	295×10^{-5}	1.26	0.108 μm	0.159 μm

worst performance is obtained when using positive position feedback (PPF) and the damping integral control (DI) scheme, while when using integral resonant control (IRC) and passive shunt-damping (PSD), errors in the middle of the range are obtained.

The error figures in terms of ME and RMSE can be changed by the control law tuning, but a reduction in RMSE typically leads to an increase in ME, due to a more oscillatory response.

The MRC scheme is the most complex scheme. It requires the implementation of a sixth-order and a seventh-order filter; a total of thirteen integrators. By comparison, the IFF based scheme only requires three integrators, but with the disadvantage of reduced range due to the force transducer. It also requires more instrumentation and good calibration. On the other hand, the noise performance is superior, due to the extremely low noise density of the force transducer, although this benefit is lost for a digital implementation, due to quantization noise and digital-to-analog converter (DAC) artifacts, as discussed below.

The simplest control schemes to implement on a digital platform are the PSD based scheme and the DI scheme, as they only require the implementation of one integrator. The DI scheme is the simplest with regards to extra instrumentation, as it is not necessary to add a shunt circuit, although for the PSD based control law, the anti-aliasing filter is not necessary. For an analog implementation, the DI scheme, and the schemes based on PPF, IRC, and PSD are almost equivalent in terms of complexity. The MRC scheme is likely too complex for an efficient analog implementation.

With regards to the DI scheme, it should also be noted that since many existing nanopositioning systems already include an integral control law as well as anti-aliasing and reconstruction filters, a significant increase in performance can be achieved by no other changes than adjusting the filter cut-off frequencies and the integral gain.

As quantization noise is the dominant noise source in the experimental system, it is not possible to obtain reliable closed-loop noise measurements. However, due to

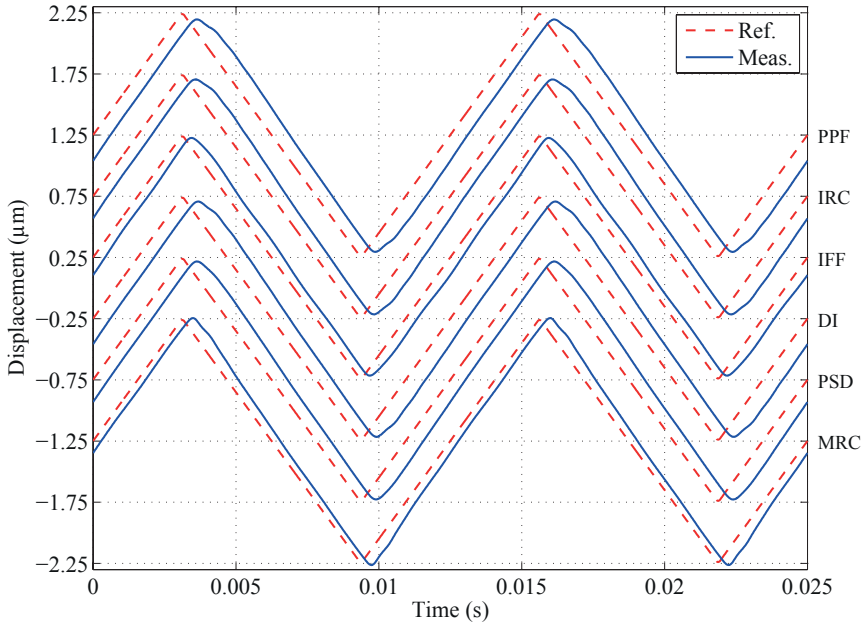

Figure 3.17: Steady-state tracking performance when applying a 1 μm amplitude, 80 Hz triangle-wave reference signal. Displacement measurement signals and reference signals.

the low noise and high sensitivity of the force transducer, the effect of quantization noise and DAC artifacts can be measured. An example of this is shown in Fig. 3.19, where the time derivative of the force measurement is shown when using the IFF based scheme and the MRC scheme. The MRC scheme, as well as the PSD and DI scheme, has a low-pass filter with a low cut-off frequency before the voltage is applied to the piezoelectric actuator, and so the noise and disturbances coming from the DAC are effectively attenuated. For the PPF, IRC, and IFF based schemes, the reconstruction filter has a cut-off frequency of 20 kHz, and thus the non-ideal DAC behavior is much more noticeable. This beneficial effect can also be achieved when using PPF and IRC schemes by implementing the damping control law $C_d(s)$ using analog components, as it takes the form of a low-pass filter in either case, but implementing the whole scheme using analog components by adding an analog integrator might then be a better option.

Overall, the performance is fairly similar among the six proposed schemes. However, since the control schemes are implemented using digital signal processing equipment, the noise performance of the PSD, DI, and MRC scheme will be better due to the attenuation of quantization noise.

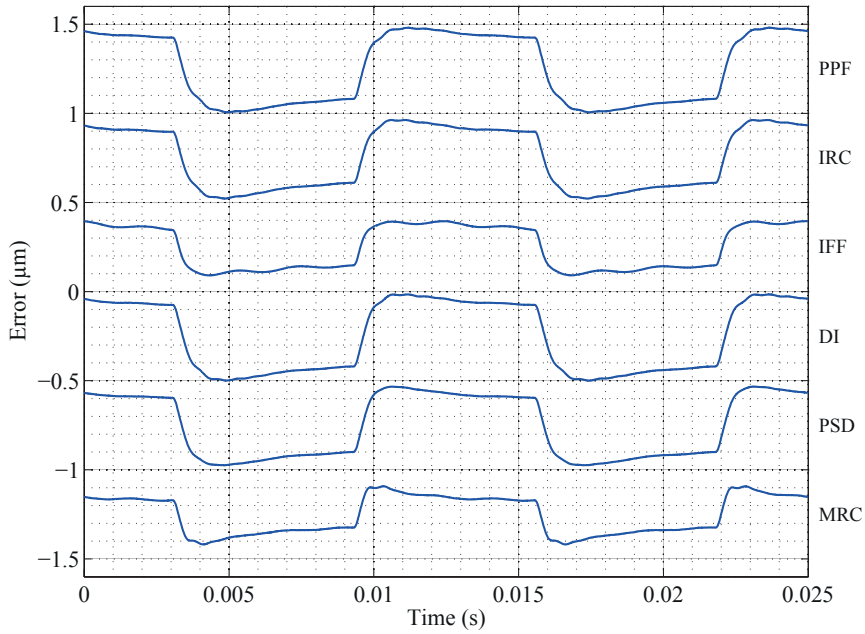

Figure 3.18: Steady-state tracking performance when applying a 1 μm amplitude, 80 Hz triangle-wave reference signal. Error signals.

3.6 PI² Anti-Windup Using Conditional Integrators

To improve tracking performance when using low-bandwidth reference signals, double integral action can be added to the tracking control law. In scanning probe microscopy applications, double integral action is sometimes used to obtain asymptotic tracking of the flanks of a triangle signal, due to the internal model principle [20].

If the integral control law 3.44 in Section 3.4.6 is augmented with a proportional and a double integral term, *i.e.*,

$$C_{pii}(s) = \frac{s^2 k_p + s k_i + k_{ii}}{s^2} \,, \tag{3.56}$$

still using the optimal tuning for the cut-off frequency ω_c and the integral gain k_i, the maximum double integral gain that renders a robustly stable closed-loop system is $k_{ii} \approx 8.0 \cdot 10^7$ when using a proportional gain $k_p = 1$.

This allows for slightly better tracking of reference signals with a low fundamental frequency. On the other hand, the PI² control law also introduces a new complex conjugate pole pair which can lead to an oscillatory response if excited, so the tracking performance for high-bandwidth reference signals deteriorate.

Using high-gain integral and double integral action makes the closed-loop system susceptible to integral windup. This is particularly a problem for for high precision positioning, since signals will often be scaled to reduce noise and to maximize resolution. For example; it is common to adjust the amplification of the signal

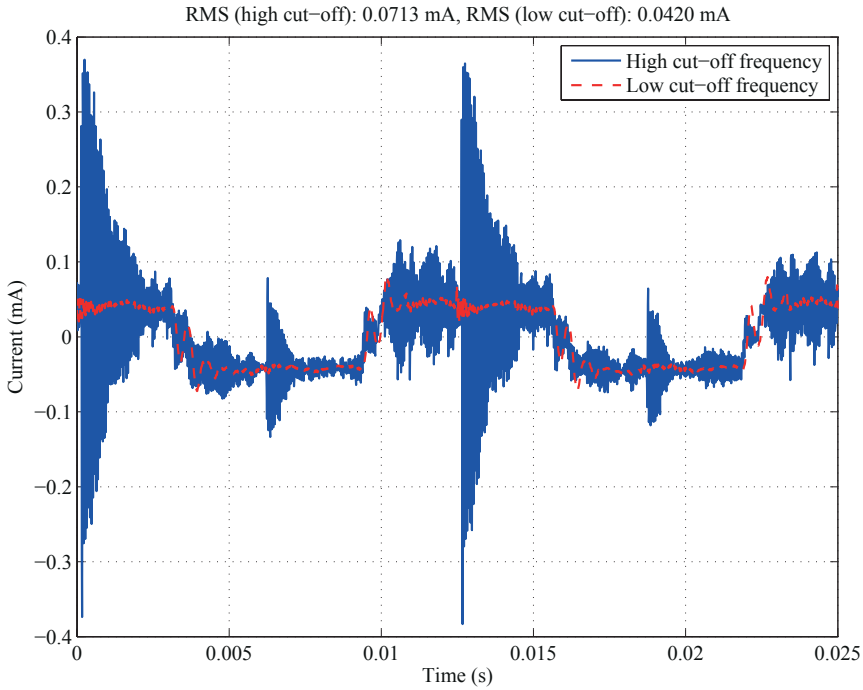

Figure 3.19: Time derivative of force measurement; when having a filter with high cut-off frequency vs. low cut-off frequency in the signal chain before the voltage is applied to the piezoelectric actuator. The effect of quantization noise and digital-to-analog-converter artifacts are much more noticeable when there the cut-off frequency is high.

from the digital-to-analog converter (DAC) such that the maximum output of the DAC corresponds to the maximum mechanical deflection desired, utilizing the full range of the DAC and thus maximizing the resolution. This leaves a small margin before saturation, and will make a control law with integral action prone to windup in the presence of disturbances such as measurement bias and uncertainties such as variable effective gain. To retain some level of performance and avoid large transients, an integral anti-windup scheme should be used.

Among the large assortment of anti-windup schemes (see, *e.g.*, [185] for a survey), the conditional integrator scheme of [203] is used in the following. It is straight forward to analyze and implement for control laws with integral action of any order. The effectiveness of the scheme is demonstrated by simulations for both input and output saturation, and by experiment for input saturation.

In order for the anti-windup scheme to effectively limit the control actuation signal, the control law should include a feed-forward term, such that the residual error, and consequently the control signal generated by the feedback control law, is fairly small.

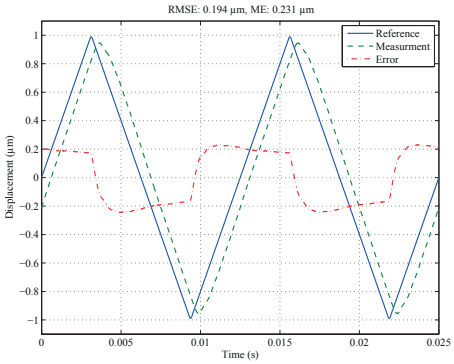

(a) Positive position feedback (PPF).

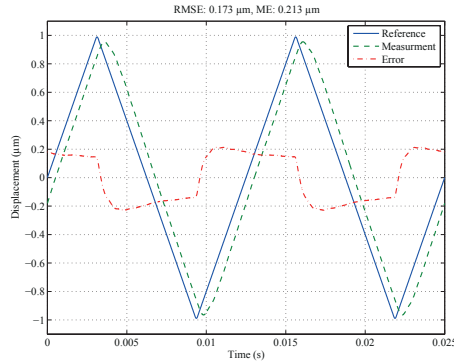

(b) Integral resonant control (IRC).

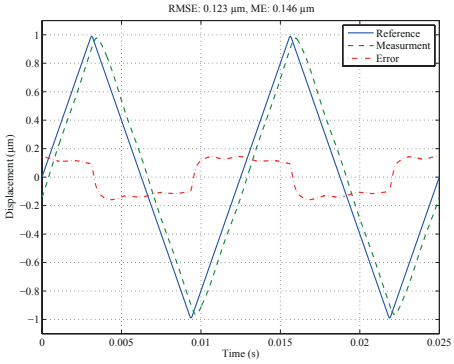

(c) Integral force feedback (IFF).

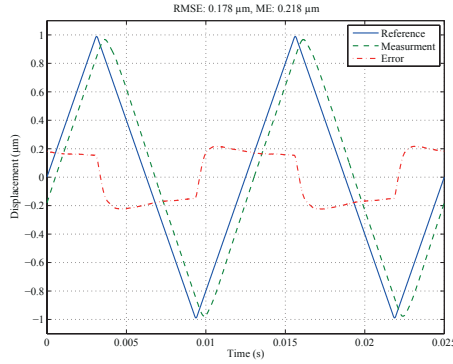

(d) Passive shunt-damping (PSD).

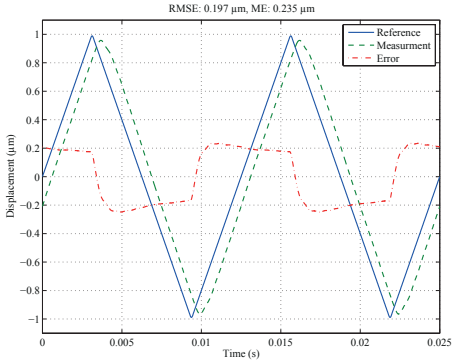

(e) Damping integral control (DI).

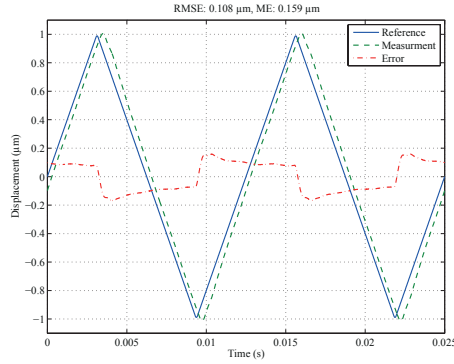

(f) Model reference control (MRC).

Figure 3.20: Tracking performance.

For low-bandwidth reference signals the feed-forward control law (2.9), *i.e.*,

$$u = \frac{1}{K} r \ ,$$

where

$$K = G_w(0) \ ,$$

is sufficient to produce a fairly small residual error $\epsilon = r - y_p$, similar to the error seen in Fig. 2.5a. The overall control law is therefore taken to be

$$u_p = C_i(s)e + \frac{1}{K} r \ . \tag{3.57}$$

Remark 3.2. If the proportional term in (3.56) is small, *i.e.*, $k_p e \approx 0$, the control law can also be augmented with the hysteresis compensation scheme from Chapter 2 in a similar manner as discussed in Section 2.10.

3.6.1 Conditional Integrators as an Anti-Windup Scheme

The conditional integrator control scheme is based on continuous sliding mode control with integral action, and is designed to only provide integral action if the value for the so-called *sliding mode variable* is below some given threshold.

The sliding mode variable is defined as

$$\varsigma = k_0\sigma_1 + k_1\sigma_2 + k_\varepsilon\varepsilon, \tag{3.58}$$

where the error ε is defined as $\varepsilon = y_m - r$. The signals $\sigma_{1,2}$ are generated by the system

$$\begin{aligned} \dot{\sigma}_1 &= \sigma_2 \\ \dot{\sigma}_2 &= -k_0\sigma_1 - k_1\sigma_2 + \mu \ \mathrm{sat}\left(\varsigma/\mu\right) \ . \end{aligned} \tag{3.59}$$

Using (3.58) and (3.59), and if the sign of the DC-gain of the plant is positive, the control signal is produced by

$$u_c = -\beta_c \ \mathrm{sat}\left(\varsigma/\mu\right) \ , \tag{3.60}$$

thus $u_c \in [-\beta_c, \beta_c]$.

In the above expressions, the saturation function $\mathrm{sat}(\cdot)$ is used. This function is defined as

$$\mathrm{sat}(z) = \begin{cases} z & \text{if } |z| \leq 1 \\ \mathrm{sgn}(z) & \text{if } |z| > 1 \ , \end{cases}$$

where $\mathrm{sgn}(z)$ denotes the sign of the quantity z. The parameter $\mu > 0$ is used to set the threshold of saturation for the sliding mode variable ς, and the parameter $\beta_c > 0$ determines the maximum value of the control signal.

By inspecting the expressions for the control law, (3.58), (3.59), and (3.60), the differential equations in (3.59) can be manipulated into the form

$$\begin{aligned} \dot{\sigma}_1 &= \sigma_2 \\ \dot{\sigma}_2 &= k_\varepsilon\varepsilon - k_0\sigma_1 - k_1\sigma_2 - k_\varepsilon\varepsilon + \mu \ \mathrm{sat}\left(\varsigma/\mu\right) \\ &= k_\varepsilon\varepsilon - \varsigma + \mu \ \mathrm{sat}\left(\varsigma/\mu\right) \\ &= k_\varepsilon\varepsilon + \tfrac{\mu}{\beta_c}\left(u_c - u_c^*\right) \ , \end{aligned} \tag{3.61}$$

where u_c^* has been introduced, which is (3.60) without saturation, *i.e.*,

$$u_c^* = -\beta_c \left(\varsigma/\mu\right) \ . \tag{3.62}$$

Saturation occurs when the absolute value for the sliding mode variable ς is above the value of μ. The control law therefore has two modes of operation; the unsaturated mode, when $|\varsigma| \leq \mu$, and the saturated mode, when $|\varsigma| > \mu$.

If $|\varsigma| \leq \mu$, it corresponds to the unsaturated case, and thus $u_c = u_c^*$. The system represented by (3.59) or (3.61) becomes

$$\begin{aligned} \dot{\sigma}_1 &= \sigma_2 \\ \dot{\sigma}_2 &= k_\varepsilon \varepsilon \ , \end{aligned}$$

and it can be seen that the signals $\sigma_{1,2}$ are time integrals of the error ε, scaled by the constant k_ε.

The control signal (3.60) is in this case given as

$$u_c = k_p e + k_i \int_{t_0}^{t} e \ \mathrm{d}\tau + k_{ii} \int_{t_0}^{t} \int_{t_0}^{\tau} e \ \mathrm{d}\tau' \, \mathrm{d}\tau \tag{3.63}$$

where $e = -\varepsilon$,

$$k_p = \frac{\beta_c}{\mu} k_\varepsilon \ , \quad k_i = \frac{\beta_c}{\mu} k_1 k_\varepsilon \ , \quad \text{and} \quad k_{ii} = \frac{\beta_c}{\mu} k_0 k_\varepsilon \ ,$$

which can be recognized as a PI² control law.

In the unsaturated mode, stability and tracking performance can then be determined by analyzing the closed-loop system using (3.63) with control law gains k_p, k_i, and k_{ii}. For a set of control gains, $\{k_p, k_i, k_{ii}\}$, the parameters for (3.58) and (3.59) are found as

$$k_\varepsilon = \frac{\mu}{\beta_c} k_p \ , \quad k_1 = \frac{k_i}{k_p} \ , \quad \text{and} \quad k_0 = \frac{k_{ii}}{k_p} \ .$$

When $|\varsigma| > \mu$, the saturated case occurs, and $u_c \neq u_c^*$. The system (3.59), or (3.61), becomes

$$\begin{aligned} \dot{\sigma}_1 &= \sigma_2 \\ \dot{\sigma}_2 &= -k_0 \sigma_1 - k_1 \sigma_2 + \mu \ \mathrm{sgn}(\varsigma) \ , \end{aligned} \tag{3.64}$$

and the control output (3.60) becomes the constant

$$u_c = -\beta_c \ \mathrm{sgn}(\varsigma) \ . \tag{3.65}$$

Inspecting (3.64), it can be seen that if the characteristic equation

$$\lambda^2 + k_1 \lambda + k_0 = 0$$

is Hurwitz, the state vector (σ_1, σ_2) converges exponentially to $(\pm\mu/k_0, 0)$, depending on the sign of the sliding mode variable ς, and this behavior prevents windup in the control law. By the Routh-Hurwitz criterion, the characteristic equation will be Hurwitz if $k_{0,1} > 0$.

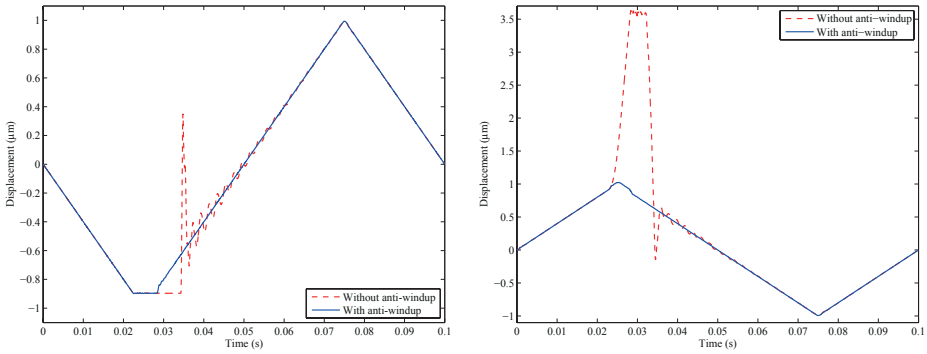

(a) Input saturation.

(b) Output saturation.

Figure 3.21: Simulated responses to input and output saturation with and without integral anti-windup scheme.

Stability Analysis

In the above analysis of the anti-windup scheme, the control signal u_c can either be the constant (3.65) in the saturated case, or generated by (3.63) for the unsaturated case. The system will therefore switch between a mode where feedback is applied, and a mode where it is driven in open-loop. The behavior of the system in the saturated case is then determined by the open-loop dynamics. The open-loop system as depicted in Fig. 3.3 consists of a series of stable sub-systems, *i.e.*,

$$W_r(s)G_w(s)W_a(s) \ ,$$

and in the absence of feedback, the location of the eigenvalues remains unchanged. Thus, If the closed-loop system when using (3.56) is stable, the overall system is stable.

Simulation Examples

The effectiveness of the anti-windup scheme when applying the control law (3.57) is demonstrated in Fig. 3.21, where displacement responses with and without the anti-windup scheme are shown for a triangle-wave signal with 1 μm amplitude and 10 Hz fundamental frequency. Here the system model as presented in Section 3.2 is used. In addition to the control law parameter values already given above, $\beta_c = 1$ and $\mu = 1$ is used.

The results for the first example are shown in Fig. 3.21a, where the input voltage is limited to be $u_p \in [-25, 100]$ V. The second example is shown in Fig. 3.21b, and displays the responses when the sensor output is limited to be $y_m \in [-10, 0.9]$ μm. In either case, it can be seen that the large transient due to integral windup is eliminated.

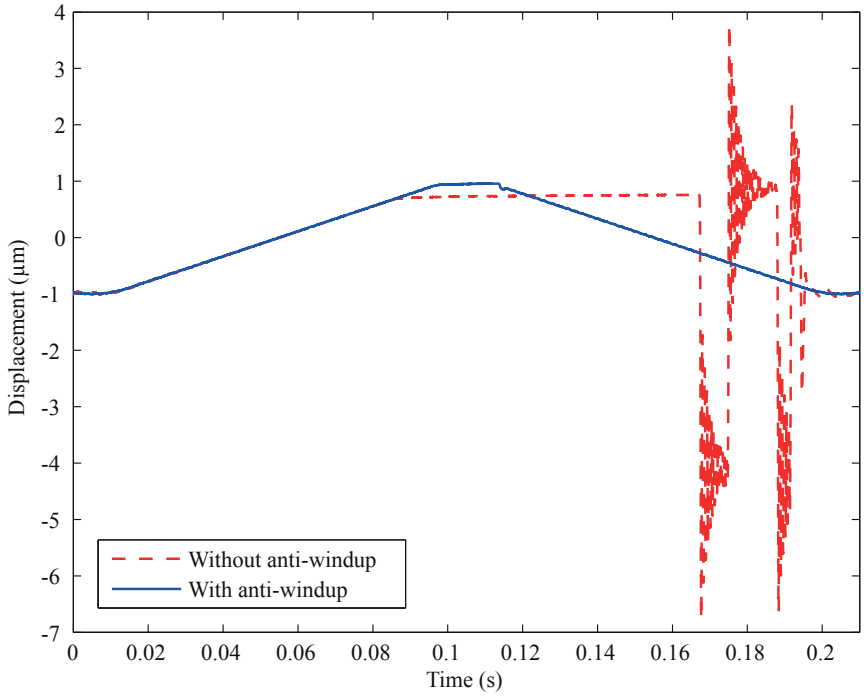

Figure 3.22: Experimental response to input saturation with and without integral anti-windup scheme.

Input Saturation Experiment

The effectiveness of the anti-windup scheme was also experimentally verified for an input saturation, using the above PI^2 control law, implemented on the experimental platform used in Chapter 2. The result is shown Fig. 3.22. The reference signal has a fundamental frequency of 5 Hz and an amplitude of 1 μm. Here, a saturation in the control signal was introduced using a SIM 964 analog limiter from Stanford Research Systems on the output from the digital-to-analog converter. As can be seen, without anti-windup there are large transients and long settling times, which are practically eliminated when using the anti-windup scheme.

3.7 Conclusions

Six fixed-structure, low-order control schemes for damping and tracking control for a nanopositioning device have been presented in this study and their performance has been assessed experimentally. Investigated schemes were based on positive position feedback (PFF), integral resonant control (IRC), integral force feedback (IFF), and passive shunt-damping (PSD), in addition to damping integral control (DI) and model reference control (MRC). A systematic tuning method was also presented for the DI scheme, and the schemes based on PPF, IRC, IFF, and PSD.

Overall, the performance was fairly similar among the schemes, but features of notice is the noise performance of the IFF based scheme and the simplicity of the DI scheme. It was also demonstrated that when implementing control schemes on a digital platform, it is beneficial to use control schemes that reduce the effect of quantization noise and digital-to-analog-converter artifacts by using low-pass filers with low cut-off frequencies before the input to the actuator. Of the schemes investigated, this is most easily done using the MRC and DI scheme, as well as the PSD based scheme. It was also demonstrated that the noise benefits of using the IFF based scheme is lost for a digital implementation, due to quantization noise and digital-to-analog converter artifacts.

In addition, a simple integral anti-windup scheme was presented. Simulation results demonstrated the effectiveness of the scheme, both for input and output saturation. Experimental results demonstrating the effectiveness for the case of input saturation was also presented.

Chapter 4

Robust Repetitive Control

4.1 Introduction

Recently, repetitive control (RC) has been introduced for nanopositioning systems [16, 155]. The RC scheme is based on the internal model principle [86, 87], and it is specifically tailored to track periodic reference trajectories and attenuate periodic disturbances. The internal model is implemented using a time-delay inside of a positive feedback loop, and corresponds to any periodic signal with a period equal to the time-delay [98]. By inclusion of the internal model in the control law, any exogenous signal that conforms to the model is nulled in the error signal, due to the internal model principle [98]. For reference trajectory tracking, the RC scheme only requires the period of the reference trajectory to be known. This makes the RC scheme robust towards plant uncertainty since the nulling property is independent of the plant dynamics, *i.e.*, it provides robust tracking performance as long as the closed-loop system is stable. Compared to traditional feedback and feedforward control laws, the tracking error when using RC diminishes as the number of operating periods increases.

In many nanopositioning applications, the period of the reference signal is known in advance, which makes RC useful. Compared to iterative learning control [35, 36, 101, 135, 160, 221], RC does not require resetting the initial conditions at the start of each iteration step, and is far less computationally demanding. A convenient feature is that an RC scheme can be plugged into an existing feedback loop to enhance performance with minimal changes to the existing control system [42, 98, 215].

The performance and stability of RC depends on the dynamics of the controlled system [98, 110]. Particularly, sharp resonant peaks can degrade performance and even make creating a stable RC scheme difficult. To provide more feasible system dynamics, the damping integral (DI) control law from Section 3.4.6 is applied to minimize the effect of the highly resonant dynamics of the nanopositioning stage. The DI control law also reduces the sensitivity of uncertain dynamics and attenuates the hysteresis and creep disturbances. This gives the overall control law (when also including the RC scheme) better robustness properties.

As discussed in Chapter 3, there are several well known methods for introducing

damping to a flexible structure, and they can be augmented with integral action to obtain good tracking performance. All of these control schemes, as well as control schemes based on $\mathcal{H}_\infty$-synthesis, are good alternatives to the DI control law.

The rationale for choosing the DI control law is based on noise performance and computational complexity. In order to achieve the lowest possible noise floor, the highest possible sampling frequency should be used. As the DI scheme only requires an integrator to be implemented, it introduces negligible computational complexity to the overall control scheme. As such, the sampling frequency will almost exclusively be determined by the computational complexity of the RC scheme. Also, since the anti-aliasing and reconstruction filters when using the DI scheme are tuned to have a minimal bandwidth, quantization and sensor noise is kept at a minimum. An additional feature is that the overall control scheme will not require any changes in instrumentation; utilizing components already present in typical nanopositioning systems.

Pertaining to robust RC, work has been done with regards to *uncertainties in signal period* [155, 156, 167, 208] and *plant uncertainty* [139, 165, 222, 224]. These results are not immediately applicable in this work, as the period for the reference signal is known, and the chosen structure of the overall control scheme and type of uncertainty differs from what has been previously studied.

4.1.1 Contributions

The presented work is practically oriented, and the objective is to obtain high performance for periodic position reference tracking for a nanopositioning device, in the sense that the tracking error should be as small as possible. It is also desirable to construct a control law with a minimum of computational complexity, in order to maximize the closed-loop sampling frequency and to simplify the implementation.

The control scheme consists of the damping integral control law presented in Section 3.4.6, and a plug-in repetitive control scheme, as described in [42, 98, 215]. The RC scheme is analyzed in continuous time, and high-order numerical integration is used in the discrete time implementation. The rationale behind this is that the resulting control scheme will be directly translatable to an analog implementation, using, *e.g.*, a bucket-brigade device [176], and that it makes it simpler to adjust the time-delay in fractions of the sampling period. A fractional delay filter [132] can then be used in the implementation to improve the accuracy of the chosen time-delay.

A specific form of the plug-in RC scheme is chosen in order to produce proper filters in the control law. To ensure robust stability, a stability criterion in the frequency domain for multiplicative plant perturbations is found. A tuning procedure aimed at maximizing the bandwidth and minimizing the order of the RC scheme is also described. Lastly, a tuning procedure for adjusting the time-delay in the internal model is described. Adjusting the time-delay is necessary to improve the accuracy of the pole locations in the internal model when it is bandwidth limited to ensure stability.

The control approach is applied to a custom-designed piezo-based nanopositioning system. Results are presented to demonstrate the effectiveness of the overall control scheme, where the maximum tracking error for scanning at 100 Hz and

400 Hz is measured at 0.22% and 1.9%, respectively, of the total positioning range. The scheme also has very low computational requirements, making it possible to use closed-loop sampling frequencies exceeding 100 kHz on standard hardware-in-the-loop equipment.

4.1.2 Outline

The Chapter is organized as follows. In Section 4.2 the system model and the plant uncertainty is presented. The overall control law consists of the RC scheme and a modified PI law, which are both discussed in Section 4.3. The tuning procedure for the different parts of the overall control scheme is presented in Section 4.4. Lastly, experimental results are presented and discussed in Section 4.5.

4.2 System Description & Modeling

The system under consideration consists of a custom-designed serial-kinematic nanopositioning stage, anti-aliasing and reconstruction filters, a voltage amplifier, a capacitive displacement sensor, and a computer equipped with digital-to-analog and analog-to-digital converters for implementing the control scheme. As the amplifier and sensor used in the experimental set-up have very fast dynamics, they have been neglected in the system analysis.

4.2.1 Mechanical Model

The nanopositioning stage used in this work is shown in Fig. 2.3, where the serial-kinematic motion mechanism is designed such that the first vibration mode is dominant and occurs in the actuation direction, generating a piston motion. More details on the design of this stage can be found in [120]. The simplified free body diagram for the mechanism is displayed in Fig. 2.1, and by this model the corresponding second-order differential equation to describe the dynamics in, *e.g.*, the x-direction, is given by

$$m\ddot{w} + d\dot{w} + kw = f_a \ , \tag{4.1}$$

where m (kg) is the mass of the sample platform, as well as any additional mass due an attached payload, d (N s m^{-1}) is the damping coefficient, and k (N m^{-1}) is the spring constant. Here it is assumed that the additional stiffness introduced by the presence of the actuator in the mechanical structure is accounted for in the spring constant k.

The piezoelectric actuator is modeled as a force transducer, generating a force proportional to the applied voltage, as described in Section A.5. The applied external force from the piezoelectric actuator f_a (N) is

$$f_a = e_a(u_a + d_u) \ , \tag{4.2}$$

where e_a (N V^{-1}) is the effective gain of the piezoelectric actuator from voltage to force, and u_a (V) is the applied voltage. The piezoelectric actuator will introduce hysteresis and creep when driven by a voltage signal. It is a reasonable assumption

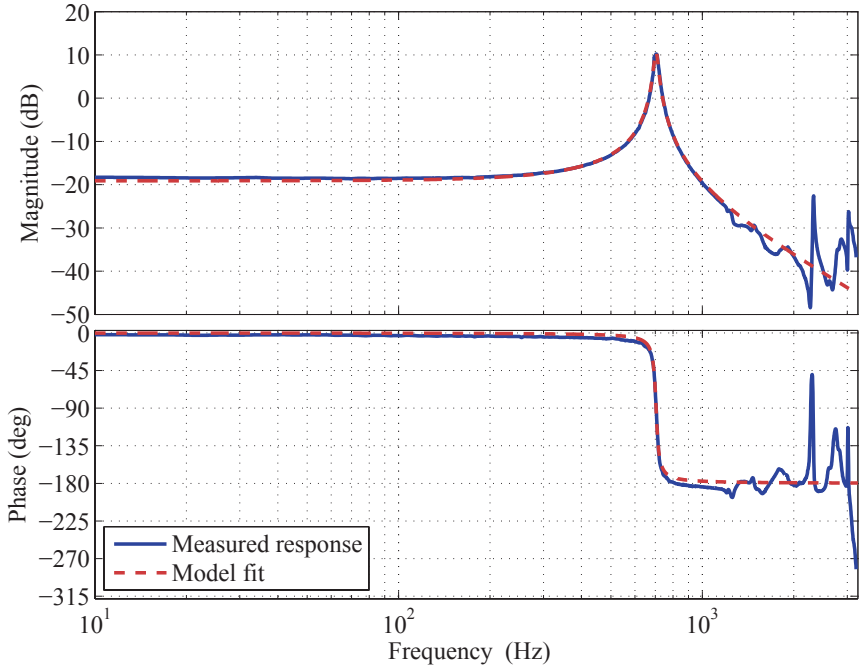

Figure 4.1: Measured frequency response for x-axis of the nanopositioning stage and the model (4.3) using parameter values from Tab. 4.1.

to consider this behavior as a bounded disturbance added to the input, represented by the term d_u (V), as discussed in Section 2.9.

The transfer-function from the voltage input u_a to the displacement w (m) for the flexible structure is

$$G_w(s) = \frac{w}{u_a}(s) = \frac{\beta_0}{s^2 + 2\zeta\omega_0 s + {\omega_0}^2} , \tag{4.3}$$

where $\beta_0 = e_a/m$ (m s^{-2} V^{-1}), $\zeta = c/2\sqrt{mk}$, and $\omega_0 = \sqrt{k/m}$ (s^{-1}). See Appendix B for a general description of the dynamics of flexible structures.

The frequency response for the x-direction is recorded using a SR780 Dynamic Signal Analyzer from Stanford Research Systems using a 200 mV RMS bandwidth-limited white noise excitation. The response is displayed in Fig. 4.1. The model (4.3) is fitted to the frequency response data using the MATLAB System Identification Toolbox, and the resulting parameter values are presented in Tab. 4.1. The response of the model (4.3) using these parameters is also displayed in Fig. 4.1 for comparison, where good agreement is achieved up to approximately 2 kHz.

4.2.2 Uncertainty

As can be seen from Fig. 4.1, the actual response of the first vibration mode is well approximated by the second-order model (4.3), and the second-order model is

Table 4.1: Identified parameters for the model (4.3).

Parameter	Value	Unit
β_0	$2.17{\cdot}10^{6}$	μm s^{-2} V^{-1}
ζ	$16.3{\cdot}10^{-3}$	-
ω_0	$2\pi \cdot 704$	s^{-1}

sufficient to describe the dominant dynamics of the system. However, in order to assess the robustness properties of the proposed control scheme, the uncertainties of the system must be accounted for.

As can be seen in Fig. 4.1, the system contains vibration modes above the dominant (first) vibration mode, particularly the second vibration mode is clearly visible. It should be noted that higher-order vibration modes are likely to have shapes and directions that will make them difficult to control using the mounted actuator (along the x-direction). The control law therefore needs sufficient attenuation at higher frequencies to avoid excitation of the higher order vibration modes. For the experimental set-up, the payload mass is constant, and no change is expected for the resonant frequencies.

The system also has a fair amount of uncertainty with regards to the parameters. The parameter that seems most susceptible to change is the effective gain e_a, as discussed in Section 2.9. The effective gain e_a is mainly determined by the piezoelectric material used in the actuator, the amount of polarization, and the driving voltage amplitude, as the amount of deflection generated changes with voltage amplitude due to hysteresis. The dependency of the effective gain on the input amplitude is demonstrated in Fig. 1.2b, and is measured for the system at hand in Fig. 4.2. Here, the relative change of the low-frequency gain $K = e_a/k = \beta_0/{\omega_0}^2$ is recorded as a function of input voltage amplitude (using a sinusoidal input signal at 10 Hz). The relative change of the gain was found to be up to 80% $\approx$ -2 dB at an amplitude of 100 V compared to the gain at 50 mV.

The peak amplitude response of the first and higher order vibration modes did, however, not seem to change as a function of input voltage amplitude. It is pointed out that this is difficult to measure over a large domain, as fairly low input amplitudes would lead to excessively large displacements when the system is excited using frequencies close to the first dominant resonant frequency. A reasonable assumption in this case would then be that the uncertainty in gain diminishes when approaching the first resonance from below. Some confirmation for this assumption can be found in the fact that, when the assumption is made during control law tuning, it results in a stable closed-loop system using the actual nanopositioning stage.

To assess the robustness of the proposed control scheme with regards to the uncertainties discussed, the uncertainty of the system model is taken into account as a multiplicative perturbation to the nanopositioner dynamics,

$$w = G_w(s)(1 + \delta_w(s)\Delta_w(s))u_a \ ; \ \|\Delta_w(s)\|_\infty \leq 1 \ . \tag{4.4}$$

The uncertainty weight $\delta_w(s)$ is determined experimentally. As the uncertainty

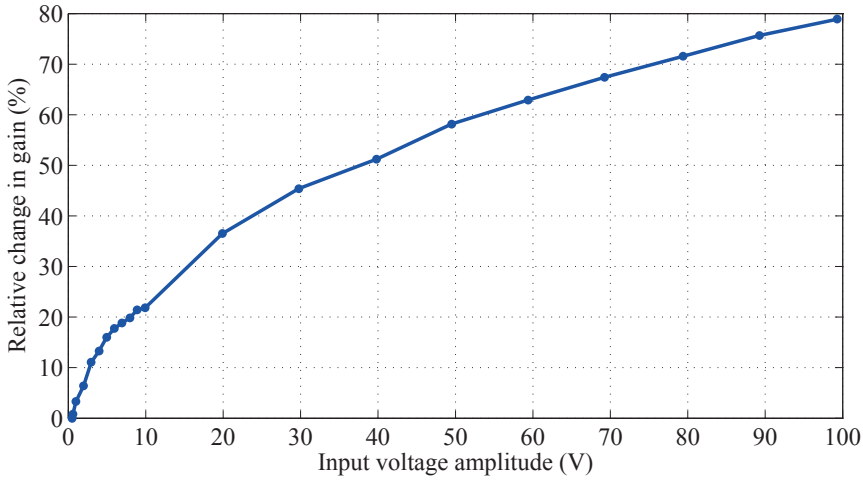

Figure 4.2: Relative change in low-frequency gain for the piezoelectric actuator due to the input voltage amplitude (using a sinusoidal input at 10 Hz).

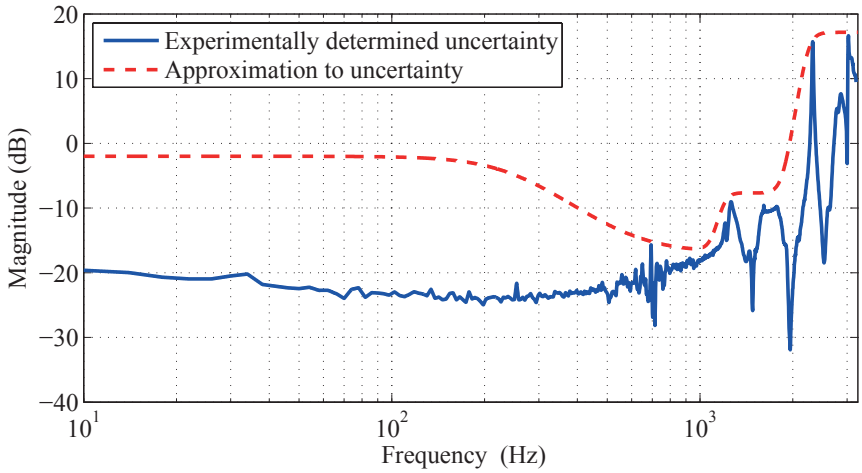

Figure 4.3: Open-loop uncertainty weight $\delta_w(s)$, using experimental data and as over-bounding transfer-function.

apparently is very large at low frequencies, but difficult to measure over a large frequency domain, an over-bounding transfer-function is proposed. These uncertainty weights are shown in Fig. 4.3.

4.3 Control Structure

The control law combines a plug-in repetitive control scheme and a proportional-integral control law as illustrated in Fig. 4.4. The PI control law is modified to in-

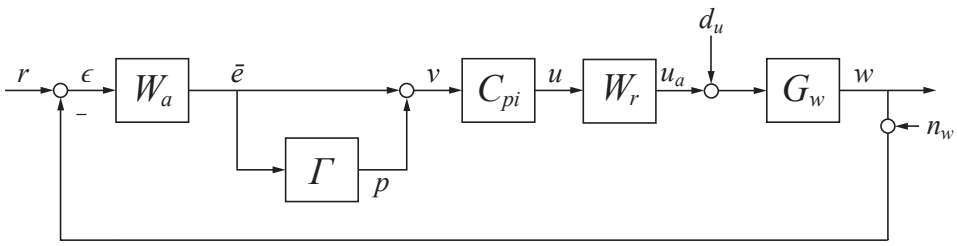

Figure 4.4: System block diagram.

clude the anti-aliasing and reconstruction filters, $W_a(s)$ and $W_r(s)$. As was demonstrated in Section 3.4.6, this modified PI control law can be used for damping and tracking control.

4.3.1 Repetitive Control

Repetitive control tracks or rejects arbitrary periodic exogenous signals of a fixed period τ_p (s). This is achieved by embedding a model of the reference r or disturbance d_u signal into the feedback loop. The minimal and exact realization of a model for any periodic signal with period τ_p is given by [224]

$$\Gamma_1(s) = \frac{\mathrm{e}^{-\tau_p s}}{1 - \mathrm{e}^{-\tau_p s}} \,. \tag{4.5}$$

For an appropriate initial function, this model can generate any signal with the given period τ_p, as it contains poles at $s = j2\pi n/\tau_p$, for $n = 0, 1, 2, 3, ..., \infty$. However, the minimal realization is not suitable for implementation on most systems since it requires the system to be bi-proper, that is, to have relative degree $n^\star = 0$, in order to be stable in closed-loop. The remedy is to introduce a stable low-pass filer $Q(s)$ in the model [98], *i.e.*,

$$\Gamma_2(s) = \frac{Q(s)\mathrm{e}^{-\tau_p s}}{1 - Q(s)\mathrm{e}^{-\tau_p s}} \,.$$

By doing so, all the poles will shift into the complex left half-plane by an amount depending on the frequency; thus, at higher frequencies the new pole location is farther away from the original location than at lower frequencies. This means that the model is no longer exact, and importantly, the nulling property with respect to the exact model (4.5), especially at higher frequencies, is degraded.

In this work, the structure shown in Fig. 4.5a is used to implement the RC scheme, and the transfer-function is given by

$$\Gamma(s) = \frac{p}{\bar{e}}(s) = \frac{R(s)\mathrm{e}^{-\tilde{\tau}_p s}}{1 - Q(s)\mathrm{e}^{-\tilde{\tau}_p s}} \,. \tag{4.6}$$

Two modifications have been introduced, the output filter $R(s)$, defined below, and a modified delay $\tilde{\tau}_p$. By modifying the time-delay in the RC block, the shift in the

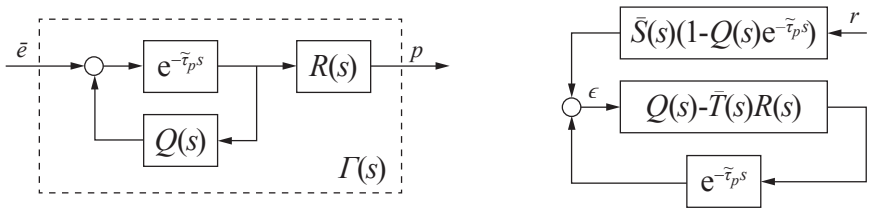

(a) Implementation of the plug-in repetitive control law block $\Gamma(s)$.

(b) Equivalent representation of the sensitivity function (4.8).

Figure 4.5: Repetitive control scheme block diagrams.

poles due to $Q(s)$ can be partially compensated for. A method for minimizing the tracking error by tuning $\tilde{\tau}_p$ is given in Section 4.4.2.

Inspecting Fig. 4.4, the closed-loop sensitivity function for the overall system is

$$S(s) = \frac{\epsilon}{r}(s) = \frac{1}{1 + \bar{L}(s) + \bar{L}(s)\Gamma(s)} = \frac{1}{P(s)} \,, \tag{4.7}$$

where $\bar{L}(s) = W_a(s)G_w(s)W_r(s)C_{pi}(s)$. The stability of the closed-loop system is determined by the denominator $P(s) = 1 + \bar{L}(s) + \bar{L}(s)\Gamma(s)$.

The sensitivity and complementary sensitivity function without the presence of the repetitive control scheme is denoted as

$$\bar{S}(s) = \frac{\epsilon}{r}(s) = \frac{1}{1 + \bar{L}(s)} \quad \text{and} \quad \bar{T}(s) = \frac{w}{r}(s) = \bar{L}(s)\bar{S}(s) \,,$$

respectively. By inserting the expression for $\Gamma(s)$, multiplying the numerator and denominator of $1/P(s)$ by $\bar{S}(s)$, and rearranging, the sensitivity function for the closed-loop system when adding the repetitive control scheme takes the form

$$S(s) = \frac{1}{P(s)} = \frac{\bar{S}(s)(1 - Q(s)e^{-\tilde{\tau}_p s})}{1 - (Q(s) - \bar{T}(s)R(s))e^{-\tilde{\tau}_p s}} \,. \tag{4.8}$$

With reference to Fig. 4.5b, it can be seen that given a bounded reference r and stable transfer-functions $\bar{S}(s)$ and $Q(s)$, the small-gain theorem provides the criterion for the stability of the closed-loop system as [98]

$$\left\| Q(s) - \bar{T}(s)R(s) \right\|_\infty < 1 \,, \tag{4.9}$$

with $|e^{-j\tilde{\tau}_p \omega}| = 1 \; \forall \; \omega \in \mathbb{R}$.

The output filter $R(s)$ is constructed as

$$R(s) = {W_T}^{-1}(s)Q(s) \,, \tag{4.10}$$

introducing a stable all-pole filter $W_T(s)$, which provides for some flexibility in meeting the stability criterion. Using a unity-gain low-pass filter $Q(s)$, the simpler criterion

$$\left\| 1 - {W_T}^{-1}(s)\bar{T}(s) \right\|_\infty < 1 \,, \tag{4.11}$$

for selecting an appropriate filter $W_T(s)$ can be used. The selection of $W_T(s)$ is described in Section 4.4.2.

Finally, to assess the robustness of the RC scheme, a multiplicative perturbation for the closed-loop complementary sensitivity is used, *i.e.*,

$$w = \bar{T}(s)(1 + \hat{\delta}_w(s)\hat{\Delta}_w(s))r \ ; \ \|\hat{\Delta}_w(s)\|_\infty \leq 1 \ , \tag{4.12}$$

where

$$\hat{\delta}_w(s)\hat{\Delta}_w(s) = \frac{\bar{S}(s)\delta_w(s)\Delta_w(s)}{1 + \bar{T}(s)\delta_w(s)\Delta_w(s)} \ \Rightarrow \ |\hat{\delta}_w(j\omega)| \leq |\bar{S}(j\omega)\delta_w(j\omega)| \ . \tag{4.13}$$

Incorporating the uncertainty into the criterion (4.9), the robust stability criterion

$$\left|Q(j\omega) - \bar{T}(j\omega)R(j\omega)\right| < 1 - \left|\bar{T}(j\omega)\hat{\delta}_w(j\omega)R(j\omega)\right| \ , \tag{4.14}$$

is obtained.

4.3.2 Damping-Tacking Control

The nanopositioning stage is a lightly damped structure. Inspecting the stability criterion for the RC scheme (4.9), it is expected that large peaks in the complementary sensitivity function $\bar{T}(s)$ can reduce the applicable bandwidth and gain, depending on how well the output filter $R(s)$ is able to match the inverse closed-loop dynamics $\bar{T}(s)$. Due to the inclusion of a damping and tracking control law $C(s)$, the robustness and bandwidth possible for the overall control scheme is increased, as this control law will reduce the sensitivity to plant uncertainty, as measured by the sensitivity function $\bar{S}(s)$, *i.e.*, since [60, 119]

$$\bar{S}(s) = \frac{\partial\bar{T}(s)/\bar{T}(s)}{\partial G_w(s)/G_w(s)} = \frac{G_{w0}(s)}{\bar{T}_0(s)}\frac{\partial\bar{T}(s)}{\partial G_w(s)}\bigg|_{\text{NOP}} \ ,$$

using a nominal operating point (NOP) for all the parameters in the transfer-functions.

As discussed in Section 3.4.6, a simple, effective, and robust damping and tracking control law for a lightly damped structure can be obtained by augmenting an integral control law by a second or higher-order low-pass filter, and optimally tuning the integral gain and cut-off frequency.

Since the control law is implemented in discrete time using digital-to-analog and analog-to-digital converters, anti-aliasing and reconstruction filters must be present in order to mitigate aliasing effects and quantization noise. By including these filters in the control law, an extra degree of freedom can be added for the tuning of the control law, which is the cut-off frequency of the filters. The nominal choice for the cut-off frequency would usually be close to the Nyquist frequency if high bandwidth is required. In order to mitigate the effects of aliasing and quantization on the system, it is desirable to choose a low cut-off frequency, but this usually impacts the closed-loop stability margins negatively. However, using the damping integral control law, the optimal cut-off frequency turns out to be close to the first

resonant frequency, which *has* to be well below the Nyquist frequency to avoid aliasing.

Using the proposed tuning procedure from Chapter 3 it is therefore possible to utilize the filters to good effect; damping the dominant vibration mode, reducing the sensitivity to plant uncertainty and disturbances, and reducing the impact of aliasing and quantization on the system. Compared to a regular integral control law the damping integral control law will also marginally reduce the overall noise level due to sensor noise, even when not considering the added noise due to quantization.

Proportional-Integral Control Law

In this Chapter, a proportional-integral (PI) control law is used, rather than the integral control law used in Section 3.4.6, in the hopes that a slightly higher bandwidth can be achieved. This would be due to the increased effective stiffness introduced by the proportional action, which should increase the allowable integral gain.

A PI control law is typically given as

$$C_{pi}(s) = \frac{k_p s + k_i}{s}, \tag{4.15}$$

where k_p and k_i are the proportional and integral gains, respectively. The anti-aliasing and reconstruction filters are here taken to be second-order low-pass Butterworth filters

$$W_a(s) = W_r(s) = \frac{{\omega_c}^2}{s^2 + \sqrt{2}\omega_c s + {\omega_c}^2}, \tag{4.16}$$

where ω_c is the cut-off frequency. For convenience they are chosen to be identical when tuning the control law. The modified PI control law is therefore

$$C(s) = W_a(s) C_{pi}(s) W_r(s) \ . \tag{4.17}$$

Proportional Gain Margin

When applying a proportional control law

$$C_p(s) = k_p$$

to the second order system (4.3), in the ideal case with perfect sensors and actuators, it is straight forward to verify that the closed-loop system has an unlimited stability margin, that is, k_p can be chosen arbitrarily large. The proportional action increases the effective stiffness of the system, and the product $\zeta {\omega_0}^3$ in (3.16) will therefore be larger, and thus proportional action should increase the allowable gain when combined with integral action.

However, in the presence of phase-lag, the margin for a proportional control law is rather limited. Considering for instance sensor dynamics in the form of the first-order low-pass filter with cut-off frequency ω_c

$$W_y(s) = \frac{\omega_c}{s + \omega_c} \ , \tag{4.18}$$

in cascade with (4.3), the margin k_p^* for the combined system determined by the Routh-Hurwitz criterion is

$$k_p < \frac{2\zeta\omega_0({\omega_0}^2 + 2\zeta\omega_0\omega_c + {\omega_c}^2)}{\omega_c\beta_0} = k_p^* \,. \tag{4.19}$$

With parameter values from Tab. 4.1, and considering the specifications for a fast state-of-the-art capacitive probe from ADE Technologies (ADE 6810), which is well described by (4.18) with $\omega_c = 2\pi \cdot 100$ rad/s, the gain is limited to $k_p \lessapprox 40$. Adding more low-pass characteristic elements degrades the limit even more, and the increased performance due to proportional action is therefore modest.

4.4 Control Scheme Tuning & Analysis

The tuning and analysis of the damping and tracking control law and the repetitive control scheme is presented below.

4.4.1 Damping & Tracking Control Law

The damping and tracking control law is as presented in Section 3.4.6, with the addition of proportional action. As the proportional gain is limited by phase-lag due to instrumentation, it is set to a constant, low value. The tuning procedure is then identical with the method presented in Chapter 3.

Effects of Low-Pass Filters in the Signal Chain

The modified PI control law (4.17) has an extra degree of freedom, in the choice of the cut-off frequency of the filters (4.16). As discussed in Section 3.4.6, damping can be introduced and the overall bandwidth can be increased, by adjusting the cut-off frequency ω_c. For the system used in the experimental set-up for this Chapter, this is illustrated in Fig. 4.6a. Setting the control gains to $k_p = 1$ and $k_i = k_i^* \approx 1300$, *i.e.*, setting the PI control law gains close to the margin of stability, the eigenvalue loci of the closed-loop system is generated by varying the cut-off frequency ω_c of the anti-aliasing and reconstruction filters.

As can be seen from the detail in Fig. 4.6b, using filters with a cut-off frequency equal to the Nyquist frequency, $\omega_c = \omega_n = 2\pi \cdot 50$ rad/s, the system is unstable. The Figs. 4.6a and 4.6b indicate, however, that reducing the cut-off frequency for the filters, all eigenvalues can be moved further into the left-half plane. Minimizing the maximum value of the real part of the eigenvalues for the closed-loop system as a function of the cut-off frequency ω_c resulted in

$$\underset{\omega_c \in \mathbb{R}^+/\{0\}}{\arg\min} \left[\underset{\mathrm{Re}(\lambda)\in\mathbb{R}^-}{\arg\max} [\det(A(\omega_c) - \lambda I) = 0] \right] \approx 2\pi \cdot 584 \text{ rad/s} \,, \tag{4.20}$$

where $A(\omega_c)$ is a state matrix realization for the closed-loop system for a given ω_c. Thus, setting $\omega_c = 2\pi \cdot 584$ rad/s, produces the fastest modes for this system with the selected control gains.

By inspecting Figs. 4.6a and 4.6b, it is evident that by using the computed optimal value for the cut-off frequency, the stability margins for the closed-loop

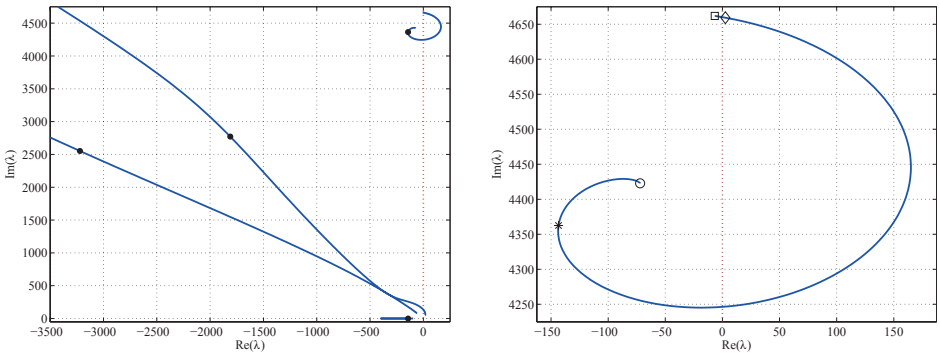

(a) The positive imaginary part of the complex conjugate eigenvalue loci for the vibration mode in addition to the modes due to the filters (4.16), and the real valued mode due to the integral action in (4.15). The optimal root locations according to (4.20) are indicated by dots.

(b) Detail from the upper-right corner of Fig. 4.6a. The eigenvalue when $\omega_c \to 0$ is indicated by a circle, ω_c due to (4.20) a star, $\omega_c = \omega_n$ a diamond shape, and $\omega_c \to +\infty$ a square.

Figure 4.6: Eigenvalue loci for the closed-loop system as a function of the filter cut-off frequency ω_c. The loci are symmetric about the real axis.

Table 4.2: Optimal parameters for (4.17).

Parameter	Value
ω_c	$2\pi{\cdot}737$
k_i	$8.33{\cdot}10^3$

system will be larger. This should allow for a larger closed-loop bandwidth. The new stability margin is found numerically to be about $12 \cdot k_i^*$, thus reducing the cut-off frequency increases the integral gain limit significantly.

As pointed out in Section 3.4.6, the closed-loop pole locations depend on both k_i and ω_c, and for the PI control law, also k_p. Optimal values for k_i and ω_c was therefore found solving (3.15), keeping k_p fixed. As different values for k_p that generated a stable closed-loop system did not seem to impact the bandwidth noticeably, this gain value was set to $k_p = 1$. The optimal control law parameters for (4.17) with $k_p = 1$ found when solving (3.15) are presented in Tab. 4.2.

As an example of the feasibility of the cost-function (3.14), the surface of the cost-function in a neighborhood of the optimal values is shown in Fig. 4.7. For this system it can be seen that the cost-function provides a smooth and convex surface, and that the solution of (3.15) for a reasonable domain of control law parameters is unique.

It might also be interesting to compare the optimal tuning with a nominal tuning for the control law (4.17). A nominal tuning of the anti-aliasing and reconstruction filters corresponds to using $\omega_c = \omega_n$, *i.e.*, the Nyquist frequency. Tuning the PI control law for maximum bandwidth in this case requires the highest possi-

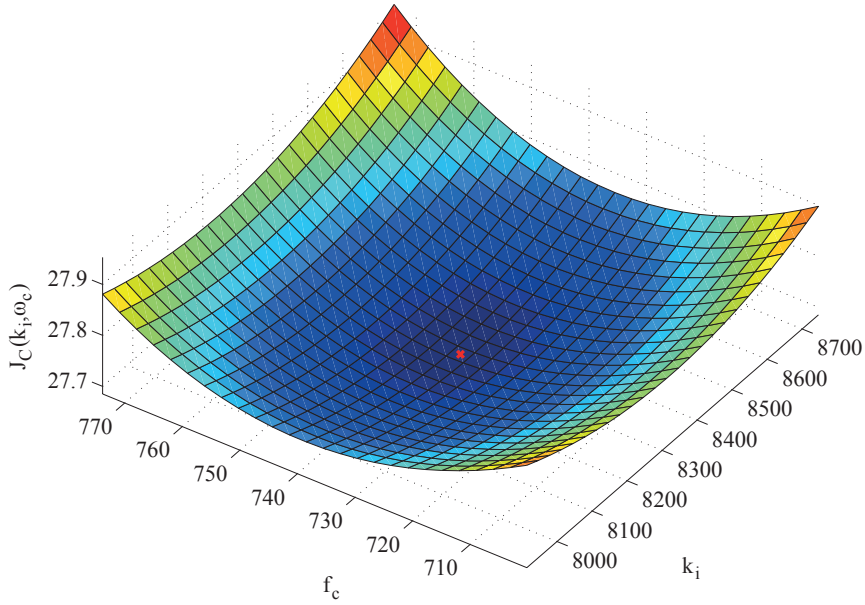

Figure 4.7: Surface of the cost-function (3.14). Here, $\omega_c = 2\pi f_c$.

ble gain for the proportional and integral term, but due to the undamped vibration mode, high gain provides little robustness, and from Fig. 4.6b it can be seen that the system is unstable for $\omega_c = \omega_n$ and $k_i \approx k_i^*$. Using the control law parameters from Tab. 4.2, a gain margin of $\Delta K = 5.81$ dB and a phase margin of $\Psi = 61.6°$ is found for the loop transfer-function. To obtain similar robustness properties, a comparable gain and phase margin when using $\omega_c = \omega_n$ is found for $k_p = 1$ and $k_i = 650$, which yields $\Delta K = 5.18$ dB and $\Psi = 96.3°$.

The resulting frequency responses for sensitivity and complementary sensitivity functions for the two control law configurations are displayed in Figs. 4.8a and 4.8b. As can be seen from Fig. 4.8a, the optimal tuning very effectively attenuates the resonant peak, from 18 dB in the nominal case, to 0.88 dB in the optimal case. From Fig. 4.8b it can be seen the there is a significant increase in closed-loop bandwidth; from approximately 13 Hz in the nominal case to approximately 110 Hz in the optimal case.

Due to the increased bandwidth, the effect of input disturbances d_u on the output are reduced. The effects can be measured by the input sensitivity function (3.11), *i.e.*, $\bar{S}(s)$, which provides the amount of attenuation of input disturbances d_u to the input u_a. By inspection the response of $\bar{S}(s)$ in Fig. 4.8b, it can be seen that the suppression of external disturbances is in general better for the optimally tuned control law. Disturbances will have a higher degree of suppression at lower frequencies, but less suppression in a narrow band close to the dominant resonant peak. Due to the restriction posed by the Bode sensitivity integral, there is no suppression outside of the bandwidth of the control law.

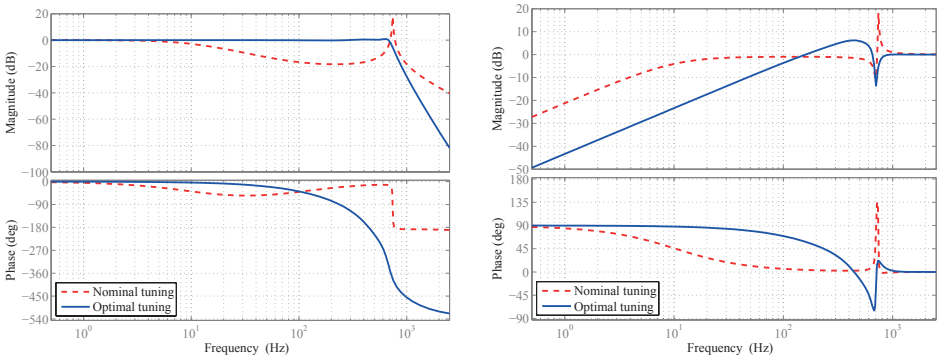

(a) Complementary sensitivity function $\bar{T}(s)$.

(b) Sensitivity function $\bar{S}(s)$.

Figure 4.8: Amplitude and phase responses, using nominal and optimal tuning.

Noise Performance

With regards to sensor noise performance, the transfer-function from sensor noise to displacement is measured by (3.9), *i.e.*, $-\bar{T}(s)$. As an example, the approximate effect of the displacement sensor noise can be evaluated. The sensor used has a bandwidth of 100 kHz, and the root-mean-square (RMS) noise is measured to be less than 2.5 nm. Assuming that the noise spectrum is fairly flat, the spectral density of the noise is

$$\sqrt{S_{n_w}(j\omega)} \approx 7.9 \text{ pm}/\sqrt{\text{Hz}} \, .$$

Computing the RMS value of the noise response for $-\bar{T}(s)$, *i.e.*,

$$\sigma_w = \sqrt{S_{n_w}} \cdot \| - \bar{T}(s)\|_2 \, ,$$

for both the nominally and optimally tuned control law, provides an estimate of the RMS position noise due to sensor noise. It turns out to be $\sigma_w = 0.34$ nm for the nominal tuning, and $\sigma_w = 0.31$ nm for the optimal tuning. Thus, even though the bandwidth of the control law is increased by about an order of magnitude, the noise contribution due to sensor noise is slightly decreased.

Robustness

The robustness of the modified PI control law with regards to the uncertainties displayed in Fig. 4.3 is determined. The criterion [206]

$$\|\delta_w(s)\bar{T}(s)\|_\infty < 1 = 0 \text{ dB} \tag{4.21}$$

is evaluated, and the results are shown in Fig. 4.9. As can be seen, the control law allows for very large uncertainty in high-frequency dynamics. This means that the presence of higher order modes will not interfere with the stability. If the vibration modes above the first mode should be more closely spaced and have higher peak magnitudes than what is the case for the system at hand, anti-aliasing

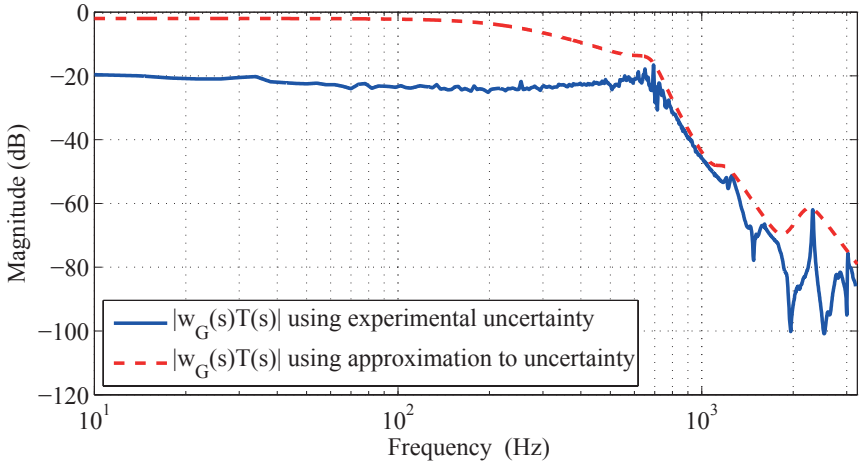

Figure 4.9: Evaluation of robust stability criterion $|\delta_w(j\omega)\bar{T}(j\omega)|$ for the modified PI control law.

and reconstruction filters with a higher roll-off rate can be used. It should be noted that the nominal tuning do not satisfy (4.21) when using the over-bounding uncertainty weight, due to the presence of the undamped resonant peak, thus the suggested gain margin in Section 4.4.1 is not sufficient in this case.

4.4.2 Repetitive Control Law

Choosing $R(s)$ and $Q(s)$

The repetitive control scheme has inherent robustness against plant uncertainty due to the nulling property. However, robust tracking performance is not the same as robust stability. Considering the stability criterion for the repetitive control law (4.11), the ideal choice for the included filter would be $W_T(s) = \bar{T}(s)$, as this would produce the minimum of the norm (4.11). As such, a sufficient choice for $W_T(s)$ would be a filter that matches $\bar{T}(s)$ sufficiently to meet the stability criterion. The filter $W_T(s)$ should be of minimal order, to reduce computational complexity, and the specific choice of the filter can also provide some flexibility in meeting the robust stability criterion (4.14).

The complementary sensitivity function $\bar{T}(s)$ has seven poles and one zero, and thus has relative degree $n^\star = 6$. By inspection of Figs. 4.8a and 4.8b one can infer that the complementary sensitivity function has a response that closely resembles a sixth-order all-pole low-pass filter. In order to minimize the order of $W_T(s)$, the zero in $\bar{T}(s)$ can be neglected.

Due to the frequency response of $\bar{T}(s)$, $W_T(s)$ is chosen to be a sixth-order Butterworth filter with DC-gain $1/k_T$, and it is assumed that $W_T(s) \approx \bar{T}(s)$. An optimal choice for the cut-off frequency ω_T and DC-gain k_T for $W_T(s)$ is found

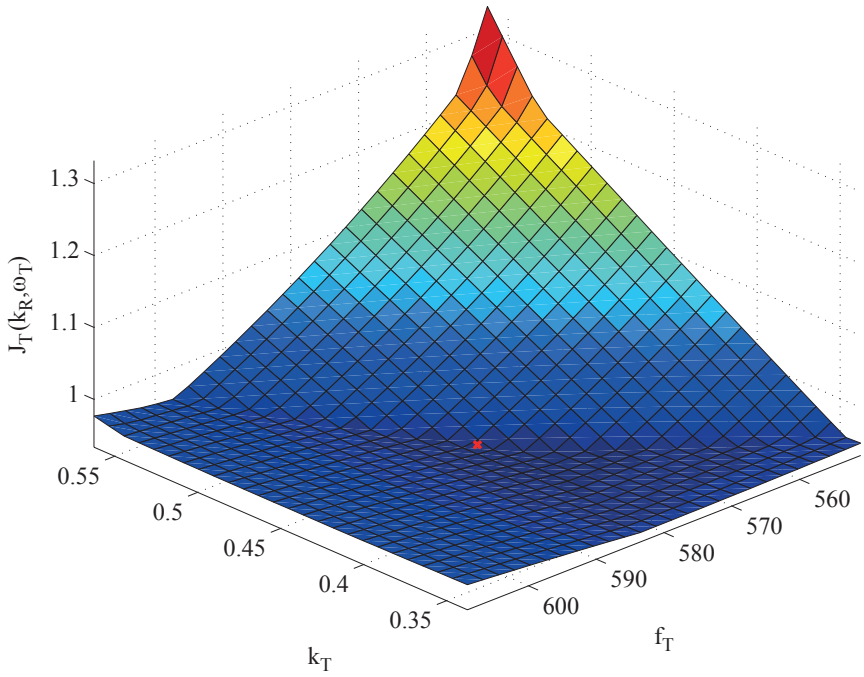

Figure 4.10: Surface of the cost-function (4.22). Here, $\omega_T = 2\pi f_T$.

minimizing the cost-function

$$J_T(k_T, \omega_T) = \sup\{|Q(j\omega) - \bar{T}(j\omega)R(j\omega, \omega_T, k_T))| + |\bar{T}(j\omega)\hat{\delta}_w(j\omega)R(j\omega, \omega_T, k_T))| : \omega \in \mathbb{R}\}, \quad (4.22)$$

where $R(j\omega, \omega_T, k_T) = W_T(j\omega, \omega_T, k_T)^{-1}Q(j\omega)$. The evaluation of the cost-function must satisfy $J_T(k_T^\star, {\omega_T}^\star) < 1$ in order for the system to be robustly stable. The closed-loop uncertainty weight $\hat{\delta}_w(s)$ for the system, using experimental data and the overbounding approximation, are shown in Fig. 4.11. The approximation is used for the optimization.

The filter $Q(s)$ must be chosen before performing the optimization. This is done with consideration to the filter $R(s)$, and chosen to be a unity-gain sixth-order Butterworth filter, such that $R(s) = {W_T}^{-1}Q(s)$ is a proper filter. By inspection of the frequency response in Fig. 4.1, a cut-off frequency for $Q(s)$ is chosen in order to attenuate the second and higher order vibration modes, in order to satisfy (4.14). A cut-off frequency $\omega_Q = 2\pi \cdot 2000$ rad/s provided sufficient attenuation, yielding the optimal values $k_T^\star \approx 0.45$ and ${\omega_T}^\star \approx 2\pi \cdot 580$ when minimizing (4.22).

The surface of the cost-function in a neighborhood of the optimal values is shown in Fig. 4.10. As can be seen, there is a domain along a line segment, or narrow area, where the sensitivity of the cost-function is low, and thus there are several values for k_T and ω_T that evaluate to approximately the same cost. This means that the value of k_T and ω_T can be increased while still being robustly

Table 4.3: Optimal parameters for $W_T(s)$ and $W_Q(s)$.

Parameter	Value
k_T	0.45
ω_T	$2\pi \cdot 580$
ω_Q	$2\pi \cdot 2000$

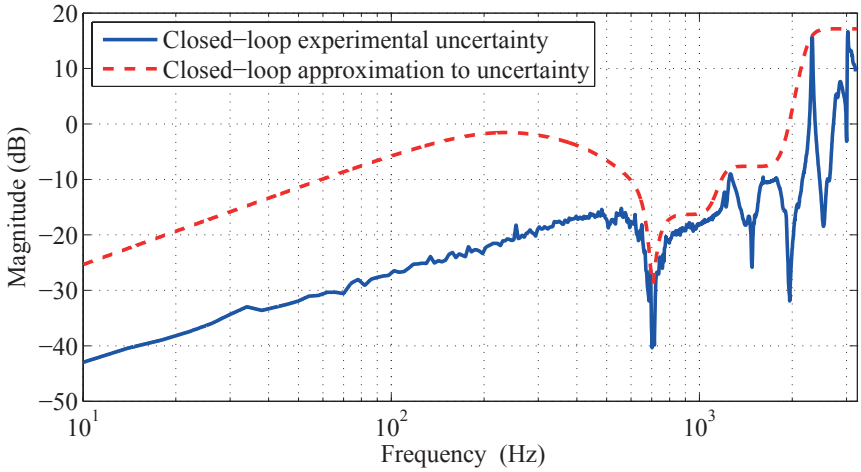

Figure 4.11: Closed-loop uncertainty weight $\hat{\delta}_w(s)$, using experimental data and as an over-bounding transfer-function.

stable. Adjusting k_T and ω_T impacts the transient response and the specific form of the closed-loop frequency response. There could therefore be other values of these parameters that provide faster convergence or less sensor noise contribution. Choosing $W_T(s) = \bar{T}(s)$ will essentially eliminate the transient response, since it yields $P(s) = 1$ in (4.8), but it will not impact the stationary response as long as the reference signal conforms to the internal model.

The evaluation of (4.14) is shown in Fig. 4.12, and demonstrates that the choice of ω_Q and the optimal values for k_T and ω_T indeed provide robust stability of the closed-loop system.

It should be noted at this point that the choice of $W_T(s) = \bar{T}(s)$ does not provide as good results when evaluating (4.14). In this case the cut-off frequency must be $\omega_Q < 2\pi \cdot 1700$ to be robustly stable. As the bandwidth of $Q(s)$ is one of the most important factors for obtaining good reference trajectory tracking, ω_Q should be as high as possible.

It should also be noted that (4.14) appears to provide a somewhat conservative result. By tuning the system manually, it is possible to increase the cut-off frequency for $Q(s)$ to $\omega_Q = 2\pi \cdot 3000$, while decreasing the DC-gain to $k_T = 0.275$, keeping ω_T that same. This tuning violates (4.14), but provides a larger bandwidth for the RC scheme, and thus increases the tracking performance.

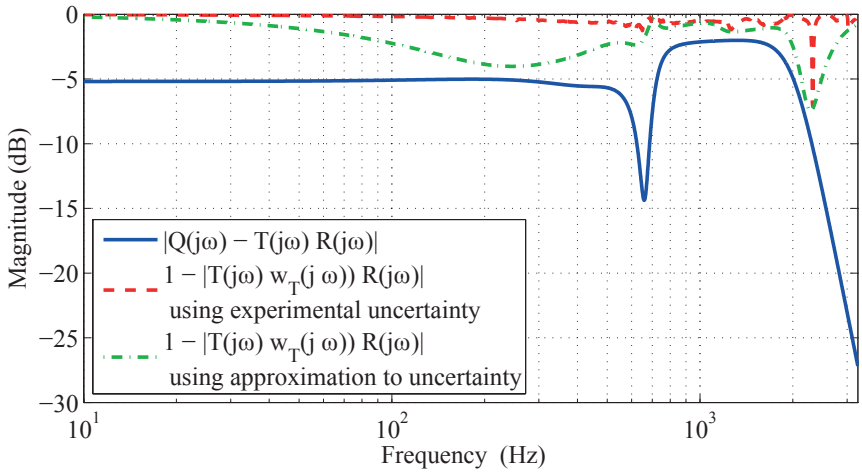

Figure 4.12: Evaluation of stability criteria (4.9) and (4.14).

Tuning of the Time-Delay

Inspecting the sensitivity function (4.8), note that the numerator contains the expression

$$\tilde{Z}(s) = 1 - Q(s)\mathrm{e}^{-\tilde{\tau}_p s} \ .$$

Had the exact model (4.5) been used, the expression would have been

$$Z(s) = 1 - \mathrm{e}^{-\tau_p s} \ ,$$

which evaluates to

$$\mathcal{L}^{-1}\left[(1 - \mathrm{e}^{-\tau_p s})r(s)\right] = r(t) - r(t - \tau_p) = 0 \ \forall \ t > \tau_p \ ,$$

when $r(t) = 0 \ \forall \ t < 0$ and $r(t) = r(t + \tau_p)$. Thus, *disregarding the initial value response of the system*, the reference signal is perfectly nulled in the error after one period τ_p of the reference signal, and perfect tracking is obtained. For the actual implementation

$$\mathcal{L}^{-1}\left[(1 - Q(s)\mathrm{e}^{-\tilde{\tau}_p s})r(s)\right] = r(t) - \tilde{r}(t - \tilde{\tau}_p)$$

where $\tilde{r}(t) = Q(t) * r(t) \neq r(t)$, is used. Since the filter $Q(s)$ alters the reference signal, perfect tracking can not be obtained. The residual error depends both on $Q(s)$ and the time-delay $\tilde{\tau}_p$, and thus, a simple method to improve the tracking performance is to adjust $\tilde{\tau}_p$.

By filtering the intended reference signal by $\tilde{Z}(s)$, it is possible to numerically evaluate the amount of suppression, or nulling, of the reference signal. By adjusting $\tilde{\tau}_p = \tau_p - \tau_\delta$ by varying τ_δ, an optimal τ_δ that produces the best tracking performance can be found, *i.e.*, minimizing

$$J(\tau_\delta) = \left\| \mathcal{L}^{-1}\left(\tilde{Z}(s,\delta)\right) * r(t) \right\|_2 \quad , \quad t \in [\tau_p m, \tau_p(m+1)] \ ,$$

Table 4.4: Optimal values for τ_δ at various reference frequencies for $Q(s)$ with $\omega_Q = 2\pi \cdot 2000$ rad/s.

f_p	τ_δ
25 Hz	$3.07709 \cdot 10^{-4}$ s
50 Hz	$3.08076 \cdot 10^{-4}$ s
100 Hz	$3.08384 \cdot 10^{-4}$ s
200 Hz	$3.08982 \cdot 10^{-4}$ s
400 Hz	$3.09129 \cdot 10^{-4}$ s

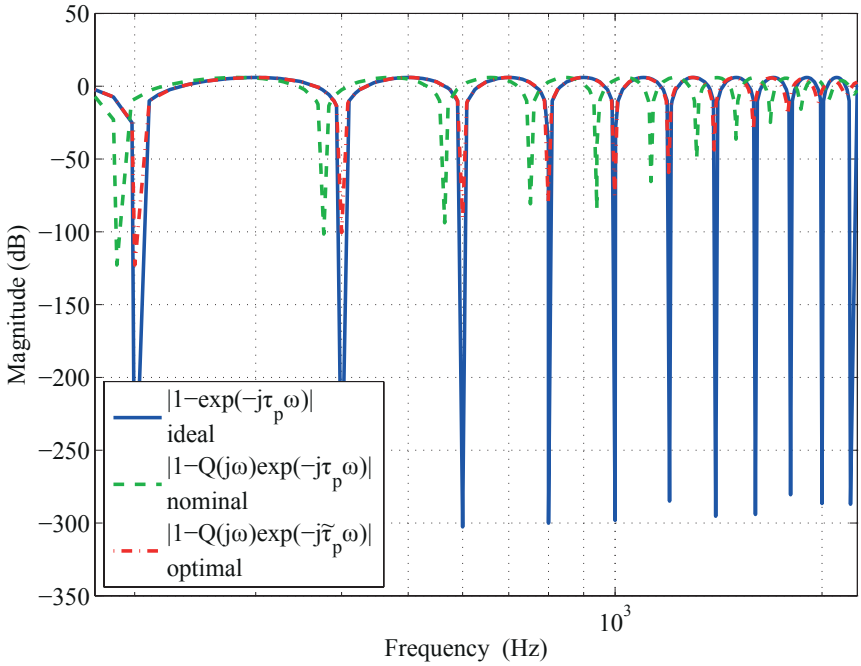

Figure 4.13: Zero locations for different configurations of $\tilde{Z}(s)$, using $\tau_p = 1/200$ s.

where $\tau_\delta \in (0, \tau_p)$, and m is a positive integer to make sure $\tau_p m$ is large enough for the transient response of $Q(s)$ to have died out. Results are presented in Tab. 4.4. Note that it is possible to implement time-delays with a non-integer multiple of the sampling time using Thiran approximation [132].

An example of the effect on the zero locations of $\tilde{Z}(s)$ is shown in Fig. 4.13. Here the amplitude response of $\tilde{Z}(s)$ is computed with and without the filter $Q(s)$, for τ_p and $\tilde{\tau}_p$, using $f_p = 200$ Hz.

Noise Performance

Sensor noise performance for the case when including the RC scheme in the feedback loop, can be measured using $-T(s)$, where

$$T(s) = \frac{\bar{L}(s) + \bar{L}(s)\Gamma(s)}{1 + \bar{L}(s) + \bar{L}(s)\Gamma(s)} = \frac{\bar{T}(s)(1 - (Q(s) - R(s))\mathrm{e}^{-\tilde{\tau}_p s})}{1 - (Q(s) - \bar{T}(s)R(s))\mathrm{e}^{-\tilde{\tau}_p s}} \, .$$

As in the example for the modified PI control law, a noise spectral density of

$$\sqrt{S_{n_w}(j\omega)} \approx 7.9 \text{ pm}/\sqrt{\text{Hz}} \, ,$$

is assumed. The RMS value of the noise response for $-T(s)$ is then

$$\sigma_w = \sqrt{S_{n_w}} \cdot \| - T(s)\|_2 \, .$$

This value depends on the time-delay value $\tilde{\tau}_p$, but upper and lower bounds for the amplitude response that are independent of the time-delay value can be found as

$$\frac{\big|1 - |Q(j\omega) - R(j\omega)|\,\big|}{1 + \big|Q(j\omega) - \bar{T}(j\omega)R(j\omega)\big|} \leq |T(j\omega)| \leq \frac{1 + |Q(j\omega) - R(j\omega)|}{\big|1 - \big|Q(j\omega) - \bar{T}(j\omega)R(j\omega)\big|\,\big|} \, .$$

An example of the power spectral density for $-T(s)$ is shown in Fig. 4.14, using $\tilde{\tau}_p = 1$, together with the upper and lower bound, and the power spectral density for $-\bar{T}(s)$.

The RMS value of the noise response for the power spectral density in Fig. 4.14 for $-T(s)$ can be computed to be $\sigma_w = 0.48$ nm, by numerically integrating the area under the curve and taking the square root. This means that the noise contribution is larger when adding the RC scheme, compared to when using the modified PI control law alone.

Numerically integrating the area under the bounds and taking the square root, yields 1.5 nm for the upper bound and 0.098 nm for the lower bound. The bounds are therefore not very tight.

Assuming that $R(s) = \bar{T}^{-1}(s)Q(s)$, the complementary sensitivity function is

$$T(s) = \bar{T}(s) + Q(s)\bar{S}(s)\mathrm{e}^{-\tilde{\tau}_p s} \, ,$$

and a bound for the $\mathcal{H}_2$-norm can be found as

$$\|-T(s)\|_2 = \|T(s)\|_2 \leq \|\bar{T}(s)\|_2 + \|Q(s)\bar{S}(s)\|_2 \, .$$

Another approximate estimate can therefore be found computing

$$\sqrt{S_{n_w}} \cdot \big(\|\bar{T}(s)\|_2 + \|Q(s)\bar{S}(s)\|_2\big) \, ,$$

which yields $\sigma_w = 0.90$ nm in this case.

If the bandwidth of $Q(s)$ is significantly larger than $\bar{T}(s)$, and if $|\bar{T}(j\omega)| + |\bar{S}(j\omega)| \approx 1$, the spectral density can be seen to be dominated by the filter $Q(s)$. Thus, yet another approximation for the noise contribution be found computing

$$\sqrt{S_{n_w}} \cdot \|Q(s)\|_2 \, ,$$

which yields $\sigma_w = 0.50$ nm in this case.

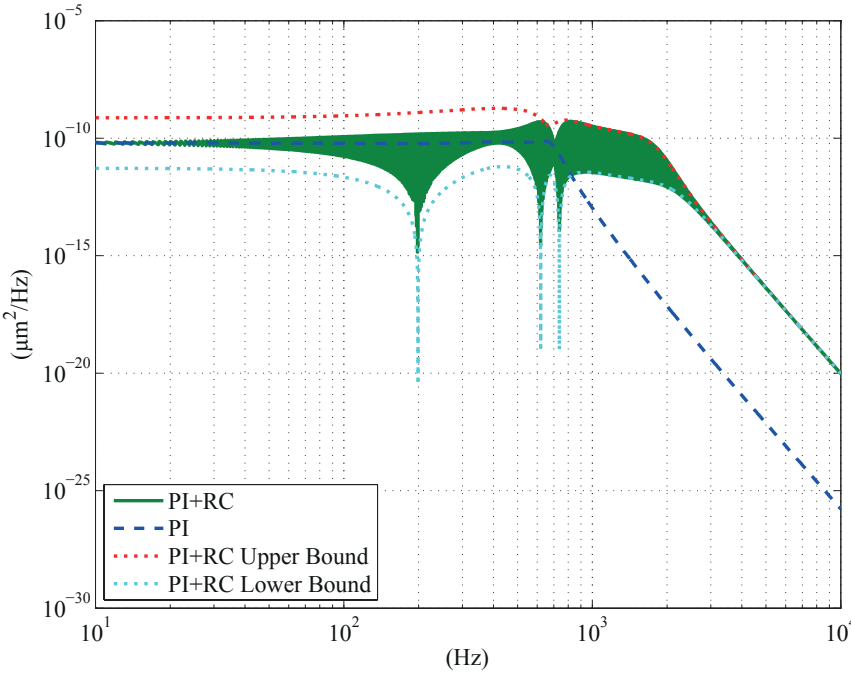

Figure 4.14: Power spectral densities for $-\bar{T}(s)$ and $-T(s)$, with upper and lower bounds.

Summary of the Tuning Procedure

The tuning procedure can be summarized to the following steps:

1. Identify the parameters of the model (4.3) for the dominant vibration mode in the system.
2. Construct the uncertainty weight $\delta_w(s)$ in (4.4).
3. Find the optimal parameters for the anti-aliasing and reconstruction filters and the integral control law by solving (3.15).
4. Verify the stability of the modified PI control law using (4.21). If non-modeled high-frequency dynamics is a problem, anti-aliasing and reconstruction filters with a higher roll-off rate should be used.
5. Compute the uncertainty weight $\hat{\delta}_w(s)$ using (4.13).
6. Choose an appropriate filter $W_T(s)$ with the cut-off frequency ω_T and the DC-gain k_T as tunable parameters, using, *e.g.*, (4.11).
7. Chose an appropriate order and cut-off frequency ω_Q for the unity-gain low-pass filter $Q(s)$. The cut-off frequency must be chosen in order to provide sufficient attenuation of high-frequency dynamics. The filter $R(s) = W_T(s)^{-1}Q(s)$ should be proper.
8. Find the optimal values for ω_T and k_T using (4.22).

9. Verify the stability of the overall control scheme using (4.14). If high-frequency dynamics is a problem, reduce the cut-off frequency ω_Q.

4.5 Experimental Results & Discussion

To validate the performance and robustness of the proposed control scheme, experiments were performed for tracking a modified triangle-wave reference signal, using different fundamental frequencies and amplitudes, as well as tuning parameters for the PI control law and the combined PI and RC control law.

4.5.1 Description of the Experimental System

The experimental set-up consisted of a dSPACE DS1103 hardware-in-the-loop system, a ADE 6810 capacitive gauge and ADE 6501 capacitive probe from ADE Technologies, a Piezodrive PDL200 voltage amplifier, the custom-made long-range serial-kinematic nanopositioner (see Fig. 2.3), two SIM 965 programmable filters and a SIM983 scaling amplifier from Stanford Research Systems. The capacitive measurement has a sensitivity of $k_s = 1/5$ V/μm and the voltage amplifier has a gain of 20 V/V. With the DS1103 board, a sampling time of $T_s = 1 \cdot 10^{-5}$ s ($f_s = 100$ kHz) was used for all the experiments. For numerical integration, a fourth-order Runge-Kutta scheme [62] was used.

The scaling amplifier was used to modify the sensitivity of the capacitive gauge in order to maximize the resolution obtained from the analog-to-digital converter. The sensitivity was set to $k_s = 3.25/5$ V/μm for the largest reference signal amplitude, and $k_s = 6.5/5$ V/μm for the smallest reference signal amplitude. The quiescent noise in the system was measured. The measured time-series and power spectral density (PSD) estimates for the two sensitivity settings are presented in Fig. 4.15 for reference. The noise floor is determined by the performance of the analog-to-digital converter (ADC), and for an ideal ADC the noise spectral density due to quantization is determined as [145, 175]

$$S_q(j\omega) = \frac{1}{f_s}\frac{{\Delta_{qr}}^2}{6}\,, \tag{4.23}$$

where the quantization resolution Δ_{qr} is determined by $\Delta_{qr} = R_{adc}/2^{n_b}$ where R_{adc} is the range and n_b is the word length (number of bits) of the ADC. The hardware-in-the-loop system used has a range of $R_{adc} = 20$ V and a word length of $n_b = 16$ bits. The signal-to-noise ratio is better than 83 dB, which means that, depending on the method used [3, 145, 175], the effective number of bits is between 13 and 15. Assuming the best case scenario of $n_b = 15$ effective bits, the noise floor $S_{nf}(j\omega) = {k_s}^2 S_q(j\omega)$ should be -118 dB/Hz for the sensitivity setting for large signals and -124 dB/Hz for the sensitivity setting for small signals. Considering again Fig. 4.15b, it is reasonable to assume that the noise contribution is dominated by quantization noise above 1 kHz.

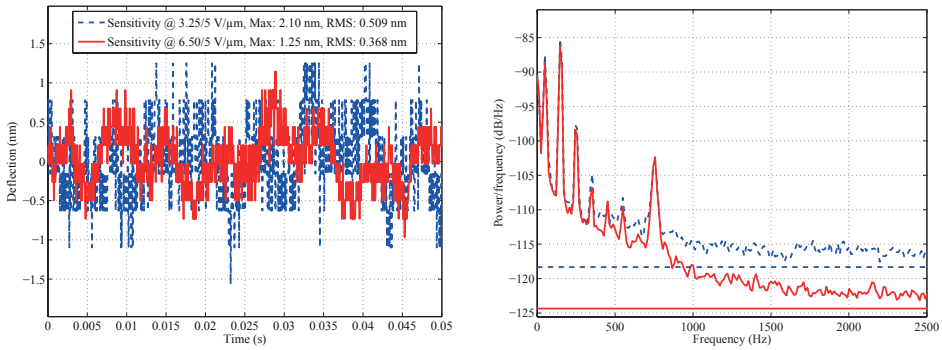

(a) Time-series.

(b) Power spectral density estimate.

Figure 4.15: Measured quiescent noise from displacement sensor filtered by the anti-aliasing filter.

4.5.2 Results

Two results from the experiments are presented in Fig. 4.16 and 4.18. The first result is for scanning at 25 Hz when using a nominal and optimal tuning of the PI control law. As the nominal tuning proposed in Section 4.4.1 turned out the render an unstable control law, it was necessary to reduce the nominal integral gain to $k_i = 525$. Fig. 4.16a displays the steady-state measured deflection signals $y_m = W_a(s)w$, and Fig. 4.16b shows the power spectral density (PSD) estimate of the measured steady-state error signals $\bar{e} = W_a(s)r - y_m$. The second result is when scanning at 200 Hz using the optimally tuned PI control law and the repetitive control law. Fig. 4.18a displays the initial transient response of the measured deflection and error, Fig. 4.18b the steady-state measured deflection and Fig. 4.18d the steady-state measured error. Fig. 4.18c is a PSD estimate of the steady-state error. In Fig. 4.18e the steady-state control input u is shown. A summary of all the experiments performed are presented in Tab. 4.5.

The results of the experiments in Tab. 4.5 are rated using both the maximum error (ME) and the root-mean-square error (RMSE), both in absolute terms with respect to the measured deflection, and relative to the maximum value of the reference signal for ME, and the RMS value of the reference signal for RMSE.

4.5.3 Discussion

Considering Fig. 4.16a and the results for the PI control law in Tab. 4.5, it is immediately apparent that the bandwidth is increased, as the tracking error for the 25 Hz fundamental frequency signal decreases from 80% when using the nominal tuning to 12% when using the optimal tuning. From Fig. 4.16b, it is also evident that damping is introduced, as the prominent peak appearing around 750 Hz[1], due to the mechanical resonance, is reduced by about 40 dB/Hz.

[1]The frequency resolution is low due to windowing of the data prior to computing the power spectral density.

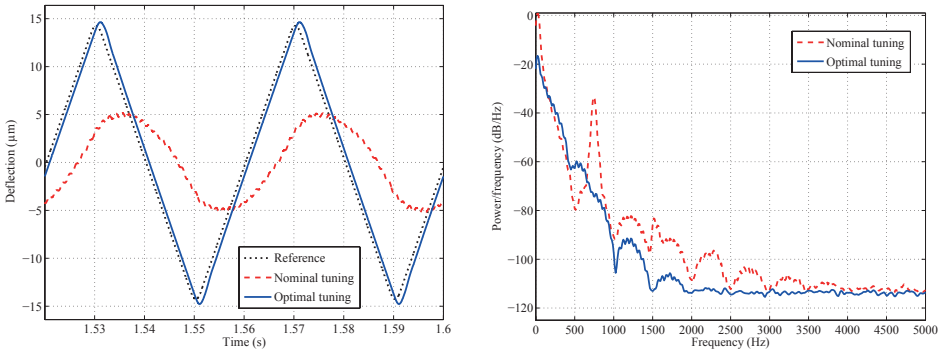

(a) Steady-state measured deflection y_m.

(b) Power spectral density estimate of the error in steady-state.

Figure 4.16: PI control law performance when using nominal and optimal tuning. Reference at 25 Hz with 14.25 μm amplitude (27 μm linear range).

With regards to the RC performance, as can be seen from Tab. 4.5, the closed-loop error using references with low fundamental frequency yields errors close to the measurement noise. The performance depends both on the gain k_T and the bandwidth of the filter $Q(s)$. The error decreases when increasing the bandwidth for $Q(s)$, as the pole locations in the filtered signal model will correspond better to the pole locations in the ideal signal model.

Since the filtered signal model does not correspond perfectly to the reference signal, the gain k_T influences the tracking performance. A higher value for k_T will decrease the error for reference signals with high fundamental frequencies, but not for low fundamental frequencies, where a larger gain results in amplification of measurement noise. Some of the error at low fundamental frequencies is due to the quantization noise, as the quantization noise floor is reached within the bandwidth of the RC. The gain k_T also influences the time-constant for the transient response envelope, that is, larger k_T results in faster convergence to steady state. As the fundamental frequency increases, the error increases, as would be expected, since the bandwidth of the RC scheme is mostly determined by the filter $Q(s)$. The choice of k_T will therefore mostly encapsulate the trade-off between noise performance, tracking performance, and convergence rate, whereas the bandwidth of $Q(s)$ should be chosen as large as possible while still ensuring stability in closed-loop.

Inspecting Fig. 4.18a, the transient response and convergence to steady state is clearly visible. There is some saturation in the deflection measurement, suggesting that the scheme has some robustness towards the saturation non-linearitites in the system. From Fig. 4.18d it can be seen that the maximum error occurs at the maxima and minima of the reference signal, thus, increasing the linear proportion of the reference signal will also increase the maximum error, which is to be expected. The PSD estimate for the error signal in Fig. 4.18c has very prominent peaks at odd harmonics of the fundamental frequency up to the bandwidth of the RC. In this case, most of the error is therefore due to the limited bandwidth of the control

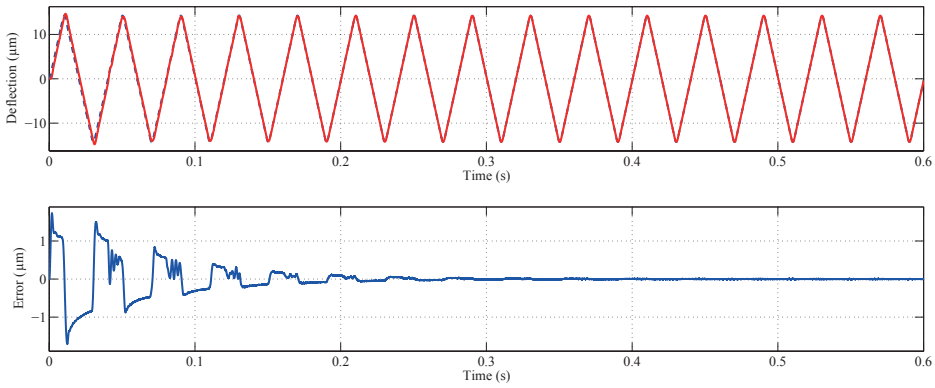

(a) Initial transient measured deflection y_m and measured error ε.

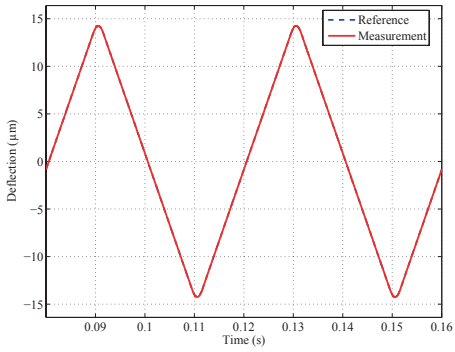

(b) Steady-state measured deflection y_m.

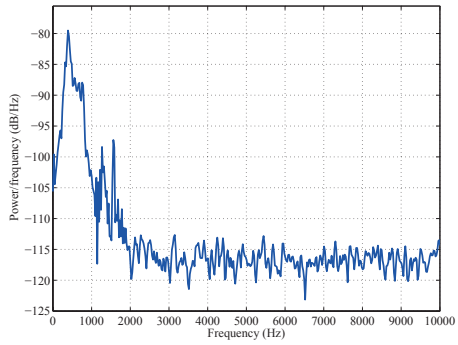

(c) Power spectral density estimate of the error in steady-state.

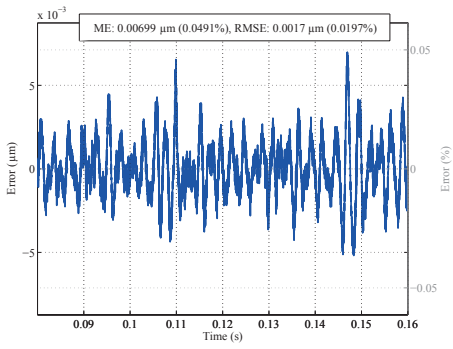

(d) Steady-state measured error ε.

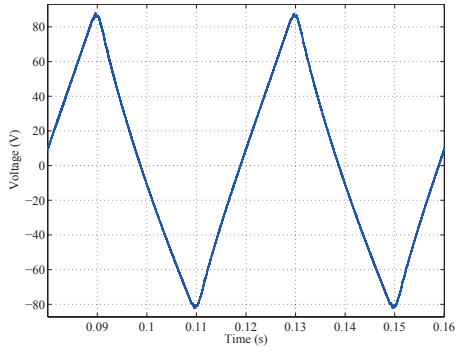

(e) Steady-state input voltage u.

Figure 4.17: Reference at 25 Hz with 14.25 μm amplitude (27 μm linear range).

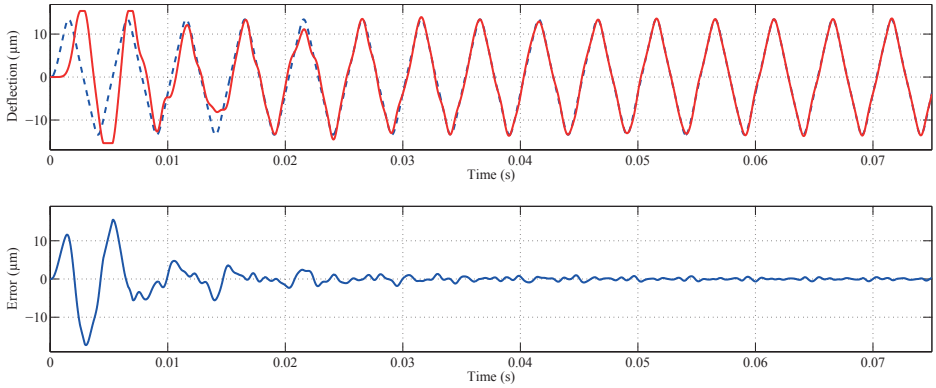

(a) Initial transient measured deflection y_m and measured error ε.

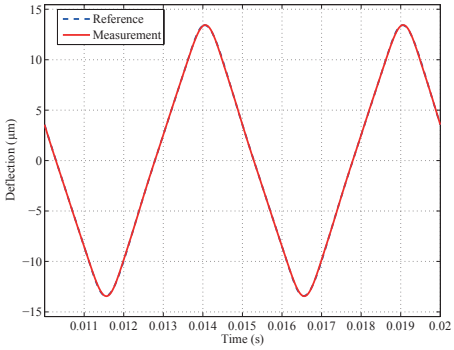

(b) Steady-state measured deflection y_m.

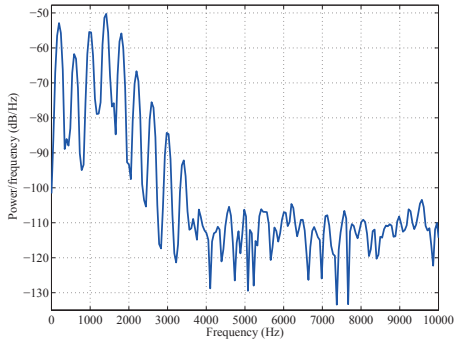

(c) Power spectral density estimate of the error in steady-state.

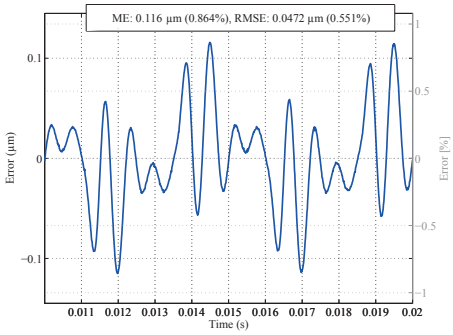

(d) Steady-state measured error ε.

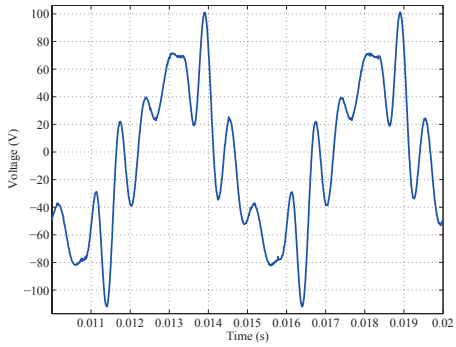

(e) Steady-state input voltage u.

Figure 4.18: Reference at 200 Hz with 14.25 μm amplitude (27 μm linear range).

Table 4.5: Norms of the measured error ε in steady-state, using various configurations and reference signals. f_p and 2λ denotes the fundamental frequency and linear range, respectively, of the reference signal. Entries marked with "†" are obtained using a tuning that violates the robust stability criterion (4.14).

f_p (Hz)	2λ (μm)	k_T	f_Q (kHz)	ME abs. (μm)	ME rel. (%)	RMSE abs. (μm)	RMSE rel. (%)
When using nominally tuned PI control law							
25	27.0	–	–	11	80	7.1	83
When using optimally tuned PI control law							
25	27.0	–	–	1.7	12	1.0	12
200	27.0	–	–	16	120	9.8	110
When using PI control law and repetitive control law							
25	13.5	0.450	2	0.0034	0.048	0.00067	0.016
25	13.5	0.100	3†	0.0023	0.032	0.00053	0.012
25	13.5	0.275	3†	0.0036	0.050	0.00091	0.021
25	27.0	0.350	2	0.0048	0.033	0.0011	0.013
25	27.0	0.450	2	0.0072	0.050	0.0017	0.020
50	27.0	0.450	2	0.011	0.077	0.0028	0.032
100	27.0	0.450	2	0.031	0.22	0.010	0.12
200	13.5	0.450	2	0.61	0.91	0.025	0.59
200	13.5	0.275	3†	0.030	0.44	0.012	0.27
200	27.0	0.450	2	0.12	0.86	0.047	0.55
400	13.5	0.450	2	0.12	1.9	0.064	1.6

law. The voltage range of the signal in Fig. 4.18e should also be noted. In this case the full range of the amplifier, ± 110 V is used, and it provides a hard limit with regards to the spectral content and the range of the reference signal, as well as the bandwidth of the control law. Increasing either one of these properties in this case, would have resulted in saturation in the amplifier.

4.6 Conclusions

It has been demonstrated through experiments that by using a damping proportional-integral control law and a well configured plug-in repetitive control scheme, it is possible to achieve a maximum error of less than 1% relative to the reference signal, at reference signal frequencies exceeding 25% of the dominant resonant frequency of a nanopositioning stage. The methods used are straight forward to implement and tune, and the overall control scheme is applicable for tracking control on flexible smart structures in general. Additionally, the control scheme is computationally

light, and is therefore well suited for implementation on both microcontrollers and field-programmable-arrays. It should also be implementable using analog components and a bucket-brigade device, which could be beneficial with regards to quantization noise, which is the dominant source of noise in the system. The proposed scheme can also be implementable on existing hardware configurations for nanopositioning, as it requires very small, or no, modifications to a standard configuration.

Part III

Adaptive Control

Chapter 5

Online Parameter Identification

5.1 Introduction

When applying damping control, or damping and tracking control, to highly resonant flexible structures, it is possible to find optimal control law parameters that will maximize the introduced damping, as was demonstrated in Chapter 3. Finding the optimal control law parameters requires knowledge of the dynamics of the flexible structure at hand. The approach in Chapter 3 was to use an accurate description of the dynamics obtained from frequency response data, and the optimal control law parameters was found using an optimization scheme incorporating these data. This would also be the typical approach taken when using $\mathcal{H}_\infty$-synthesis.

In some applications, system parameters can be expected to change during operation. As discussed in Section 1.2.1 and Chapter 2, parameter uncertainty in nanopositioning devices is experienced in the effective gain for the piezoelectric actuator and the resonant frequencies. The effective gain is influenced by the presence of hysteresis, actuator temperature and age, as well as payload mass. The main cause of change in resonant frequencies is due to variable payload mass. In scanning probe microscopy applications, the most severe example of this is when the sample must be contained in, *e.g.*, liquid cells with heating elements [85].

Due to changing system model parameters, feed-forward and feedback control law parameters should be adjusted accordingly to maintain optimal performance. An example of the reduction in performance that can occur if the system model parameters does not correspond to the actual system was discussed in Section 2.4, where a set of hysteresis model parameters were applied under different conditions than what they where found for, resulting in poor reference trajectory tracking.

It is apparent that control schemes for such devices can benefit from some form of online adaptation or learning to maintain optimal performance, or even stability, during operation.

For periodic reference trajectories, this has been studied on the form of iterative learning control (see Sections 1.3 and 4.1). Here, the method often relies on batch processing of measurement data, as the implementation of iterative learning control methods can be very computationally demanding, but can provide practically perfect reference tracking. Feedback in the form of repetitive control, as discussed

in Chapter 4, also provides a method which is asymptotically invariant to plant uncertainties for periodic exogenous signals.

Standard online parameter identification techniques [111, 204], however, does not seem to have been studied extensively for experimental systems that can be modeled as mass-spring-damper systems. Such techniques include the gradient method, recursive least-squares method, and the extended Kalman filter. One example applying the extended Kalman filter can be found for a geometric mass-spring system in [90].

Parameter identification with good accuracy is immediately applicable when using feed-forward model inversion [44], and for model reference adaptive control [111], and could contribute to better performance for reference trajectory tracking and disturbance rejection for arbitrary signals.

5.1.1 Contributions

Two common schemes for online parameter identification are compared experimentally in order to assess their ability to learn the parameters for a simple second-order linear model (a mass-spring-damper model) of the vibration dynamics in a nanopositioning device in open-loop. The schemes investigated are the recursive least-squares method (RLS) and two different versions of the extended Kalman filter (EKF); continuous EKF and hybrid EKF.

The main contribution is the specific choice of pre-filters for the various signals involved in the identification method. It is demonstrated using measured time-series data acquired when operating a standard experimental set-up, that these filters have to be present in order to obtain reasonable parameter convergence.

5.1.2 Outline

The Chapter is organized as follows. The system is described in Section 5.2, including the plant model, the signal chain, and how to select the pre-filters needed to obtain parameter estimate convergence. This is followed by a description of how to apply the RLS and EKF methods to the plant model in Section 5.3. The experiments are described in Section 5.4, as well as implementation specific details, such as choice of initial values and various tunable parameters. The results from the experiments are presented in Section 5.5, followed by a discussion in Section 5.6.

5.2 System Description & Modeling

5.2.1 Mechanical Model

As has been discussed in previous Chapters, the dynamics of the flexible structure of a nanopositioning device is often adequately described by a lumped parameter, truncated linear model. The positioning stage used in the experiments is shown in Fig. 2.3. This is a well-designed positioning stage which has one dominant vibration mode with a mode shape that generates a piston-like motion. The governing differential equation for the displacement w (m) of a point on the structure is

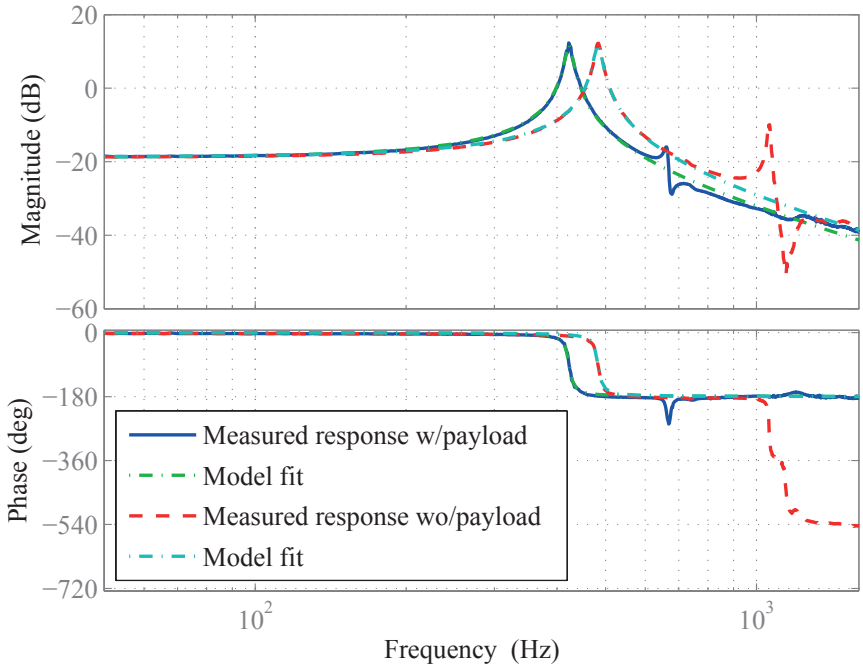

Figure 5.1: Measured frequency response for one axis of the nanopositioning stage, and the corresponding response using the model (5.2) with parameter values from Tab. 5.1, with and without payload attached to the sample platform.

therefore

$$m\ddot{w} + d\dot{w} + kw = f_a \ ,$$

where m (kg) is the mass of the moving sample platform, d (N s m^{-1}) is the damping coefficient, k (N m^{-1}) is the spring constant, and f_a (N) is the force developed by the actuator. The applied force f_a (N) is accurately described using the expression

$$f_a = e_a(u_a + d_u) \ ,$$

where e_a (N V^{-1}) is the effective gain of the piezoelectric actuator, u_a (V) is the applied voltage, and d_u (V) is the disturbance generated by hysteresis and creep. The transfer-function from applied voltage to displacement is

$$G_w(s) = \frac{w}{u_a}(s) = \frac{\beta_0}{s^2 + 2\zeta\omega_0 s + {\omega_0}^2} = \frac{b_0}{s^2 + a_1 s + a_0} \ , \tag{5.1}$$

and denoting $x_1 = w$, the state-space formulation for the system is given as

$$\begin{aligned} \dot{x}_1 &= x_2 \\ \dot{x}_2 &= -a_0 x_1 - a_1 x_2 + b_0 u, \end{aligned} \tag{5.2}$$

where $\beta_0 = b_0 = e_a/m$ (m s^{-2} V^{-1}), $a_0 = k/m$ (s^{-2}), $a_1 = d/m$ (s^{-1}), $\zeta = c/2\sqrt{mk}$, and $\omega_0 = 2\pi f_0 = \sqrt{k/m}$ (s^{-1}).

Table 5.1: Identified parameters for the model (5.2), for two payload configurations, using frequency response data.

Parameter	Value	Unit	Parameter	Value	Unit
1) With payload on sample platform					
b_0	$0.808{\cdot}10^6$	$\mu\text{m/s}^2\text{V}$	b_0/a_0	0.114	μm/V
a_0	$7.06{\cdot}10^6$	$1/\text{s}^2$	f_0	423	Hz
a_1	77.6	1/s	ζ	0.0146	
2) Without payload on sample platform					
b_0	$1.07{\cdot}10^6$	$\mu\text{m/s}^2\text{V}$	b_0/a_0	0.116	μm/V
a_0	$9.21{\cdot}10^6$	$1/\text{s}^2$	f_0	483	Hz
a_1	86.8	1/s	ζ	0.0143	

The frequency response for y-axis of the positioner was recorded, with and without a payload of approximately 24.75 g attached to the sample platform, using bandwidth-limited white noise excitation. The physical implementation of the two payload configurations is shown in Fig. 5.2. The two responses are displayed in Fig. 5.1. The model (5.2) was fitted to the frequency response data using the MATLAB System Identification Toolbox, and the resulting parameter values are presented in Tab. 5.1. The response of the model (5.2) using these parameters are also displayed in Fig. 5.1.

As can be seen, the actual response of the first vibration mode is well approximated by the model. There are higher order modes in the system, and the second vibration mode is clearly visible in Fig. 5.1. The higher order modes have fairly negligible magnitude responses in comparison to the first, thus a second-order model should be sufficient to describe the dominant dynamics of the system. The measured phase response in Fig. 5.1 is not only in the range between -180° and 0°, indicating that the sensor is not perfectly co-located with the actuator.

5.2.2 Signal Chain

The complete system used in the experiments consisted of the nanopositioning stage, a reconstruction filter, an anti-aliasing filter, an amplifier, and a displacement sensor, as well as a standard hardware-in-the-loop (HIL) system. The signal chain is shown schematically in Fig. 5.3.

The sampling frequency used was 10 kHz. The anti-aliasing and reconstruction filters, $W_a(s)$ and $W_r(s)$ were configured as second-order low-pass Butterworth filters with conservative cut-off frequencies at 1 kHz. The amplifier, given the capacitive load of the piezoelectric actuator, provided a bandwidth of approximately 10 kHz, and the displacement sensor was configured with a bandwidth of 100 kHz. The dynamic response of both the amplifier and the capacitive probe can accurately be described using a first-order low-pass filter.

As the reconstruction and anti-aliasing filters noticeably impact the observed dynamics, these were taken into account when generating the input signal fed to

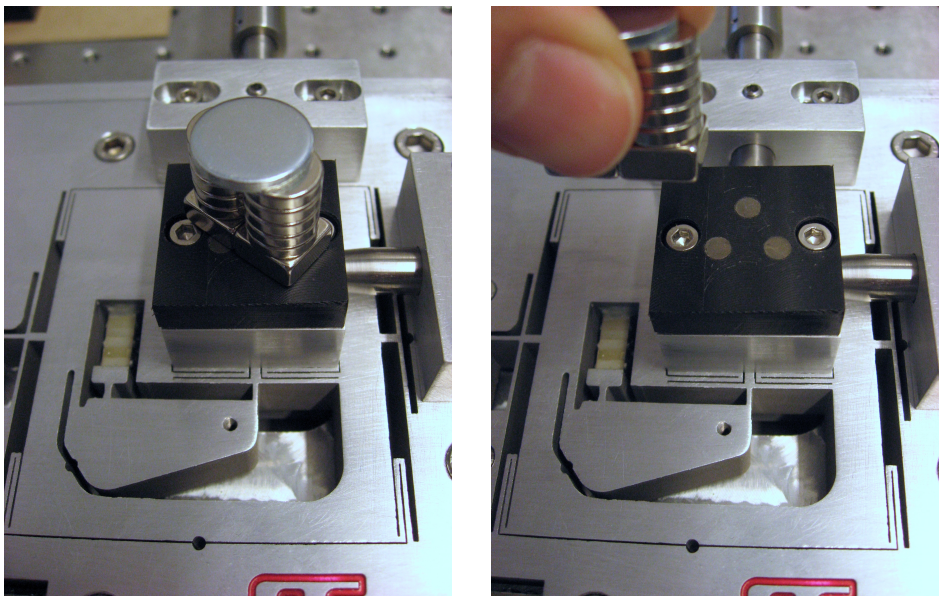

(a) With payload attached. (b) Without payload attached.

Figure 5.2: Payload configurations.

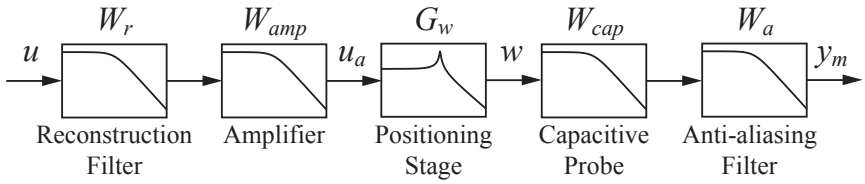

Figure 5.3: Signal chain for the overall system.

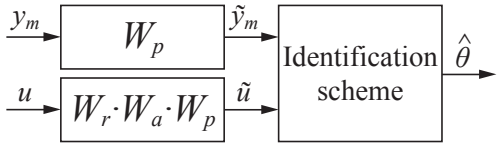

Figure 5.4: Signals fed to identification schemes.

the identification schemes, as shown in Fig. 5.4. This ensured that the input signal $\tilde{u}$ would match the change in gain and phase introduced by these filters in the measured signal $\tilde{y}_m$. The effects of the amplifier and the displacement sensor were neglected, as it would be impossible to implement replicas of these filters digitally with the chosen sampling frequency.

To improve the results obtained from the parameter identification schemes, a

pre-filter, $W_p(s)$, was used. This was chosen with consideration to the sensitivity functions for the parameters of the model. For a transfer-function, *i.e.*, $G_w(s)$, the Bode sensitivity function with respect to some parameter θ, is defined as

$$S_\theta^{G_w(s)} \triangleq \frac{\partial G_w(s)/G_w(s)}{\partial\theta/\theta} = \frac{\theta_0}{G_w(s)_0}\frac{\partial G_w(s)}{\partial\theta}\bigg|_{\text{NOP}},$$

using a nominal operating point (NOP) for all the parameters in the transfer-function [119].

The sensitivity functions for the parameters b_0, a_0, and a_1 in the system model (5.2), using the parameters found for the system with payload as the NOP, are displayed in Fig. 5.5. Most notably, the parameter related to damping, a_1, has very little impact on the observed output at low and high frequencies. For parameter identification it is considered good practice to concentrate signal power in the frequency domains that contain peaks in the sensitivity functions. This is done in order to maximize the information content of the signals used, *i.e.*, some norm on the Fisher information matrix [144].

The pre-filter was chosen to be a band-pass filter, using a first-order high-pass filter with a lower cut-off frequency of $f_{lc} = 100$ Hz, and a resonant second-order low-pass filter, with a natural frequency of

$$f_c = 450 \approx \frac{483 + 423}{2}\,\text{Hz},$$

and a damping ratio of $\zeta = 0.1$, thus amplifying the frequency content close to the resonant peaks of the two configurations (with and without payload):

$$W_p(s) = \frac{s}{s + 2\pi f_{lc}}\frac{(2\pi f_c)^2}{s^2 + 2\zeta\pi f_c s + (2\pi f_c)^2} \tag{5.3}$$

When applying the RLS method, numerical first and second derivatives of the displacement signal are needed. In order to generate proper transfer-functions for filtering the displacement signal, the low-pass filter should be at least second-order. To keep the order of the pre-filter at a minimum, the high-pass filter was chosen to be first-order, and the low-pass filter second-order.

5.3 Identification Schemes

5.3.1 Application of the Recursive Least-Squares Method

The recursive least-squares (RLS) method summarized in Section D.1. Here the specific application of the method to the system model (5.1) is described.

The model (5.1) can be put on the form

$$\ddot{w} + a_1\dot{w} + a_0 = b_0 u_a \quad \Rightarrow \quad z = \theta^{\mathrm{T}}\varphi$$

where a parameter vector θ can be found as

$$\theta = [b_0,\ a_1,\ a_0]^{\mathrm{T}},$$

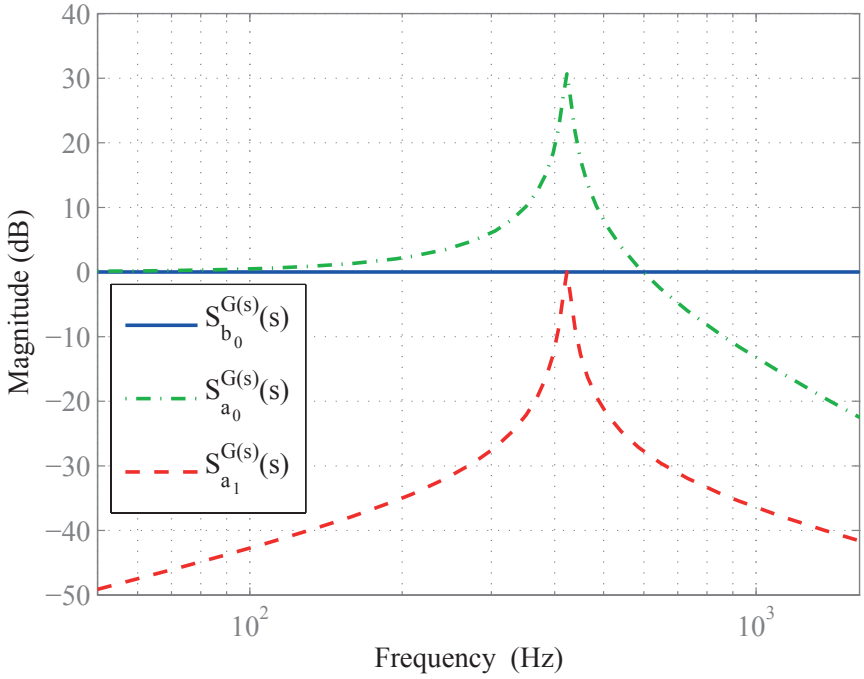

Figure 5.5: Sensitivity functions for the parameters b_0, a_0, and a_1, using data from Tab. 5.1.

which yields a regressor vector φ as

$$\varphi = [u_a,\ -\dot{w},\ -w]^{\mathrm{T}} \ ,$$

and the output z of the model as

$$z = \ddot{w} \ .$$

To avoid pure numerical differentiation, the output z and regressor vector φ should be generated using proper filters. Also, taking into consideration the signal chain in Fig. 5.3 as is done in Fig. 5.4, the output and regressor is generated using

$$z = s^2 W_p(s) y_m$$

and

$$\varphi = [W_r(s)W_a(s)W_p(s)u,\ -sW_p(s)y_m,\ -W_p(s)y_m]^{\mathrm{T}} \ .$$

Since the pre-filter (5.3) has relative degree $n^\star = 2$, the resulting filters in the expression above are at least bi-proper.

5.3.2 Application of the Extended Kalman Filter

Two versions of the extended Kalman filter (EKF) were implemented, the continuous time version which is described in Section D.3.1, and the hybrid (combined continuous and discrete time) version which is described in Section D.3.2.

Applying the EKF to the model (5.2), the state vector $x = [x_1,\ x_2]^{\mathrm{T}}$ is augmented to also include the parameter vector $\theta = [b_0,\ a_0,\ a_1]^{\mathrm{T}}$. The augmented state vector χ is therefore

$$\chi = \begin{bmatrix} x \\ \theta \end{bmatrix} = \begin{bmatrix} x_1 & x_2 & a_0 & a_1 & b_0 \end{bmatrix}^{\mathrm{T}} .$$

The state and input matrix can be parameterized as

$$A(\theta) = \begin{bmatrix} 0 & 1 \\ -a_0 & -a_1 \end{bmatrix} , \quad B(\theta) = \begin{bmatrix} 0 \\ b_0 \end{bmatrix} ,$$

which yields the output matrix

$$C(\theta) = \begin{bmatrix} 1 & 0 \end{bmatrix} .$$

The Jacobians required to compute the error covariance matrix P and Kalman gain K can be found to be

$$F(x, \theta, u) = \begin{bmatrix} 0 & 1 & 0 & 0 & 0 \\ -a_0 & -a_1 & -x_1 & -x_2 & u \\ 0 & 0 & 0 & 0 & 0 \\ 0 & 0 & 0 & 0 & 0 \\ 0 & 0 & 0 & 0 & 0 \end{bmatrix} ,$$

and

$$H(x, \theta) = \begin{bmatrix} 1 & 0 & 0 & 0 & 0 \end{bmatrix} .$$

The above expressions are used both in the continuous and the hybrid version of the extended Kalman filter. The signals fed to the filters were generated as illustrated Fig. 5.4, *i.e.*, the measurement y and the input u used in the expressions in Section D.3 were taken to be $y = \tilde{y}_m$ and $u = \tilde{u}$.

5.3.3 Parameter Convergence

The RLS method will theoretically converge to the correct parameter values when using a sufficiently rich input signal (which results in a PE regressor vector) [111, 144]. For the EKF there does not exist any general proof of convergence. The EKF can provide good performance, but the convergence properties for the estimates are susceptible to the choice of initial values and covariance tuning, as well as the input signal [33, 91, 143, 180]. *For this particular system, neither method provided good overall performance without careful pre-filtering of the signals used.*

5.4 Experiments

5.4.1 Instrumentation

The experiment set-up consisted of the long-range serial-kinematic nanopositioning stage from EasyLab shown in Fig. 2.3, already described in Sections 2.2.2 and

4.2.1, as well as a Piezodrive PDL200 linear voltage amplifier (20 V/V), an ADE 6810 capacitive gauge and ADE 6501 capacitive probe from ADE Technologies to measure displacement (5 μm/V), and two SIM 965 programmable filters from Stanford Research Systems, used as anti-aliasing and reconstruction filters. The actuation signal and measured response were generated and recorded using a dSPACE DS1103 hardware-in-the-loop board, at a sampling frequency of $f_s = 10$ kHz.

The capacitance of the piezoelectric actuator was measured to be $C_p \approx 700$ nF; thus the amplifier would, according to the specifications, provide a first-order low-pass filter dynamic response with a cut-off frequency of 10 kHz. The specifications for the capacitive gauge and probe state that the response should be like a first-order low-pass filter with a cut-off frequency of 100 kHz. The programmable filters were both configured as second-order Butterworth filters with cut-off frequencies at 1 kHz. This provided sufficient bandwidth to capture the dynamic response of the positioner, as the dominant resonant frequency for this system occurs at less than 500 Hz.

5.4.2 Performed Experiments

Two experiments were performed. One used a pseudo random binary signal (PRBS) [144] as the input to the system, and one used a more typical signal for this particular kind of device: a smoothed triangle-wave. The PRBS was generated to provide frequency content in the band from 0 to 1 kHz. The triangle-wave signal had a fundamental frequency of 10 Hz. Both signals had an amplitude of 1 V.

The PRBS yielded a high level of excitation, and thus provided an ideal response with regards to parameter identification. The triangle-wave signal, on the other hand, yielded a low excitation of the dynamics of the system, and therefore provided a much more challenging task for the parameter identification schemes.

Both experiments were performed by first attaching the payload, a small block of steel weighing 24.75 g, to a magnet fixed to the sample platform. Measurements of the displacement were then recorded for approximately 100 seconds with the payload attached, before the payload was removed (while the system was running), and approximately 100 seconds more was recorded with the payload detached.

5.4.3 Implementation & Tuning

For all methods the fourth-order Runge-Kutta scheme [62] was used for numerical integration of the continuous-time differential equations. All methods were initialized with the initial parameter estimates:

$$\theta_0 = [b_0,\ a_1,\ a_0]_0^{\mathrm{T}} = \left[5 \cdot 10^5,\ 7 \cdot 10^1,\ 6 \cdot 10^6\right]^{\mathrm{T}}$$

For the EKFs, the initial state estimates were set to zero, *i.e.*, $\hat{x}_1(0) = \hat{x}_2(0) = 0$. Note that in the implementation, $\theta = [b_0,\ a_1,\ a_0]^{\mathrm{T}}$ for RLS, and $\theta = [a_0,\ a_1,\ b_0]^{\mathrm{T}}$ for EKF.

RLS

The applied RLS method provides two tuning parameters, the forgetting factor κ_f, and the initial covariance matrix $P(0)$. The initial covariance matrix will only affect the initial transient of the parameter estimates, thus, convergence rate is mostly determined by κ_f. It was found that the maximal forgetting factor that did not make the norm of the covariance matrix P grow excessively large was about $\kappa_f = 0.25$. The initial covariance matrix was set to

$$P(0) = \text{diag}\left(\left[1 \cdot 10^6,\ 1 \cdot 10^{-1},\ 1 \cdot 10^7\right]\right) ,$$

which provided a fairly fast initial convergence rate. The choice was motived by the results in Fig. 5.5; a large variance is expected for b_0, and an even larger for a_0, whereas a small variance is expected for a_1.

Continuous EKF & Hybrid EKF

The EKFs required tuning of the covariance parameters R, R_d, and Q, and the initial error covariance matrix $P(0)$. The measurement noise variance was found to be $\sigma_y^2 \approx 1.6 \cdot 10^{-6}$ μm^2, thus $R_d = \sigma_y^2$ for the hybrid EKF, and $R = R_d T_s$ for the continuous EKF, where $T_s = 1/f_s$ is the sampling period The process noise spectral density matrix Q was tuned for each dataset, opting to find a balance between fast convergence and small transients.

Good results when applying triangle-wave excitation were obtained when using:

$$Q_1 = \text{diag}\left(\left[1 \cdot 10^{-12},\ 1 \cdot 10^{-6},\ 6 \cdot 10^8,\ 5 \cdot 10^{-2},\ 1 \cdot 10^6\right]\right)$$

When using PRBS excitation, the variances in the parameter estimates were very large when using the above tuning. Reducing the spectral densities for the parameters improved the results, and good results for the dataset was obtained using:

$$Q_2 = \text{diag}\left(\left[1 \cdot 10^{-12},\ 1 \cdot 10^{-6},\ 2 \cdot 10^5,\ 2 \cdot 10^{-4},\ 2 \cdot 10^3\right]\right)$$

The initial error covariance matrix was in all cases set to:

$$P(0) = 10 \cdot Q_i$$

In the hybrid EKF, the continuous part was run at a faster rate than the sampling frequency. For both datasets we found that a step length of $T_s/4$ produced good results (yielding a rate of 40 kHz).

5.5 Results

5.5.1 Parameter Estimates

The parameter estimates when using triangle-wave signal excitation are presented in Fig. 5.6, and the parameter estimates when using PRBS excitation are shown in Fig. 5.7.

To obtain some form of validation of the parameter estimates, the following procedure was used: the mean value of each parameter estimate time-series was

Table 5.2: RMSE of simulated vs. measured responses in nm. Measurement noise is approximately 1.26 nm RMS.

	EKF	RLS	HEKF	Tab. 5.1
With payload on sample platform				
PRBS	20.2	70.8	70.0	96.9
Triangle-wave	1.67	1.66	1.65	1.92
Without payload on sample platform				
PRBS	29.7	83.1	68.5	31.7
Triangle-wave	1.70	1.72	1.70	2.44

computed for $\Delta t_1 \in (75, 100)$ s and $\Delta t_2 \in (175, 200)$ s. Using these values, the response of the model (5.2) was computed for Δt_1 and Δt_2, using the input signal and mass configuration for which the parameter values were found. The simulated responses were then compared to the measured responses. Tab. 5.2 summarizes the resulting root-mean-square-errors (RMSE). The RMSE when using the values in Tab. 5.1 are also shown.

5.6 Discussion

The RLS method, the continuous EKF, and the hybrid EKF all perform well for parameter identification on this system when applying the pre-filter $W_p(s)$ to the signals used. Judging by the results in Tab. 5.2, the continuous EKF provides the best estimates overall. It is interesting to note that the parameters obtained using frequency response data provided the worst performance, suggesting that the parameters changed in the brief period between recording each dataset, and that the optimal parameter values are dependent on the input signal.

For all the schemes, the first transient is somewhat faster than the second transient. This is likely to be due to the step-like input experienced when the input signal is turned on, which generates a large excitation which might have been beneficial with regards to convergence, and that the elements of the error covariance matrix converges to smaller values after some time, providing less gain in the estimate update equations. When removing the mass, a brief, but fairly large, external disturbance was introduced into the measurements, adding biases to the parameter estimates.

Using PRBS excitation, all schemes converged to reasonable values, even without the pre-filter $W_p(s)$ and careful tuning of process noise spectral densities required by the EKFs. Using the pre-filter and better tuning further improved the results.

Using triangle-wave excitation, none of the schemes converged to reasonable values without using a high-pass filter. When a high-pass pre-filter was employed, all schemes improved significantly. Using the resonant low-pass filter in addition to the high-pass filter, *i.e.*, $W_p(s)$, improved the results, especially the estimates obtained using RLS.

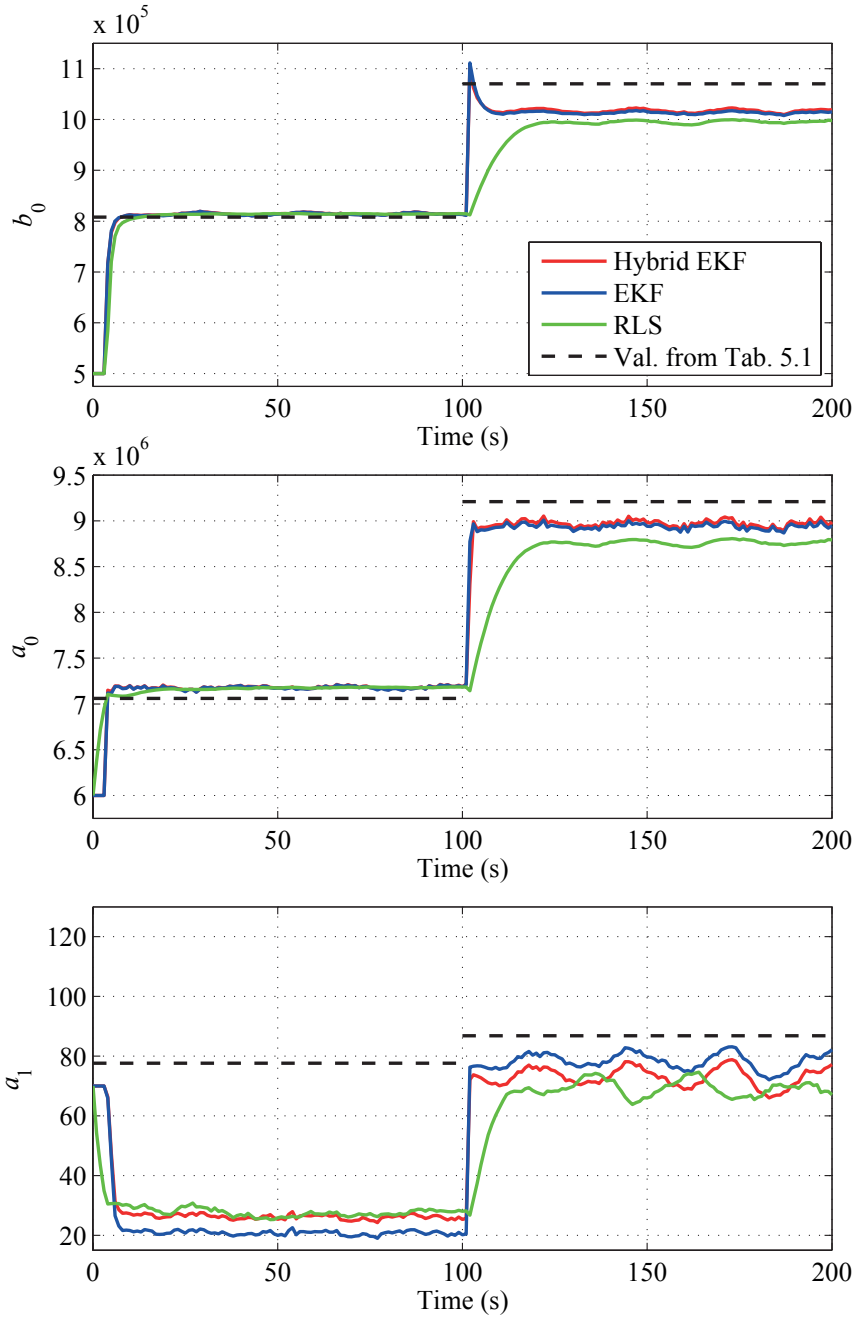

Figure 5.6: Parameter estimates when using triangle-wave excitation. The time-series have been down-sampled to 1 Hz.

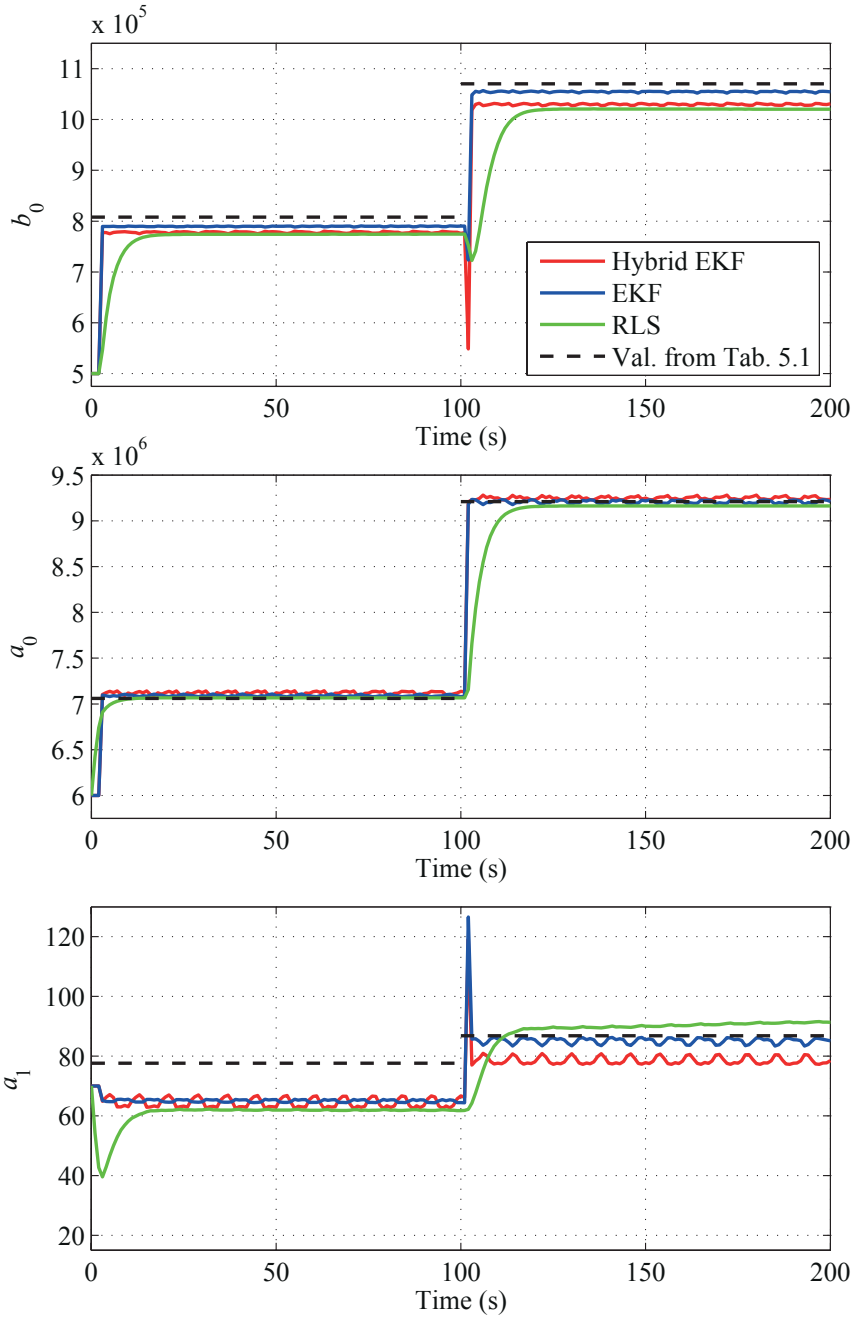

Figure 5.7: Parameter estimates when using PRBS excitation. The time-series have been down-sampled to 1 Hz.

For the EKFs, it was observed that different spectral density settings would lead to different, but small, biases in the parameter estimates. Some settings would also lead to very poor transient behavior, with very large excursions and slow convergence. For some settings, the parameter estimates would diverge and asymptotically approach steady-state values far from the values obtained using RLS and frequency response data; this is in accordance with the results in [143]. Thus, global convergence to one unique solution is not guaranteed when using EKF for parameter identification on this system.

When using PRBS excitation, the variance in the parameter estimates from the EKFs was rather large. Reducing the process noise spectral densities improved this, but reducing them too much led to divergence; the amount of reduction in parameter estimate variance was therefore limited. The RLS method had a much more consistent behavior with regards to parameter estimate variance, as well as transient behavior, when using different excitations.

The EKFs provide a convenient method to trade off between rate of convergence and the variance in the parameter estimates, by tuning the process noise spectral densities. Tuning the forgetting factor in the RLS method did not provide as dramatic effects on convergence rate, and it consistently seemed rather slow with regards to convergence rate. Using a non-normalized regressor increased the parameter convergence rate for RLS, but at the expense of larger transients and weaker properties for the signals in the estimation scheme.

As can be seen from Figs. 5.6 and 5.7, there are noticeable biases in the parameter estimates for each parameter identification scheme, and the biases also appear to depend on the excitation signal. Some bias can be attributed to the configuration of the pre-filter, $W_p(s)$, as well as the tuning of the process noise spectral densities. There is likely some influence from the hysteresis effect in the piezoelectric actuator, though most of this effect should have been removed by the high-pass filter.

The parameter estimates found using each of the EKFs are very similar, but most noticeably they differ in the obtained value for a_0. This difference did not seem to depend on spectral density tuning. The slightly different transient behavior, on the other hand, was tuning dependent. It can be conjectured that with more careful tuning, the transient behavior can be made more similar.

The quality of the estimates produced by the RLS method were highly dependent on the pre-filter, and different filter configurations led to different biases. The RLS method produced noticeably different estimates than the EKFs. Tuning the forgetting factor and the initial covariance matrix only influenced the transient behavior and the variance of the parameter estimates. The mean values obtained asymptotically were the same.

5.7 Conclusions

The RLS method, the continuous EKF, and the hybrid EKF all performed well for parameter identification on this system, when applying a pre-filter to the signals used. The RLS method was particularly sensitive to the configuration of the pre-filter. The RLS method provided slower convergence than the extended Kalman

filters, but it performed in a more consistent manner with regards to the input signal. The extended Kalman filters needed careful tuning to yield good performance and to avoid divergence. It was found that the continuous EKF provided the overall best performance, yielding parameter values that produced the least discrepancy between model response and measured response.

Chapter 6

Robust Adaptive Control

6.1 Introduction

As the dynamic response of typical nanopositioning devices has a fair amount of uncertainty, both inherently and due to the specific application, the control laws used also need to have sufficient robustness. This was taken into account for the damping and tracking control laws in Chapter 3 and the repetitive control scheme in Chapter 4.

Although the dynamic response is uncertain, it is dominantly linear and can be well described for specific operating points. As was demonstrated in Chapter 5, it is possible to obtain good parameter estimates for a linear mass-spring-damper model applied to a nanopositioning device operated in open-loop. Nanopositioning devices should therefore be amenable to model based adaptive control, which in principle can provide higher and more consistent performance than standard robust static control schemes.

Much of the work pertaining to learning or adaptive type of control for nanopositioning has been done for periodic reference and disturbance signals, in the form of iterative learning control, as discussed in Sections 1.3 and 4.1. The repetitive control scheme discussed in Chapter 4 is also asymptotically invariant to plant uncertainty.

For reference trajectory tracking and disturbance rejection of arbitrary signals, however, the signal repetitiveness can not be exploited. Non-repetitive signals can for example occur in manipulation and fabrication tasks based on user interaction, and for vertical topography tracking on irregular sample surfaces.

For adaptive control of linear systems, the model reference adaptive control (MRAC) framework [111] is arguably the most exhaustively researched. As such, it is interesting to assess the performance of MRAC applied to a nanopositioning device. *The main goal in this Chapter is to implement a standard MRAC scheme, and to make the minimum amount of changes to the standard scheme in order for it to work as intended.*

6.1.1 Contributions

The standard indirect model reference adaptive control (MRAC) framework is applied in this Chapter in order to develop a complete adaptive control scheme for a nanopositioning device of common design. The MRAC implementation used in this Chapter is a straight forward extension to the model reference control (MRC) design presented in Section 3.4.7. Extension comes in the form of the implementation of a suitable adaptive law, and the specifics of the implementation of the control law in order to accommodate for time varying parameters.

As was demonstrated in Chapter 5, there are some important considerations to be made with regards to how to obtain parameter convergence for the adaptive law. The most important observation was that a special pre-filter needed in order to obtain parameter convergence. When operating in closed-loop, the choice of pre-filter must be further refined.

A similar type of experiment as in Chapter 5 is conducted, where the payload mass is changed while operating the nanopositioning device. This experiment provides a good indication of the ability the adaptive law has to track changes in model parameters. The resulting control scheme is believed to be a well performing MRAC scheme, although the comparison would be the standard textbook implementation, which does not work at all. The experimental results should therefore be indicative of the performance that can be expected applying MRAC to this particular type of systems.

6.1.2 Outline

The Chapter is organized as follows. In Section 6.2 the system model used in Chapter 5 is reviewed. This forms the basis for the adaptive law. The system model as used in Section 3.4.7 and Chapter 4 is also discussed, as it forms the basis for the control law. Some background and discussion on the model reference adaptive control (MRAC) scheme is presented in Section 6.3. Specific design choices for the control law and the adaptive law are discussed in Section 6.4. Finally, experimental results for the specific implementation of the MRAC scheme are presented and discussed in Section 6.5.

6.2 System Description & Modeling

The experimental system used in this Chapter is almost identical to the system used in Chapter 5. This is a fairly typical device configuration in systems used for motion control in general. As described in Section 5.2, it consists of the positioning mechanism shown in Fig. 2.3, as well as additional necessary instrumentation, including anti-aliasing and reconstruction filters, a voltage amplifier, a capacitive displacement sensor, and a standard hardware-in-the-loop (HIL) system.

As was the case for the model reference control (MRC) scheme in Section 3.4.7, a plant model which includes the dynamics for the nanopositioning stage, as well as the dynamics of the anti-aliasing and reconstruction filters, is used. A more complete model would also include the amplifier and sensor dynamics, and the time-delay incurred by the zero-order-hold (ZOH) elements in the digital-to-analog

Table 6.1: Identified parameters for the model (6.1), using frequency response data.

Parameter	Value	Unit	Parameter	Value	Unit
1) With payload on sample platform					
b_0	$1.97{\cdot}10^6$	$\mu\text{m/s}^2\text{V}$	b_0/a_0	0.109	μm/V
a_0	$18.1{\cdot}10^6$	$1/\text{s}^2$	f_0	677	Hz
a_1	127	1/s	ζ	0.0149	
2) Without payload on sample platform					
b_0	$2.33{\cdot}10^6$	$\mu\text{m/s}^2\text{V}$	b_0/a_0	0.107	μm/V
a_0	$21.9{\cdot}10^6$	$1/\text{s}^2$	f_0	744	Hz
a_1	131	1/s	ζ	0.0140	

converter (DAC) and analog-to-digital converter (ADC). The attainable sampling rate is fast enough for the phase-lag due to the ZOH elements to be insignificant within the bandwidth of the control law, and the amplifier and sensor dynamics is faster than what is possible to represent with a discretized model when using the attainable sampling rate. A higher order model results in a control law of higher order, which also reduces the attainable sampling rate. The main reason for using the highest possible sampling rate is that the noise floor due to the DAC and ADC, given a fixed quantization unit, can only be reduced by increasing the sampling rate, cf. Section 4.5.1. The sampling rate also determines the accuracy and stability of the numerical integration scheme [62].

This plant model is the model which has the highest practically obtainable accuracy for this system. A diagram of the plant model is found in Fig. 3.3.

6.2.1 Mechanical Model

The mechanical model used is as presented in Section 5.2.1, and is also equivalent to the model used in Section 3.4.7. Denoting the deflection w (m), the transfer-function from applied voltage u_a (V) to the displacement for the nanopositioning stage is

$$G_w(s) = \frac{w}{u_a}(s) = \frac{\beta_0}{s^2 + 2\zeta\omega_0 s + {\omega_0}^2} = \frac{b_0}{s^2 + a_1 s + a_0}\,, \tag{6.1}$$

noting that $\beta_0 = b_0$ and $\omega_0 = 2\pi f_0$.

The frequency response is recorded for the x-axis (the y-axis was used in Chapter 5), using bandwidth-limited white noise excitation. As was the case in Chapter 5, the system is operated in two different payload configurations. The payload mass is approximately 15.7 g. The responses are displayed in Fig. 6.1. The model (6.1) is fitted to the frequency response data using the MATLAB System Identification Toolbox, and the resulting parameter values are presented in Tab. 6.1. The response of the model (6.1) using these parameters is also displayed in Fig. 6.1 for comparison.

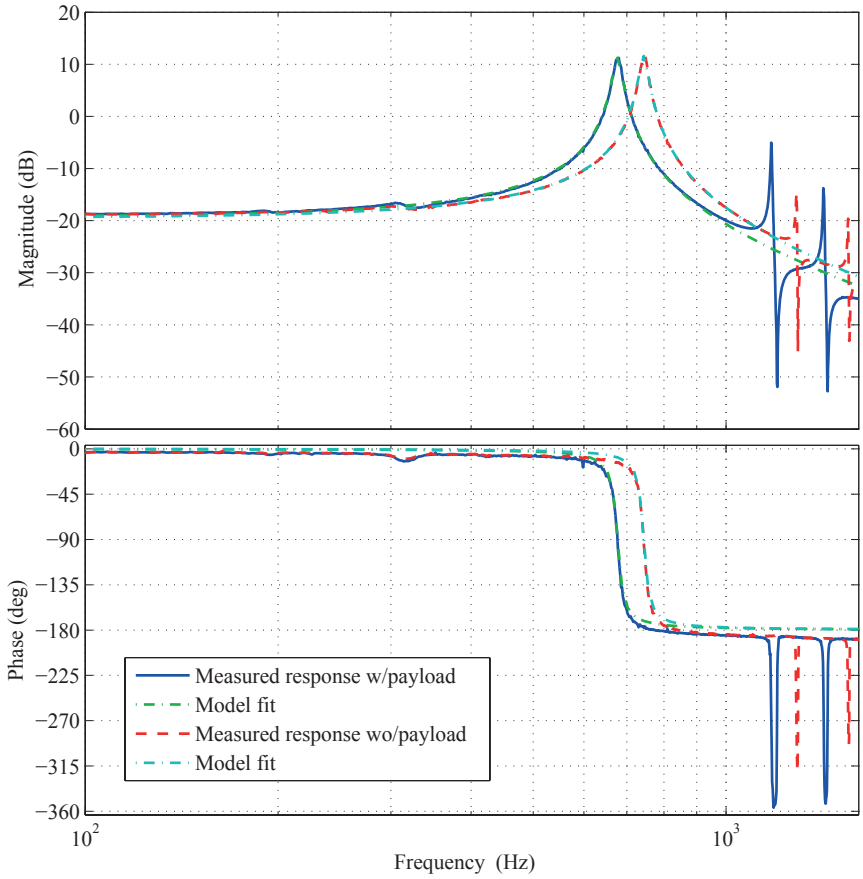

Figure 6.1: Measured frequency response and model response, for the two payload configurations, and corresponding model fits.

6.2.2 Anti-Aliasing & Reconstruction Filters

The anti-aliasing and reconstruction filters, $W_a(s)$ and $W_r(s)$ respectively, are second-order Butterworth filters, and are chosen to be identical, $W_r(s) = W_a(s)$, for convenience. They have a transfer-function of the form

$$W_a(s) = W_r(s) = \frac{{\omega_c}^2}{s^2 + \sqrt{2}\omega_c s + {\omega_c}^2} \,, \tag{6.2}$$

where ω_c is the cut-off frequency. As the cut-off frequency ω_c for the anti-aliasing and reconstruction filters used in the experimental set-up is user programmable, the filters provide an extra degree of freedom for the control law tuning. As noted in Section 3.4.7, the filters can be used to attenuate non-modeled high-frequency dynamics, as well as to attenuate quantization and sensor noise, given that the cut-off frequency ω_c is below the Nyquist frequency. The cut-off frequency selection

can also to some degree improve the nominal closed-loop sensitivity response and robustness properties.

6.2.3 Complete Plant Model

The complete model for the system presented in Fig. 3.3 is

$$\frac{y_m}{u}(s) = W_a(s)G_w(s)W_r(s) \ .$$

The usage of this model for the design of the MRAC scheme will not provide good performance with respect to the closed-loop sensitivity function, as it will have constant gain at low frequencies. Due to external disturbances, introduced by the hysteresis and creep non-linearities, and in order to reduce the impact of model uncertainty, it is advisable to add integral action to the control law [157]. The response of the closed-loop sensitivity function at lower frequencies will then improve. This can be done by augmenting the system with an integrator, implemented as part of the control scheme. The plant model, with regards to the synthesis equations in Appendix E, used is thus

$$\tilde{G}_p(s) = \frac{1}{s}G_w(s)W_r(s)W_a(s) \ , \tag{6.3}$$

which is the same structure as for (3.50). The overall model order is $n_p = 7$.

6.2.4 Model Uncertainty

The uncertainty in the nanopositioner dynamics is due to specific user applications, as well as inherent properties in the actuator and mechanical structure.

Users will typically need to position payloads of various masses, and therefore the resonance frequencies and the effective control gain of the mechanical structure will change every time a new payload is attached [140]. This is clearly demonstrated by inspecting the frequency responses for the two payload configurations in Fig. 6.1, and the corresponding parameter values for the model (6.1) in Tab. 6.1.

As can be seen from Fig. 6.1, the response of the first vibration mode is well approximated by the second-order model (6.1) using the identified parameters in Tab. 6.1, for both payload configurations. It is evident that there exist higher order modes in the system, and the second and third vibration modes are clearly visible in Fig. 6.1. These higher order modes have relatively small magnitude responses in comparison to the first, and they have shapes and directions that will make them difficult to control using the mounted actuator; thus the only practical solution is to avoid exiting these modes by limiting the bandwidth of the control law.

As discussed in Section 1.2.1 and Chapter 2, another second source of uncertainty is due to the piezoelectric actuator, which has inherent variations in the effective control gain due to changes in actuator temperature, offset voltage, displacement range, as well as due to depolarization of the piezoelectric actuator. The hysteresis and creep non-linearities present in all piezoelectric actuators are the main contributors to the change in effective gain, and this is directly dependent

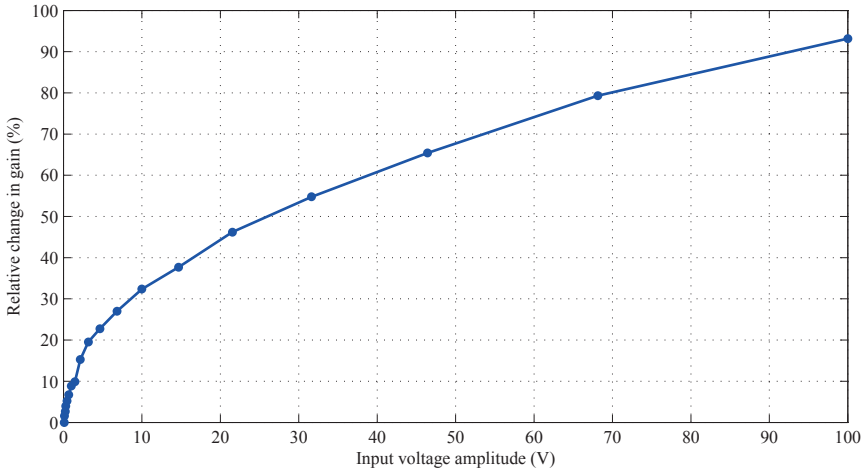

Figure 6.2: Relative change in low-frequency gain b_0/a_0 for the piezoelectric actuator due to the input voltage amplitude (using a sinusoidal input at 10 Hz).

on the offset voltage and input voltage amplitude, or displacement range. The dependence on input voltage amplitude for the x-axis of the nanopositioning device is shown in Fig. 6.2, where the relative change of the low-frequency gain b_0/a_0 is recorded as a function of the amplitude (when using a 10 Hz sinusoid). The relative change of the gain is found to be over 90% at an amplitude of 100 V compared to the gain at 100 mV. This is more than what was found in Fig. 4.2 in Chapter 4, and could be due to changes in polarization after extended use and the modifications done when adding the magnetized sample holder.

To assess the nominal robustness of the proposed control scheme, the uncertainty of the mechanical model is taken into account as a multiplicative perturbation to the positioner dynamics,

$$w = G_w(s)(1 + \delta_w(s)\Delta_w(s))u_a \ ; \ \|\Delta_w(s)\|_\infty \leq 1 \ . \tag{6.4}$$

The uncertainty weight $\delta_w(s)$ is determined experimentally for the two payload configurations, and incorporating the uncertainty of the effective gain, an overbounding uncertainty weight is found and shown together the experimentally determined uncertainties in Fig. 6.3.

6.3 Model Reference Adaptive Control

As the only measurement available in the system is the displacement of the sample platform, a control scheme for the system must use output-feedback. Readily available adaptive control schemes for output-feedback includes model reference adaptive control (MRAC) [111], $\mathcal{L}_1$ adaptive output-feedback control [106], and adaptive observer backstepping [126]. MRAC and adaptive observer backstepping can formally provide asymptotic output tracking.

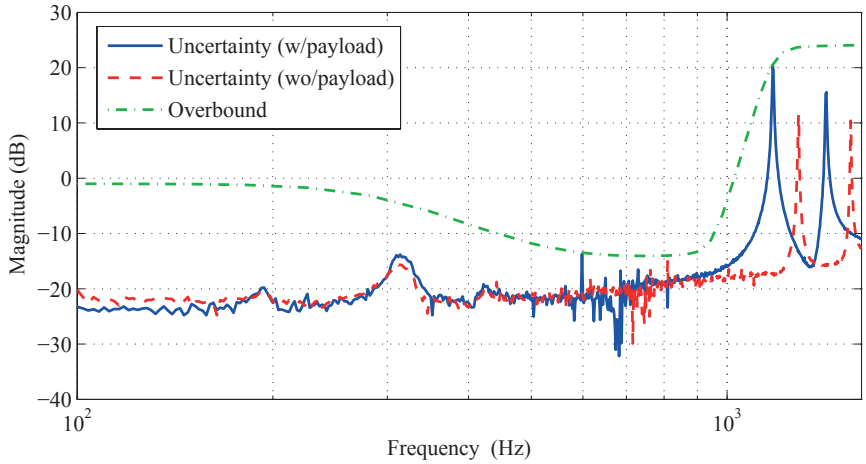

Figure 6.3: Open-loop uncertainty weight $\delta_w(s)$, for the two payload configurations and an over-bounding approximation.

$\mathcal{L}_1$ adaptive output-feedback control provides an disturbance observer adapting to the discrepancy between the plant output and a reference model, and the stability and performance will depend on the choice of reference model and a low-pass filter which is non-trivial to find in general. For a first-order reference model, however, it is fairly straight forward to find these filters. The control scheme will in that case be equivalent to a proportional-integral (PI) control law [106], and the tuning procedure for the modified PI control law used in Chapter 4 also provide good performance for the first-order reference model $\mathcal{L}_1$ adaptive control scheme.

Adaptive observer backstepping is dependent on non-linear damping terms, which can lead to impractically large actuation forces, and also produces very complicated control laws. The MRAC scheme was deemed to be the most feasible choice. The control law and adaptive law is decoupled, such that the control law and adaptive law can be designed separately. The design procedures for the control law and adaptive law are also fairly straight forward.

6.3.1 Control Scheme Description

Model reference adaptive control (MRAC), and the static variety, model reference control (MRC) is described in Appendix E. As described in Appendix E, the MRAC scheme consists of a control law and an adaptive law, that can be designed independently and then combined using the certainty equivalence principle [111]. An MRAC scheme can generally be implemented in direct and indirect form. The main difference is that for the direct form, the control law parameters are estimated directly, whereas for the indirect form, the plant parameters are estimated and subsequently mapped to the control law parameters.

The chosen plant model order is $n_p = 7$, which for the direct case requires $2n_p = 14$ parameters to be estimated. As only three plant parameters, b_0, a_1, and a_0, are uncertain and require estimation, employing an indirect MRAC reduces

the complexity and computational requirements of the parameter identification significantly. In addition, experience suggests that parameter convergence is much more difficult to achieve with a larger number of estimated parameters.

The indirect MRAC scheme requires the application of a normalized adaptive law, which is necessary for the stability properties of the indirect MRAC scheme, according to Theorem 6.6.2 in [111]. Normalization ensures boundedness of the measured signals used in the adaptive law.

Applicable (normalized) adaptive laws include the gradient method based on either instantaneous or integral cost functions, and the least-squares method. The (normalized) recursive least-squares method was used in Chapter 5, together with the extended Kalman filter. For the extended Kalman filter there does not exist any general proofs of convergence, and the estimates are not guaranteed to be bounded. Stability can therefore not be established theoretically when using the extended Kalman filter for parameter estimation.

All four of the above mentioned methods were implemented and applied together with the MRAC control law, and for the system at hand all four methods provided reasonable parameter convergence, given that the signals used were carefully pre-filtered. The gradient method based on the integral cost function (integral adaptive law) behaves similarly to the least-squares method, but with the added benefit of user selectable convergence rate. The method also provides theoretical stability results for the overall scheme, and was therefore chosen to be used in the implemented MRAC scheme. The integral adaptive law is described in Section D.2.

6.4 Design Choices

6.4.1 Control Law

In this Section, the control law design from Section 3.4.7 is reviewed. Assuming good knowledge of the plant model $G_p(s)$, there are two main design choices with regards to the control law, which is the choice of the reference model $W_m(s)$ and the output filter $1/\Lambda(s)$. The main limiting factor in determining these filters, is the uncertainty of the plant model, which for the system at hand is due to non-modeled high-frequency dynamics. As described in Section E.2, the nominal control law can also be expressed in terms of the feed-forward filter

$$\bar{C}(s) = \frac{c_0\Lambda(s)}{\Lambda(s) - {\theta_1}^{\mathrm{T}}\alpha(s)}$$

and feedback filter

$$\bar{F}(s) = -\frac{{\theta_2}^{\mathrm{T}}\alpha(s) + \theta_3\Lambda(s)}{c_0\Lambda(s)} ,$$

i.e., the control law can be written as

$$u_p = \bar{C}(s)(r - \bar{F}(s)y_p) .$$

The complementary sensitivity function for a set of nominal plant parameter estimates can then be found as

$$T(s) = \frac{\bar{C}(s)G_p(s)}{1 + \bar{C}(s)\bar{F}(s)G_p(s)}.$$

Since $T(s) = W_m(s)$, the stability criterion

$$\|\bar{F}(s)W_m(s)\delta_w(s)\|_\infty < 1 \tag{6.5}$$

can be used to choose $W_m(s)$ and $1/\Lambda(s)$ to obtain robustness against uncertain dynamics.

For simplicity, the reference model $W_m(s)$ was chosen to be a seventh order Butterworth filter with cut-off frequency ω_m, *i.e.*$q_m = 0$ and $p_m = 7$, and since the plant model $G_p(s)$ does not have any zeros, the polynomial $\Lambda(s)$ should be of degree $n_p - 1 = 6$, and the zeros of $\Lambda(s)$ was chosen to have a Butterworth pattern with radius ω_l.

The plant model includes the reconstruction and anti-aliasing filters, $W_r(s)$ and $W_a(s)$, both having the user-programmable cut-off frequency ω_c. As already noted, the filters can be used to attenuate non-modeled high-frequency dynamics, as well as to attenuate quantization and sensor noise, given that the cut-off frequency ω_c is below the Nyquist frequency. The cut-off frequency selection can also to some degree improve the nominal closed-loop sensitivity response and robustness properties.

The nominal tuning of the control law depends on the choice of ω_m, ω_l, and ω_c. As the plant is open-loop stable, and since it is augmented with an integral state, the performance in terms of the sensitivity function

$$S(s) = \frac{1}{1 + \bar{C}(s)\bar{F}(s)G_p(s)}$$

of the nominal closed-loop system is in general improved by choosing a bandwidth as high as possible for the reference model $W_m(s)$ and the output filter $1/\Lambda(s)$, *i.e.*, choosing ω_m and ω_l as large as possible.

The choice of ω_c is not as straight forward, as there can be found an optimal value which minimizes $\|S(s)\|_\infty$. By a course exhaustive grid search over ω_m, ω_l, and ω_c, evaluating (6.5) when using the nominal parameters for the two payload configurations from Tab. 6.1, an approximate optimal value for ω_c, and the approximate highest bandwidth for $W_m(s)$ and $1/\Lambda(s)$ without violating (6.5) was selected, and the result is shown in Tab. 6.2. The nominal frequency responses of the complementary sensitivity function, $T(s)$, the transfer-function (3.10) from r to ϵ, $E(s)$, the transfer-function (3.12) from d_u to w, and the sensitivity function $S(s)$ using the parameters in case 1) in Tab. 6.1 are shown in Fig. 6.4. As can be seen, the expected bandwidth is approximately 150 Hz.

The evaluation of the robust stability criterion (6.5) is shown is Fig. 6.6, for the over-bounding uncertainty weight in Fig. 6.3.

The control law is implemented as shown in Fig. 6.5. With reference to the augmented plant model (6.3), the filters $W_r(s)$, $W_a(s)$ and the nanopositioning device, modeled as $G_w(s)$, are physical components, whereas the integrator is implemented in software. The control law (E.1) is therefore modified to be

$$u_p = \frac{1}{s}\left({\theta_1}^{\mathrm{T}}\frac{\alpha(s)}{\Lambda(s)}u_p + {\theta_2}^{\mathrm{T}}\frac{\alpha(s)}{\Lambda(s)}y_p + \theta_3 y_p + c_0 r\right) .$$

Table 6.2: Control law parameters for MRAC.

Parameter	Value
ω_c	$2\pi \cdot 1100$
ω_m	$2\pi \cdot 900$
ω_l	$2\pi \cdot 900$

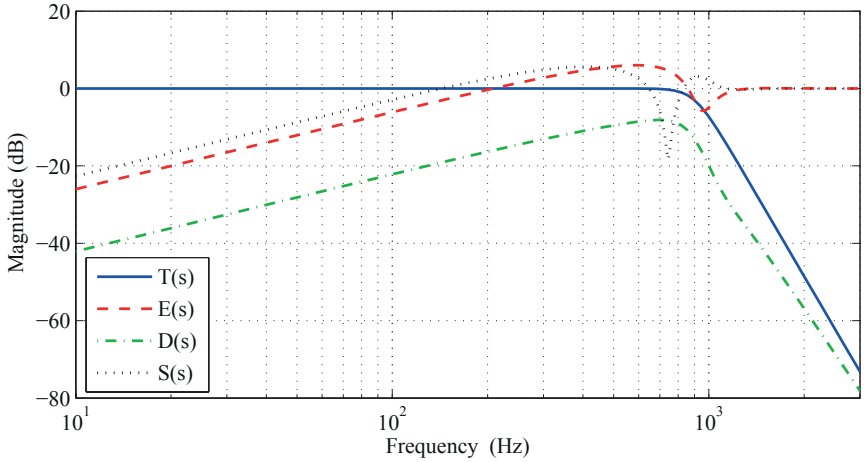

Figure 6.4: Nominal responses for $T(s)$, $E(s)$, $D(s)$, and $S(s)$.

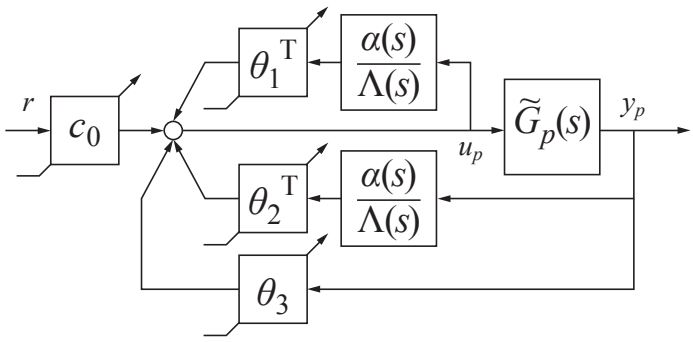

Figure 6.5: The MRAC control law structure.

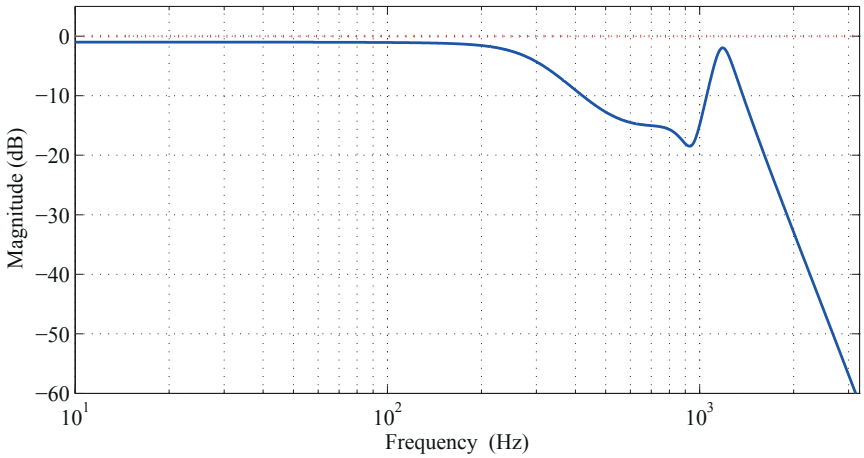

Figure 6.6: Evaluation of the robust stability criterion (6.5).

6.4.2 Adaptive Law

For the integral adaptive law, as presented in Section D.2, values for the forgetting factor κ_f, the normalization constant α_0, and the gains in Γ, must be selected. In addition, the selected reference signal should at minimum produce a sufficiently rich input signal (which results in a PE regressor vector).

The integral adaptive law will theoretically provide convergence to the correct parameter values when using a sufficiently rich input signal [111, 144]. However, for the system at hand, none of the four parameter identification schemes tried (the gradient method based on instantaneous or integral cost functions, the least-squares method, and the extended Kalman filter) provided reasonable parameter convergence without careful pre-filtering of the signals used. As was done in Chapter 5, a pre-filter $W_p(s)$ must also be selected.

The main limitation for the selection of κ_f, α_0, and Γ is the numerical stability of the adaptive law. If either κ_f or Γ are too large, or if α_0 is too small, depending on the selected numerical integration scheme and step size, the adaptive law can become unstable. As long as the adaptive law remains stable, the choice of κ_f, α_0, and Γ does not seem to influence the mean values of the stationary response for the estimated parameter values. The mean values will mostly depend on the pre-filter $W_p(s)$. However, the choice of κ_f, α_0, and Γ determines the rate of convergence, as well as the amount of averaging, and thus how much fluctuation there will be in the estimates due to noise and other disturbances.

The choice of the pre-filter is done considering the concepts of dominantly rich signals and experiment design, as they provide guidance on how to choose input signals that should provide better parameter estimates under non-ideal conditions.

The deterministic concept of dominantly rich signals [111] provides conditions on the choice of an input signal in the presence of non-modeled dynamics and bounded disturbances, in order to obtain small biases in the parameter estimates. Summarily, the input signal should be chosen to excite the dominant dynamics of

the system to a level that dominates the disturbances, and have a spectral content that avoids excitation of non-modeled dynamics.

Somewhat similarly, the stochastic concept of experiment design [93, 182], provides methods to construct input signals of finite power that will maximize conditions on the Fisher information matrix, which should then provide parameter estimates with minimal variance when using measurements corrupted by colored noise. The Fisher information matrix in the frequency domain involves the parameter sensitivity functions for the plant model. A finite energy signal will then typically be optimal for some condition on the information matrix if the spectral content is concentrated in frequency domains where the parameter sensitivity functions of a model have peaks. An optimal input signal in this sense should also improve the convergence rate of the parameter estimates [150].

As designing an optimal input signal is usually not feasible for arbitrary tracking control tasks, a practically feasible solution is to find a pre-filter which emphasizes certain frequency domains in the signals used in the parameter identification scheme [144, 157], as discussed in Chapter 5. In addition to provide more optimal signals with regards to the information matrix, the pre-filter is also beneficial since it can attenuate disturbances and non-modeled effects; thus a more dominantly rich signal.

A heuristic approach is chosen in order to select a reasonable pre-filter $W_p(s)$. As prior knowledge of approximate parameter values is available from frequency response data, a nominal model reference control law (MRC) is found. Data collected from the plant while running in closed-loop using the MRC then provide a reasonable approximation to the expected input signal and noise correlation when using the MRAC. Using these data off-line, different filter choices are tested, according to the following considerations.

As was demonstrated in Chapter 5, the parameter sensitivities of a mass-spring-damper system suggest an emphasis on a frequency domain around the expected resonance frequencies of the system, a bandpass filter. As the scheme requires differentiation of the measured deflection, the bandpass filter must have a relative degree equal to the highest order of differentiation needed, so that the filters will be proper. To provide some low-pass filtering, the relative degree should be higher.

Choosing only a bandpass filter $W_1(s)$ with a narrow passband around expected dominant resonant frequencies results in poor low-frequency gain estimation for this system, *i.e.*, the ratio b_0/a_0 is too low. Adding another bandpass filter in parallel, with a narrow passband around the fundamental frequency of the reference signal and a selectable gain $k_2 W_2(s)$, increases the parameter identification accuracy. The gain k_2 can not be too large, as it will impact the accuracy of parameters depending on the natural frequency and damping coefficient, a_1 and a_0. The filter that is used is thus

$$W_p(s) = W_1(s) + k_2 W_2(s) \,, \tag{6.6}$$

where the cut-off frequencies for $W_1(s)$ is $[f_1^l, f_1^h] = [475, 900]$ and for $W_2(s)$ is $[f_2^l, f_2^h] = [f_r - 10, f_r + 10]$, f_r being the fundamental frequency of the reference signal. The filter gain was chosen to be $k_2 = 0.01$. The chosen pre-filter is shown in Fig. 6.7.

For the model (6.1), assuming a displacement measurement w, the parameter vector θ in the parametric model (D.1) is here denoted θ_p as given as

$$\theta_p = [b_0,\ a_1,\ a_0]^{\mathrm{T}}\,.$$

The regressor vector is then found as

$$\varphi = [u_a,\ -\dot{w},\ -w]^{\mathrm{T}}\,,$$

and the output of the model is $z = \ddot{w}$. To account for the known dynamics in the reconstruction and anti-aliasing filters, determined by the cut-off frequency ω_c, and incorporating the pre-filter, the output z and regressor φ is constructed as

$$z = s^2 W_p(s) y_m$$

and

$$\varphi(s) = [W_r(s)W_a(s)W_p(s)u_p,\ -sW_p(s)y_m,\ -W_p(s)y_m]^{\mathrm{T}}\,,$$

as illustrated in Fig. 5.4.

Reasonable values for κ_f, α_0, and Γ, trading-off convergence rate and forgetting rate or averaging, were found as $\kappa_f = 2$, $\alpha_0 = 0.001$, and

$$\Gamma = \mathrm{diag}\left(\left[5\cdot 10^6,\ 5\cdot 10^1,\ 5\cdot 10^7\right]\right)\,.$$

The parameter vector θ for the plant model (6.3), $\tilde{G}_p$, is determined by the convolution of the polynomials in the numerator and denominator of $W_r(s)$, $W_a(s)$, and $G_w(s)$, as well as the integrator $1/s$. The parameter mapping from the adaptive law to the control parameters is therefore $\theta_p \to \theta \to \bar{\theta}_c$, where

$$\bar{\theta}_c = \left[{\theta_1}^{\mathrm{T}},\ {\theta_2}^{\mathrm{T}},\ \theta_3,\ c_0\right]^{\mathrm{T}}\,.$$

6.5 Experimental Results & Discussion

6.5.1 Description of the Experimental System

The experimental set-up consisted of a Dell Optiplex 760 computer equipped with a PCI-6221 data acquisition board from National Instruments, running the xPC Target real-time operating system for hardware-in-the-loop simulations, a ADE 6810 capacitive gauge and ADE 6501 capacitive probe from ADE Technologies, a Piezodrive PDL200 voltage amplifier, the custom-made long-range serial-kinematic nanopositioner (see Fig. 2.3), two SIM 965 programmable filters, and a SIM983 scaling amplifier from Stanford Research Systems. With the xPC Target, a maximum sampling frequency of $f_s = 40$ kHz was achieved for the complete MRAC scheme, and used for all the experiments. For numerical integration, a third-order Runge-Kutta scheme (Bogacki-Shampine) [62] was used. In order to achieve a higher sampling frequency, the adaptive law and parameter mapping was implemented using the C programming language.

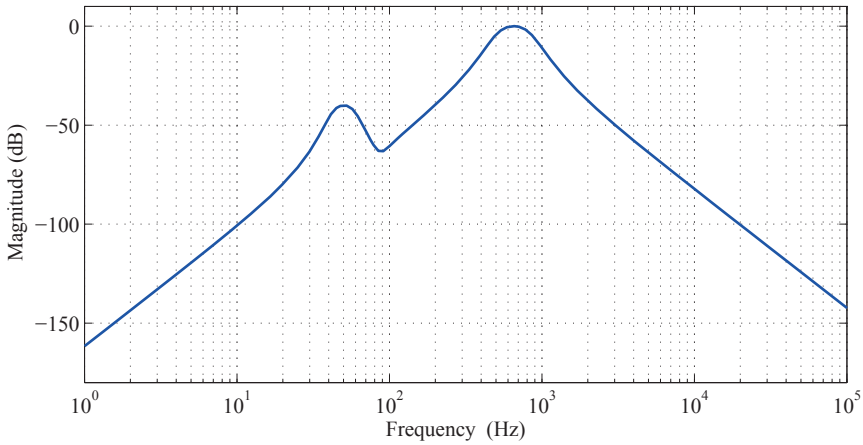

Figure 6.7: Pre-filter $W_p(S)$.

6.5.2 Experiments

Four experiments are performed to assess the tracking and parameter estimation performance. A triangular reference signal with a fundamental frequency $f_r = 50$ Hz is used, which is sufficiently rich for parameter estimation for this system. The control bandwidth is approximately 150 Hz, thus using a relatively high fundamental frequency should help elucidate model discrepancies and disturbances in the system response. First, the ability to track parameter changes is evaluated by adding a payload of 15.7 g while the system is running. Next, three experiments were done to find the asymptotic parameter estimates for various configurations, as well as the stationary tracking error.

6.5.3 Results & Discussion

The experimental results are presented in Figs. 6.8 and 6.9, and Tab. 6.3.

From Fig. 6.8 it is evident that reasonable parameter convergence is achieved, and the adaptive law is able to track parameter changes when the payload is added after approximately 5 seconds. There are discrepancies in the estimates compared to the values in Tab. 6.1, especially for the b_0 and a_1 parameters. The discrepancy for b_0 is mainly due to the larger driving voltage amplitude used in the experiment, compared to the amplitude used to find the frequency response. The discrepancy for a_1 is likely due to the presence of colored noise due to feedback and the hysteresis disturbance, since the parameter sensitivity for the model (6.1) with respect to a_1 is very small, as was pointed out in Chapter 5. The small oscillations in the a_1 estimate is due to noise, and can be reduced by decreasing, *e.g.*, the corresponding gain in Γ, at the expense of slower convergence.

By inspection of case 1) and 2) in Tab. 6.3, it can seen that the estimates for the natural frequency and the damping ratio is underestimated in case 1), and overestimated in case 2). This is likely due to the tuning of the pre-filter, as the bias change, and the accuracy improves, by fine tuning of the pre-filter to the specific

Table 6.3: Asymptotic values for the estimates for the parameters in the model (6.1) and stationary tracking errors for the MRAC scheme for various configurations.

1) No payload; 50 Hz, 3 μm amp. triangle-wave ref.					
b_0	$2.79{\cdot}10^6$	μm/s^{2}V	b_0/a_0	0.130	μm/V
a_0	$21.4{\cdot}10^6$	1/s^2	f_0	737	Hz
a_1	297	1/s	ζ	0.0321	
RMSE:		0.113 μm	RMSE relative:		6.52 %
Max. error:		0.213 μm	Max. relative error:		7.31 %
2) Payload; 50 Hz, 3 μm amp. triangle-wave ref.					
b_0	$2.33{\cdot}10^6$	μm/s^{2}V	b_0/a_0	0.131	μm/V
a_0	$17.8{\cdot}10^6$	1/s^2	f_0	672	Hz
a_1	32.9	1/s	ζ	0.00390	
RMSE:		0.101 μm	RMSE relative:		5.82 %
Max. error:		0.186 μm	Max. relative error:		6.40 %
3) Payload; 50 Hz, 6 μm amp. triangle-wave ref.					
b_0	$2.46{\cdot}10^6$	μm/s^{2}V	b_0/a_0	0.144	μm/V
a_0	$17.1{\cdot}10^6$	1/s^2	f_0	657	Hz
a_1	-95.0	1/s	ζ	-0.0115	
RMSE:		0.282 μm	RMSE relative:		8.15 %
Max. error:		0.520 μm	Max. relative error:		8.94 %

configuration. Case 2) and 3) demonstrate the ability to track the change in low-frequency gain b_0/a_0 due to change in displacement range, as should be expected by the results in Fig. 6.2, but there is also a noticeable change in the estimated natural frequency and damping ratio, which also depend on the pre-filter tuning.

As already noted in Section 6.4.2, the low-frequency gain is always underestimated. This can be seen by looking at Fig. 6.9, where it is apparent that the system response overshoots the reference. This can be confirmed by fixing the parameter estimates and manually increasing the b_0 estimate, in which case the error can be reduced.

6.6 Conclusions & Future Works

6.6.1 Conclusions

A working implementation of a MRAC scheme has been demonstrated, and the experimental results obtained provide an indication of the achievable performance that can be expected when applied to a flexible smart structure. The main challenge was to achieve reasonable convergence for the parameter estimation scheme, and this was demonstrated to be possible by the use of a special pre-filter. One major limitation with regards to performance is the difficulty in having simulta-

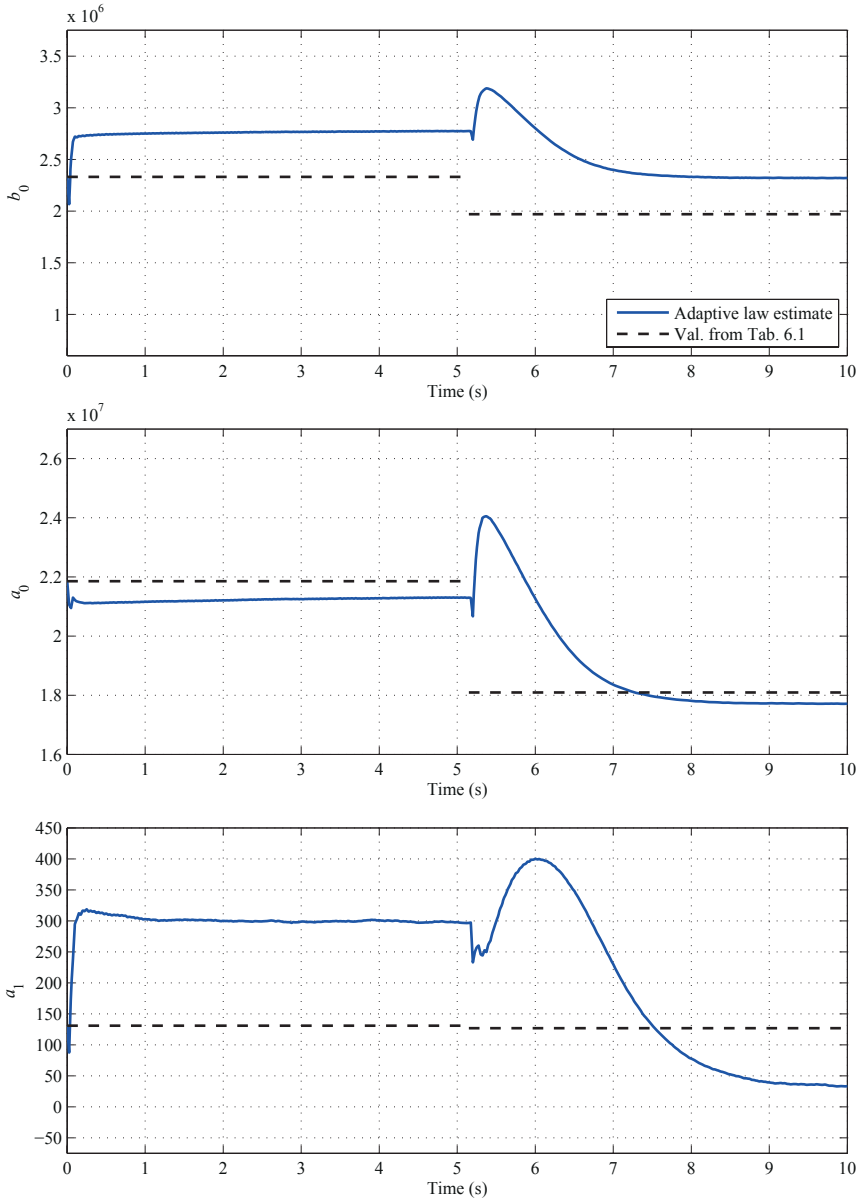

Figure 6.8: Estimated parameters when adding a payload to the sample platform, using a 50 Hz triangle-wave reference signal with 3 μm amplitude. The time-series have been down-sampled to 40 Hz.

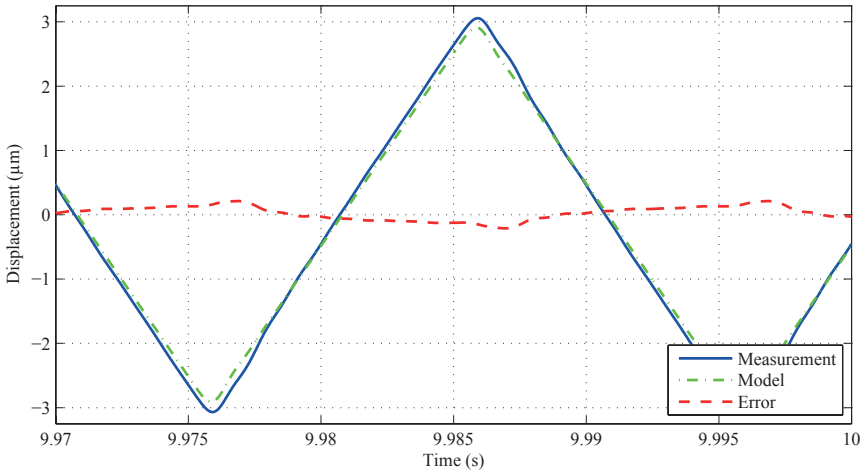

Figure 6.9: Stationary response, with payload on the sample platform, using a 50 Hz triangle-wave reference signal with 3 μm amplitude.

neous accurate estimation of the parameters determining the low-frequency gain and the parameters dependent on the damping ratio and natural frequency of the system. This is most likely due to the presence colored noise due to feedback and the hysteresis and creep nonlinearities, which also causes bounded disturbances, and necessitates integral action in the control law. The suppression of these disturbances are dependent on the achievable control law bandwidth, which main limiting factor is the presence of non-modeled and practically uncontrollable higher-order vibration modes.

6.6.2 Future Works

The parameter estimation is very sensitive to the choice of pre-filter $W_p(s)$, the actual plant parameters, the chosen control law parameters, and reference signal. To improve on the parameter estimation performance, it might be possible to find better choices for $W_p(s)$, and the application of more elaborate identification schemes, specifically tailored for closed-loop identification such as the recursive instrumental variable method [88], should be investigated.

In order to make the control scheme more robust in general, well known techniques such as parameter projection and adaptation dead-zones should be used to avoid large parameter drift. Since integral action is added to the control law, a suitable anti-windup scheme should also be added.

Some performance improvement for the MRAC scheme presented can possibly be achieved by a better nominal tuning of the control law, which is determined by the choice of reference model $W_m(s)$, anti-aliasing and reconstruction filters $W_r(s), W_a(s)$, and output filter $1/\Lambda(s)$.

Appendices

Appendix A

Piezoelectric Transducers

This Appendix is a summary of the standard theory on piezoelectric transducers. It is collated from material found in [1, 2, 7, 23–25, 38, 54, 55, 62, 112, 115, 134, 162, 164, 171–173]. Some details are added to clarify the usage of the theory.

A.1 Piezoelectricity

Piezoelectricity is the ability of some materials to generate an electric charge in response to applied mechanical stress. If the material is not short-circuited, the generated charge induces a voltage across the material that can be measured by a voltmeter. The piezoelectric effect is reversible, and an applied electric field generates strain in the material, resulting in a change in geometry, which can be measured by a pair of calipers. The production of charge when a stress is applied is called the direct piezoelectric effect, and the production of strain when an electric field is applied is called the converse piezoelectric effect.

The direct effect is illustrated in Fig. A.1, which shows a cylinder of piezoelectric material under a no-load condition, and subjected to a tensile stress and a compressive stress. The generated charge is due to a change in dipole moment, and appears as a voltage that can be measured, analogous to a voltage appearing on the terminals of a capacitor that has been charged.

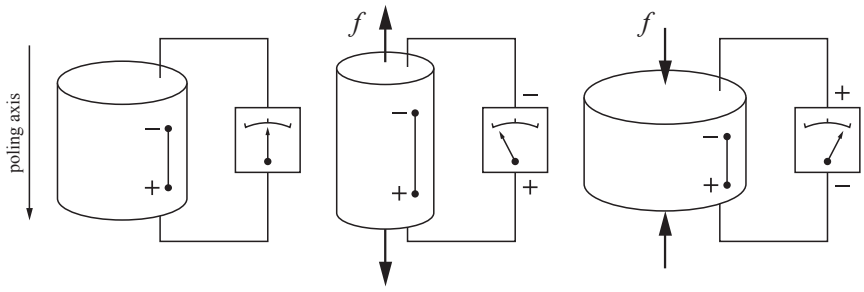

Figure A.1: Illustration of the direct piezoelectric effect.

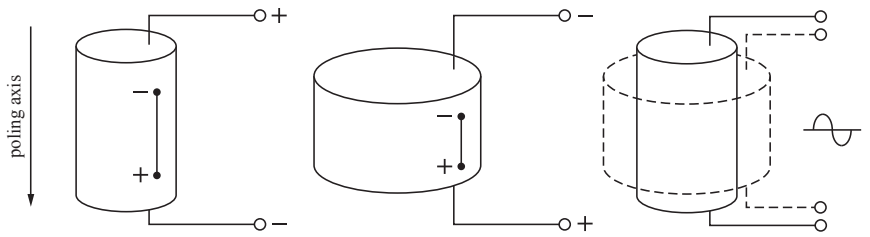

Figure A.2: Illustration of the converse piezoelectric effect.

The converse effect is illustrated in Fig. A.2, which shows a cylinder of piezoelectric material when applying an electric field with polarity in the same direction as the poling axis, which produces a positive strain (lengthening) along the poling axis, and when applying an electric field with polarity in the opposite direction of the poling axis, which produces a negative strain (shortening) along the poling axis.

The direct piezoelectric effect was discovered in 1880 by the Pierre and Jacques Curie during experiments on crystals of tourmaline, quartz, topaz, cane sugar, and Rochelle salt. The existence of the converse piezoelectric effect was predicted by Gabriel Lippmann in 1881 and the existence was experimentally confirmed by Pierre and Jacques Curie. The 20 natural crystal classes capable of piezoelectricity, and the physical properties involved, were rigorously defined using tensor analysis by Woldemar Voigt in 1910. The first step toward an engineering application was taken in 1916 by Paul Langevin, who constructed an underwater ultrasonic source consisting of a piezoelectric quartz element sandwiched between steel plates, which was one of the first sonar devices, used for submarine detection.

The piezoelectric effect is anisotropic, and can only be found in materials whose crystal structure has no center of symmetry. In addition to naturally occurring materials, some modern synthetic materials exhibit piezoelectricity. These include lead zirconate titanate, a ceramic, and polyvinylidene fluoride, a polymer, which are commonly used in transducers, as they have high piezoelectric constants.

Most materials used for transducers are *ferroelectric*, and for these materials piezoelectricity always occur below a certain temperature called the Curie temperature. The most common example of a ferroelectric is lead zirconate titanate (PZT), which has the chemical formula $\mathrm{Pb}[\mathrm{Zr}_x\mathrm{Ti}_{1-x}]\mathrm{O}_3$, $x \in [0, 1]$. The material can be considered to be a mass of minute crystallites. These crystallites have different properties above and below the Curie temperature, and an elementary cell of PZT material is illustrated in Fig. A.3, for these two states.

Above the Curie temperature, the structure is centrosymmetric with negative and positive charge sites coinciding, so there are no dipoles present in the material, and it is said to be *paraelectric*. Below the Curie temperature, the elementary cell has a built-in electric dipole, due to a tetragonal symmetry, where the negative and positive charge sites do no longer coincide. The dipoles are aligned in regions called Weiss domains, generating a net dipole moment for a domain, but the domains throughout the material are randomly oriented, and the net macroscopic effect is therefore zero for the whole material. The dipoles can be aligned, however, in

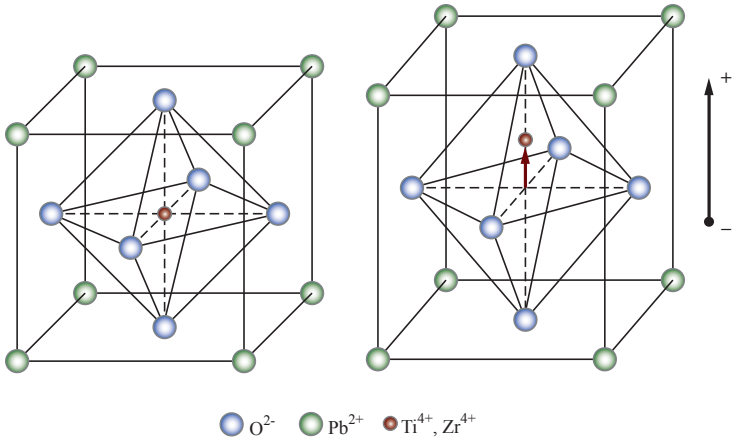

Figure A.3: Lead zirconate titanate ($Pb[Zr_xTi_{1-x}]O_3$) (PZT) elementary cell, above the Curie temperature (left) and below (right).

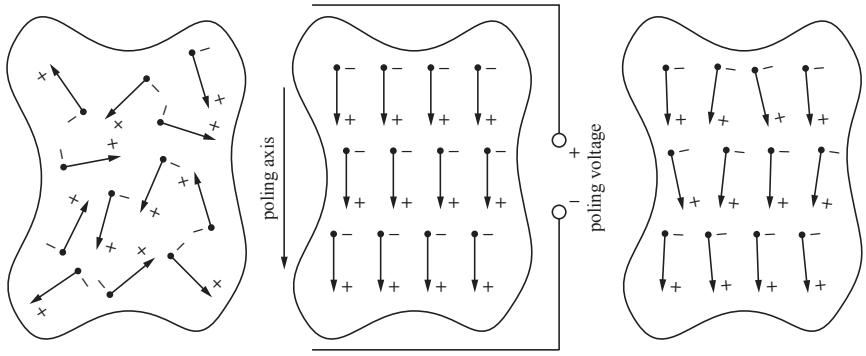

Figure A.4: Electric dipole moments in Weiss domains, before (left), during (middle), and after (right) polarization.

a process called poling. If the material is poled, some Weiss domains are grown at the expense of others, such that the net dipole moment can be noticed on a macroscopic scale.

The poling process involves heating the material above the Curie temperature and subsequently cooling the material in the presence of a high electric field. The electric field aligns the dipoles, and the dipoles become fixed below the Curie temperature, thus making the material permanently piezoelectric. This is illustrated in Fig. A.4. The property is lost if the material is reheated above the Curie temperature, if an excessive electric field is applied in the direction opposed to the poling direction, or due to excessive vibrations. The dipoles also naturally tend to change alignment over time, a process known as aging.

The word piezoelectricity means “electricity by pressure”, and is derived from the Greek *piezein*, which means *to push*.

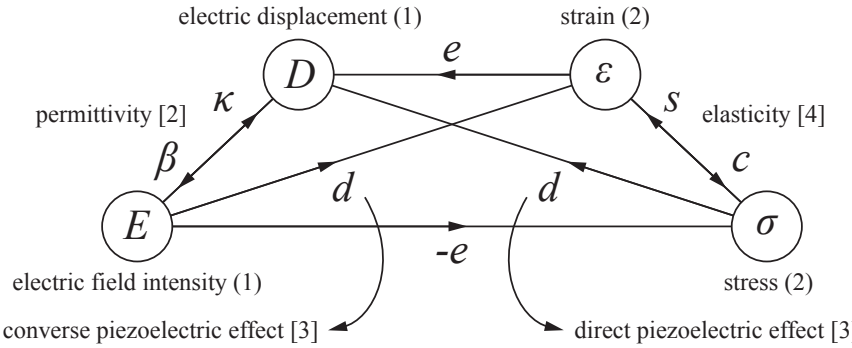

Figure A.5: Electromechanical relations in crystals (piezoelectricity). Tensor ranks of the variables are shown in parentheses, and tensor ranks of the properties are shown in square brackets.

A.1.1 Piezoelectric Constitutive Equations

Materials exhibiting piezoelectric effects can also exhibit electrothermal effects (pyroelectricity) and thermoelastic effects, but this will not be considered here. The tensor relationships describing piezoelectric effects are presented diagrammatically in Fig. A.5. The tensor description here gives multilinear relationships between variables through constant properties, and is considered to be a small-signal model. It will therefore not explain the non-linear effects observed in piezolectric transducers, such as hysteresis and creep. The tensor relationships are given in matrix form.

Piezoelectric constitutive equations can be found on several different forms, which are equivalent. The properties used are measured under different conditions, but properties found using one set of conditions can be transformed to another set of conditions using certain relationships.

Four equivalent forms of the constitutive equations

The *strain-charge* form of the constitutive equations are given as

$$\varepsilon = s^E \sigma + d^{\mathrm{T}} E \tag{A.1}$$
$$D = d\sigma + \kappa^\sigma E \,, \tag{A.2}$$

the *stress-charge* form as

$$\sigma = c^E \varepsilon - e^{\mathrm{T}} E \tag{A.3}$$
$$D = e\varepsilon + \kappa^\varepsilon E \,, \tag{A.4}$$

the *strain-voltage* form as

$$\varepsilon = s^D \sigma + g^{\mathrm{T}} D \tag{A.5}$$
$$E = -g\sigma + \beta^\sigma D \,, \tag{A.6}$$

and the *stress-voltage* form as

$$\sigma = c^D \varepsilon - h^{\mathrm{T}} D \tag{A.7}$$

$$E = -h\varepsilon + \beta^{\varepsilon} D \ . \tag{A.8}$$

The symbols used for for the *variables* are:

ε	strain (m/m), second order tensor
σ	stress (N/m^2), second order tensor
E	electric field (V/m), first order tensor
D	electric displacement (C/m^2), first order tensor

The symbols used for for the *properties* are:

s	elastic compliance (m^2/N), fourth order tensor
c	elastic stiffness (N/m^2), fourth order tensor
e	piezoelectric *strain-charge* modulus (C/m^2), third order tensor
d	piezoelectric *stress-charge* modulus (m/V) = (C/N), third order tensor
g	piezoelectric *stress-voltage* modulus ((V m)/N) = (m^2/C), third order tensor
h	piezoelectric *strain-voltage* modulus (V/m) = (N/C), third order tensor
κ	permittivity (dielectric constant) (F/m) = (C/(V m)), second order tensor
β	impermittivity (m/F), second order tensor

The measurement conditions used when finding a property is indicated by a superscript. A property found under a constant electric field is denoted $()^E$. In this case the electrodes are short circuited (closed circuit). Conversely, a property measured under a constant electric displacement is denoted $()^D$, and this means that the electrodes are not connected (open circuit). A property found under constant stress is denoted $()^\sigma$. The material is then free to expand, and is not mechanically constrained in any way. The converse situation is when a property is found under constant strain, which is denoted $()^\varepsilon$. In this case, the material is clamped, which means that it is mechanically constrained and unable to expand in any direction.

$()^E$	closed circuit condition
$()^D$	open circuit condition
$()^\sigma$	constant stress (free) condition
$()^\varepsilon$	constant strain (clamped) condition

Example A.1:
Referring to the illustration in Fig. A.1, the generated charge is due to

$$D = d\sigma \ ,$$

and there is no applied electric field, only applied stress. Similarly, referring to Fig. A.2, the generated strain is due to

$$\varepsilon = d^{\mathrm{T}} E$$

when applying an electric field, and there is no stress due to the absence of mechanical constraints.

Property transformations

Transforming the properties used in the different forms of the constitutive equations can be done using the following relationships. To transform from strain-charge form to stress-charge form the properties are transformed by

$$\begin{aligned} c^E &= \left(s^E\right)^{-1} \\ e &= dc^E \\ \kappa_\varepsilon &= \kappa^\sigma - ed^{\mathrm{T}} \,, \end{aligned}$$

and from stress-charge form to stress-voltage form by

$$\begin{aligned} \beta_\varepsilon &= \left(\kappa^\varepsilon\right)^{-1} \\ h &= \beta_\varepsilon e \\ c^D &= c^E + e^{\mathrm{T}} h \,, \end{aligned}$$

from strain-charge form to strain-voltage form by

$$\begin{aligned} \beta^\sigma &= \left(\kappa^\sigma\right)^{-1} \\ g &= \beta^\sigma d \\ s^D &= s^E - d^{\mathrm{T}} g \,, \end{aligned}$$

and from strain-voltage form to stress-voltage form by

$$\begin{aligned} c^D &= \left(s^D\right)^{-1} \\ h &= gc^D \\ \beta^\sigma &= \beta^\varepsilon + hd^{\mathrm{T}} \,. \end{aligned}$$

A.2 Matrix Notation

Due to symmetry in various tensors, it is possible to reduce the number of coefficients needed in a tensor, and this makes it possible to use matrix notation, which often simplifies calculations. Matrix notation requires that the coordinate system is aligned with the orthotropy axes of the material, and that the direction of polarization is along direction 3. The orthotropy axes are the axes for which the properties are measured. Orthotropic materials are anisotropic, which means the their properties depend on the direction in which they are measured. An isotropic material, in contrast, has the same properties in every direction. The coordinate system and designation of the different axes are illustrated in Fig. A.6. Translational directions are designated from 1 to 3, and rotational directions from 4 to 6.

Different materials belong to different crystal classes, which all have different symmetry properties. The most common material used for transducers is lead zirconate titanate. This material belongs to the tetragonal class 4mm, and the specific structure for the various matrices in the strain-charge form of the constitutive equations for this class are illustrated in Fig. A.7.

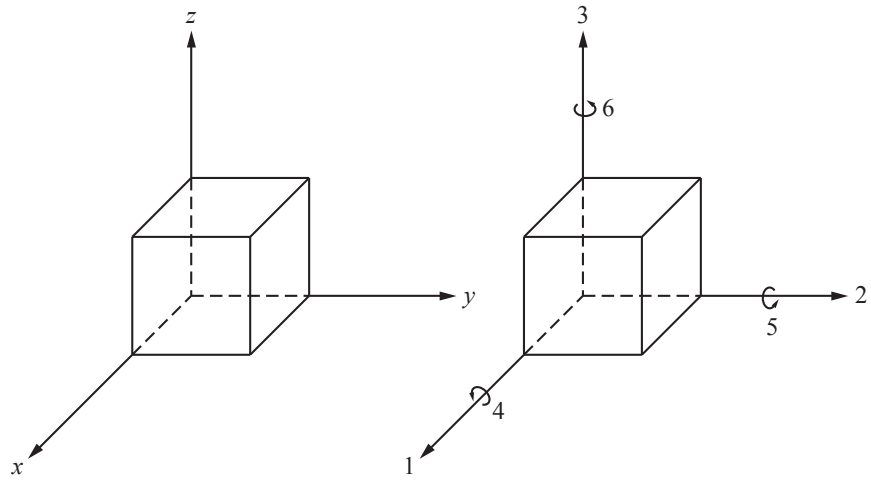

Figure A.6: Designation of the axes and directions for variables and properties.

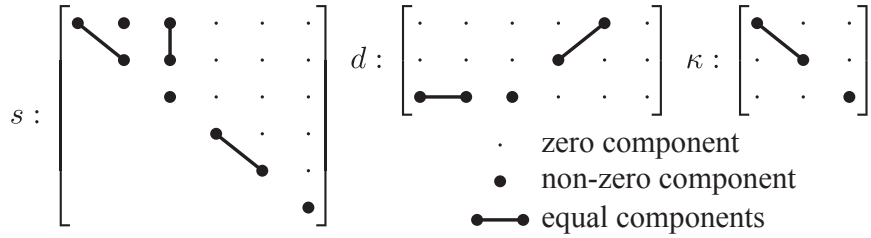

Figure A.7: Structure of the matrices for the compliances, piezoelectric moduli, and dielectric constants belonging to the tetragonal class 4mm.

The full matrices for the strain-charge can then be written out as

$$\begin{bmatrix} \varepsilon_1 \\ \varepsilon_2 \\ \varepsilon_3 \\ \varepsilon_4 \\ \varepsilon_5 \\ \varepsilon_6 \\ \\ D_1 \\ D_2 \\ D_3 \end{bmatrix} = \begin{bmatrix} s_{11}^E & s_{12}^E & s_{13}^E & 0 & 0 & 0 & 0 & 0 & d_{31} \\ s_{12}^E & s_{11}^E & s_{13}^E & 0 & 0 & 0 & 0 & 0 & d_{31} \\ s_{13}^E & s_{13}^E & s_{33}^E & 0 & 0 & 0 & 0 & 0 & d_{33} \\ 0 & 0 & 0 & s_{44}^E & 0 & 0 & 0 & d_{15} & 0 \\ 0 & 0 & 0 & 0 & s_{44}^E & 0 & d_{15} & 0 & 0 \\ 0 & 0 & 0 & 0 & 0 & s_{66}^E & 0 & 0 & 0 \\ \\ 0 & 0 & 0 & 0 & d_{15} & 0 & \kappa_1^\sigma & 0 & 0 \\ 0 & 0 & 0 & d_{15} & 0 & 0 & 0 & \kappa_1^\sigma & 0 \\ d_{31} & d_{31} & d_{33} & 0 & 0 & 0 & 0 & 0 & \kappa_3^\sigma \end{bmatrix} \begin{bmatrix} \sigma_1 \\ \sigma_2 \\ \sigma_3 \\ \sigma_4 \\ \sigma_5 \\ \sigma_6 \\ \\ E_1 \\ E_2 \\ E_3 \end{bmatrix} .$$

The matrices for the other forms of the constitutive equations can be found from the transformations given in the previous section. The values for the various coefficients can sometimes be obtained from manufacturers, but are often of little practical value, as variations between batches of material and the specifics of the geometrical configuration, manufacturing, and mounting of a transducer will alter

s_{11}^E	12.3	10^{-12} m^2/N
s_{33}^E	15.5	
s_{44}^E	39.0	
s_{66}^E	32.7	
s_{12}^E	-4.05	
s_{13}^E	-5.31	
d_{31}	-123	10^{-12} m/V
d_{33}	289	
d_{15}	496	
κ_1^σ/κ_0	1475	$\kappa_0 = 8.854 \cdot 10^{-12}$ F/m
κ_3^σ/κ_0	1300	
ρ	7.5	10^3 kg/m^3
Curie point	328	°C

Table A.1: Typical properties of one type of lead zirconate titanate (PZT-4).

the properties actually observed. The parameters will also change with temperature, the frequency of applied stimuli, and due to depolarization. Also, some of the coefficients are not actually constant, notably the permittivity κ. The electric displacement is determined by the polarization P, which when assuming that the material is isotropic with regards to this property is given as

$$P = \kappa_0 \chi E \,,$$

where χ is the dielectric susceptibility. The electric displacement is therefore given as

$$D = \kappa_0 E + P = \kappa_0 (1 + \chi) E = \kappa E \,.$$

The dielectric susceptibility for ferroelectric materials can only be considered constant when used in a small-signal model. It can not be considered a constant when there are large variations of the electric field intensity E. In those cases it is rather a function of the electric field intensity, and this is the cause of hysteresis. An indication of the small-signal behavior, compared to the large-signal behavior, can be inferred from Fig. 1.2b.

As an example, some typical property values of one type of lead zirconate titanate (PZT-4) are presented in Tab. A.1.

A.3 Stack Actuator Blocking Force

As an example of how to perform calculations using the tensor relationships presented, the expression for the blocking force for a piezoelectric stack actuator found in the following.

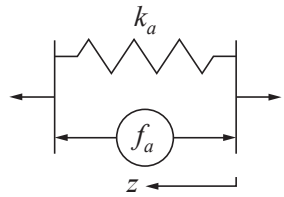

Figure A.8: Stack actuator free body diagram, the blocking force is f_a.

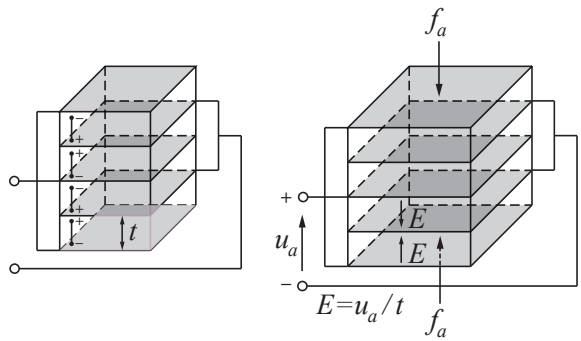

Figure A.9: Stack actuator diagram.

The blocking force is the amount of force developed by the actuator, working against the internal stiffness of the actuator and any attached mechanical structure. A free body diagram is provided in Fig. A.8.

A piezoelectric stack consists of multiple layers of piezoelectric material. The stack is designed such that the applied electric field is in parallel to the poling direction of the ceramic. This causes the developed force to work on any attached mechanical structure in the same direction. The blocking force of the actuator can be found by assuming that the stack is clamped in the poling direction, but free to expand in other directions. All forces are also assumed to be working along the poling direction, as well as the applied electric field. These conditions can be summed up as

$$\begin{aligned} \varepsilon_3 = 0, \quad \varepsilon_1 \neq 0\ ,\ \varepsilon_2 \neq 0 \\ \sigma_1 = \sigma_2 = 0, \quad \sigma_3 \neq 0\ , \end{aligned}$$

and

$$E_1 = E_2 = 0, \quad E_3 \neq 0\ .$$

This is a typical mounting configuration in many applications. The geometry of this configuration when using a stack actuator is shown in Fig. A.9.

The strain-charge form of the constitutive equations (A.1) under the stated

conditions yield

$$\varepsilon_1 = s_{13}^E \sigma_3 + d_{31} E_3 \tag{A.9}$$

$$\varepsilon_2 = s_{13}^E \sigma_3 + d_{31} E_3, \tag{A.10}$$

while from the stress-charge form (A.3), the stress in the poling direction is expressed as

$$\sigma_3 = c_{13}^E \varepsilon_1 + c_{13}^E \varepsilon_2 - e_{33} E_3. \tag{A.11}$$

Substituting (A.9) and (A.10) into (A.11) yields

$$\sigma_3 = 2c_{13}^E \left(s_{13}^E \sigma_3 + d_{31} E_3 \right) - \left(2d_{31} c_{13}^E + d_{33} c_{33}^E \right) E_3 = 2c_{13}^E s_{13}^E \sigma_3 - d_{33} c_{33}^E E_3 \ ,$$

since

$$e_{33} = 2d_{31} c_{13}^E + d_{33} c_{33}^E \ .$$

This provides the stress on an element in the poling direction as

$$\sigma_3 = -d_{33} \left(c_{33}^E - 2c_{13}^E \nu \right) E_3.$$

where ν is (the dimensionless) Poisson's ratio

$$\nu = -\frac{\varepsilon_1}{\varepsilon_3} = -\frac{\varepsilon_2}{\varepsilon_3} = -\frac{s_{13}^E \sigma_3}{s_{33}^E \sigma_3} = -\frac{s_{13}^E}{s_{33}^E} = \frac{c_{13}^E}{c_{11}^E + c_{12}^E} \ ,$$

since

$$s_{13}^E = \frac{c_{13}^E}{2(c_{13}^E)^2 - c_{33}^E (c_{11}^E + c_{12}^E)} \ ,$$

$$s_{33}^E = -\frac{c_{11}^E + c_{12}^E}{2(c_{13}^E)^2 - c_{33}^E (c_{11}^E + c_{12}^E)} \ .$$

The geometry of one stack element should be well approximated by a rectangular cuboid, with length, or thickness, t, and having a surface area of A for the faces normal to the direction of the length. Any forces working on an attached mechanical structure should be distributed over these faces, and any voltage applied over electrodes on these faces, must be distributed over the thickness. The stress on the element due to a force f_a in the poling direction, distributed over the surface area A, should therefore be

$$\sigma_3 = \frac{f_a}{A} \ ,$$

and electric field due to the applied voltage u_a over the thickness t of the element is

$$E_3 = \frac{u_a}{t}.$$

In a static configuration there should now be a balance of stress in the element as

$$\frac{f_a}{A} = -d_{33} \left(c_{33}^E - 2c_{13}^E \nu \right) \frac{u_a}{t} \ ,$$

and thus the blocking force developed by the piezoelectric element is

$$f_a = -d_{33}\left[\frac{\left(c_{33}^E - 2c_{13}^E\nu\right)A}{t}\right]u_a \ .$$

If n elements are stacked on top of each other with each of them having the thickness $t = \ell/n$, ℓ being the length of the stack, and if it is recognized that the stiffness of the stack will be given as

$$k_a = \frac{\left(c_{33}^E - 2c_{13}^E\nu\right)A}{\ell} \ \text{(N/m)} \ ,$$

an expression for the developed blocking force for a stack actuator is obtained as

$$f_a = -nd_{33}k_a u_a \ . \tag{A.12}$$

By also allowing motion along the poling direction, $\varepsilon \neq 0$, the stress, σ_3, can be found as

$$\sigma_3 = \left(c_{33}^E - 2c_{13}^E\nu\right)\varepsilon_3 - d_{33}\left(c_{33}^E - 2c_{13}^E\nu\right)E_3 \ . \tag{A.13}$$

Since the strain of the element is defined as the ratio of the increase in length, or displacement, w, of the element, and the original length, t. That is,

$$\varepsilon_3 = \frac{w}{t} \ ,$$

and (A.13) can be put on the form

$$f_a = k_a w - nd_{33}k_a u_a \ . \tag{A.14}$$

A.4 Charge in Actuator Circuit

As another example, the expression for the charge in the actuator circuit is found for a piezoelectric stack. From the strain-charge form of the constitutive equations the generated electric displacement in the poling direction of a piezoelectric element is found when

$$\begin{aligned} &\varepsilon_1 \neq 0 \ , \ \varepsilon_2 \neq 0 \ , \ \varepsilon_3 \neq 0 \\ \sigma_1 = \sigma_2 = 0, \quad &\sigma_3 \neq 0 \\ E_1 = E_2 = 0, \quad &E_3 \neq 0 \end{aligned}$$

as

$$D_3 = d_{33}\sigma_3 + \kappa_{33}^\sigma E_3 \ . \tag{A.15}$$

Here, the stack is also allowed to move along direction 3. The strains ε_1 and ε_2 due to a uniaxial stress σ_3 on the element can be found using Hooke's law as

$$\begin{aligned} \varepsilon_1 &= s_{13}^E\sigma_3 \\ \varepsilon_2 &= s_{13}^E\sigma_3 \ , \end{aligned}$$

and these relationships can be used to solve for the resulting stress σ_3 due to the strain ε_3 as

$$\sigma_3 = c_{13}^E \varepsilon_1 + c_{13}^E \varepsilon_2 + c_{33}^E \varepsilon_3 = 2c_{13}^E s_{13}^E \sigma_3 + c_{33}^E \varepsilon_3 \ ,$$

which yields

$$\sigma_3 = \left(c_{33}^E - 2c_{13}^E \nu\right) \varepsilon_3 \ , \tag{A.16}$$

where ν is Poisson's ratio. The strain of the element is defined as the ratio of the increase in length, or displacement, w, of the element, and the original length, t. That is,

$$\varepsilon_3 = \frac{w}{t} \ .$$

The generated charge q on the surface area A of the n rectangular cuboid elements will be

$$q = nAD_3 \ . \tag{A.17}$$

Thus, using (A.15), yields

$$q = nA \left(d_{33}\sigma_3 + \kappa_{33}^\sigma E_3\right) \ . \tag{A.18}$$

Substituting in the expressions (A.16), $\varepsilon_3 = w/t$, $E_3 = u_a/t$, and $t = \ell/n$ yields

$$q = nA \left(d_{33} \left(c_{33}^E - 2c_{13}^E \nu\right) \varepsilon_3 + \kappa_{33}^\sigma E_3\right) = nd_{33}k_a w + \frac{\kappa_{33}^\sigma A}{\ell} u_a \ ,$$

where

$$C_p = \frac{\kappa_{33}^\sigma A}{\ell} \ \ (\mathrm{C/V})$$

is recognized as the capacitance of the stack. The expression for the charge in the actuator circuit is therefore

$$q = nd_{33}k_a w + C_p u_a \ . \tag{A.19}$$

A.5 One-Dimensional Transducers

As previously noted, the values for the various coefficients as obtained from data sheets provided by manufacturers are often not accurate, and the actual observed response from a system is dependent on the specifics of the geometrical configuration, manufacturing, and mounting of a transducer. Property values also change with temperature, and due to depolarization, or aging, and other factors. Transducers are also typically always working with regards to one direction only. The interconnection with other systems produce lumped parameter expressions, where individual identification of various parameters in the expression might be impossible. From a practical perspective, it is therefore convenient to regard all transducers to be one-dimensional, with unknown parameters. The derivation of models are then much simplified, and system identification can be done once a model structure is determined.

As the two examples in the previous Sections show, the stress-charge form of the constitutive equations can, for a stack actuator operating in one direction, be put on the form

$$\begin{bmatrix} f_a \\ q \end{bmatrix} = \begin{bmatrix} k_a & -e_a \\ e_a & C_p \end{bmatrix} \begin{bmatrix} w \\ u_a \end{bmatrix} , \tag{A.20}$$

where $e_a = nd_{33}k_a$ (N/V = C/m). Similarly, the strain-charge form can be expressed as

$$\begin{bmatrix} w \\ q \end{bmatrix} = \begin{bmatrix} 1/k_a & d_a \\ d_a & C_p(1+k^2) \end{bmatrix} \begin{bmatrix} f_a \\ u_a \end{bmatrix} , \tag{A.21}$$

where $d_a = e_a/k_a$ (m/V = C/N), and

$$k^2 = \frac{n^2 {d_{33}}^2 k_a}{C_p} , \tag{A.22}$$

which is a constant sometimes used in the literature, called the electromechanical coupling factor. It provides a measure of the ratio of energy converted from electrical to mechanical energy, or vice versa, *i.e.*, it is an efficiency measure.

Appendix B

Mechanical Vibrations

A summary of standard modeling techniques of mechanical vibrations, or structural dynamics, is presented. The summary is based on material found in [7, 62, 92, 152, 153, 172, 173, 178, 219, 227].

B.1 Distributed-Parameter Structures

A common experimental testbed for vibrating systems is a beam, where one end is clamped, and the other is free to vibrate, and which is fitted with a piezoelectric actuator patch which applies a force to a small area. This system is well approximated using classical Euler-Bernoulli beam theory. Solving the forced Euler-Bernoulli equation demonstrates all the steps required to obtain a set of ordinary linear differential equations as a model for a distributed parameter system.

The Euler-Bernoulli beam theory is applicable to describe small lateral elastic deformations in slender beams. A slender beam is a beam where the ratio between the length ℓ and the height h is large, *i.e.*, $\ell \gg h$. With reference to Fig. B.1, then the length of the beam is aligned with the x-axis, and the displacement from the neutral axis is along the z-axis, and is denoted $w(x,t)$. External force is denoted $f(x,t)$, and is assumed to have a distribution per unit length along the length of the beam, which is ℓ. In Euler-Bernoulli theory, it is assumed that there is no rotational moment of inertia, no shear deformation effects, and that the bending

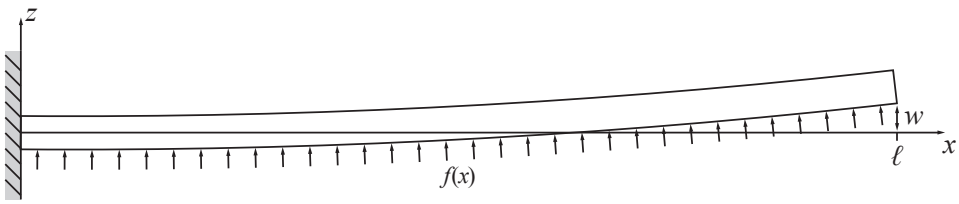

Figure B.1: Clamped-free beam, with external force.

moment is given by the constitutive equation

$$YI(x)\frac{\partial^2 w}{\partial x^2}(x,t)\ , \tag{B.1}$$

where Y is Young's modulus, and $I(x)$ is the moment of inertia about the y-axis. Young's modulus describes the response of some material to linear strain, and is therefore generalized by the elastic stiffness tensor c.

Combining the force and moment balance for an infinitesimal element of the beam and using the Euler-Bernoulli assumptions yields the partial differential equation

$$\frac{\partial^2}{\partial x^2}\left[YI(x)\frac{\partial^2 w}{\partial x^2}(x,t)\right] + \rho(x)\frac{\partial^2 w}{\partial t^2}(x,t) = f(x,t)\ , \tag{B.2}$$

where $\rho(x)$ is the mass density of the beam. Now, if in addition it is assumed that the moment of inertia is constant, that there is a linear distribution of mass, and that a force $u(t)$ is applied at a point x_u, *i.e.*,

$$f(x,t) = \delta(x - x_u)u(t)\ , \tag{B.3}$$

where $\delta(x)$ is the Dirac delta, then the equation becomes

$$\rho {c_s}^2 \frac{\partial^4 w}{\partial x^4}(x,t) + \rho\frac{\partial^2 w}{\partial t^2}(x,t) = \delta(x - x_u)u(t)\ ,\ {c_s}^2 = \frac{YI}{\rho}\ . \tag{B.4}$$

Eq. (B.4) can be solved in two steps. First, the unforced solution is found, *i.e.*, when $f(x,t) = 0$, by assuming the solution is on the form

$$w(x,t) = \sum_{i=1}^{\infty} q_i(t)\phi_i(x)\ . \tag{B.5}$$

Substituting (B.5) into (B.4) yields expressions on the form

$${c_s}^2\phi_i^{(4)}(x)q_i(t) + \phi_i(x)\ddot{q}_i(t) = 0 \tag{B.6}$$

which can be solved by separation of variables, that is, by solving the two ordinary differential equations

$${c_s}^2\frac{\phi_i^{(4)}(x)}{\phi_i(x)} = -\frac{\ddot{q}_i(t)}{q_i(t)} = K_i\ , \tag{B.7}$$

where $K_i > 0$ is a constant, as it must satisfy both differential equations simultaneously. Defining the constant as $K_i = {\omega_i}^2 = {c_s}^2{\lambda_i}^4$, the two differential equations can be expressed as

$$\ddot{q}_i(t) + {\omega_i}^2 q_i(t) = 0\ , \tag{B.8}$$

and

$$\phi_i^{(4)}(x) - {\lambda_i}^4\phi_i(x) = 0\ . \tag{B.9}$$

Eq. (B.8) is the differential equation for an harmonic oscillator, while the general solution to (B.9) is given by

$$\phi_i(x) = A_i\cos\lambda_i x + B_i\sin\lambda_i x + C_i\cosh\lambda_i x + D_i\sinh\lambda_i x\ , \tag{B.10}$$

and $\phi_i(x)$ is called a shape function. The coefficients A_i, B_i, C_i, D_i of (B.10) depend on the boundary conditions of the partial differential equation. For the case when there is one clamped end and one free end, the boundary conditions for the clamped end are

$$w(0,t) = 0 \ , \ \frac{\partial w}{\partial x}(0,t) = 0 \ , \tag{B.11}$$

which means it has zero elastic deformation and zero elastic angle, and for the free end they are

$$\frac{\partial w^2}{\partial x^2}(\ell,t) = 0 \ , \ \frac{\partial w^3}{\partial x^3}(\ell,t) = 0 \ , \tag{B.12}$$

which means that it has zero bending moment and zero shear force. By differentiating (B.10) and equating with the boundary conditions, a set of linear equations is obtained, which is

$$\underbrace{\begin{bmatrix} 1 & 0 & 1 & 0 \\ 0 & 1 & 0 & 1 \\ -\cos\lambda_i\ell & -\sin\lambda_i\ell & \cosh\lambda_i\ell & \sinh\lambda_i\ell \\ \sin\lambda_i\ell & -\cos\lambda_i\ell & \sinh\lambda_i\ell & \cosh\lambda_i\ell \end{bmatrix}}_{A_{cf}} \underbrace{\begin{bmatrix} A_i \\ B_i \\ C_i \\ D_i \end{bmatrix}}_{b_c} = \underbrace{\begin{bmatrix} 0 \\ 0 \\ 0 \\ 0 \end{bmatrix}}_{0} = \begin{bmatrix} \phi(0) \\ \phi'(0) \\ \phi''(\ell) \\ \phi'''(\ell) \end{bmatrix} . \tag{B.13}$$

Non-trivial solutions of the equations $A_{cf}b_c = 0$ are found when $\det A_{cf} = 0$, *i.e.*,

$$1 + \cos\lambda_i\ell\cosh\lambda_i\ell = 0 \ . \tag{B.14}$$

This is a transcendental equation with infinitely many solutions $\{\lambda_i\}$, which defines the set $\{A_i, B_i, C_i, D_i\}$. The solutions $\{\lambda_i\}$ must be found numerically, or can be found in standard tables. The numerical values for the clamped-free case are:

$$\begin{aligned} \lambda_1\ell &\approx 1.8751041 \\ \lambda_2\ell &\approx 4.69409113 \\ \lambda_3\ell &\approx 7.85475743 \\ \lambda_4\ell &\approx 10.99554074 \\ \lambda_5\ell &\approx 14.13716839 \\ \lambda_i\ell &\approx \frac{(2i-1)\pi}{2} \ , \ i > 5 \end{aligned}$$

For each λ_i, there is also a corresponding natural frequency in (B.8) which is $\omega_i = c_s{\lambda_i}^2$. It might be noted that for increasingly higher modes, the accuracy of the predicted modes is reduced. This is because the rotation of a infinitesimal beam element can no longer be considered negligible compared to the translation for higher order modes, as the curvature for the modes becomes more severe. This will therefore invalidate the Euler-Bernoulli assumptions.

For the shape function $\phi_i(x)$, the coefficients A_i, B_i, C_i, D_i for the clamped-free beam can be expressed in terms of A_i using $C_i = -A_i$, $D_i = -B_i$, and

$$B_i = \alpha_i A_i \ , \ \alpha_i = -\frac{\cos\lambda_i\ell + \cosh\lambda_i\ell}{\sin\lambda_i\ell + \sinh\lambda_i\ell} \ , \tag{B.15}$$

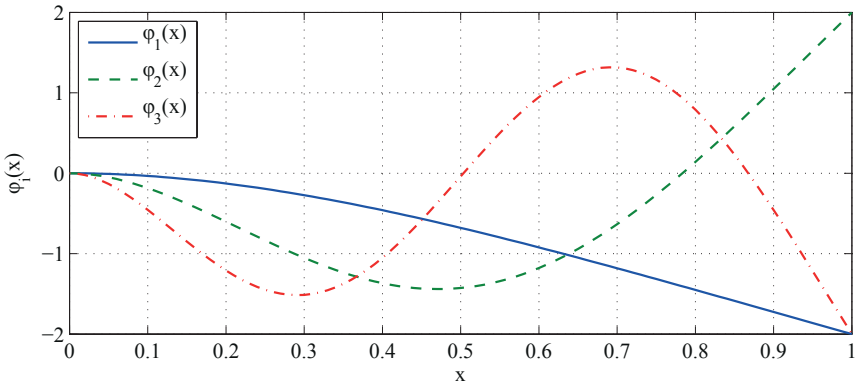

Figure B.2: The first three shape functions for a clamped-free beam of unit length.

such that

$$\phi_i = A_i \left[\cos \lambda_i x - \cosh \lambda_i x + \alpha_i(\sin \lambda_i x - \sinh \lambda_i x)\right] \ . \tag{B.16}$$

The first three shape functions for the clamped-free case are shown in Fig. B.2 for a beam of unit length and $A_i = 1$.

Normalizing the coefficients A_i such that

$$\int_0^\ell \rho[\phi_i(x)]^2 \, \mathrm{d}x = 1 \tag{B.17}$$

the complete solution to the initial value problem is given by (B.5), (B.16), and

$$q_i(t) = q_i(0) \cos \omega_i t \ . \tag{B.18}$$

For specified boundary conditions, the solutions $\{\phi_i(x)\}$ are called eigenfunctions of (B.9), and it can be shown that they are orthogonal in the sense that they satisfy, if they are normalized according to (B.17),

$$\int_0^\ell \rho[\phi_i(x)\phi_j(x)] \, \mathrm{d}x = \delta_{ij} \ , \tag{B.19}$$

and

$$\int_0^\ell \rho[\phi_i''(x)\phi_j''(x)] \, \mathrm{d}x = \lambda_i \delta_{ij} \ , \tag{B.20}$$

where δ_{ij} is the Kronecker delta.

Next, the forced solution is found. As the solution is assumed to be on the form (B.5), the partial differential equation (B.4) can be expressed as

$$\sum_{j=1}^{\infty} \rho {c_s}^2 q_j(t) \phi_j^{(4)}(x) + \rho \ddot{q}_j(t) \phi_j(x) = \delta(x - x_u) u(t) \ . \tag{B.21}$$

Substituting in (B.9), *i.e.*, $\phi_j^{(4)}(x) = {\lambda_j}^4 \phi_j(x)$, and using ${\omega_j}^2 = {c_s}^2 {\lambda_j}^4$, yields

$$\sum_{j=1}^{\infty} \rho \phi_j(x) \left[{\omega_j}^2 q_j(t) + \ddot{q}_j(t) \right] = \delta(x - x_u) u(t) \ . \tag{B.22}$$

Now, by using the Galerkin method, (B.22) is multiplied by $\phi_i(x)$ and integrated over the domain $x \in [0, \ell]$, which yields

$$\int_0^{\ell} \phi_i(x) \sum_{j=1}^{\infty} \rho \phi_j(x) \left[{\omega_j}^2 q_j(t) + \ddot{q}_j(t) \right] \, \mathrm{d}x = \int_0^{\ell} \phi_i(x) \delta(x - x_u) u(t) \, \mathrm{d}x \ . \tag{B.23}$$

Using the orthogonality property (B.19), and the fact $\int_{-\infty}^{\infty} = h(x)\delta(x-a) = h(a)$, yields

$$ {\omega_i}^2 q_i(t) + \ddot{q}_i(t) = \phi_i(x_u) u(t) \ , \tag{B.24}$$

which has the Laplace transform

$$q_i(s) = \frac{\phi_i(x_u)}{s^2 + {\omega_i}^2} u(s) \ . \tag{B.25}$$

If the displacement is measured at a point x_y along the beam,

$$y(t) = w(x_y, t) \ , \tag{B.26}$$

the transfer-function from the applied force can be found to be, using (B.5),

$$G(s) = \frac{y}{u}(s) = \sum_{i=1}^{\infty} \frac{\phi_i(x_y)\phi_i(x_u)}{s^2 + {\omega_i}^2} \ . \tag{B.27}$$

If the applied force, or actuator, and the measurement, or sensor, are co-located, that is if $x_y = x_u = x_0$, the transfer-function (B.27) have some special properties. The Fourier transform is then

$$G(j\omega) = \sum_{i=1}^{\infty} \frac{\beta_i}{{\omega_i}^2 - \omega^2} \ . \tag{B.28}$$

where $\beta_i = \phi_i(x_0)^2$, which is the square of the value of the shape function at the chosen point x_0. The function (B.28) is real valued and have infinitely many singular points where

$$\lim_{\omega \to {\omega_i}^-} G(j\omega) = +\infty$$

and

$$\lim_{\omega \to {\omega_i}^+} G(j\omega) = -\infty$$

and since

$$\frac{\mathrm{d}}{\mathrm{d}\omega} G(j\omega) = \sum_{i=1}^{\infty} \frac{2\beta_i \omega}{(\omega_i^2 - \omega^2)^2} > 0 \ \ \forall \ \ \omega > 0 \tag{B.29}$$

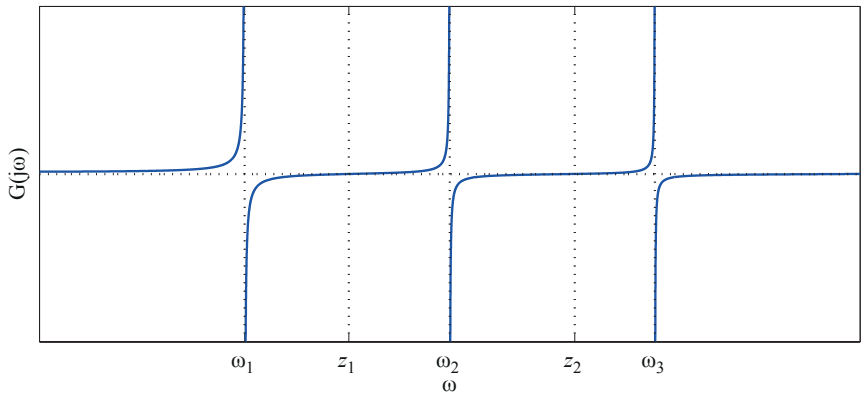

Figure B.3: The real valued Fourier transform $G(j\omega)$ of the transfer-function $G(s)$.

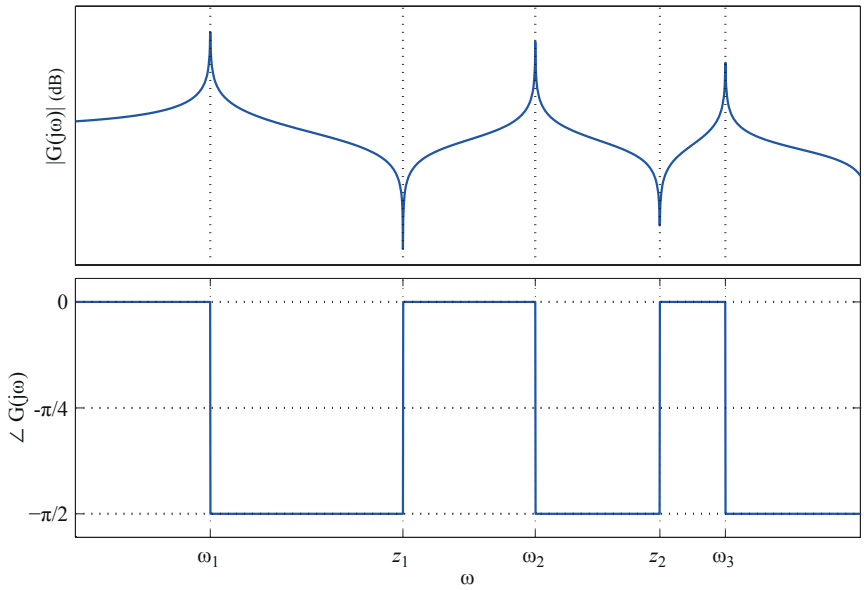

Figure B.4: The gain and phase diagram for the transfer-function $G(s)$.

the function $G(j\omega)$ is monotonously increasing between each singular point. This means that (B.27) has infinitely many poles $\{\omega_i\}$ and zeros $\{z_i\}$, and, as illustrated in Fig. B.3, the poles and zeros are interleaved, *i.e.*,

$$\omega_1 < z_1 < \omega_2 < z_2 < \omega_3 \ldots \tag{B.30}$$

which renders a phase angle $\angle G(j\omega)$ that is always between -180° and 0°, as illustrated in Fig. B.4.

Also, if the measurement is velocity, that is, if $y(t) = \dot{w}(x_y, t)$ is measured, then

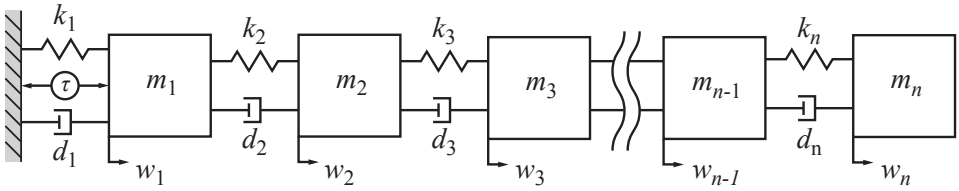

Figure B.5: Clamped-free point masses, with generalized external force.

the transfer-function is

$$H(s) = \frac{y}{u}(s) = \sum_{i=1}^{\infty} \frac{s\beta_i}{s^2 + {\omega_i}^2} \ . \tag{B.31}$$

This can be seen to be a passive, or positive real, transfer-function, as each term of the sum is (marginally) stable and has relative degree one, *i.e.*, the phase angle $\angle H(j\omega)$ is always between -90° and 90°, and this is therefore equivalent to a parallel interconnection of passive systems.

If the actuator and sensor are not co-located, *i.e.*, $x_y \neq x_u$, it may be that $\phi_i(x_y)$ and $\phi_i(x_u)$ have opposite signs for certain i. In this case the transfer-function $G(s)$ will no longer satisfy the pole-zero interleaving property, and $H(s)$ will no longer be passive.

The location of the actuator and sensor is also of significance for two additional reasons. If the actuator is located at a point x_u where $\phi_i(x_u) = 0$, then the control input $u(t)$ will have no influence on the mode i. This is equivalent to having a mode that is not controllable. Similarly, if the sensor is located at a point x_y where $\phi_i(x_y) = 0$, then the mode i will not be noticeable in the measurement y, which is equivalent to having a mode that is not observable.

B.2 Lumped-Parameter Structures

It is usually not feasible to work with an infinite series on the form (B.27), and models derived using continuum mechanics tend to reduce in accuracy for higher order modes. Discrete lumped mass models of finite order n is often used as an approximation, and an example of such a system is shown in Fig. B.5. Such models can be found by, *e.g.*, spatial discretization using finite element methods, by truncating the expression in (B.27), or by parameter identification using experimental time-series or frequency data.

The general expression for the equations of motion governing the dynamic response of non-gyroscopic, discrete, flexible structure with a finite number of degrees of freedom is

$$M\ddot{w} + D\dot{w} + Kw = \tau(t) \ , \tag{B.32}$$

where M is the real positive definite and symmetric mass matrix, while D and K are the real positive semi-definite and symmetric damping and stiffness matrices, respectively. Here, w denotes the vector of generalized displacements, and $\tau(t)$ is a

vector of generalized forces. With respect to the structure in Fig. B.5, the dynamics can be described using a mass matrix on the form

$$M = \begin{bmatrix} m_1 & 0 & 0 & & 0 \\ 0 & m_2 & 0 & \cdots & 0 \\ 0 & 0 & m_3 & & 0 \\ & \vdots & & \ddots & 0 \\ 0 & 0 & 0 & 0 & m_n \end{bmatrix} ,$$

a stiffness matrix on the form

$$K = \begin{bmatrix} k_1 + k_2 & -k_2 & 0 & & 0 \\ -k_2 & k_2 + k_3 & -k_3 & \cdots & 0 \\ 0 & -k_3 & \ddots & & \vdots \\ & \vdots & & k_{n-1} + k_n & -k_n \\ 0 & 0 & \cdots & -k_n & k_n \end{bmatrix} ,$$

and a damping matrix on the form

$$D = \begin{bmatrix} d_1 + d_2 & -d_2 & 0 & & 0 \\ -d_2 & d_2 + d_3 & -d_3 & \cdots & 0 \\ 0 & -d_3 & \ddots & & \vdots \\ & \vdots & & d_{n-1} + d_n & -d_n \\ 0 & 0 & \cdots & -d_n & d_n \end{bmatrix} .$$

The damping matrix is used to model energy dissipation, but dissipation mechanisms are often not well known. The classical dissipation model is Rayleigh damping, in which case the damping matrix has the form

$$D = \alpha M + \beta K \, . \tag{B.33}$$

With regards to the structure in Fig. B.5, Rayleigh damping corresponds to the case when $\alpha = 0$.

The undamped natural frequencies $\{\omega_i\}$ can be found from the eigenvalue problem

$$(M^{-1}K - {\omega_i}^2 I)\phi_i = 0 \, ,$$

where ϕ_i is the associated eigenvector to the eigenvalue ${\omega_i}^2$. Since M is positive definite and K is positive semi-definite, $M^{-1}K$ is diagonalizable and has non-negative eigenvalues. Assuming that the eigenvalues are non-repeated, an eigenvector basis can be found as

$$\Phi = [\phi_1, \ \phi_2, \ \cdots, \ \phi_n] \, .$$

It is common, however, to solve the eigenvalue problem using Cholesky decomposition. Then the mass matrix is decomposed into

$$M = LL^{\mathrm{T}} \, , \tag{B.34}$$

where L is a lower triangular non-singular real matrix. The eigenvalue problem can then be restated using

$$\phi_i = L^{-\mathrm{T}} p_i \tag{B.35}$$

as

$$(L^{-1} K L^{-\mathrm{T}} - {\omega_i}^2 I) p_i = 0 \,, \tag{B.36}$$

where $L^{-1} K L^{-\mathrm{T}}$ is a real symmetric matrix. Assuming that the eigenvalues are non-repeated, another eigenvector basis can be found as

$$P = [p_1,\ p_2,\ \cdots,\ p_n] \ ,$$

which in addition is orthogonal, since $L^{-1} K L^{-\mathrm{T}}$ a real symmetric matrix. The eigenvalues are the same for $M^{-1}K$ and $L^{-1} K L^{-\mathrm{T}}$, but the eigenvectors are different. Normalizing the eigenvectors such that

$$P^{\mathrm{T}} P = I \,, \tag{B.37}$$

then the basis becomes orthonormal, and the matrix $L^{-1} K L^{-\mathrm{T}}$ is then diagonalized as

$$P^{-1} (L^{-1} K L^{-\mathrm{T}}) P = \Omega^2 \,. \tag{B.38}$$

Since Ω^2 is diagonal, it has a principal square root Ω, where the undamped natural frequencies $\{\omega_i\}$ appear on the diagonal, *i.e.*,

$$\Omega = \mathrm{diag}\{\omega_i\} \,. \tag{B.39}$$

The relation between the Φ and P is given by

$$\Phi = L^{-\mathrm{T}} P \,, \tag{B.40}$$

and Φ is called the modal matrix, and it is orthonormal with respect to the mass matrix, as well as orthogonal with respect to the stiffness matrix, *i.e.*,

$$\Phi^{\mathrm{T}} M \Phi = I \tag{B.41}$$

and

$$\Phi^{\mathrm{T}} K \Phi = \Omega^2 \,. \tag{B.42}$$

If Rayleigh damping is assumed, the similarity transform defined by Φ can be used to find the modal damping ratios $\{\zeta_i\}$ on the diagonal of the diagonal matrix

$$Z = \frac{1}{2} \left(\alpha \Omega^{-1} + \beta \Omega \right) = \mathrm{diag}\{\zeta_i\} \,. \tag{B.43}$$

This follows from

$$\Phi^{\mathrm{T}} D \Phi = \alpha I + \beta \Omega^2 = 2 Z \Omega \,. \tag{B.44}$$

Now, by using the similarity transform defined by Φ, the displacement vector w can be transformed to the modal coordinates q using

$$w = \Phi q \,, \tag{B.45}$$

and this puts the equations of motion on the form

$$\ddot{q} + 2Z\Omega\dot{q} + \Omega^2 q = \Phi^{-1}\tau(t) \; . \tag{B.46}$$

Taking the Laplace transform of (B.46), yields

$$q(s) = [Is^2 + 2Z\Omega s + \Omega^2]^{-1}\Phi^{\mathrm{T}}\tau(s) \; , \tag{B.47}$$

where, due to the fact that Z and Ω are diagonal matrices,

$$[Is^2 + 2Z\Omega s + \Omega^2]^{-1} = \mathrm{diag}\left\{\frac{1}{s^2 + 2\zeta_i\omega_i s + {\omega_i}^2}\right\} \; . \tag{B.48}$$

Now, since $w = \Phi q$, the Laplace transform of (B.32) can be expressed as

$$G(s) = \frac{w}{\tau}(s) = \Phi[s^2 I + s2Z\Omega s + \Omega^2]^{-1}\Phi^{\mathrm{T}} \; , \tag{B.49}$$

which due to the diagonal matrix (B.48) can again be written as

$$G(s) = \sum_{i=1}^{n} \frac{\phi_i {\phi_i}^{\mathrm{T}}}{s^2 + 2\zeta_i\omega_i s + {\omega_i}^2} \; . \tag{B.50}$$

This is analogous to (B.27) (for the case when there is no damping), *i.e.*, the system is a parallel interconnection of independent mass-spring-damper systems. The index into the transfer transfer matrix, *e.g.*, $G_{kl}(s)$, expresses an input-output relationship, determining the response of degree of freedom k to a force applied at degree of freedom l. For a co-located actuator and sensor pair, $k = l$. With reference to the structure in Fig. B.5, there is only one force working on the structure, *i.e.*,

$$\tau = Bu = [1,\ 0,\ 0,\ \cdots,\ 0]^{\mathrm{T}}\, u \; , \tag{B.51}$$

and assuming that there is a co-located sensor, the measured displacement will be

$$y = w_1 = Cw = B^{\mathrm{T}} w \; . \tag{B.52}$$

The corresponding transfer-function is then given by $G_{11}(s)$, or

$$\frac{y}{u}(s) = CG(s)B = G_{11}(s) = \sum_{i=1}^{n} \frac{\beta_i}{s^2 + 2\zeta_i\omega_i s + {\omega_i}^2} \; , \tag{B.53}$$

where $\beta_i = \phi_i(k)\phi_i(l) = \phi_i(1)^2$. The transfer-functions for discrete lumped mass models for co-located actuator and sensor pairs will have the same properties as for the distributed mass case in the previous section.

In many practical situations, if the model has been obtained using the finite element method, or by solving the continuous partial differential equations, the model is often too large. It is then customary to truncate the model by introducing an approximation to the higher order modes by a static feed-through term R, called a residual mode. That is, the transfer-function is approximated by

$$\frac{y}{u}(s) \approx \sum_{i=1}^{m} \frac{\beta_i}{s^2 + 2\zeta_i\omega_i s + {\omega_i}^2} + R \; , \tag{B.54}$$

where

$$R = \sum_{i=m+1}^{n} \frac{\beta_i}{{\omega_i}^2} \,, \tag{B.55}$$

which can be seen to be the static response, or DC-response, of the higher order modes. The feed-through term R causes the transfer matrix to become not strictly proper, and typically improves the accuracy of the predicted zero locations.

B.3 Some Facts About Second-Order Systems

The dynamics of many nanopositioning devices is sufficiently described by a single mass-spring-damper system. As such, it is of interest to summarize some facts about such systems, *i.e.*, second-order differential equations.

The dynamics of a non-autonomous mass-spring-damper system is described by the second-order system

$$m\ddot{w} + c\dot{w} + kw = f(t) \,, \tag{B.56}$$

where k is the spring constant, c is the damping coefficient, and m is the mass. For this system, the undamped natural (angular) frequency ω_0 and damping ratio ζ are defined as

$$\omega_0 = \sqrt{\frac{k}{m}} \quad \text{and} \quad \zeta = \frac{c}{2\sqrt{mk}} \,,$$

thus, with $\beta_0 = 1/m$, (B.56) can be written

$$\ddot{w} + 2\zeta\omega_0\dot{w} + {\omega_0}^2 w = \beta_0 f(t) \,. \tag{B.57}$$

For (B.57), the damped natural frequency is found as

$$\omega_d = \omega_0\sqrt{1-\zeta^2} \,. \tag{B.58}$$

When $u(t) = 0$, the system is autonomous. The damped natural frequency is the frequency an autonomous underdamped system ($\zeta < 1$) will oscillate with given a set of initial values $(x_0, \dot{x}_0) \neq (0, 0)$.

The resonant frequency for (B.57) is

$$\omega_p = \omega_0\sqrt{1-2\zeta^2} \,. \tag{B.59}$$

The resonant frequency is the frequency at which the non-autonomous system will have the maximum amplitude response. The amplitude response will only have a peak when $0 \leq \zeta < 1/\sqrt{2}$.

The Laplace transform of (B.57) is

$$G(s) = \frac{\beta_0}{s^2 + 2\zeta\omega_0 s + \omega_0^2} \,. \tag{B.60}$$

The amplitude response is found from the Fourier transform ($s = j\omega$) as

$$|G(j\omega)| = \frac{\beta_0}{\sqrt{({\omega_0}^2 - \omega^2)^2 + (2\zeta\omega_0\omega)^2}} = \frac{\beta_0}{\sqrt{\Delta(\omega)}} \,. \tag{B.61}$$

Differentiating (B.61) with respect to the angular frequency ω yields

$$\frac{\mathrm{d}}{\mathrm{d}\omega}\,|G(j\omega)| = -\frac{1}{2}\Delta(\omega)^{-3/2}\Delta'(\omega)\ ,$$

where

$$\Delta'(\omega) = 4\omega(\omega^2 - {\omega_0}^2(1-2\zeta^2))\ .$$

Thus, it should be straight forward to verify that

$$\arg\max_{\omega\in\mathbb{R}^+} |G(j\omega)| = \omega_p\ ,$$

if $0 < \zeta < 1/\sqrt{2}$, and if $\zeta \geq 1/\sqrt{2}$,

$$\arg\max_{\omega\in\mathbb{R}^+} |G(j\omega)| = 0\ .$$

For $0 < \zeta < 1/\sqrt{2}$ the amplitude response at $\omega = \omega_p$ is

$$|G(j\omega_p)| = \frac{\beta_0}{2\zeta{\omega_0}^2\sqrt{1-\zeta^2}}\ . \tag{B.62}$$

Appendix C

Hysteresis & Creep Models

This Appendix includes a short introduction to two common frameworks for modeling hysteresis, as well as a brief description of two creep models that occur frequently in the literature.

The first framework for modeling hysteresis is the class of models that can be put on the form of the Duhem model. One such model, called the Coleman-Hodgdon model, is discussed very briefly, as this is the model used to develop the hysteresis compensation scheme in Chapter 2. The other framework is the Preisach model, which has many features in common with the Prandtl-Ishlinskii model. The Preisach model is discussed in some detail, in order to illustrate the differences in how it operates and how it is implemented, compared to the Coleman-Hodgdon model.

This Appendix is collated from material found in [45, 46, 53, 58, 114, 135, 146, 151, 218].

C.1 Hysteresis

The word *hysteresis* is derived from Greek, and means "to lag behind". A common definition is that it is a rate-independent, non-linear, multi-branch input-output map, where the branching occurs at successive extrema of the input. In many physical systems this is seen as the output lagging behind the input between input extrema, generating loops in the input-output map. The term *rate-independent* means that the branches of such hysteresis non-linearities are determined only by past extremum values, and not the rate of the input variations. Hysteresis is a *dynamical* relationship, as the output $y(t_0)$ at any instant t_0 depends on both the current value of the input $u(t_0)$ and an internal memory variable. Internal memory implies that for equal instantaneous inputs $u(t_0) = u(t_1)$, different values of the output $y(t_0) \neq y(t_1)$ can occur, depending on the state of the internal memory. Due to rate-independence, the input-output map is invariant with respect to time scaling. This means that the input-output relationship $y = \mathcal{H}u$ generates the same input-output map for $u(t)$ and $u(at + b)$ for any $a, b \in \mathbb{R}$. This is different from many other types of dynamical systems, which also exhibit a lagging effect, but

where the lagging effect is dependent on the rate of input variations. For a linear dynamical system, this would be called *phase-lag*.

Hysteresis occurs in almost all ferromagnetic and ferroelectric materials. It also occurs in other areas, and examples include systems with friction, elastic and superconductive materials, adsorption in porous media, and economics.

C.2 The Duhem Model

The Duhem model for hysteresis dates from 1897, in a work by Pierre Duhem, and focusses on the fact that the output can only change its character when the input changes direction. This model uses a phenomenological approach, postulating an integral operator or differential equation to model a hysteretic relation. A Duhem model is given by the general differential equation

$$\dot{\eta} = f_I(u,\eta)(\dot{u})^+ + f_D(u,\eta)(\dot{u})^-,\ \eta(0) = \eta_0 \tag{C.1}$$

where the expressions $(\dot{u})^+$ and $(\dot{u})^-$ are interpreted using the definitions

$$(\dot{u})^+ := \frac{|\dot{u}| + \dot{u}}{2}$$
$$(\dot{u})^- := \frac{|\dot{u}| - \dot{u}}{2}$$

and which satisfy

$$(\dot{u})^+ + (\dot{u})^- = |\dot{u}| \ .$$

This means that $(\dot{u})^+ = \dot{u}, \dot{u} > 0$, and $(\dot{u})^+ = 0, \dot{u} < 0$. Conversely, $(\dot{u})^- = 0, \dot{u} > 0$, and $(\dot{u})^- = \dot{u}, \dot{u} < 0$. The function $f_I(u,\eta)$ then determines the output when the input is increasing, and $f_D(u,\eta)$ when the input is decreasing. Models on the form (C.1) are useful as phenomenological models because the functions and parameters can be fine-tuned to match experimental results in a given situation.

C.2.1 The Coleman-Hodgdon Model

Coleman and Hodgdon have investigated the Duhem model for ferromagnetic hysteresis, but the model has also been used to describe ferroelectric hysteresis. The Coleman-Hodgdon model, as well as some analysis of the model, is presented in Chapter 2. The form of the model studied in Chapter 2 is best suited to describe hysteretic responses that are symmetric, and for cases where the input signals vary monotonously between two extremal points.

The model is given as

$$\dot{\eta} = \beta\dot{u} - \alpha\eta|\dot{u}| + \gamma|\dot{u}|u\ ,\ \eta(0) = \eta_0\ . \tag{C.2}$$

Thus,

$$f_I(u,\eta) = \beta - \alpha\eta + \gamma u \ \text{ and } \ f_D(u,\eta) = \beta + \alpha\eta - \gamma u\ .$$

Two salient observations from the analysis in Chapter 2, is that the model defines branches, and the branching occurs every time the input changes direction. An example of the behavior for the parameter values

$$\alpha = 0.06\ ,\ \beta = 0.5\ ,\ \gamma = 0.02$$

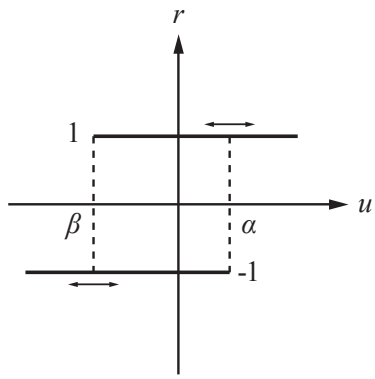

Figure C.1: Delayed relay operator.

using a sinusoidal input, and $u_0 = u_m = -30$ for the increasing branch, and $u_0 = u_M = 30$ for the decreasing branch can be seen in Fig. C.5. Note that the parameter values are chosen somewhat arbitrarily, and does not satisfy the thermodynamical conditions from Section 2.2.1.

C.3 The Preisach Model

The Preisach model is also a phenomenological model of hysteresis, but can be given a physical interpretation in terms of Weiss domains. The Preisach model is perhaps the most powerful scalar model of hysteresis among those that are known so far. This model was proposed by the physicist Ferenc Preisach in 1935 to represent scalar ferromagnetism, but has also seen widespread use to model other hysteresis phenomena.

The basis of the model is the *delayed relay operator*, $\mathcal{R}_{\alpha,\beta}$ which is defined for an arbitrary continuous input u for the initial state at $t = 0$ as

$$r(0) = \mathcal{R}_{\alpha,\beta}u(0) = \begin{cases} -1 & \text{if } u(0) \leq \beta \\ \xi_0 & \text{if } \beta < u(0) < \alpha \\ 1 & \text{if } u(0) \geq \alpha \end{cases},$$

where $\xi_0 \in \{-1, 1\}$ is the initial state of the relay, and for $t \in (0, \tau]$ as

$$r(t) = \mathcal{R}_{\alpha,\beta}u(t) = \begin{cases} -1 & \text{if } t_1 \in (0,\tau] \text{ s.t. } u(t_1) < \alpha, u(t) \leq \beta, \forall\, t \in (t_1, \tau] \\ r(0) & \text{if } \beta < u(t) < \alpha, \forall\, t \in (0, \tau] \\ 1 & \text{if } t_1 \in (0,\tau] \text{ s.t. } u(t_1) > \beta, u(t) \geq \alpha, \forall\, t \in (t_1, \tau] \end{cases}.$$

The delayed relay operator is illustrated in Fig. C.1. The output r behaves "lazily", in the sense that the relay output remains unchanged, as long as the input-output pair $\{u, y\}$ belongs to the union of the bold lines in Fig. C.1. The relay has memory in the form of the state $\xi \in \{-1, 1\}$, which determines the output of the relay in addition to the input u.

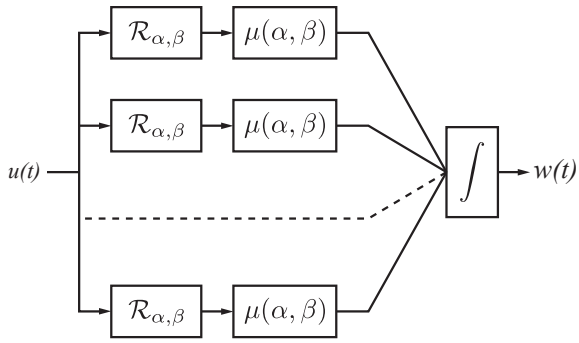

Figure C.2: Preisach model.

If an infinite set of delayed relay operators is considered, assuming $\alpha \geq \beta$, then the Preisach hysteresis model characterizes the output η of a hysteretic system as the superposition of weighted relays as

$$\eta(t) = \mathcal{H}u(t) = \iint_{\alpha \geq \beta} \mu(\alpha, \beta) \mathcal{R}_{\alpha,\beta} u(t) \, \mathrm{d}\alpha \, \mathrm{d}\beta \, , \tag{C.3}$$

where $\mu(\alpha, \beta)$ is a weight function, associated with a relay element $\mathcal{R}_{\alpha,\beta}$. Eq. (C.3) is illustrated in Fig. C.2. The relay elements represents hysteresis non-linearities with local memories, and the memory is represented by the state $\xi \in \{-1, 1\}$. This can be interpreted as modeling the switching behavior of individual (*e.g.*, magnetic or electric) dipoles within a material. The weight function $\mu(\alpha, \beta) \geq 0$ is an integrable function defined for the half-plane

$$S = \{(\alpha, \beta) : \alpha \geq \beta, \alpha \leq \alpha_m, \beta \leq \beta_m\} \, .$$

The set S is called the Preisach plane, while $\mu(\alpha, \beta)$ is the Preisach density function. For every point (α, β) of S, there exists a unique relay $\mathcal{R}_{\alpha,\beta}$.

Assume $\mu(\alpha, \beta)$ has support S, and define, for a given continuous piecewise monotone input $u(\cdot)$ and time t,

$$S^+(t) = \{(\alpha, \beta) \in S : \mathcal{R}_{\alpha,\beta} u(t) = 1\} \, ,$$
$$S^-(t) = \{(\alpha, \beta) \in S : \mathcal{R}_{\alpha,\beta} u(t) = -1\}.$$

Then the boundary $L(t) = S^+(t) \cap S^-(t)$, called the Preisach state, is a descending "staircase" with vertices at values of α or β corresponding to a subset of previous local maxima or minima of the input $u(\cdot)$, see Fig. C.3. The final link of $L(t)$ is attached to $\alpha = \beta$ at $(u(t), u(t))$ by a vertical segment when $u(\cdot)$ is decreasing at t, and by a horizontal segment when $u(\cdot)$ is increasing at t. Eg. (C.3) can therefore be reformulated as

$$\eta(t) = \iint_{S^+(t)} \mu(\alpha, \beta) u(t) \, \mathrm{d}\alpha \, \mathrm{d}\beta - \iint_{S^-(t)} \mu(\alpha, \beta) u(t) \, \mathrm{d}\alpha \, \mathrm{d}\beta \, .$$

The operator $\mathcal{H}$ is characterized to a large extent by the evolution in time of $S^+(t)$, $S^+(t)$ and the measure $\mu(\alpha, \beta)$.

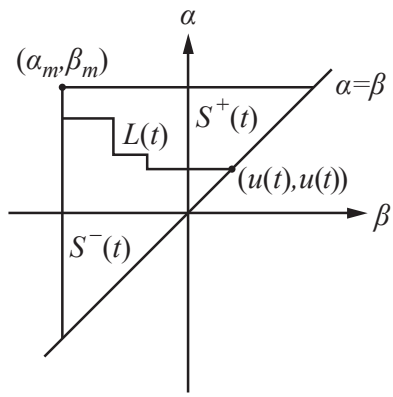

Figure C.3: Preisach plane.

The Presiach model has two salient properties, which are the *wiping out property* and the *congruence property*. The wiping out property can be formulated as whenever $u(t)$ attains a local maximum, all vertices on $L(t)$ with "up"-switching values α less than this maximum are wiped out. Conversely, each local minimum of $u(\cdot)$ wipes out all vertices on $L(t)$ with "up"-switching values β greater than this minimum. So only the alternating dominant input extrema are stored by the Preisach model, other input extrema are wiped out. The congruence property means that all primitive hysteresis loops corresponding to the same extreme values of input are congruent. If $u(t)$ varies monotonously between two consecutive extremal values u_m and u_M, then for all initial states, the resulting loops are congruent. That is, they have the same shape.

To implement the Preisach model numerically, the Preisach plane can be discretized. Perhaps the simplest method for doing this, is to partition S into subregions as shown in Fig. C.4. Within each sub-region, the relays are assumed to switch, up (+1) or down (-1), simultaneously depending on the applied input $u(\cdot)$, and the weighting values μ associated with all the relays in each sub-region are the same. As a result, the Preisach model (C.3) takes the form

$$\eta(t) = \sum_{i=1}^{n_q} \mu_i A_i \mathcal{R}_i u(t) + \eta_0 \ , \tag{C.4}$$

where n_q represents the total number of sub-regions, μ_i is the weighting value for the relay $\mathcal{R}_i$ in the ith sub-region of area A_i, and η_0 is the bulk contribution to the output from sub-regions outside of the Preisach plane. If the Preisach plane has been partitioned into n_h levels uniformly along the β and α axes, the total number of sub-regions is $n_q = (n_h(n_h+1))/2$. The number of relays that needs to be implemented is therefore n_q.

Assuming the possible (α, β) pairs are scaled to accommodate maximum and minimum input values, u_m and u_M, *i.e.*, $\alpha_m \geq u_M$ and $\beta_m \leq u_m$, the weights $\{\mu_i\}$ can be found by sampling the input u and output η of a hysteretic system, in order to obtain a primitive hysteresis loop. The primitive hysteresis loop is found by

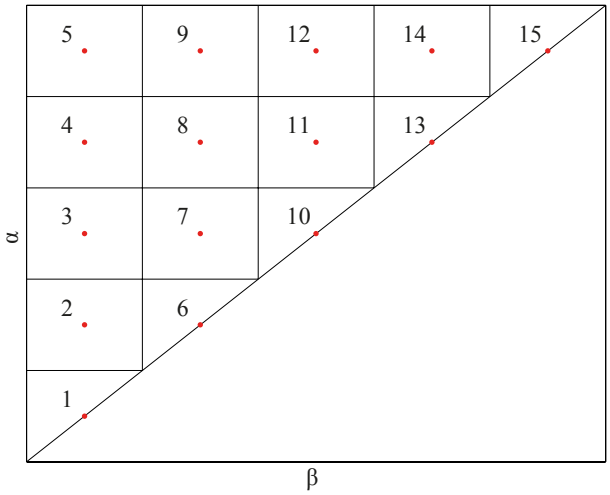

Figure C.4: Preisach plane partitioning for $n_h = 5$ levels.

cycling the input monotonously from a minimum u_m to a maximum u_M and back to the minimum u_M. Since the Preisach model might not capture all observed effects in a real hysteretic system, this is best done under stationary conditions using a periodic input signal. The resulting time-series $\{\eta(t_k)\}$ and $\{u(t_k)\}$, of length n_t, is then used to construct an over-determined system of linear equations on the form

$$\begin{bmatrix} \eta(t_1) \\ \eta(t_2) \\ \vdots \\ \eta(t_{n_t}) \end{bmatrix} = \begin{bmatrix} A_1\mathcal{R}_1u(t_1) & A_2\mathcal{R}_2u(t_1) & \dots & A_q\mathcal{R}_qu(t_1) \\ A_1\mathcal{R}_1u(t_2) & A_2\mathcal{R}_2u(t_2) & \dots & A_q\mathcal{R}_qu(t_2) \\ \vdots & & & \\ A_1\mathcal{R}_1u(t_{n_t}) & A_2\mathcal{R}_2u(t_{n_t}) & \dots & A_q\mathcal{R}_qu(t_{n_t}) \end{bmatrix} \begin{bmatrix} \mu_1 \\ \mu_2 \\ \vdots \\ \mu_{n_q} \end{bmatrix} + \eta_0 \,. \quad \text{(C.5)}$$

This can be put on the more compact form

$$c_\eta = A_u b_\mu + \eta_0 \,, \quad \text{(C.6)}$$

where c_η is $n_t \times 1$, A_u is $n_t \times n_q$, and b_μ is $n_q \times 1$. The least-squares fit for $b_\mu = [\mu_1, \mu_2, ..., \mu_{n_q}]^{\mathrm{T}}$ is then found using, *e.g.*, the pseudo-inverse as

$$b_\mu = {A_u}^{+}(c_\eta - \eta_0) \,. \quad \text{(C.7)}$$

The input-output map generated by the discrete Preisach model fitted to a hysteresis loop generated using the Coleman-Hodgdon model (C.2) can be seen in Fig. C.5. The smooth path is generated by the Coleman-Hodgdon model, and the staircase formed path is generated by the discrete Preisach model. Here $n_h = 50$ levels were used, translating to $n_q = 1275$ relays, thus, the Preisach model becomes orders of magnitude more computationally demanding than the Coleman-Hogdon model for reasonable model accuracy.

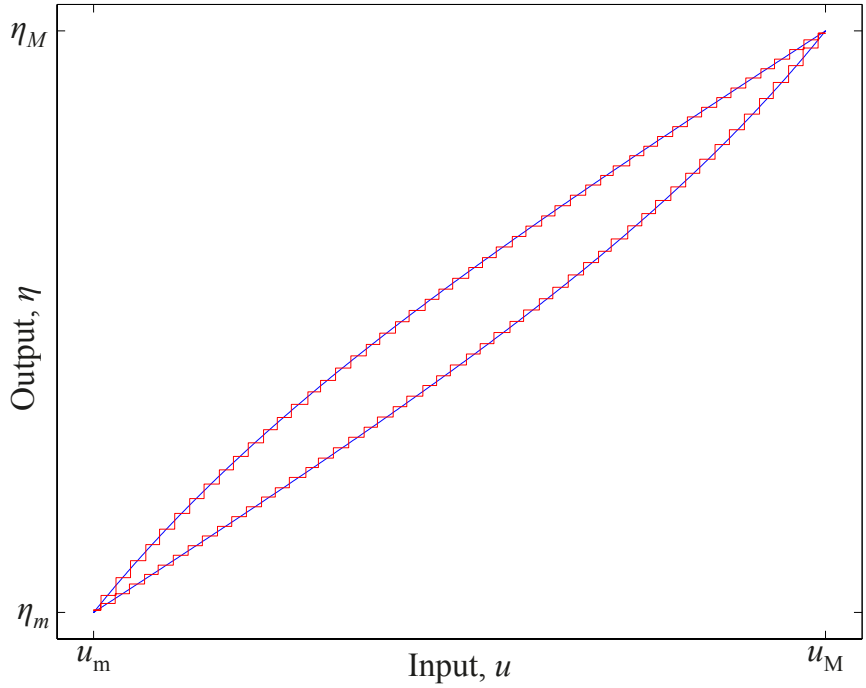

Figure C.5: Input-output map generated by the Coleman-Hogdon model and the discrete Preisach model.

C.4 Creep Models

Piezoelectric actuators exhibit a rate-dependent non-linearity in addition to the rate-independent hysteresis. This effects is known as creep, and can typically be observed as a slow change, or creep, in the displacement measurement after a constant voltage is applied to the actuator. Experimental data to illustrate the effect are show in Fig. C.6. The effect can also be observed as a slow lengthening or shortening if the actuator is mechanically loaded by a tensile or compressive force, respectively.

The effect it mainly a problem for open-loop, or feed-forward, control. Feed-forward control is common in older scanning probe microscopy instruments, and when noise amplification due to feedback is unacceptable.

There are two models for creep that commonly appear in the literature, both are phenomenological. The first model is a non-linear model, which is

$$w(t) = w_0 \left(1 + \gamma \log \frac{t}{t_0}\right) ,$$

where t_0 is the time at which some constant stimuli is applied, w_0 is the displacement at that time, and the constant γ is used to fit the model to experimental data. The model is not very convenient to use for arbitrary excitation signals, due to the need to handle the initial condition and since $\lim_{z\to 0} \log(z)$ is undefined.

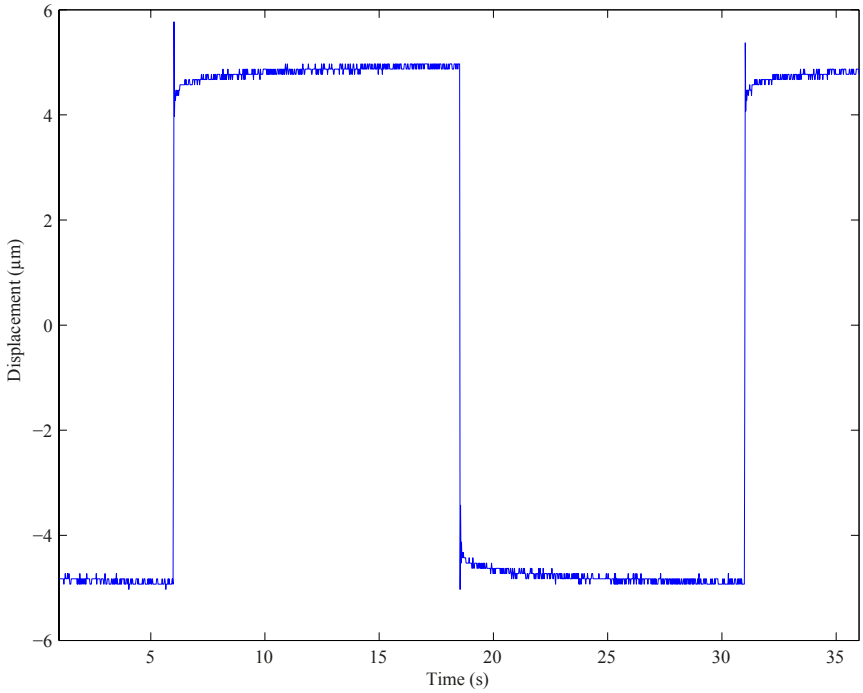

Figure C.6: Piezoelectric actuator creep response to a voltage square-wave.

The second model is more convenient with regards to arbitrary input signals, and consists of a superposition of linear first-order low-pass filters with a feedthrough term, *i.e.*,

$$G_c(s) = \frac{1}{k_0} + \sum_{i=1}^{m} \frac{1}{d_i s + k_i} \ .$$

This can be considered as a series of springs and dampers, where $\{k_0, k_i\}$ are the spring constants and $\{d_i\}$ are the damping constants. The first spring constant k_0 provides the initial static displacement, and the remaining spring-damper elements models the low-frequency creep motion. One advantage of this model is that it is straightforward find the inverse $G_c^{-1}(s)$, and the feed-forward actuation signal can be found for sufficiently smooth reference signals. Another advantage is that it can be combined with a model of the vibrational dynamics of the system and be explicitly accounted for during control design.

Appendix D

Online Parameter Identification Schemes

The parameter identification schemes used in Chapters 2, 5, and 6 are summarized below. The presentation provides some background and technical details, but is aimed at explaining how the schemes were implemented. This Appendix is collated from material entirely found in [33, 37, 62, 88, 89, 91, 102, 111, 143, 180, 181, 204, 207].

D.1 Recursive Least-Squares Method

The least-squares method is perhaps the best known method for parameter identification. It can be used in recursive and non-recursive form. It works by fitting experimental data to a given model by minimizing the sum of the squares of the difference between the computed response from the model and the actual measured response. Noise and disturbances in the measured signal is then expected to have less effect on the accuracy of the resulting parameter estimates.

The starting point is a model of the system, assuming the measured response z can be described as a vector of model parameters θ appearing affinely with a vector of known signals, φ, called the regressor,

$$z = \theta^{\mathrm{T}}\varphi \ . \tag{D.1}$$

The objective of the method is to find a good estimate of the vector of parameter values, $\hat{\theta}$. By computing the estimated response

$$\hat{z} = \hat{\theta}^{\mathrm{T}}\varphi$$

the estimate error ϵ can be formed as

$$\epsilon = \frac{z - \hat{z}}{m^2} \tag{D.2}$$

where m^2 is a normalization signal defined below in (D.4). The (modified) least-squares estimate of the parameters is obtained by minimizing the cost-function

$$J(\hat{\theta}) = \frac{1}{2}\int_0^t \mathrm{e}^{-\kappa_f(t-\tau)}\epsilon^2 m^2 \,\mathrm{d}\tau + \frac{1}{2}\mathrm{e}^{-\kappa_f t}(\hat{\theta} - \hat{\theta}_0)^{\mathrm{T}} Q_0 (\hat{\theta} - \hat{\theta}_0) \ , \tag{D.3}$$

where a forgetting factor $\kappa_f > 0$ is introduced to discount past data in order to achieve exponential convergence. The matrix Q_0 is used to weigh the significance of the initial parameter estimates, $\hat{\theta}_0$, in minimizing the cost-function.

The above expressions can be used to derive both the recursive and the non-recursive form of the least-squares method. The recursive form is of interest, as it is amenable to online implementation. The parameter update law is then given by

$$\dot{\hat{\theta}} = P\epsilon\varphi\,,\ \theta(0) = \theta_0$$

The matrix P is called the covariance matrix, and can be found by computing

$$\dot{P} = \begin{cases} \kappa_f P - \frac{P\varphi\varphi^{\mathrm{T}}P}{m^2}\,, & \text{if}\,\|P\| \leq R_0 \\ 0 & \text{otherwise} \end{cases}\ ,\ P(0) = Q_0^{-1}\ .$$

The initial covariance matrix must be symmetric and positive definite, $P(0) = Q_0^{-1} = Q_0^{-\mathrm{T}} > 0$. By using the forgetting factor κ_f when updating the covariance P, there is a possibility for P to grow without bound. To avoid this, some norm on P, $\|P\|$, is not allowed to grow larger than R_0, by stopping the update of P by setting $\dot{P} = 0$. The initial covariance matrix should therefore also satisfy $\|P(0)\| \leq R_0$.

The normalization signal m^2 can be constructed in various ways. Here it is taken to be

$$m^2 = 1 + {n_s}^2,\ {n_s}^2 = \varphi^{\mathrm{T}}P\varphi\,. \tag{D.4}$$

Normalization ensures boundedness of the signals used in the identification scheme.

This method is referred to as modified least-squares with forgetting factor. It has the properties $\epsilon, \epsilon n_s, \hat{\theta}, \dot{\hat{\theta}}, P \in \mathcal{L}_\infty$ and $\epsilon, \epsilon n_s, \dot{\hat{\theta}} \in \mathcal{L}_2$. In addition it has the formal property that if the regressor φ is persistently exciting (PE), then $\hat{\theta}$ converges exponentially to θ.

It should also be noted the to avoid pure numerical differentiation when estimating parameters of an linear differential equation of degree n, the output z and regressor vector φ should be filtered by a filter with relative degree ${n_f}^\star \geq n$.

D.1.1 Persistency of Excitation

A piecewise continuous signal vector $\varphi : \mathbb{R}^+ \to \mathbb{R}^n$ is said to be persistently exciting (PE) in $\mathbb{R}^n$ with a level of excitation $\alpha_0 > 0$ if there exist constants $\alpha_1, T_0 > 0$ such that

$$\alpha_1 I \geq \frac{1}{T_0}\int_t^{t+T_0} \varphi\varphi^{\mathrm{T}}\,\mathrm{d}\tau \geq \alpha_0 I,\ \forall t \geq 0\,.$$

For linear single-input-single-output (SISO) models, a PE regressor vector is obtained if the input signal u is sufficiently rich. In brief, an input signal is sufficiently rich if it contains more frequency components than half the number of unknown parameters in the model.

D.2 Integral Adaptive Law

The gradient method based on the integral cost function (integral adaptive law) behaves similarly to the least-squares method, but with the added benefit of a user selectable convergence rate, and it eliminates the need for the initial covariance matrix Q_0^{-1}.

The method recursively minimizes the cost-function

$$J(\hat{\theta}) = \frac{1}{2}\int_0^t \mathrm{e}^{-\kappa_f(t-\tau)}\epsilon^2 m^2 \,\mathrm{d}\tau \,, \tag{D.5}$$

which is identical to (D.3), except for the term including the inverse of the initial covariance matrix Q_0^{-1}. Eq. (D.5) includes the estimate error ϵ as defined in (D.2), the normalization signal m^2 defined below in (D.6), and a forgetting factor $\kappa_f > 0$ to discount past data in order to achieve exponential convergence. Applying the gradient method, $\dot{\hat{\theta}} = -\Gamma\nabla J(\hat{\theta})$, to find the minimum of (D.5) results in the recursive expressions

$$\begin{aligned}
\dot{\hat{\theta}} &= -\Gamma(R\hat{\theta} + Q) \,,\ \hat{\theta}(0) = \hat{\theta}_0 \\
\dot{R} &= -\kappa_f R + \frac{\varphi\varphi^{\mathrm{T}}}{m^2} \,,\ R(0) = 0 \\
\dot{Q} &= -\kappa_f Q - \frac{z\varphi}{m^2} \,,\ Q(0) = 0
\end{aligned}$$

where $\Gamma = \Gamma^{\mathrm{T}} > 0$ is the adaptive gain, and the normalization signal m^2 is constructed as

$$m^2 = 1 + {n_s}^2 \,,\ {n_s}^2 = \alpha_0\varphi^{\mathrm{T}}\varphi \,,\ \alpha_0 > 0 \,. \tag{D.6}$$

This method has the properties $\epsilon, \epsilon n_s, \hat{\theta}, \dot{\hat{\theta}}, P \in \mathcal{L}_\infty$, $\epsilon, \epsilon n_s, \dot{\hat{\theta}} \in \mathcal{L}_2$, and

$$\lim_{t\to\infty} |\dot{\hat{\theta}}| = 0 \,.$$

The method has the formal property that if the regressor φ is persistently exciting (PE), and $n_s, \varphi \in \mathcal{L}_\infty$, then $\hat{\theta}$ will converge exponentially to θ, and for $\Gamma = \gamma_0 I$, the convergence rate can be made arbitrarily large by increasing the value of γ_0.

D.3 Extended Kalman Filter

The extended Kalman filter is a popular method for recursive parameter identification. It is based on a weighted least-squares criterion, but unlike the recursive least-squares method and the integral adaptive law, both the parameters and the states of the system are estimated.

D.3.1 Continuous Extended Kalman Filter

A general non-linear system is described by

$$\begin{aligned}
\dot{x} &= f(x,u) + w \\
y &= h(x) + v
\end{aligned} \tag{D.7}$$

where $x \in \mathbb{R}^n$ are the states, $y \in \mathbb{R}^m$ are the measurements, $u \in \mathbb{R}^l$ is the input, and w and v are zero-mean Gaussian white noise processes, described uniquely by the process noise covariance $Q\delta(t)$, and the measurement noise covariance $R\delta(t)$, respectively:

$$E[w(t)w(\tau)^{\mathrm{T}}] = Q\delta(t-\tau)$$
$$E[v(t)v(\tau)^{\mathrm{T}}] = R\delta(t-\tau)$$

The extended Kalman filter (EKF) is obtained when the states of the system (D.7) are estimated by linearizing about state trajectory of the filter. Linearization is done by computing the Jacobians

$$F = \left.\frac{\partial f}{\partial x}\right|_{\hat{x}} , \; H = \left.\frac{\partial h}{\partial x}\right|_{\hat{x}} .$$

Now the state estimates $\hat{x}$ can be computed by solving

$$\begin{aligned}
\hat{x}(0) &= E[x(0)] \\
P(0) &= E[(x(0)-\hat{x}(0))(x(0)-\hat{x}(0))^{\mathrm{T}}] \\
\dot{\hat{x}} &= f(\hat{x},u) + K[y - h(\hat{x})] \\
K &= PH^{\mathrm{T}}R^{-1} \\
\dot{P} &= FP + PF^{\mathrm{T}} + Q - KHP ,
\end{aligned}$$

where P is the error covariance, and K is the Kalman gain. The above recursion is equivalent to minimizing the cost function

$$J(\hat{x}) = \frac{1}{2}(\hat{x}-\hat{x}(0))^{\mathrm{T}}P(0)^{-1}(\hat{x}-\hat{x}(0)) + \frac{1}{2}\int_0^t \left((y-h(\hat{x}))^{\mathrm{T}}R^{-1}(y-h(\hat{x})) + w^{\mathrm{T}}Q^{-1}w\right) \mathrm{d}\tau$$

subject to $\dot{x} = f(x,u) + w$. To summarize; large measurement noise covariance parameters will penalize the use of measurements, and large process noise covariance parameters will penalize the use of predicted states from the system model. $P(0)^{-1}$ has the same effect as Q_0 in (D.3).

The extended Kalman filter can be used for parameter identification by modeling unknown parameters as Wiener processes. Consider the linear system

$$\dot{x} = A(\theta)x + B(\theta)u + w$$
$$y = C(\theta)x + v$$

with unknown parameters $\theta \in \mathcal{R}^p$. By augmenting the state vector to include the unknown parameters, $\chi^{\mathrm{T}} = [x^{\mathrm{T}}, \theta^{\mathrm{T}}]$, the non-linear system $\dot{\chi} = f(\chi,u) + w$, $y = h(\chi) + v$ is obtained, where

$$f(\chi,u) = \begin{bmatrix} A(\theta)x + B(\theta)u \\ 0 \end{bmatrix}$$
$$h(\chi) = C(\theta)x .$$

The Jacobians F and H for this system are found as

$$F = \left[\begin{array}{cc} A(\theta) & \frac{\partial}{\partial\theta}[A(\theta)x + B(\theta)u] \\ 0 & 0 \end{array} \right]_{\hat{x},\hat{\theta}},$$
$$H = \left[\begin{array}{cc} C(\theta) & \frac{\partial}{\partial\theta}[C(\theta)x] \end{array} \right]_{\hat{x},\hat{\theta}}.$$

D.3.2 Hybrid Extended Kalman Filter

When using a numerical integration scheme for solving continuous time differential equations, a smaller step size should provide more accurate results. Applying a continuous-discrete, or hybrid, version of the EKF (HEKF) might therefore improve the accuracy of the estimates, since the continuous part of the method can be run at a higher rate than the sampling rate.

The system response (D.7) is now modified to the hybrid system

$$\begin{aligned} \dot{x} &= f(x, u_k) + w \\ y_k &= h(x_k) + v_k \end{aligned}$$

where y_k is sampled sequence of measurements, u_k is the input sequence, and v_k is a Gaussian white noise sequence, and the noise properties are given by

$$\begin{aligned} E[w(t)w(\tau)^{\mathrm{T}}] &= Q\delta(t-\tau) \\ E[v_k v_i^{\mathrm{T}}] &= R_d\delta_{ki} \end{aligned}$$

where $R_d \approx R/T_s$, and T_s is the sampling period. Using the initial values

$$\hat{x}_0 = E[x(0)] \text{ and } P_0 = E[(x(0) - \hat{x}_0)(x(0) - \hat{x}_0)^{\mathrm{T}}],$$

the state estimates $\hat{x}_k$ for $k = 1, 2, 3, ...$ are computed by the hybrid EKF in two parts.

(1) The a priori state estimates and error covariance, from time-step $k-1$ to k^- (*i.e.*, for the sampling period T_s), are found by solving

$$\begin{aligned} \dot{x} &= f(x, u_{k-1}) \\ \dot{P} &= FP + PF^{\mathrm{T}} + Q, \end{aligned}$$

where the initial values are given by $\hat{x}(0) = \hat{x}_{k-1}$ and $P(0) = P_{k-1}$.

(2) Given the a priori estimates $\hat{x}_k^- = \hat{x}(kT_s)$ and error covariance $P_k^- = P(kT_s)$, the a posteriori state estimates $\hat{x}_k$ and error covariance P_k are found by computing:

$$\begin{aligned} K_k &= P_k^- H^{\mathrm{T}}(HP_k^- H^{\mathrm{T}} + R_d)^{-1} \\ \hat{x}_k &= \hat{x}_k^- + K_k(y_k - h(\hat{x}_k^-)) \\ P_k &= (I - K_k H)P_k^-(I - K_k H) + K_k R_d K_k^{\mathrm{T}} \end{aligned}$$

D.3.3 Convergence Properties for the Extended Kalman Filter

For the extended Kalman filter (EKF) there does not exist any general proof of convergence. The EKF can provide good performance, but the convergence properties for the estimates are susceptible to the choice of initial values and covariance

tuning, as well as the input signal. As in the case for the recursive least-squares method and the integral adaptive law, the input signal used when applying the EKF must provide sufficient excitation in some sense for the state and parameter estimates to converge. In many practical applications, this happens for signals that are PE.

Appendix E

Model Reference Adaptive Control & Model Reference Control

A brief and somewhat simplified summary of the model reference adaptive control (MRAC) and the model reference control (MRC) schemes is presented. The summary is entirely based on material from [111].

E.1 Model Reference Adaptive Control

The objective for the model reference adaptive control (MRAC) scheme is to output measurement y_p of a plant with uncertain parameters perfectly track the output of a reference model y_m. The scheme consists of a control law and an adaptive law, where the adaptive law is used to learn the parameter values of the uncertain plant model. The convergence of the plant parameter estimates ensures output tracking. The control law and an adaptive law can be designed independently and then combined using the certainty equivalence principle. The adaptive law can for example be the recursive least-squares method as presented Section D.1 or the gradient method based on the integral cost function as presented Section D.2.

An MRAC scheme can generally be implemented in direct and indirect form. The main difference is that for the direct form, the control law parameters are estimated directly, whereas for the indirect form, the plant parameters are estimated and subsequently mapped to the control parameters. If only some plant parameters are unknown, the indirect MRAC typically reduces the complexity and computational requirements of the parameter identification scheme significantly.

The plant model can be expressed as

$$\frac{y_p}{u_p}(s) = G_p(s) = k_p \frac{Z_p(s)}{R_p(s)} \ .$$

It is assumed that $R_p(s)$ and $Z_p(s)$ are monic polynomials. The polynomial $Z_p(s)$ is also Hurwitz, and is of degree m_p. In addition, the degree n_p of $R_p(s)$, the relative degree $n^\star = n_p - m_p$ of $G_p(s)$, and the sign of the high-frequency gain k_p are known.

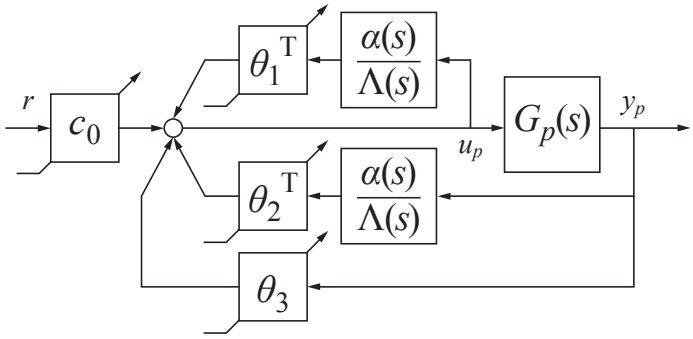

Figure E.1: The MRAC control law structure.

The reference model

$$\frac{y_m}{r}(s) = W_m(s) = k_m \frac{Z_m(s)}{R_m(s)}$$

consists of the monic Hurwitz polynomials $Z_m(s)$ and $R_m(s)$ of degrees q_m and p_m, respectively, where $p_m = n_p$, and the relative degree $n_m{}^\star = p_m - q_m = n^\star$.

The control law, as shown in Fig. E.1, is given by

$$u_p = \theta_1{}^{\mathrm{T}} \frac{\alpha(s)}{\Lambda(s)} u_p + \theta_2{}^{\mathrm{T}} \frac{\alpha(s)}{\Lambda(s)} y_p + \theta_3 y_p + c_0 r \tag{E.1}$$

where

$$\begin{array}{ll} \alpha(s) = [s^{n_p-2},\ s^{n_p-3},\ ...,\ s,\ 1]^{\mathrm{T}} & \text{for } n_p \geq 2 \\ \alpha(s) = 0 & \text{for } n_p = 1 \end{array} \tag{E.2}$$

and

$$\Lambda(s) = \Lambda_0(s) Z_m(s) \tag{E.3}$$

is a monic and Hurwitz polynomial of degree $n_p - 1$. Thus, $\Lambda_0(s)$ is a monic and Hurwitz polynomial of degree $n_0 = n_p - 1 - q_m$.

By using the control law structure in Fig. E.1 it is possible to generate the required signals using the scalar products of the time varying parameters in the vectors θ_1 and θ_2 and the signal vectors generated by the two linear time invariant filters given by $\frac{\alpha(s)}{\Lambda(s)}$. This greatly simplifies the implementation and the stability analysis of the MRAC scheme.

The control law parameter vector is

$$\bar{\theta}_c = \left[\theta_1{}^{\mathrm{T}},\ \theta_2{}^{\mathrm{T}},\ \theta_3,\ c_0\right]^{\mathrm{T}}$$

and should be chosen such that the closed-loop complementary sensitivity function matches the reference model, *i.e.*,

$$\frac{y_p}{r}(s) = T(s) = W_m(s) = \frac{y_m}{r}(s)\ .$$

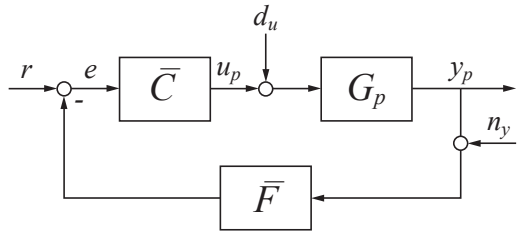

Figure E.2: General control structure.

With the above control law, the closed-loop complementary sensitivity is given by

$$T(s) = \frac{c_0 k_p Z_p(s)\Lambda(s)^2}{\Lambda(s)\left[\left(\Lambda(s) - {\theta_1}^{\mathrm{T}}\alpha(s)\right)R_p(s) - k_p Z_p(s)\left({\theta_2}^{\mathrm{T}}\alpha(s) + \theta_3\Lambda(s)\right)\right]} = k_m \frac{Z_m(s)}{R_m(s)} \,. \quad \text{(E.4)}$$

By choosing

$$c_0 = \frac{k_m}{k_p} \,, \quad \text{(E.5)}$$

eq. (E.4) can be written as the Bézout identity

$${\theta_1}^{\mathrm{T}}\alpha(s)R_p(s) + k_p Z_p(s)\left({\theta_2}^{\mathrm{T}}\alpha(s) + \theta_3\Lambda(s)\right) = \Lambda(s)R_p(s) - Z_p(s)\Lambda_0(s)R_m(s) \,,$$

which again can be expressed as

$$S\theta_c = p \,, \quad \text{(E.6)}$$

where $\theta_c = \left[{\theta_1}^{\mathrm{T}},\ {\theta_2}^{\mathrm{T}},\ \theta_3\right]^{\mathrm{T}}$ and S is a $(2n_p - 1) \times (2n_p - 1)$ Sylvester matrix that depends on the coefficients of the polynomials $R_p(s)$, $k_p Z_p(s)$ and $\Lambda(s)$, and p is a $(2n_p - 1)$ vector with the coefficients of the polynomial

$$\Lambda(s)R_p(s) - Z_p(s)\Lambda_0(s)R_m(s) \,.$$

For the indirect scheme, the adaptive law is used to learn the uncertain plant parameters θ of $G_p(s)$. For a specific choice of a reference model $W_m(s)$ and an output filter $1/\Lambda(s)$, the control law parameters $\bar{\theta}_c$ are determined by using the parameter mapping $\theta \to \bar{\theta}_c$ defined by (E.5) and (E.6).

E.2 Model Reference Control

The model reference control (MRC) scheme is equivalent to the MRAC scheme, excluding the adaptive law. The MRC objective is also to make the plant output y_p perfectly track the output of a reference model y_m, but it is assumed that the plant parameters are constant and known. This makes is possible to dispense of

the structure in Fig. E.1, and to use linear time invariant filters exclusively. The control law can then be expressed in the form of the general control structure in Fig. E.2.

The MRC control law is therefore given by

$$u_p = \bar{C}(s)(r - \bar{F}(s)y_p) \ ,$$

where $\bar{C}(s)$ is a feed-forward filter given as

$$\bar{C}(s) = \frac{c_0^\star \Lambda(s)}{\Lambda(s) - \theta_1^{\star\mathrm{T}} \alpha(s)} \ , \tag{E.7}$$

and $\bar{F}(s)$ is a feedback filter given as

$$\bar{F}(s) = -\frac{\theta_2^{\star\mathrm{T}} \alpha(s) + \theta_3^\star \Lambda(s)}{c_0^\star \Lambda(s)} \ . \tag{E.8}$$

This can be seen from (E.4), since

$$\begin{aligned}
&\frac{c_0^\star \Lambda(s) k_p Z_p(s)}{\left(\Lambda(s) - \theta_1^{\star\mathrm{T}} \alpha(s)\right) R_p - k_p Z_p(s) \left(\theta_2^{\star\mathrm{T}} \alpha(s) + \theta_3^\star \Lambda(s)\right)} \\
&\qquad = \frac{\frac{c_0^\star \Lambda(s)}{\Lambda(s) - \theta_1^{\star\mathrm{T}} \alpha(s)} k_p \frac{Z_p(s)}{R_p(s)}}{1 + \frac{c_0^\star \Lambda(s)}{\Lambda(s) - \theta_1^{\star\mathrm{T}} \alpha(s)} \left(-\frac{\theta_2^{\star\mathrm{T}} \alpha(s) + \theta_3^\star \Lambda(s)}{c_0^\star \Lambda(s)}\right) k_p \frac{Z_p(s)}{R_p(s)}} \\
&\qquad\qquad = \frac{\bar{C}(s) G_p(s)}{1 + \bar{C}(s) \bar{F}(s) G_p(s)} = T(s) \ .
\end{aligned}$$

The polynomials $\alpha(s)$ and $\Lambda(s)$ are still as defined in (E.2) and (E.3), and the feed-forward and feedback filters are determined by the known plant parameters $\theta^\star$ of $G_p(s)$, the chosen reference model $W_m(s)$ and output filter $1/\Lambda(s)$, since the control law parameters $\bar{\theta}_c^\star$ are determined by using the parameter mapping $\theta^\star \to \bar{\theta}_c^\star$ defined by (E.5) and (E.6).

References

[1] *Piezoelectric Ceramics – Properties and Applications*. Morgan Electro Ceramics.

[2] IEEE Standard on Piezoelectricity. *IEEE Std. 176-1987*, 1988. doi: 10.1109/IEEESTD.1988.79638.

[3] IEEE Standard for Terminology and Test Methods for Analog-to-Digital Converters. *IEEE Std. 1241-2000*, 2000. doi: 10.1109/IEEESTD.2001.92771.

[4] D. Y. Abramovitch and G. Franklin. A Brief History of Disk Drive Control. *Control Systems Magazine, IEEE*, 22(3):28–42, 2002.

[5] D. Y. Abramovitch, S. B. Andersson, L. Y. Pao, and G. Schitter. A Tutorial on the Mechanisms, Dynamics, and Control of Atomic Force Microscopes. In *American Control Conference, Proceedings of the*, New York, NY, 2007.

[6] D. Y. Abramovitch, S. Hoen, and R. Workman. Semi-Automatic Tuning of PID Gains for Atomic Force Microscopes. *Asian Journal of Control*, 11(2): 188–195, 2009.

[7] H. J. M. T. A. Adriaens, W. L. de Koning, and R. Banning. Modeling Piezoelectric Actuators. *Mechatronics, IEEE/ASME Transactions on*, 5(4): 331–341, 2000.

[8] A. Amthor, S. Zschack, and C. Ament. Position Control on Nanometer Scale Based on an Adaptive Friction Compensation Scheme. In *34th Annual Conference of the IEEE Industrial Electronics Society, In Proceedings of the*, pages 2568–2573, Orlando, FL, 2008.

[9] B. D. O. Anderson. Controller Design: Moving From Theory to Practice. *Control Systems Magazine, IEEE*, 13(4):16–25, 1993.

[10] S. B. Andersson and L. Y. Pao. Non-Raster Sampling in Atomic Force Microscopy: A Compressed Sensing Approach. In *American Control Conference, Proceedings of the*, pages 2485–2490, Montreal, 2012.

[11] T. Ando, N. Kodera, E. Takai, D. Maruyama, K. Saito, and A. Toda. A high-speed atomic force microscope for studying biological macromolecules. *Proceedings of the National Academy of Sciences*, 98(22):12468–12472, 2001.

[12] S. S. Aphale, A. J. Fleming, and S. O. R. Moheimani. High speed nano-scale positioning using a piezoelectric tube actuator with active shunt control. *Micro & Nano Letters*, 2(1):9–12, 2007.

[13] S. S. Aphale, A. J. Fleming, and S. O. R. Moheimani. Integral Resonant Control of Collocated Smart Structures. *Smart Materials and Structures*, 16 (2):439–446, 2007.

[14] S. S. Aphale, B. Bhikkaji, and S. O. R. Moheimani. Minimizing Scanning Errors in Piezoelectric Stack-Actuated Nanopositioning Platforms. *Nanotechnology, IEEE Transactions on*, 7(1):79–90, 2008.

[15] S. S. Aphale, S. Devasia, and S. O. R. Moheimani. High-Bandwidth Control of a Piezoelectric Nanopositioning Stage in the Presence of Plant Uncertainties. *Nanotechnology*, 19:125503 (9 pages), 2008.

[16] U. Aridogan, Y. Shan, and K. K. Leang. Design and Analysis of Discrete-Time Repetitive Control for Scanning Probe Microscopes. *Journal of Dynamic Systems Measurement and Control, Transactions of the ASME*, 131 (6):061103 (12 pages), 2009.

[17] K. J. Åström and T. Hagglund. The future of PID control. In *Control Engineering Practice*, pages 1163–1175, 2001.

[18] R. Banning, W. L. de Koning, H. J. M. T. A. Adriaens, and R. K. Koops. State-space analysis and identification for a class of hysteretic systems. *Automatica*, 37(12):1883–1892, 2001.

[19] H. Barnard, C. Randall, D. Bridges, and P. K. Hansma. The long range voice coil atomic force microscope. *Review of Scientific Instruments*, 83(2):023705 (4 pages), 2012.

[20] R. C. Barrett and C. F. Quate. Optical scan-correction system applied to atomic force microscopy. *Review of Scientific Instruments*, 62(2):1393–1399, 1991.

[21] S. Bashash and N. Jalili. Robust Multiple Frequency Trajectory Tracking Control of Piezoelectrically Driven Micro/Nanopositioning Systems. *Control Systems Technology, IEEE Transactions on*, 15(5):867–878, 2007.

[22] A. Bazaei, Y. K. Yong, and S. O. R. Moheimani. High-speed Lissajous-scan atomic force microscopy: Scan pattern planning and control design issues. *Review of Scientific Instruments*, 83(6):063701 (10 pages), 2012.

[23] D. A. Berlincourt and H. Jaffe. Elastic and Piezoelectric Coefficients of Single-Crystal Barium Titanate. *Physical Review*, 111(1):143–148, 1958.

[24] D. A. Berlincourt, C. Cmolik, and H. Jaffe. Piezoelectric Properties of Polycrystalline Lead Titanate Zirconate Compositions. *Proceedings of the IRE*, 48(2):220–229, Feb. 1960.

[25] D. A. Berlincourt, B. Jaffe, H. Jaffe, and H. Krueger. Transducer Properties of Lead Titanate Zirconate Ceramics. *Ultrasonic Engineering, IRE Transactions on*, 7(1):1–6, 1960.

[26] B. Bhikkaji, M. Ratnam, and S. O. R. Moheimani. PVPF control of piezoelectric tube scanners. *Sensors and Actuators A: Physical*, 135:700–712, 2007.

[27] B. Bhikkaji, S. O. R. Moheimani, and I. R. Petersen. A Negative Imaginary Approach to Modeling and Control of a Collocated Structure. *Mechatronics, IEEE/ASME Transactions on*, 17(4):717–727, 2012.

[28] B. Bhushan, editor. *Springer Handbook of Nanotechnology*. Springer, 3rd edition, 2010.

[29] G. Binnig and D. P. E. Smith. Single-tube three-dimensional scanner for scanning tunneling microscopy. *Review of Scientific Instruments*, 57(8):1688–1689, 1986.

[30] G. Binnig, H. Rohrer, C. Gerber, and E. Weibel. Surface Studies by Scanning Tunneling Microscopy. *Physical Review Letters*, 49(1):57–61, 1982.

[31] G. Binnig, H. Rohrer, C. Gerber, and E. Weibel. 7x7 Reconstruction on Si(111) Resolved in Real Space. *Physical Review Letters*, 50(2):120–123, 1983.

[32] G. Binnig, C. F. Quate, and C. Gerber. Atomic Force Microscope. *Physical Review Letters*, 56(9):930–933, 1986.

[33] M. Boutayeb, H. Rafaralahy, and M. Darouach. Convergence Analysis of the Extended Kalman Filter Used as an Observer for Nonlinear Deterministic Discrete-Time Systems. *Automatic Control, IEEE Transactions on*, 42(4): 581–586, 1997.

[34] S. Boyd and C. Barratt. *Linear Controller Design: Limits of Performance*. Prentice-Hall, 1991.

[35] D. A. Bristow, M. Tharayil, and A. G. Alleyne. A Survey of Iterative Learning Control. *Control Systems Magazine, IEEE*, 26(3):96–114, 2006.

[36] D. A. Bristow, J. Dong, A. G. Alleyne, P. Ferreira, and S. Salapaka. High bandwidth control of precision motion instrumentation. *Review of Scientific Instruments*, 79(10):103704 (14 pages), 2008.

[37] R. G. Brown and P. Y. C. Hwang. *Introduction to Random Signals and Applied Kalman Filtering*. Wiley-Interscience, 1997.

[38] J. C. Burfoot. *Ferroelectrics – An Introduction to the Physical Principles*. Van Nostrand, 1967.

[39] D. J. Burns, G. E. Fantner, and K. Youcef-Toumi. Automatic lateral resonance identification from cantilever deflection information in high speed atomic force microscopy. In *American Control Conference, Proceedings of the*, pages 3240–3246, Montreal, 2012.

[40] P. I. Chang, P. Huang, J. Maeng, and S. B. Andersson. Local raster scanning for high-speed imaging of biopolymers in atomic force microscopy. *Review of Scientific Instruments*, 82(6):063703 (7 pages), 2011.

[41] C. J. Chen. *Introduction to Scanning Tunneling Microscopy*. Oxford University Press, 2nd edition, 2008.

[42] K. K. Chew and M. Tomizuka. Digital Control of Repetitive Errors in Disk Drive Systems. *Control Systems Magazine, IEEE*, 10(1):16–20, 1990.

[43] G. M. Clayton and S. Devasia. Iterative image-based modeling and control for higher scanning probe microscope performance. *Review of Scientific Instruments*, 78(8):083704 (12 pages), 2007.

[44] G. M. Clayton, S. Tien, K. K. Leang, Q. Zou, and S. Devasia. A Review of Feedforward Control Approaches in Nanopositioning for High-Speed SPM. *Journal of Dynamic Systems Measurement and Control, Transactions of the ASME*, 131(6):061101 (19 pages), 2009.

[45] B. D. Coleman and M. L. Hodgdon. A Constitutive Relation for Rate-Independent Hysteresis in Ferromagnetically Soft Materials. *International Journal of Engineering Science*, 24(6):897–919, 1986.

[46] B. D. Coleman and M. L. Hodgdon. On a Class of Constitutive Relations for Ferromagnetic Hysteresis. *Archive for Rational Mechanics and Analysis*, 99 (4):375–396, 1987.

[47] R. M. Corless, G. H. Gonnet, D. E. G. Hare, D. J. Jeffrey, and D. E. Knuth. On the Lambert W function. *Advances in Computational Mathematics*, 5(4): 329–359, 1996.

[48] D. Croft and S. Devasia. Vibration compensation for high speed scanning tunneling microscopy. *Review of Scientific Instruments*, 70(12):4600–4605, 1999.

[49] D. Croft, S. Stilson, and S. Devasia. Optimal tracking of piezo-based nanopositioners. *Nanotechnology*, 10(2):201–208, 1999.

[50] D. Croft, G. Shed, and S. Devasia. Creep, Hysteresis, and Vibration Compensation for Piezoactuators: Atomic Force Microscopy Application. *Journal of Dynamic Systems Measurement and Control, Transactions of the ASME*, 123:35–43, 2001.

[51] M. L. Culpepper and G. Anderson. Design of a low-cost nano-manipulator which utilizes a monolithic, spatial compliant mechanism. *Precision Engineering*, 28:469–482, 2004.

[52] H. Czichos, T. Saito, and L. Smith, editors. *Springer Handbook of Metrology and Testing*. Springer, 2nd edition, 2011.

[53] P. R. Dahl. A Solid Friction Model. Technical Report TOR-0158(3107-18)-1, The Aerospace Corporation, El Segundo, CA 90245, May 1968.

[54] D. Damjanovic. Hysteresis in Piezoelectric and Ferroelectric Materials. In G. Bertotti and I. D. Mayergoyz, editors, *The Science of Hysteresis*, pages 338–465. Academic Press, 2005.

[55] D. Damjanovic. Comments on Origins of Enhanced Piezoelectric Properties in Ferroelectrics. *Ultrasonics, Ferroelectrics and Frequency Control, IEEE Transactions on*, 56(8):1574–1585, 2009.

[56] J. David and B. De Moor. The opposite of analytic centering for solving minimum rank problems in control and identification. In *32nd IEEE Conference on Decision and Control, Proceedings of the*, pages 2901–2902, San Antonio, TX, 1993.

[57] S. Devasia. Should model-based inverse inputs be used as feedforward under plant uncertainty? *Automatic Control, IEEE Transactions on*, 47(11):1865–1871, 2002.

[58] S. Devasia, E. Eleftheriou, and S. O. R. Moheimani. A Survey of Control Issues in Nanopositioning. *Control Systems Technology, IEEE Transactions on*, 15(5):802–823, 2007.

[59] L. Dong and B. J. Nelson. Robotics in the Small. *IEEE Robotics & Automation Magazine*, 14(3):111–121, 2007.

[60] J. Doyle, B. Francis, and A. Tannenbaum. *Feedback Control Theory*. Macmillian, 1990.

[61] M. Edardar, X. Tan, and H. K. Khalil. Sliding-Mode Tracking Control of Piezo-Actuated Nanopositioners. In *American Control Conference, Proceedings of the*, pages 3825–3830, Montreal, 2012.

[62] O. Egeland and J. T. Gravdahl. *Modeling and Simulation for Automatic Control*. Marine Cybernetics, 2002.

[63] A. A. Eielsen and A. J. Fleming. Passive Shunt Damping of a Piezoelectric Stack Nanopositioner. In *American Control Conference, Proceedings of the*, pages 4963–4968, Baltimore, MD, 2010.

[64] A. A. Eielsen and J. T. Gravdahl. Adaptive Control of a Nanopositioning Device. In *51st IEEE Conference on Decision and Control, Proceedings of the*, Maui, HI, 2012.

[65] A. A. Eielsen, M. Vagia, J. T. Gravdahl, and K. Y. Pettersen. Damping and Tracking Control Schemes for Nanopositioning. *Mechatronics, IEEE/ASME Transactions on*. (Second version in review).

[66] A. A. Eielsen, J. T. Gravdahl, K. Y. Pettersen, and L. Vogl. Tracking Control for a Piezoelectric Nanopositioner Using Estimated States and Feedforward Compensation of Hysteresis. In *5th IFAC Symposium on Mechatronic Systems, Proceedings of the*, pages 96–104, Cambridge, MA, 2010.

[67] A. A. Eielsen, M. Burger, J. T. Gravdahl, and K. Y. Pettersen. PI^2-Controller Applied to a Piezoelectric Nanopositioner Using Conditional Integrators and Optimal Tuning. In *18th IFAC World Congress, Proceedings of the*, pages 887–892, Milano, 2011.

[68] A. A. Eielsen, T. Polóni, T. A. Johansen, and J. T. Gravdahl. Experimental comparison of adaptive control schemes for a nanopositioning device. In *Advanced Intelligent Mechatronics, 2011 IEEE/ASME International Conference on*, pages 510–517, Budapest, 2011.

[69] A. A. Eielsen, J. T. Gravdahl, and K. Y. Pettersen. Adaptive feed-forward hysteresis compensation for piezoelectric actuators. *Review of Scientific Instruments*, 83(8):085001 (8 pages), 2012.

[70] A. A. Eielsen, K. K. Leang, and J. T. Gravdahl. Robust Damping PI Repetitive Control for Nanopositioning. In *American Control Conference, Proceedings of the*, pages 3803–3810, Montreal, 2012.

[71] A. A. Eielsen, M. Vagia, J. T. Gravdahl, and K. Y. Pettersen. Fixed-Structure, Low-Order Damping and Tracking Control Schemes for Nanopositioning. In *6th IFAC Symposium on Mechatronic Systems, Proceedings of the*, 2013. (Submitted).

[72] D. M. Eigler and E. K. Schweizer. Positioning single atoms with a scanning tunnelling microscope. *Nature*, 344:524–526, 1990.

[73] L. El Ghaoui and P. Gahinet. Rank Minimization Under LMI Constraints: a Framework for Output Feedback Problems. In *European Control Conference, Proceedings of the*, pages 1176–1179, Groningen, 1993.

[74] O. el Rifai and K. Youcef-Toumi. Coupling in Piezoelectric Tube Scanners Used in Scanning Probe Microscopes. In *American Control Conference, Proceedings of the*, pages 3251–3255, Arlington, VA, 2001.

[75] O. el Rifai and K. Youcef-Toumi. Design and Control of Atomic Force Microscopes. In *American Control Conference, Proceedings of the*, pages 3714–3719, Denver, CO, 2003.

[76] J. L. Fanson and T. K. Caughey. Positive Position Feedback-Control for Large Space Structures. *AIAA Journal*, 28(4):717–724, 1990.

[77] A. J. Fleming. Time-domain adaptive feed-forward control of nanopositioning systems with periodic inputs. In *American Control Conference, Proceedings of the*, pages 1676–1681, St. Louis, MO, 2009.

[78] A. J. Fleming. Nanopositioning System With Force Feedback for High-Performance Tracking and Vibration Control. *Mechatronics, IEEE/ASME Transactions on*, 15(3):433–447, 2010.

[79] A. J. Fleming. Dual-Stage Vertical Feedback for High-Speed Scanning Probe Microscopy. *Control Systems Technology, IEEE Transactions on*, 19(1):156–165, 2011.

[80] A. J. Fleming and K. K. Leang. Charge drives for scanning probe microscope positioning stages. *Ultramicroscopy*, 108(12):1551–1557, 2008.

[81] A. J. Fleming and K. K. Leang. Integrated Strain and Force Feedback for High Performance Control of Piezoelectric Actuators. *Sensors and Actuators A: Physical*, 161(1-2):256–265, 2010.

[82] A. J. Fleming and S. O. R. Moheimani. Sensorless Vibration Suppression and Scan Compensation for Piezoelectric Tube Nanopositioners. *Control Systems Technology, IEEE Transactions on*, 14(1):33–44, 2006.

[83] A. J. Fleming and A. G. Wills. Optimal Periodic Trajectories for Band-Limited Systems. *Control Systems Technology, IEEE Transactions on*, 17 (3):552–562, 2009.

[84] A. J. Fleming, A. G. Wills, and S. Moheimani. Sensor Fusion for Improved Control of Piezoelectric Tube Scanners. *Control Systems Technology, IEEE Transactions on*, 16(6):1265–1276, 2008.

[85] A. J. Fleming, S. Aphale, and S. O. R. Moheimani. A New Method for Robust Damping and Tracking Control of Scanning Probe Microscope Positioning Stages. *Nanotechnology, IEEE Transactions on*, 9(4):438–448, 2010.

[86] B. A. Francis and W. M. Wonham. The Internal Model Principle for Linear Multivariable Regulators. *Applied Mathematics and Optimization*, 2(2):170–194, 1975.

[87] B. A. Francis and W. M. Wonham. Internal Model Principle of Control-Theory. *Automatica*, 12(5):457–465, 1976.

[88] H. Garnier and L. Wang, editors. *Identification of Continuous-time Models from Sampled Data*. Springer, 2008.

[89] J. Gauthier and G. Bornard. Observability for Any u(t) of a Class of Nonlinear Systems. *Automatic Control, IEEE Transactions on*, 26(4):922–926, 1981.

[90] M. Gautier and P. Poignet. Extended Kalman filtering and weighted least squares dynamic identification of robot. *Control Engineering Practice*, 9(12): 1361–1372, 2001.

[91] A. Gelb, editor. *Applied Optimal Estimation*. The MIT Press, 1974.

[92] M. Géradin and D. Rixen. *Mechanical Vibrations – Theory and Applications to Structural Dynamics*. Wiley, 2nd edition, 1997.

[93] G. C. Goodwin and R. L. Payne. *Dynamic System Identification: Experiment Design and Data Analysis*. Academic Press, 1977.

[94] G. C. Goodwin, S. F. Graebe, and M. E. Salgado. *Control System Design*. Prentice Hall, 2000.

[95] K. M. Grigoriadis and R. E. Skelton. Low-order Control Design for LMI Problems Using Alternating Projection Methods. *Automatica*, 32(8):1117–1125, 1996.

[96] N. W. Hagood and A. von Flotow. Damping of Structural Vibrations with Piezoelectric Materials and Passive Electrical Networks. *Journal of Sound and Vibration*, 146(2):243–268, 1991.

[97] P. Hansma, G. Schitter, G. E. Fantner, and C. Prater. High-Speed Atomic Force Microscopy. *Science*, 314:601–602, 2006.

[98] S. Hara, Y. Yamamoto, T. Omata, and M. Nakano. Repetitive Control System: a New Type Servo System for Periodic Exogenous Signals. *Automatic Control, IEEE Transactions on*, 33(7):659–668, 1988.

[99] L. Harriott. Limits of Lithography. *Proceedings of the IEEE*, 89(3):366–374, 2001.

[100] W. P. Heath and S. Gayadeen. Simple robustness measures for control of MISO and SIMO plants. In *18th IFAC World Congress, Proceedings of the*, pages 11356–11361, Milano, 2011.

[101] B. E. Helfrich, C. Lee, D. A. Bristow, X. H. Xiao, J. Dong, A. G. Alleyne, S. M. Salapaka, and P. M. Ferreira. Combined H∞-Feedback Control and Iterative Learning Control Design With Application to Nanopositioning Systems. *Control Systems Technology, IEEE Transactions on*, 18(2):336–351, 2010.

[102] R. Hermann and A. J. Krener. Nonlinear Controllability and Observability. *Automatic Control, IEEE Transactions on*, 22(5):728–740, 1977.

[103] K. J. G. Hinnen, R. Fraanje, and M. Verhaegen. The application of initial state correction in iterative learning control and the experimental validation on a piezoelectric tube scanner. *Proceedings of the Institution of Mechanical Engineers, Part I: Journal of Systems and Control Engineering*, 218:503–511, 2004.

[104] C. Hol and C. Scherer. Fixed Order H∞-Synthesis: Computing Optimal Values by Robust Performance Analysis. In *American Control Conference, Proceedings of the*, pages 3285–3290, Boston, MA, 2004.

[105] R. Horowitz, Y. Li, K. Oldham, S. Kon, and X. Huang. Dual-stage servo systems and vibration compensation in computer hard disk drives. *Control Engineering Practice*, 15(3):291–305, 2007.

[106] N. Hovakimyan and C. Cao. $\mathcal{L}_1$ *Adaptive Control Theory: Guaranteed Robustness with Fast Adaptation*. Society for Industrial and Applied Mathematics, 2010.

[107] S. Hudlet, M. Saint Jean, D. Royer, J. Berger, and C. Guthmann. In situ measurement of large piezoelectric displacements in resonant atomic force microscopy. *Review of Scientific Instruments*, 66(4):2848–2852, 1995.

[108] A. D. L. Humphris, J. K. Hobbs, and M. J. Miles. Ultrahigh-speed scanning near-field optical microscopy capable of over 100 frames per second. *Applied Physics Letters*, 83(1):6–8, 2003.

[109] S. Ibaraki and M. Tomizuka. Tuning of a Hard Disk Drive Servo Controller Using Fixed-Structure H∞ Controller Optimization. *Journal of Dynamic Systems Measurement and Control, Transactions of the ASME*, 123(3):544–560, 2001.

[110] T. Inoue. Practical Repetitive Control System Design. In *29th IEEE Conference on Decision and Control, Proceedings of the*, pages 1673–1678, Honolulu, HI, 1990.

[111] P. A. Ioannou and J. Sun. *Robust Adaptive Control*. Prentice Hall, 1995.

[112] F. Irgens. *Continuum Mechanics*. Springer, 2008.

[113] T. Iwasaki. The Dual Iteration for Fixed-Order Control. *Automatic Control, IEEE Transactions on*, 44(4):783–788, 1999.

[114] R. V. Iyer and X. Tan. Control of Hysteretic Systems Through Inverse Compensation. *Control Systems Magazine, IEEE*, 29(1):83–99, 2009.

[115] H. Jaffe and D. A. Berlincourt. Piezoelectric Transducer Materials. *Proceedings of the IEEE*, 53(10):1372–1386, 1965.

[116] H. Janocha and K. Kuhnen. Real-time compensation of hysteresis and creep in piezoelectric actuators. *Sensors and Actuators A: Physical*, 79:83–89, 2000.

[117] H. Jung, J. Y. Shim, and D. Gweon. New open-loop actuating method of piezoelectric actuators for removing hysteresis and creep. *Review of Scientific Instruments*, 71(9):3436–3440, 2000.

[118] H. Kaizuka and B. Siu. A Simple Way to Reduce Hysteresis and Creep When Using Piezoelectric Actuators. *Japanese Journal of Applied Physics, Part 2: Letters*, 27(5):L773–L776, 1988.

[119] W. J. Karnavas, P. J. Sanchez, and A. T. Bahill. Sensitivity Analyses of Continuous and Discrete Systems in the Time and Frequency Domains. *Systems, Man and Cybernetics, IEEE Transactions on*, 23(2):488–501, 1993.

[120] B. J. Kenton and K. K. Leang. Design and Control of a Three-Axis Serial-Kinematic High-Bandwidth Nanopositioner. *Mechatronics, IEEE/ASME Transactions on*, 17(2):356–369, 2012.

[121] B. J. Kenton, A. J. Fleming, and K. K. Leang. Compact ultra-fast vertical nanopositioner for improving scanning probe microscope scan speed. *Review of Scientific Instruments*, 82(12):123703 (8 pages), 2011.

[122] K.-S. Kim and Q. Zou. Model-less Inversion-based Iterative Control for Output Tracking: Piezo Actuator Example. In *American Control Conference, Proceedings of the*, pages 2710–2715, Seattle, WA, 2008.

[123] N. Kodera, H. Yamashita, and T. Ando. Active damping of the scanner for high-speed atomic force microscopy. *Review of Scientific Instruments*, 76(5): 053708 (5 pages), 2005.

[124] N. Kodera, M. Sakashita, and T. Ando. Dynamic proportional-integral-differential controller for high-speed atomic force microscopy. *Review of Scientific Instruments*, 77(8):083704 (7 pages), 2006.

[125] K. R. Koops, P. M. L. O. Scholte, and W. L. de Koning. Observation of zero creep in piezoelectric actuators. *Applied Physics A: Materials Science & Processing*, 68(6):691–697, 1999.

[126] M. Krstic, I. Kanellakopoulos, and P. V. Kokotovic. *Nonlinear and Adaptive Control Design*. Wiley-Interscience, 1995.

[127] S. Kuiper and G. Schitter. Active damping of a piezoelectric tube scanner using self-sensing piezo actuation. *Mechatronics*, 20(6):656–665, 2010.

[128] S. Kuiper and G. Schitter. Model-based feedback controller design for dual actuated atomic force microscopy. *Mechatronics*, 22(3):327–337, 2012.

[129] S. Kuiper, A. J. Fleming, and G. Schitter. Dual Actuation for High Speed Atomic Force Microscopy. In *5th IFAC Symposium on Mechatronic Systems, Proceedings of the*, pages 220–226, Cambridge, MA, 2010.

[130] Y. Kuk and P. J. Silverman. Scanning tunneling microscope instrumentation. *Review of Scientific Instruments*, 60(2):165–180, 1989.

[131] J. Kwon, J. Hong, Y.-S. Kim, D.-Y. Lee, K. Lee, S.-m. Lee, and S.-i. Park. Atomic force microscope with improved scan accuracy, scan speed, and optical vision. *Review of Scientific Instruments*, 74(10):4378–4383, 2003.

[132] T. I. Laakso, V. Välimäki, M. Karjalainen, and U. K. Laine. Splitting the Unit Delay. *Signal Processing Magazine, IEEE*, 13(1):30–60, 1996.

[133] J. C. Lagarias, J. A. Reeds, M. H. Wright, and P. E. Wright. Convergence Properties of the Nelder-Mead Simplex Method in Low Dimensions. *SIAM Journal on Optimization*, 9(1):112–147, 1998.

[134] L. Landau, E. Lifshitz, A. Kosevich, and L. Pitaevskii. *Theory of Elasticity*, volume 7 of *Course of Theoretical Physics*. Butterworth-Heinemann, 3rd edition, 1984.

[135] K. K. Leang and S. Devasia. Design of hysteresis-compensating iterative learning control for piezo-positioners: Application to atomic force microscopes. *Mechatronics*, 16:141–158, 2006.

[136] K. K. Leang and A. J. Fleming. High-Speed Serial-Kinematic SPM Scanner: Design and Drive Considerations. *Asian Journal of Control*, 11(2):144–153, 2009.

[137] K. K. Leang, Q. Zou, and S. Devasia. Feedforward Control of Piezoactuators in Atomic Force Microscope Systems. *Control Systems Magazine, IEEE*, 29 (1):70–82, 2009.

[138] C. Lee and S. M. Salapaka. Robust broadband nanopositioning: fundamental trade-offs, analysis, and design in a two-degree-of-freedom control framework. *Nanotechnology*, 20:035501 (16 pages), 2009.

[139] J. Li and T.-C. Tsao. Robust Performance Repetitive Control Systems. *Journal of Dynamic Systems Measurement and Control, Transactions of the ASME*, 123(3):330–337, 2001.

[140] Y. Li and J. Bechhoefer. Feedforward control of a closed-loop piezoelectric translation stage for atomic force microscope. *Review of Scientific Instruments*, 78(1):013702 (8 pages), 2007.

[141] Y. Li and J. Bechhoefer. Feedforward Control of a Piezoelectric Flexure Stage for AFM. In *American Control Conference, Proceedings of the*, pages 2703–2709, Seattle, WA, 2008.

[142] H. C. Liaw, B. Shirinzadeh, and J. Smith. Robust motion tracking control of piezo-driven flexure-based four-bar mechanism for micro/nano manipulation. *Mechatronics*, 18(2):111–120, 2008.

[143] L. Ljung. Asymptotic Behavior of the Extended Kalman Filter as a Parameter Estimator for Linear Systems. *Automatic Control, IEEE Transactions on*, 24(1):36–50, 1979.

[144] L. Ljung. *System Identification: Theory for the User*. Prentice Hall, 2nd edition, 1999.

[145] R. G. Lyons. *Understanding Digital Signal Processing*. Prentice Hall, 3nd edition, 2010.

[146] J. W. Macki, P. Nistri, and P. Zecca. Mathematical Models for Hysteresis. *SIAM Review*, 35(1):94–123, 2008.

[147] J. Maess, A. J. Fleming, and F. Allgöwer. Simulation of Piezoelectric Tube Actuators by Reduced Finite Element Models for Controller Design. In *American Control Conference, Proceedings of the*, pages 4221–4226, New York, NY, 2007.

[148] J. Maess, A. J. Fleming, and F. Allgöwer. Model-Based Vibration Suppression in Piezoelectric Tube Scanners Through Induced Voltage Feedback. In *American Control Conference, Proceedings of the*, pages 2022–2027, Seattle, WA, 2008.

[149] E. Manske, T. Hausotte, R. Mastylo, T. Machleidt, K.-H. Franke, and G. Jäger. New applications of the nanopositioning and nanomeasuring machine by using advanced tactile and non-tactile probes. *Measurement Science and Technology*, 18(2):520–527, 2007.

[150] I. M. Y. Mareels, M. Gevers, R. R. Bitmead, C. R. Johnson, R. L. Kosut, and M. A. Poubelle. How exciting can a signal really be? *Systems & Control Letters*, 8(3):197–204, 1987.

[151] I. D. Mayergoyz. *Mathematical Models of Hysteresis and their Applications*. Academic Press, 2003.

[152] L. Meirovitch. *Elements of Vibration Analysis*. Electronic and Electrical Engineering. McGraw-Hill, 2nd edition, 1986.

[153] L. Meirovitch. *Dynamics and Control of Structures*. Wiley-Interscience, 1990.

[154] R. J. E. Merry, M. Uyanik, R. van de Molengraft, R. K. Koops, M. van Veghel, and M. Steinbuch. Identification, Control and Hysteresis Compensation of a 3 DOF Metrological AFM. *Asian Journal of Control*, 11(2):130–143, 2009.

[155] R. J. E. Merry, D. J. Kessels, W. P. M. H. Heemels, M. J. G. van de Molengraft, and M. Steinbuch. Delay-varying repetitive control with application to a walking piezo actuator. *Automatica*, 47(8):1737–1743, 2011.

[156] R. J. E. Merry, M. J. C. Ronde, R. van de Molengraft, K. R. Koops, and M. Steinbuch. Directional Repetitive Control of a Metrological AFM. *Control Systems Technology, IEEE Transactions on*, 19(6):1622–1629, 2011.

[157] R. H. Middleton, G. C. Goodwin, D. J. Hill, and D. Q. Mayne. Design Issues in Adaptive Control. *Automatic Control, IEEE Transactions on*, 33(1):50–58, 1988.

[158] S. O. R. Moheimani and Y. K. Yong. Simultaneous sensing and actuation with a piezoelectric tube scanner. *Review of Scientific Instruments*, 79(7): 073702 (5 pages), 2008.

[159] B. Mokaberi and A. A. G. Requicha. Compensation of Scanner Creep and Hysteresis for AFM Nanomanipulation. *Automation Science and Engineering, IEEE Transactions on*, 5(2):197–206, 2008.

[160] K. L. Moore, M. Dahleh, and S. P. Bhattacharyya. Iterative Learning Control: A Survey and New Results. *Journal of Robotic Systems*, 9(5):563–594, 1992.

[161] C. V. Newcomb and I. Flinn. Improving the Linearity of Piezoelectric Ceramic Actuators. *Electronics Letters*, 18(11):442–444, 1982.

[162] B. Noheda, J. A. Gonzalo, L. E. Cross, R. Guo, S.-E. Park, D. E. Cox, and G. Shirane. Tetragonal-to-monoclinic phase transition in a ferroelectric perovskite: The structure of PbZr0.52Ti0.48O3. *Physical Review B*, 61(13): 8687–8695, 2000.

[163] R. B. Northrop. *Introduction to Instrumentation and Measurement*. CRC Press, 2nd edition, 2005.

[164] J. F. Nye. *Physical Properties of Crystals*. Oxford University Press, 1985.

[165] A. W. Osburn and M. A. Franchek. Designing Robust Repetitive Controllers. *Journal of Dynamic Systems Measurement and Control, Transactions of the ASME*, 126(4):865–872, 2004.

[166] I. R. Petersen and A. Lanzon. Feedback Control of Negative-Imaginary Systems. *Control Systems Magazine, IEEE*, 30(5):54–72, 2010.

[167] G. Pipeleers, B. Demeulenaere, J. De Schutter, and J. Swevers. Robust High-Order Repetitive Control. In *American Control Conference, Proceedings of the*, pages 1080–1085, Seattle, WA, 2008.

[168] T. Polóni, A. A. Eielsen, B. Rohaľ-Ilkiv, and T. A. Johansen. Adaptive Model Estimation of Vibration Motion for a Nanopositioner with Moving Horizon Optimized Extended Kalman Filter. *Journal of Dynamic Systems Measurement and Control, Transactions of the ASME*. (Second version in review).

[169] T. Polóni, A. A. Eielsen, B. Rohaľ-Ilkiv, and T. A. Johansen. Moving Horizon Observer for Vibration Dynamics with Plant Uncertainties in Nanopositioning System Estimation. In *American Control Conference, Proceedings of the*, pages 3817–3824, Montreal, 2012.

[170] H. Pota, S. O. R. Moheimani, and M. Smith. Resonant Controllers for Smart Structures. *Smart Materials and Structures*, 11(1):1–8, 2002.

[171] A. Pramanick, D. Damjanovic, J. C. Nino, and J. L. Jones. Subcoercive Cyclic Electrical Loading of Lead Zirconate Titanate Ceramics I: Nonlinearities and Losses in the Converse Piezoelectric Effect. *Journal of the American Ceramic Society*, 92(10):2291–2299, 2009.

[172] A. Preumont. *Vibration Control of Active Structures: An Introduction*. Kluwer Academic Publishers, 2nd edition, 2002.

[173] A. Preumont. *Mechatronics*. Springer, 2006.

[174] A. Preumont, J. Dufour, and C. Malekian. Active Damping by a Local Force Feedback with Piezoelectric Actuators. *Journal of Guidance Control and Dynamics*, 15(2):390–395, 1992.

[175] J. G. Proakis and D. G. Manolakis. *Digital Signal Processing*. Prentice Hall, 1995.

[176] C. Raffel and J. Smith. Practical Modeling of Bucket-Brigade Device Circuits. In *13th International Conference on Digital Audio Effects, Proceedings of the*, pages 1–7, Graz, 2010.

[177] M. Rakotondrabe, C. Clévy, and P. Lutz. Complete Open Loop Control of Hysteretic, Creeped, and Oscillating Piezoelectric Cantilevers. *Automation Science and Engineering, IEEE Transactions on*, 7(3):440–450, 2007.

[178] S. S. Rao. *Mechanical Vibrations*. Addison-Wesley, 3rd edition, 1995.

[179] M. Ratnam, B. Bhikkaji, A. J. Fleming, and S. O. R. Moheimani. PPF Control of a Piezoelectric Tube Scanner. In *44th IEEE Conference on Decision and Control and European Control Conference, Proceedings of the*, pages 1168–1173, Seville, Dec. 2005.

[180] K. Reif, F. Sonnemann, and R. Unbehauen. An EKF-based nonlinear observer with a prescribed degree of stability. *Automatica*, 34(9):1119–1123, 1998.

[181] K. Reif, S. Gunther, E. Yaz, and R. Unbehauen. Stochastic Stability of the Discrete-Time Extended Kalman Filter. *Automatic Control, IEEE Transactions on*, 44(4):714–728, 1999.

[182] C. R. Rojas, J. S. Welsh, G. C. Goodwin, and A. Feuer. Robust optimal experiment design for system identification. *Automatica*, 43(6):993–1008, 2007.

[183] M. J. Rost, L. Crama, P. Schakel, E. van Tol, G. B. E. M. van Velzen-Williams, C. F. Overgauw, H. ter Horst, H. Dekker, B. Okhuijsen, M. Seynen, A. Vijftigschild, P. Han, A. J. Katan, K. Schoots, R. Schumm, W. van Loo, T. H. Oosterkamp, and J. W. M. Frenken. Scanning probe microscopes go video rate and beyond. *Review of Scientific Instruments*, 76(5):053710 (9 pages), 2005.

[184] M. J. Rost, G. J. C. van Baarle, A. J. Katan, W. M. van Spengen, P. Schakel, W. A. van Loo, T. H. Oosterkamp, and J. W. M. Frenken. Video-Rate Scanning Probe Control Challenges: Setting the Stage for a Microscopy Revolution. *Asian Journal of Control*, 11(2):110–129, 2009.

[185] L. Rundqwist. *Anti-Reset Windup for PID Controllers*. PhD thesis, Lund Institute of Technology, 1991.

[186] S. M. Salapaka and M. V. Salapaka. Scanning Probe Microscopy. *Control Systems Magazine, IEEE*, 28(2):65–83, 2008.

[187] S. M. Salapaka and A. Sebastian. Control of the Nanopositioning Devices. In *42nd IEEE Conference on Decision and Control, Proceedings of the*, pages 2644–2649, Maui, HI, 2003.

[188] S. M. Salapaka, A. Sebastian, J. P. Cleveland, and M. V. Salapaka. High bandwidth nano-positioner: A robust control approach. *Review of Scientific Instruments*, 73(9):3232–3240, 2002.

[189] D. Sarid. *Scanning Force Microscopy*. Oxford University Press, rev. edition, 1994.

[190] G. Schitter and N. Phan. Field Programmable Analog Array (FPAA) based Control of an Atomic Force Microscope. In *American Control Conference, Proceedings of the*, pages 2690–2695, Seattle, WA, 2008.

[191] G. Schitter and M. J. Rost. Scanning probe microscopy at video-rate. *Materials Today*, 11(S):40–48, 2008.

[192] G. Schitter and A. Stemmer. Fast closed loop control of piezoelectric transducers. *Journal of Vacuum Science & Technology B*, 20(1):350–352, 2002.

[193] G. Schitter and A. Stemmer. Identification and Open-Loop Tracking Control of a Piezoelectric Tube Scanner for High-Speed Scanning-Probe Microscopy. *Control Systems Technology, IEEE Transactions on*, 12(3):449–454, 2004.

[194] G. Schitter, P. Menold, H. F. Knapp, F. Allgöwer, and A. Stemmer. High performance feedback for fast scanning atomic force microscopes. *Review of Scientific Instruments*, 72(8):3320–3327, 2001.

[195] G. Schitter, R. W. Stark, and A. Stemmer. Sensors for closed-loop piezo control: strain gauges versus optical sensors. *Measurement Science and Technology*, 13:N47–N48, 2002.

[196] G. Schitter, F. Allgöwer, and A. Stemmer. A new control strategy for high-speed atomic force microscopy. *Nanotechnology*, 15:108–114, 2004.

[197] G. Schitter, R. W. Stark, and A. Stemmer. Fast contact-mode atomic force microscopy on biological specimen by model-based control. *Ultramicroscopy*, 100:253–257, 2004.

[198] G. Schitter, A. Stemmer, and F. Allgöwer. Robust Two-Degree-of-Freedom Control of an Atomic Force Microscope. *Asian Journal of Control*, 6(2): 156–163, 2004.

[199] G. Schitter, W. F. Rijkée, and N. Phan. Dual actuation for high-bandwidth nanopositioning. In *47th IEEE Conference on Decision and Control, Proceedings of the*, pages 5176–5181, Cancun, 2008.

[200] G. Schitter, P. J. Thurner, and P. K. Hansma. Design and input-shaping control of a novel scanner for high-speed atomic force microscopy. *Mechatronics*, 18(5-6):282–288, 2008.

[201] A. Sebastian and S. M. Salapaka. Design Methodologies for Robust Nano-Positioning. *Control Systems Technology, IEEE Transactions on*, 13(6):868–876, 2005.

[202] A. Sebastian, A. Pantazi, S. O. R. Moheimani, H. Pozidis, and E. Eleftheriou. A Self Servo Writing Scheme for a MEMS Storage Device with Subnanometer Precision. In *17th IFAC World Congress, Proceedings of the*, pages 9242–9247, Seoul, 2008.

[203] S. Seshagiri and H. K. Khalil. Robust output feedback regulation of minimum-phase nonlinear systems using conditional integrators. *Automatica*, 41:43–54, 2005.

[204] D. Simon. *Optimal State Estimation*. Wiley-Interscience, 2006.

[205] M. Sitti. Microscale and Nanoscale Robotics Systems. *IEEE Robotics & Automation Magazine*, 14(1):53–60, 2007.

[206] S. Skogestad and I. Postlethwaite. *Multivariable Feedback Control: Analysis and Design*. Wiley-Interscience, 2005.

[207] H. W. Sorenson. Least-squares estimation: from Gauss to Kalman. *Spectrum, IEEE*, 7(7):63–68, 1970.

[208] M. Steinbuch, S. Weiland, and T. Singh. Design of noise and period-time robust high-order repetitive control, with application to optical storage. *Automatica*, 43(12):2086–2095, 2007.

[209] C. Su. Industrial Perspectives of AFM Control. *Asian Journal of Control*, 11(2):104–109, 2009.

[210] V. L. Syrmos, C. T. Abdallah, P. Dorato, and K. Grigoriadis. Static Output Feedback—A Survey. *Automatica*, 33(2):125–137, 1997.

[211] N. Tamer and M. Dahleh. Feedback Control of Piezoelectric Tube Scanners. In *33rd IEEE Conference on Decision and Control, Proceedings of the*, pages 1826–1831, Lake Buena Vista, FL, 1994.

[212] X. Tan and O. Bennani. Fast Inverse Compensation of Preisach-Type Hysteresis Operators Using Field-Programmable Gate Arrays. In *American Control Conference, Proceedings of the*, pages 2365–2370, Seattle, WA, 2008.

[213] S. Tien and S. Devasia. Rapid AFM Imaging of Large Soft Samples in Liquid with Small Forces. *Asian Journal of Control*, 11(2):154–165, 2009.

[214] S. Tien, Q. Zou, and S. Devasia. Iterative Control of Dynamics-Coupling-Caused Errors in Piezoscanners During High-Speed AFM Operation. *Control Systems Technology, IEEE Transactions on*, 13(6):921–931, 2005.

[215] M. Tomizuka, T.-C. Tsao, and K.-K. Chew. Analysis and Synthesis of Discrete-Time Repetitive Controllers. *Journal of Dynamic Systems Measurement and Control, Transactions of the ASME*, 111(3):353–358, 1989.

[216] T. Tuma, J. Lygeros, A. Sebastian, and A. Pantazi. Optimal Scan Trajectories for High-Speed Scanning Probe Microscopy. In *American Control Conference, Proceedings of the*, pages 3791–3796, Montreal, 2012.

[217] R. Tyson. *Principles of Adaptive Optics*. CRC Press, 3rd edition, 2011.

[218] A. Visintin. *Differential Models of Hysteresis*, volume 111 of *Applied Mathematical Sciences*. Springer, 1994.

[219] W. Weaver, Jr., S. P. Timoshenko, and D. H. Young. *Vibration Problems in Engineering*. Wiley-Interscience, 5th edition, 1990.

[220] B. Widrow, I. Kollar, and M.-C. Liu. Statistical Theory of Quantization. *Instrumentation and Measurement, IEEE Transactions on*, 45(2):353–361, 1996.

[221] Y. Wu and Q. Zou. Iterative Control Approach to Compensate for Both the Hysteresis and the Dynamics Effects of Piezo Actuators. *Control Systems Technology, IEEE Transactions on*, 15(5):936–944, 2007.

[222] K. Yamada, T. Arakawa, H. Hoshi, and T. Okuyama. Two-Step Design Method for Robust Repetitive Control Systems. *JSME International Journal Series C: Mechanical Systems Machine Elements and Manufacturing*, 46(3): 1068–1074, 2003.

[223] K. Yamakawa, K. Furutani, and N. Mohri. XYZ-Stage for Scanning Probe Microscope by Using Parallel Mechanism. In *1999 ASME Design Engineering Technical Conferences, Proceedings of the*, pages 1–6, Las Vegas, NV, 1999.

[224] Y. Yamamoto. Learning Control and Related Problems in Infinite-Dimensional Systems. In H. Trentelman and J. Willems, editors, *Essays on Control: Perspectives in the Theory and Its Applications*, pages 191–222. Birkhäuser, 1993.

[225] Y. K. Yong, S. S. Aphale, and S. O. Reza Moheimani. Design, Identification, and Control of a Flexure-Based XY Stage for Fast Nanoscale Positioning. *Nanotechnology, IEEE Transactions on*, 8(1):46–54, 2009.

[226] Y. K. Yong, K. Liu, and S. O. R. Moheimani. Reducing Cross-Coupling in a Compliant XY Nanopositioner for Fast and Accurate Raster Scanning. *Control Systems Technology, IEEE Transactions on*, 18(5):1172–1179, 2010.

[227] D. Young and R. P. Felgar. Tables of Characteristic Functions Representing Normal Modes of Vibration of a Beam. The University of Texas, July 1949.

[228] R. Young. The Topografiner: An Instrument for Measuring Surface Microtopography. *Review of Scientific Instruments*, 43(7):999–1011, 1972.

[229] Q. Zhong, D. Inniss, K. Kjoller, and V. B. Elings. Fractured polymer/silica fiber surface studied by tapping mode atomic-force microscopy. *Surface Science*, 290:L688–L692, 1993.

[230] Q. Zou and S. Devasia. Preview-Based Optimal Inversion for Output Tracking: Application to Scanning Tunneling Microscopy. *Control Systems Technology, IEEE Transactions on*, 12(3):375–386, 2004.

[231] Q. Zou, K. K. Leang, E. Sadoun, M. Reed, and S. Devasia. Control Issues in High-speed AFM for Biological Applications: Collagen Imaging Example. *Asian Journal of Control*, Jan. 2004.